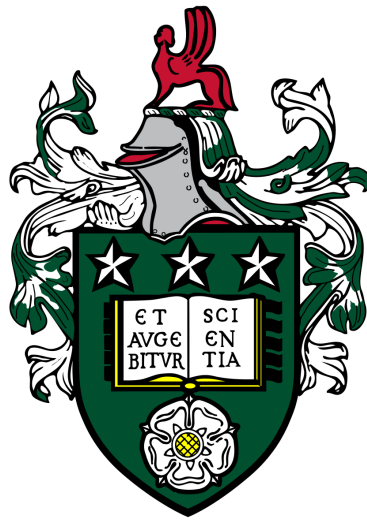# The effects of orbital configurations on the climate, habitability, chemistry and observability of Earth-like exoplanets

Binghan Liu

School of Physics and Astronomy

University of Leeds

Submitted in accordance with the requirements for the degree of

Doctor of Philosophy

September 2024

Intellectual Property

The candidate confirms that the work submitted is his own, except where work which has formed part of jointly authored publications has been included. The candidate confirms that appropriate credit has been given where reference has been made to the work of others. This copy has been supplied on the understanding that it is copyright material and that no quotation from the thesis may be published without proper acknowledgement.

Signed

Preface

The chapters in this thesis are based on work presented in the following publications:

1. Binghan Liu, Daniel R Marsh, Catherine Walsh, Greg Cooke, Higher water loss on Earth-like exoplanets in eccentric orbits, Monthly Notices of the Royal Astronomical Society, Volume 524, Issue 1, September 2023, Pages 1491–1502.

2. Binghan Liu, Daniel R Marsh, Catherine Walsh, Greg Cooke, Sainsbury-Martinez Felix, Eccentric orbits may enhance the habitability of earth-like exoplanets, Monthly Notices of the Royal Astronomical Society, Volume 532, Issue 4, August 2024, Pages 4511–4523.

This thesis consists of three main science chapters. The first and second chapters are based on published papers, while the third chapter presents research expected to be submitted for publication later this year.

The research was primarily conducted by Binghan Liu, under the supervision of Daniel R. Marsh and Catherine Walsh. Our team members, Greg Cooke and Sainsbury-Martinez Felix, provided invaluable support in resolving simulation-related issues and offered feedback on the two published papers. Greg Cooke was particularly instrumental in conducting most of the Proxima Centauri b simulations in the third science chapter. I extended his simulation cases by branch-running for additional outputs for several years, focusing on specific scientific questions. All the co-authors advised resolving the WACCM6 simulation crashes, while Greg Cooke offered advice on using the Planetary Spectrum Generator.

Acknowledgements

My passion for astronomy began in childhood when my father took me to the city square in my hometown, where amateur astronomers gathered to stargaze using their telescopes. Gazing at the night sky, I wondered about the mysteries beyond the shining stars, and a seed of curiosity was planted deep in my heart.

Although I experienced many difficulties, my enthusiasm for astronomy never waned. After my parents' divorce when I was a high school student, my mother decided to immigrate our family to Canada, which was a significant change in my life. The passing of my father due to a heart attack in China on what was supposed to be a day of celebration for my birthday was an incredibly sad moment for me. Attending his funeral made me realize how short life is and motivated me to pursue something meaningful.

I worked hard during the remainder of my undergraduate studies at the University of British Columbia, improving my grades and adding mathematics as a double major alongside astronomy. While many of my friends had already graduated and started their careers at the time, I felt pressure when comparing myself to others of the same age. Nonetheless, I decided to continue my education. Completing a master's degree in astrophysics at Queen Mary University of London boosted my confidence, as I excelled in my exams and my thesis. This milestone encouraged me to take another step forward.

Starting my PhD studies abroad in 2019 was a significant decision, especially as the world faced the COVID-19 pandemic and ensuing lockdowns. I am very fortunate to have found my supervisors, Prof. Dan Marsh and Dr. Catherine Walsh, who are incredibly

supportive, sincere, and encouraging, and my interest in exoplanetary science and my childhood dreams aligned perfectly with their research projects.

The first year of my PhD was mentally challenging. The pandemic isolated me from the outside world as I was confined to the university dormitory alone, suffering feelings of depression and homesickness. However, the encouragement and care from my supervisors pulled me out of that difficult time. Their support rekindled my determination not to give up on my dream and to contribute, even in a small way, to the research community. I am proud to have published two papers in the field that have fascinated me since childhood.

I want to express my deepest gratitude to my supervisors for their unwavering support, guidance, and encouragement throughout the past four years at the University of Leeds. I am also sincerely grateful to the members of our research group, especially Greg and Felix, for their time, constructive comments, and valuable suggestions that significantly contributed to this research.

I appreciate all my peers at the School of Astrophysics, especially Greg, Marcin, Heather, Isaac, Eve, Rob, Joe, Sam and Javiera, for their collaborative spirit, open discussions, and constant support, which made my graduate experience pleasant.

Special thanks to my family for their unconditional love and encouragement. To my mother, Jane, and my stepfather, Peter, thank you for your steady belief in me and for instilling the values of perseverance. To my girlfriend at the time, Grace, your patience, understanding, and love have been my anchor throughout this journey. To my lovely cat, Morty, thank you for your companionship and for always being there with me during the long nights of work.

Lastly, I would like to thank all those who have, in one way or another, contributed to the completion of this thesis. Your support is unforgettable, and I am truly fortunate to have you in my life.

Abstract

Understanding the climates and habitability of Earth-like exoplanets is important for assessing the potential for life beyond our Solar System. These planets are influenced by a complex interplay of factors, including host star type, atmospheric composition, surface characteristics, and orbital configurations such as high eccentricity and tidal locking. Many rocky exoplanets exhibit higher orbital eccentricities than those in our Solar System, and terrestrial exoplanets orbiting M dwarfs are often tidally-locked due to their proximity to the host stars.

In this thesis, I employ the Whole Atmosphere Community Climate Model Version 6 (WACCM6), a fully coupled Earth-system model, to simulate and examine the climates of Earth-like exoplanets in highly eccentric and tidally-locked orbits. I aim to provide a basic understanding of how these two orbital parameters influence planetary climate, surface habitability and observational signatures. My simulations reveal that orbital eccentricity and tidal locking both have a significant and distinct impact on the climate. A highly eccentric Earth-like exoplanet ($e = 0.4$) exhibits a warmer global mean surface temperature than its circular orbit counterpart ($e = 0$) due to lower surface and cloud albedo and weaker longwave cloud forcing. The seasonally asymmetric stellar irradiance in the highly eccentric orbit redistributes surface albedo feedback and cloud radiative effects spatially and temporally. This leads to an increased surface temperature, with enhanced meridional heat transport when the planet is closer to its star, improving habitability at higher latitudes. Additionally, we find a non-linear rise in stratospheric water vapor concentration as surface temperatures increase, which drives a corresponding

annual mean increase in water loss rates via the thermal escape of hydrogen species. Despite the higher water loss rate, the highly eccentric Earth-like planet can retain its water reservoir throughout the system's lifetime. For a case study of the tidally-locked Proxima Centauri b with the substellar point over the Pacific Ocean, our results reveal a colder climate than pre-industrial Earth, attributed to lower stellar irradiance, higher surface albedo, and reduced greenhouse effects. Nonetheless, the planet sustains an "eyeball-shaped" open ocean around the substellar point. The stratospheric ozone layer is significantly thinner than that of the pre-industrial Earth, largely due to reduced atomic oxygen production resulting from the lower photolysis rate of molecular oxygen and water vapor, a consequence of the host star's weaker ultraviolet radiation. Notably, atmospheric circulation, ocean dynamics and topography are critical in modulating the day-night temperature contrast and shaping the ozone distribution of the tidally-locked planet. We find that the surface ozone levels remain below harmful concentrations, further supporting the potential habitability in the open ocean region.

Using the Planetary Spectrum Generator, we simulate idealized spectra for both studies considering eccentricity and tidal locking effects. The highly eccentric planet shows stronger water vapor absorption features, suggesting that such exoplanets may be prime targets for future atmospheric characterization. For the tidally-locked planet, water vapor signals are much weaker despite the planet being an ocean world. Nevertheless, ozone and carbon dioxide produce the more notable absorption features in the spectra, indicating a higher possibility of detection through direct imaging and transmission spectroscopy.

Overall, this thesis highlights the profound impact of orbital configurations, such as eccentricity and tidal locking, on the climate dynamics, atmospheric composition, potential habitability and theoretical observations of Earth-like exoplanets. My research addresses the necessity of using comprehensive three-dimensional global circulation models coupled with interactive chemistry and ocean dynamics to better assess the spatial and temporal variations in climate. This research contributes to the broader quest to identify and

characterize potentially habitable worlds beyond our Solar System.

Contents

List of Figures

List of Tables

Chapter 1

Introduction

Are we alone in the Universe? For centuries, this profound question was primarily the domain of philosophy and science fiction. However, recent advancements in observational techniques, telescopes and sophisticated modelling have significantly enhanced our ability to address this enduring question. Since the first confirmed exoplanet detection around a pulsar in 1992 (Wolszczan et al., 1992) and the discovery of 51 Pegasi b around a G dwarf in 1995 (Mayor et al., 1995), the number of known exoplanets has surged to over 5700 as of 2024 (NASA Exoplanet Science Institute, 2024). The search for life beyond our solar system has shifted from speculation to systematic investigation. Central to this quest is the study of Earth-like exoplanets, worlds orbiting stars outside our solar system that might share the fundamental characteristics necessary for life as we know it. Yet, the potential habitability of these planets is influenced by their orbital configurations. Variations in orbital parameters can shape a planet's climate, alter its atmospheric chemistry, and impact the habitability and potential bio-signatures.

I used WACCM6, a state-of-the-art Earth System Model, to explore how different orbital configurations, such as eccentricity, obliquity, and tidal locking, can influence Earth-analogue or Earth-like exoplanets' climate, atmospheric chemistry, habitability, and observability. While the terms "Earth-analogue" and "Earth-like" are often used interchangeably, this thesis distinguishes them based on the extent of model modifica-

tions. Earth-analogues, which involve changes only in orbital configurations without altering internal parameters, are considered in our studies of orbital eccentricity. In contrast, Earth-like exoplanets, as in our simulations of Proxima Centauri b, involve modifications to planetary radii and rotation rates while leaving most internal parameters unchanged. This chapter introduces observations, climate modelling, habitability studies, and fundamental knowledge of terrestrial exoplanets' atmospheres, providing the necessary background for understanding the research.

1.1 Exoplanet Observations

The number of confirmed and candidate exoplanets has surged rapidly over the past two decades. This increase is driven by significant advancements in observational techniques, the development of more powerful telescopes, and humanity's enduring curiosity about the universe. Figure 1.1 shows the cumulative number of exoplanets over time, highlighting the surge in discoveries following the launch of dedicated space missions such as Kepler. However, an Earth-analogue exoplanet has yet to be found, and many of the discovered exoplanets are distinctly different from our solar system planets. This diversity of exoplanets challenges our understanding of planetary formation and habitability archetypes.

Figure 1.1 illustrates 11 different detection methods, each with its own strengths and limitations (Ramirez et al., 2013). The majority of exoplanet discoveries have been made using four primary methods: the transit method (T), radial velocity (RV), gravitational microlensing (M), and direct imaging (I). Among these, the transit and direct imaging methods are particularly notable for their success in detecting exoplanets and their applications in observing and characterising the atmospheres of these distant worlds. This section briefly introduces the transit and direct imaging methods, as well as their applications in transit spectroscopy and direct imaging spectroscopy for studying the atmospheres of rocky planets beyond our solar system.
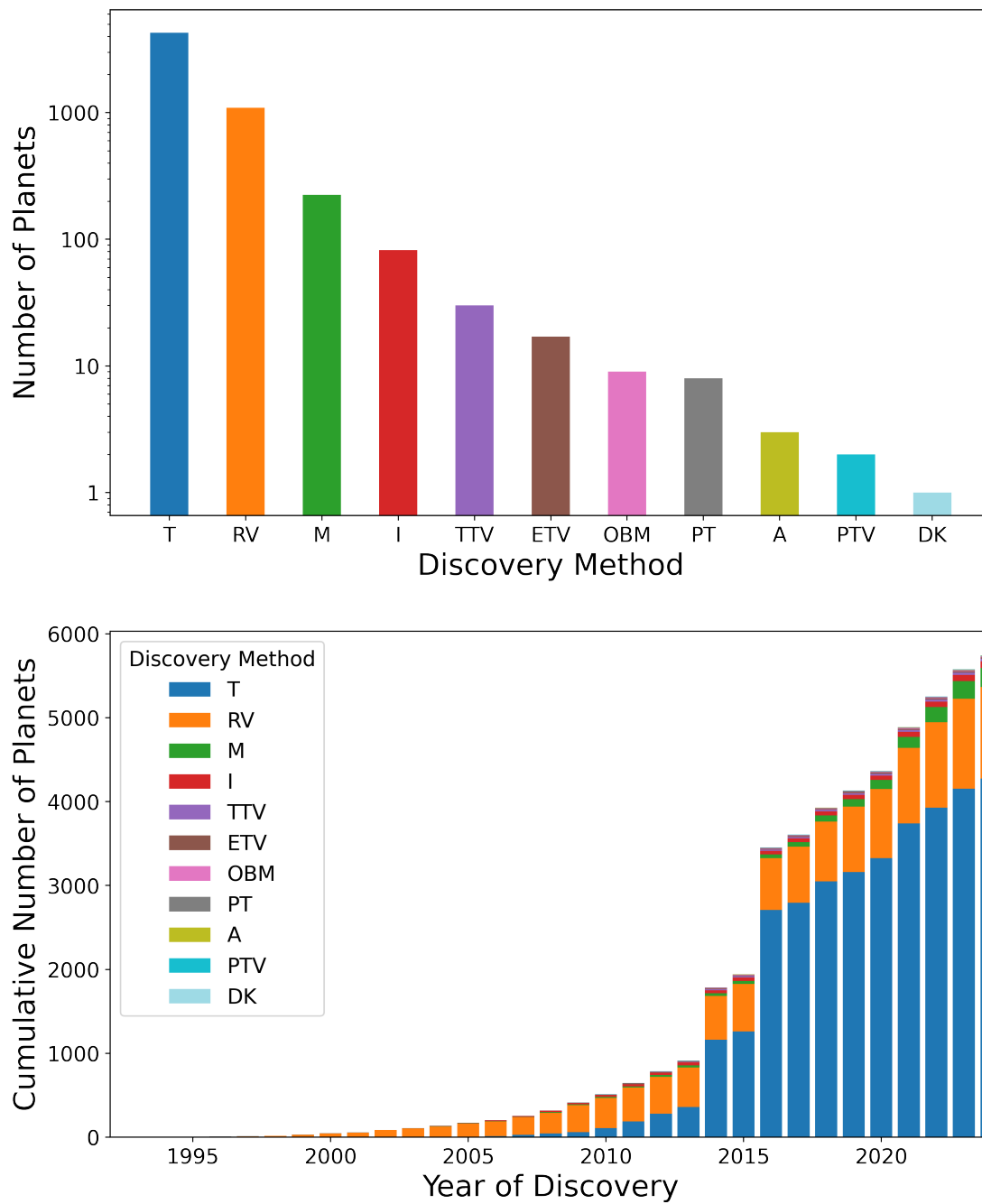
Figure 1.1: Figure illustrates the distribution of exoplanets discovered using different detection methods, according to data from the NASA Exoplanet Archive. The detection methods are labelled as T (Transit), RV (Radial Velocity), M (Microlensing), I (Direct Imaging), TTV (Transit Timing Variations), ETV (Eclipse Timing Variations), OBM (orbital brightness modulation), PT (Pulsar Timing), PTV (Pulsation Timing Variations), A (Astrometry), and DK (Disk Kinematics)

1.1.1 Transit Observations

The transit method is the most successful of these primary detection techniques, accounting for over 4000 confirmed exoplanets. This method involves monitoring a star's light over time; if an exoplanet passes in front of the star in its orbit, a portion of the starlight is blocked, causing a measurable dimming. The extent of this dimming is directly related to the planet's size relative to the star, allowing for the calculation of the planet's radius if the stellar radius is known (see Figure 1.2 for a demonstration). Space-based missions, such as the 2009-launched Kepler spacecraft, have significantly advanced the number of exoplanet discoveries by the transit method. This spacecraft discovered over 2700 confirmed exoplanets, and the mission was later extended (dubbed K2), adding over 500 confirmed exoplanets (see NASA Exoplanet Science Institute, 2024). The Transiting Exoplanet Survey Satellite (TESS), launched in 2018, has further contributed to the discovery of over 7000 candidate exoplanets, with over 500 confirmed so far and many more expected to be confirmed in the coming years (see NASA Exoplanet Science Institute, 2024). Compared to the Kepler mission, TESS conducts a much larger, nearly all-sky survey that includes the Kepler field with extended observation time, contributing to the discovery of additional exoplanets and enabling more precise characterization of planetary orbital parameters (Christ et al., 2019; Kane et al., 2021).

When an exoplanet with an atmosphere transits its star, the observed specific flux can be expressed by considering the atmospheric absorption. If the exoplanet had no atmosphere, the flux F_{tel} observed by the telescope would be reduced solely by the opaque disk of the planet, given by:

$$F_{\text{tel}} = F_* \left(1 - \frac{\pi R_{\text{p}}^2}{\pi R_*^2} \right) \tag{1.1}$$

Here, R_{p} and R_* are the radii of the exoplanet and the host star, respectively, and F_*
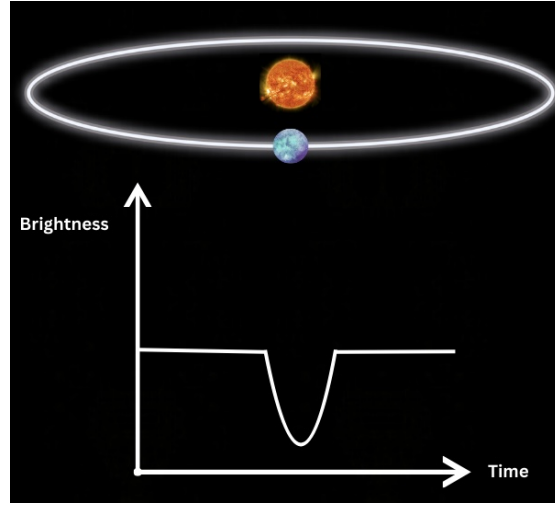
Figure 1.2: Demonstration of a planet transiting its host star, resulting in the stellar brightness dimming during the transit. Image credit. B. Liu.

is the incident flux from the star. This equation reflects the fraction of starlight blocked by the planet.

However, when atmospheric absorption is included, this expression becomes:

$$F_{\text{tel}} = F_* \left(1 - \frac{\Sigma_\lambda + \pi R_{\text{p}}^2}{\pi R_*^2} \right) \tag{1.2}$$

$$= F_* \left(1 - \frac{\pi (R_{\text{p}} + \Delta R_\lambda)^2}{\pi R_*^2} \right) \tag{1.3}$$

Here, Σ_λ represents the equivalent disk surface area of absorption due to the wavelength-dependent atmospheric opacity, as described by Figure 1.3 in Ehrenreich et al. (2006). The value of Σ_λ depends on factors such as atmospheric pressure, temperature, and chemical composition and is given by:

$$\Sigma_\lambda = 2\pi \int_{R_{\text{p}}}^{b_{\text{max}}} b \left(1 - e^{-\tau(b)} \right) db \tag{1.4}$$

5

In this equation, b is the impact parameter, $\tau(b)$ is the optical depth as a function of b, and b_{max} is the maximum impact parameter, which refers to the altitude above which a molecular species in the atmosphere (such as H_2O, O_3, CO_2, O_2) is likely to be destroyed or modified either by photolysis or ionizing radiation, such as Lyman-alpha or EUV (Ehrenreich et al., 2006). So, Σ_λ increases for a denser atmosphere or one with molecules strongly absorbing at the observed wavelength. Alternatively, the flux can also be described using an effective altitude ΔR_λ, representing the planet's apparent radius increase (i.e., effective height) due to the atmosphere's opacity at a specific wavelength (λ).
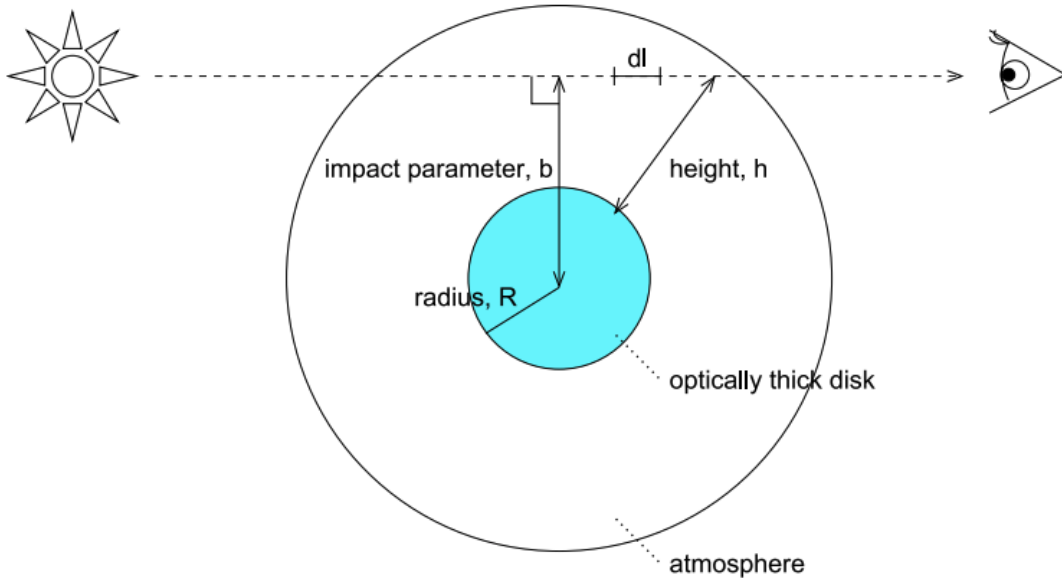
Figure 1.3: Adapted from Ehrenreich et al. (2006): schematic view of the transmitted stellar radiation through the planetary atmosphere. The planet is optically thick and is indicated as a solid circle (blue) with a radius R. The absorption of the stellar radiation occurs along the line of sight dl with an altitude h and impact parameter b.

The transit method allows astronomers to determine the size of a transiting planet by analyzing the light curve during the transit event. When combined with the radial velocity method, which measures the planet's mass, it becomes possible to calculate its density, providing valuable insights into the planet's interior composition and structure. As the planet transits its star, starlight passes through and interacts with the planet's

atmosphere, where different wavelengths of light are absorbed or scattered depending on the atmospheric constituents present. Transmission spectroscopy, obtained by subtracting the in-transit spectrum from the out-of-transit spectrum, reveals features in the chemical absorption, aerosol scattering, cloud and haze optical effects at the day-night terminator of the planet. For example, in the ultraviolet (UV) range, absorption can occur due to ozone in the Hartley and Huggins bands between 200-360 nm, and ionized metals may be absorbed in the Lyman-α region (~ 121.5 nm). In the visible spectrum, Rayleigh scattering and the absorption by metal elements and oxides, such as sodium (Na), potassium (K), and titanium oxide (TiO), are prominent. In the infrared spectrum, molecules such as water (H_2O), methane (CH_4), carbon monoxide (CO), carbon dioxide (CO_2), and ozone (O_3) play significant roles in absorption (e.g. Madhusudhan et al., 2016).

Transmission spectroscopy, when combined with spectra retrieval methods, is a powerful tool for characterizing planetary atmospheres. Spectra retrieval methods work by identifying the model parameters that best match the observed data, thereby constraining the properties of the planetary atmosphere. For instance, LHS 1140 b, a planet with a mass of 5.6 $M_\oplus$ and a radius of 1.73 $R_\oplus$, is located within the radius valley—a rare zone that separates rocky super-Earths from mini-Neptunes, typically between 1.5 to 2 $R_\oplus$ (Fulton et al., 2017). Initially, there was uncertainty regarding whether LHS 1140 b was a mini-Neptune with a thin hydrogen atmosphere or a water world (a mini-Neptune with a substantial fraction of its mass composed of water) (Cadieux et al., 2024b). This uncertainty exists because planets with the same mass and radius can have varying interior compositions and structures. The spectra retrieval method helps resolve this ambiguity by ruling out unphysical atmospheric compositions based on observational data. Using the NIRSpec instrument on James Webb Space Telescope (JWST), the scenario of LHS 1140 b being a mini-Neptune with a thin hydrogen atmosphere was ruled out, favouring the possibility that it is more likely a water world (Damiano et al., 2024; Cadieux et al., 2024a). Furthermore, recent JWST transit spectroscopy has detected

CH_4 and CO_2 in the atmospheres of sub-Neptune planets K2-18 b (Madhusudhan et al., 2023) and TOI-270d (Benneke et al., 2024), enhancing our understanding of atmospheric characterization in the sub-Neptune regime.

Besides the study of super-Earth and sub-Neptune planets, the search for rocky planet atmospheres around M dwarf stars is a major focus of JWST due to the favourable planet-to-star size ratios and the proximity of the habitable zone around the host star, which can enhance the detectability of atmospheric features. Also, M dwarfs are the most common type of stars in the Universe. This is because they are formed in significantly greater numbers than higher-mass stars, as described by the Initial Mass Function (IMF) which represents the distribution of stellar masses that form in one star formation event in a given volume of space (e.g. Kroupa, 2002; Li et al., 2023), and their long lifespans (Adams et al., 1997; Laughlin et al., 1997; Bochanski et al., 2010, e.g.). It is estimated for the lowest-mass main sequence stars ($> 0.08 \ M_\odot$) that the hydrogen-burning timescale is on the order of 10^{13} years (Laughlin et al., 1997). For example, the hydrogen-burning timescale is estimated to be on the order of 10^{13} years for the lowest-mass main sequence stars ($0.08 \ M_\odot$) (Laughlin et al., 1997). As a result, the statistical likelihood of finding potentially habitable exoplanets around M dwarfs is much higher than around other types of stars (Shields et al., 2016a). However, little is currently known about the compositions of these planets, and solid evidence of atmospheres around terrestrial exoplanets orbiting M dwarfs has yet to be confirmed (e.g. Lustig-Yaeger et al., 2023; Lincowski et al., 2023). Given the highly variable and extreme UV radiation environments of M dwarfs (e.g. Van Looveren et al., 2024), the persistence of a secondary atmosphere remains uncertain (e.g. Van Looveren et al., 2024; Diamond-Lowe et al., 2024).

Characterizing the atmospheres of rocky planets around M dwarfs using transmission spectroscopy is an ongoing focus of JWST's Near InfraRed Spectrograph (NIRSpec). While direct imaging of the TRAPPIST-1 system remains beyond current capabilities, secondary eclipse observations of TRAPPIST-1 b from JWST's Mid-Infrared Instrument (MIRI) (Greene et al., 2023) and TRAPPIST-1 c (Zieba et al., 2023) have shown that

TRAPPIST-1 b is consistent with having no atmosphere, and that TRAPPIST-1 c could either be a bare rock or host a thin atmosphere. Follow-up studies on TRAPPIST-1 c compared the observed secondary eclipse depth with synthetic spectra across a broader range of plausible environments. These studies confirmed that a thick atmosphere is implausible for TRAPPIST-1 c but found that a wider range of thin atmospheres remains possible; however, additional data is needed to discriminate between these possibilities or to confirm the bare rock scenario proposed earlier (Lincowski et al., 2023). Another example is LHS 475 b, a rocky exoplanet with a size nearly identical to Earth (0.99 $R_{\oplus}$), was first detected by TESS and later confirmed by JWST. Its featureless near-infrared transmission spectra leave several possibilities open: the planet may possess a high-altitude cloud deck similar to Venus, a thin atmosphere like Mars, or it might lack a significant atmosphere entirely, resembling Mercury (Lustig-Yaeger et al., 2023). Similarly, other terrestrial planets around M dwarfs, such as GJ 341 b (Kirk et al., 2024), GJ 1132 b (May et al., 2023), and GJ 486 b (Moran et al., 2023), have also shown spectra consistent with the absence of an atmosphere. In these studies, the challenge lies in distinguishing whether deviations from a featureless spectrum are due to stellar flare contamination or the presence of an atmosphere, addressing the importance of multi-visit repeatability with JWST before making definitive claims about atmospheric detections.

1.1.2 Direct Imaging Observations

Unlike indirect methods like the transit or radial velocity methods, direct imaging is a method that involves capturing the actual light of exoplanets by separating the light from the planet from the overwhelming glare of its host star. This technique is particularly useful for detecting planets far from their host stars, where the contrast between the star's brightness and the planet's reflected light is less extreme. Direct imaging is a challenging technique because stars are immensely brighter than the planets that orbit them—often by a factor of 10^{10} for Earth-like planets in the habitable zone (e.g. Currie et al., 2023).

To overcome this challenge, coronagraphs are equipped on telescopes to block out the star's light, allowing the much fainter light from the planet to be detected (e.g. Currie et al., 2023). Additionally, adaptive optics (AO) systems are used for ground-based telescopes to correct for the distortion caused by Earth's atmosphere, producing sharper images (e.g. Hippler, 2019).

Using a spectrograph, the light from a planet produced by the direct imaging method can be divided into two distinct components: reflection and emission (infrared). The reflection spectra capture the stellar radiation reflected by the planet in the UV and visible ranges, while the emission spectra reveal the planetary flux emitted at the infrared wavelengths. For a face-on orbit, where the inclination angle is 0°, observations capture a mix of both the day-side and night-side hemispheres, which is similar to an edge-on orbit at quadrature phase. In contrast, for a transiting orbit with an inclination angle of 90°, the optimal time to observe a planet using the direct imaging method is just before it enters its secondary eclipse or occultation, close to an orbital phase of 180°, when one side of the planet is nearly fully illuminated (Madhusudhan, 2018). The spectra obtained from direct imaging are often presented in units of the planet-star flux ratio (ppm) due to the relatively small amount of flux reflected or emitted by the planet compared to that of the star. By probing the thermal emission across specific wavelength bands as a function of the orbital phase, astronomers can generate a phase curve that reveals variations in the signal, offering insights into potential seasonality and heat redistribution due to atmospheric circulation.

To date, thermal emission observations have characterized several rocky planets around M dwarfs as bare rock planets. For instance, LHS 3844 b, a rocky planet with a radius of 1.3 $R_\oplus$ orbiting an M dwarf, has been shown to be consistent with having no atmosphere since the spectral retrieval indicated that the data are best fitted by a bare-rock model with a low Bond albedo (Kreidberg et al., 2019). Similarly, GJ 1252 b, a hot rocky super-Earth, has also been shown to lack a significant atmosphere based on data from the Spitzer Space Telescope (Crossfield et al., 2022). Recent spectroscopic emission

observations of hot Earth-sized planets around M dwarfs have generally refuted the existence of thick atmospheres, suggesting that any atmospheres on such short-period planets struggle to survive. Nevertheless, the airless worlds that are to be confirmed can help us narrow down the distribution and abundance of potentially habitable worlds around M dwarfs.

1.1.3 Future Observations

As discussed above, the presence of atmospheres on rocky planets around M dwarfs has not been completely ruled out by recent transit and direct imaging observations. M dwarfs, particularly late M dwarfs, are among the most active stars, and their stellar activity poses significant challenges to detecting and characterizing exoplanetary atmospheres (Roettenbacher et al., 2017). Discriminating between stellar contamination and genuine atmospheric signals in observed spectra requires follow-up observations to refute, or otherwise, the presence of an atmosphere.

In the next decades, detecting and characterizing Earth-analogue exoplanets in the habitable zone for habitability and biosignature studies remains a central goal for next-generation telescopes and missions. For example, Proxima Centauri b, the closest known exoplanet to Earth, is unlikely to transit and, hence, is a promising target for future direct imaging observations (Kipping et al., 2017; Vaughan et al., 2024). Ground-based telescopes like the Extremely Large Telescope (ELT, Gilmozzi et al. (2007) and Padovani et al. (2023)) are expected to provide the spectral and angular resolution necessary to detect Earth-sized rocky worlds around G-type stars (Snellen et al., 2013; Vaughan et al., 2024). Future space telescopes, such as the PLAnetary Transits and Oscillations of stars (PLATO), aim to detect terrestrial exoplanets in the habitable zone around Sun-like stars using the transit method (Rauer et al., 2016). Moreover, future space telescopes and concept missions such as the Habitable Worlds Observatory (HWO) and the Large Interferometer For Exoplanets (LIFE) mission will characterize the atmospheres of long-period rocky planets and search for potential biosignatures through direct imag-

ing spectroscopy (Quanz et al., 2022). Furthermore, it has been suggested that HWO could detect exomoons around Earth-sized rocky exoplanets by observing mutual stellar and lunar eclipse events, by which the effects of exomoons or exorings on potentially habitable planet observations could be disentangled (Limbach et al., 2024).

1.2 Climate Modelling

With the rapid advancement of next-generation telescopes, we are entering a new era in which the detection and characterization of terrestrial exoplanetary atmospheres are becoming increasingly feasible. Meanwhile, growing research using numerical models to simulate the potential climate states of these planets enables us to better predict and understand the actual climate of the exoplanets. Climate refers to the statistical description of the mean and variability of relevant quantities, such as surface temperature, over periods ranging from months to millions of years (Intergovernmental Panel on Climate Change (IPCC), 2023). The concept of "radiative forcing," or simply "forcing," is widely used in climate studies to compare the climatic effects of various planetary changes. A strong radiative forcing is generally expected to result in a significant and proportionate change in global mean temperature (e.g. Carslaw, 2022). Figure 1.4 illustrates a broad range of periodic climate variations across timescales from millions of years to days, alongside corresponding external forcings and internal variability mechanisms (see the figure caption for more details). This thesis focuses on macroweather climate, evaluating (inter)annual mean and seasonal climate variability of Earth-analogue and Earth-like exoplanets. The climate models used for studying rocky exoplanets generally span macroweather to macroclimate scales unless specified otherwise. Short-timescale climate (i.e., weather) involves greater uncertainty and requires higher grid resolution, making it more suited for regional weather forecasts. On the other hand, megaclimate variability requires model simulations over millions of years, and the associated internal variability, such as tectonism, is beyond the scope of current remote observations.
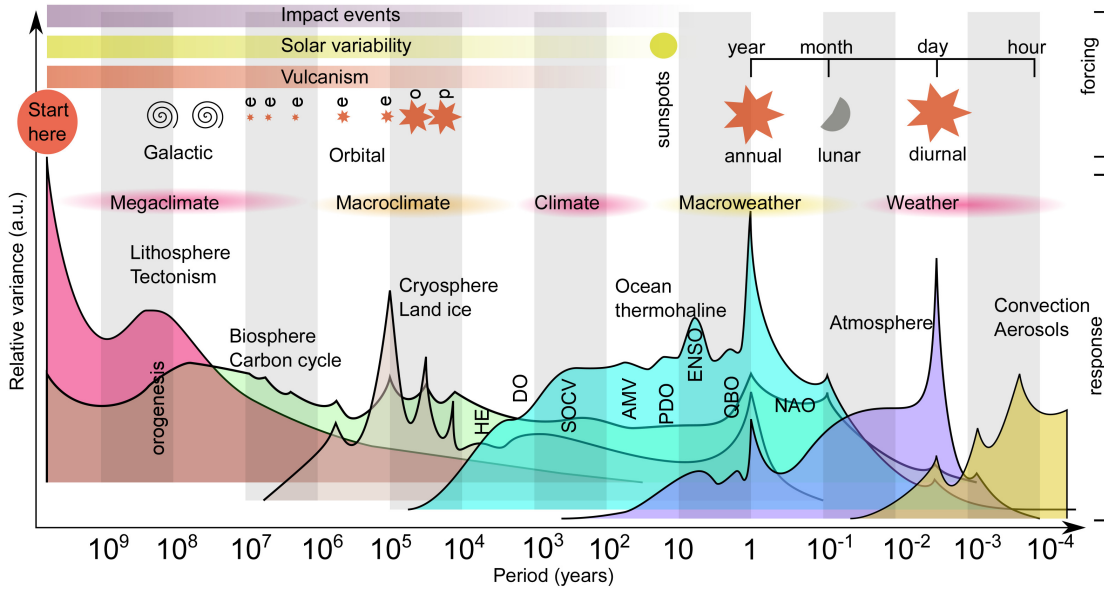
Figure 1.4: Adapted from von der Heydt et al. (2021): This figure illustrates a broad range of climate variations spanning timescales from millions of years to days. The upper part highlights external forcings, while the lower part illustrates internal variabilities. Different climate definitions are also provided based on their timescale, such as megaclimate, which refers to climate behavior over galactic timescales (10^7 to 10^9 years), and macroweather, which covers climate variations from a month to a few decades. Abbreviations of a list of Earth's climate variability modes are shown in the cyan region according to their respective timescales, including HE (Heinrich Event), DO (Dansgaard Oeschger Event), SOVC (Southern Ocean Centennial Variability), AMV (Atlantic Multidecadal Variability), PDO (Pacific Decadal Oscillation), ENSO (El Nino-Southern Oscillation), QBO (Quasi-biennial Oscillation) and NAO (North Atlantic Oscillation).

1.2.1 Model Hierarchy

Climate models have evolved in complexity, starting from simple zero-dimensional energy balance models (EBMs) and one-dimensional column models to more advanced 3D global circulation models (GCMs) and Earth system models (ESMs). As models become more comprehensive, they incorporate more mathematical and physical factors to better explain and predict real-world climate systems based on observations. However, this increasing complexity can sometimes make the models difficult to understand, as noted by Polvani et al. (2017). Additionally, complex models are computationally expensive and often lack the flexibility of simpler models, making it challenging to simulate long-term climate evolution on timescales greater than 10^3 years or to explore a wide range of parameter spaces. As the well-known phrase from Box (1979) suggests, "All models

are wrong, but some are useful", highlighting the need for a spectrum of models with varying degrees of complexity tailored to different scientific objectives.

Figure 1.5, adapted from Bony et al. (2013), illustrates the complexity of climate models along two axes: simplicity in understanding (y-axis) versus system complexity (x-axis). The "Platonosphere" at the top represents the fundamental laws we understand, while the conceptual and understanding abyss refers to processes that are both conceptually and computationally challenging. Bony et al. (2013) argue that simpler models are essential for understanding underlying processes, especially when those that more complex models struggle to explain. They emphasize the need to "close the conceptual gaps" by developing a framework that connects model behaviour across different levels of realism and simplification.

Figure 1.6, adapted from Maher et al. (2019), shows how simple atmospheric models connect to reality through a sequence of models, with Atmospheric General Circulation Models (AGCMs) positioned within the model hierarchy. The figure highlights different hierarchies: dynamical (equations), process (boundary conditions and diabatic processes), and scale (convective organization across varying domain sizes and resolutions).

Recent advancements in machine learning (ML) have introduced a powerful data-driven method in climate modelling, leveraging vast datasets to learn complex, nonlinear relationships. Unlike traditional models based on physical principles, ML models primarily rely on empirical data, offering a novel approach to modelling processes, weather forecasting, and climate systems. These models complement the existing model hierarchy by improving accuracy, accelerating simulations, and uncovering new insights. ML approaches are increasingly integrated into climate studies, enabling process isolation and model calibration (Mansfield et al., 2023).
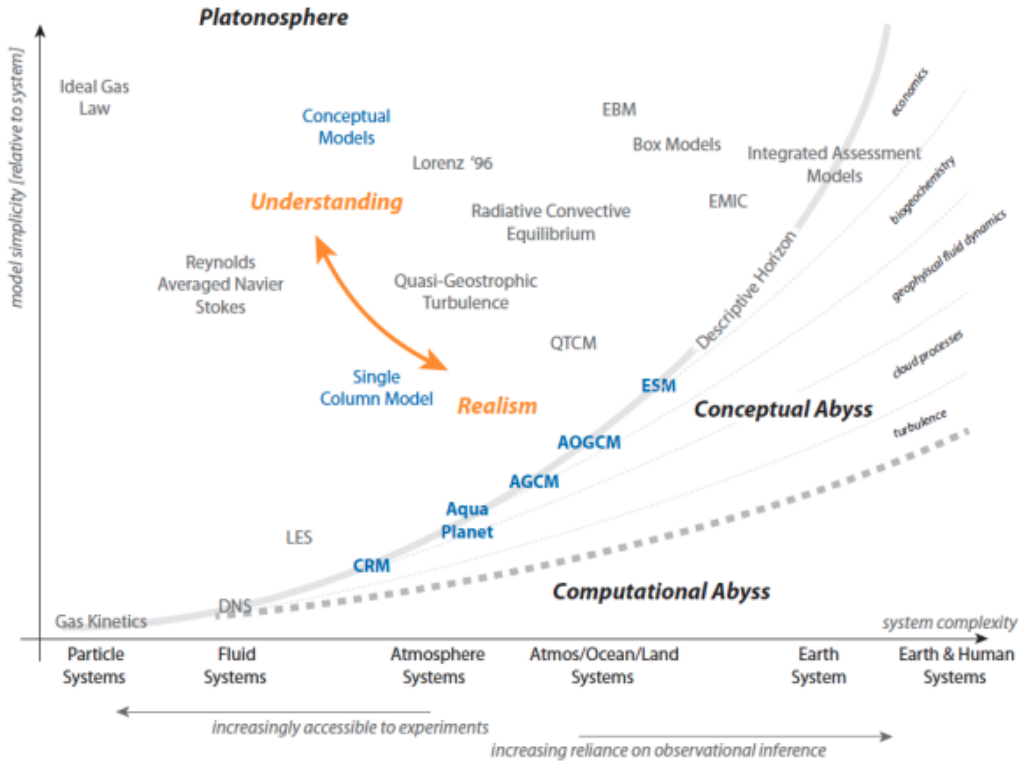
Figure 1.5: Adapted from Bony et al. (2013): This figure illustrates the distribution of models based on their simplicity relative to the system they aim to represent (vertical axis) and the system's complexity (horizontal axis). Adding more complexity doesn't necessarily enhance realism if underlying processes are not fully understood with simpler models. Progress requires bridging conceptual gaps across models with varying realism, advancing understanding through a framework that connects model behaviours across this abstraction-complexity space.

1.2.2 Energy Balance Model

The simplest climate model, known as the Energy Balance Model (EBM), is derived from the basic principle that in a closed system, the energy entering the system should equal the energy leaving it. In this context, the planet absorbs stellar radiation (shortwave) and emits infrared radiation (longwave) as a blackbody:

$$\frac{S}{4}(1 - A) = \sigma T_s^4 \tag{1.5}$$

15
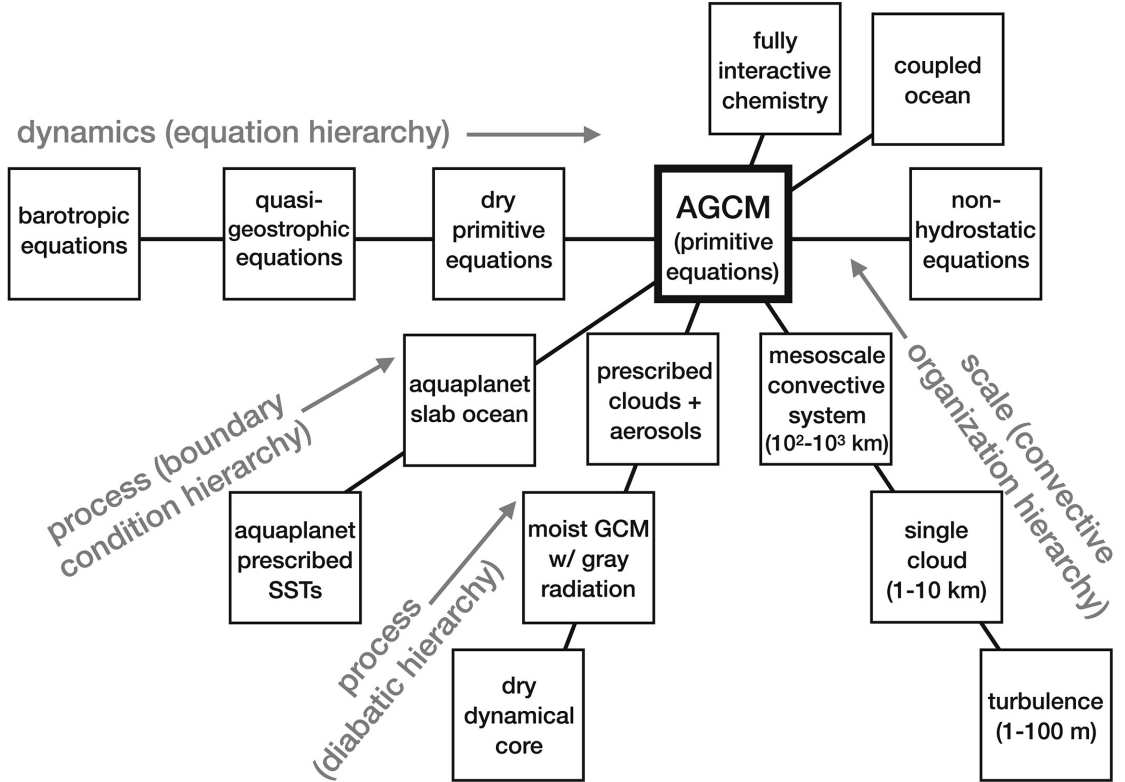
Figure 1.6: Adapted from Maher et al. (2019): This figure illustrates the connection between simple atmospheric models and comprehensive models used for weather and climate prediction. It complements Figure 1.5, highlighting the links to Atmospheric General Circulation Models (AGCMs) through different hierarchies: dynamical (equations), process (boundary conditions and diabatic processes), and scale (convective organization across varying domain sizes and resolutions).

Rearrange it, we get:

$$T_s^4 = \frac{S(1 - A)}{4\sigma} \tag{1.6}$$

Where T_s is the equilibrium surface temperature of the planet (in K), S is the stellar flux at the planet's orbital distance (in W m^{-2}), A is the planetary albedo, σ is the Stefan-Boltzmann constant (in kg s^{-3} K^{-4}). The factor of 4 arises from the difference in geometry: while the stellar flux S is incident on a circular disk with an area of πR^2 where R is the planetary radius (in m) at the planet's orbital distance, the total surface area of the planet is $4\pi R^2$. Therefore, the planetary surface, on average, receives $\frac{S}{4}$ of

the stellar flux.

Using this basic EBM with Earth's planetary albedo $A = 0.3$ and solar constant $S = 1365\,\mathrm{W\,m^{-2}}$ results in a surface temperature of 255 K. This is much colder than Earth's actual temperature, suggesting that Earth would be outside its habitable zone.

To account for the greenhouse effect, which warms the Earth's surface above the temperature predicted by the simple EBM, we can assume a fixed transmissivity τ for the atmosphere. This transmissivity conceptually represents the fraction of the emission from the surface that makes it all the way to space $(\tau \sigma T_s^4)$. Substituting this into the energy balance equation and simplifying, we get:

$$T_s = \left(\frac{L(1 - A)}{4\tau\sigma} \right)^{\frac{1}{4}} \tag{1.7}$$

This equation considers the greenhouse effect by modifying the effective outgoing radiation, influencing the predicted surface temperature T_s. As τ decreases, representing a stronger greenhouse effect, the surface temperature T_s increases.

Substituting the known values for solar constant $(S = 1365\,\mathrm{W\,m^{-2}})$, Earth's planetary albedo $(A = 0.3)$ and Earth's atmosphere transitivity $(\tau = 0.6)$, the EBM predicts a surface temperature of approximately 288.15 K. Note that this model is purely analytical and empirical, and does not predict temperature for the atmosphere.

Further improvements from the simple EBM involve adding additional atmospheric layers, each accounting for the emissivity of the outgoing longwave radiations. The emissivity represents the proportion of blackbody radiation that is absorbed or emitted.

The one-layer leaky greenhouse model is a simple 1D case that can be solved analytically. This model accounts for not all outgoing longwave radiation (OLR) escaping directly to space; some is absorbed and re-emitted by the single-layer atmosphere. Figure 1.7 demonstrates the energy balance above and below the one-layer atmosphere.

Leaky Greenhouse Model
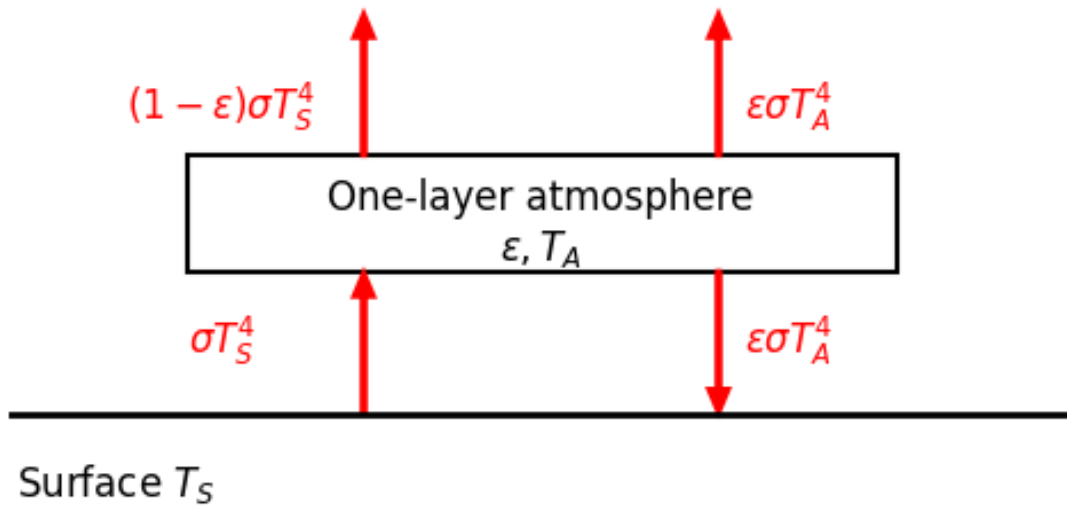
Figure 1.7: Illustration of the Leaky Greenhouse Model. This model depicts the energy balance for a planet with a single-layer atmosphere. The surface emits longwave radiation as σT_s^4, where T_s is the surface temperature. The atmosphere absorbs and re-emits some of this radiation, characterized by the emissivity ϵ. The outgoing longwave radiation from the atmosphere is depicted as $\epsilon \sigma T_A^4$, where T_A is the atmospheric temperature, and the fraction of surface emission that escapes directly to space is $(1 - \epsilon)\sigma T_s^4$. Image credit. B. Liu.

The incoming solar radiation at the top of the atmosphere is $\frac{L}{4}$. The reflected solar radiation is $\frac{LA}{4}$. The outgoing longwave radiation (OLR) from the top of the atmosphere (which includes the emission by the atmosphere and the fraction that escapes from the surface) is given by:

$$\text{OLR} = \epsilon \sigma T_A^4 + (1 - \epsilon)\sigma T_s^4 \tag{1.8}$$

where ϵ is the emissivity of the atmosphere (i.e., the proportion of blackbody radiation that is absorbed or emitted.), $1 - \epsilon$ represents the transmissivity of the atmosphere (i.e.,

the proportion of blackbody radiation that can pass through the atmosphere), T_A is the temperature of the atmosphere, and T_s is the surface temperature.

The energy balance at the top of the atmosphere (TOA) takes place when the downwelling flux from the star ($\frac{S}{4}$) balances the reflected stellar flux ($\frac{SA}{4}$) and OLR:

$$\frac{S}{4} = \frac{SA}{4} + \epsilon \sigma T_A^4 + (1 - \epsilon) \sigma T_s^4 \tag{1.9}$$

Similarly, the energy balance on the surface states that the downwelling flux from the star ($\frac{S}{4}$) and the one-layer atmosphere ($\epsilon \sigma T_A^4$) balances the reflected stellar flux on the surface ($\frac{SA}{4}$) and the surface emission (σT_s^4):

$$\frac{S}{4} + \epsilon \sigma T_A^4 = \frac{SA}{4} + \sigma T_s^4 \tag{1.10}$$

Combining Equation 1.9 and Equation 1.10 and solving for T_s, we can find:

$$T_s^4 = 2 T_A^4 \tag{1.11}$$

Equation 1.11 indicates that the one-layer atmosphere must be cooler than the surface to maintain the law of energy conservation. Substituting Equation 1.11 into either Equation 1.9 or Equation 1.10, we can solve for T_s^4 in terms of S:

$$T_s^4 = \frac{S(1 - A)}{4\sigma(1 - \frac{\epsilon}{2})} \tag{1.12}$$

Compared with the energy balance model without considering the atmosphere (see Equation 1.6), the surface temperature in the leaky greenhouse model shown above becomes higher due to the greenhouse effects of the one-layer atmosphere.

Overall, though 0D and 1D EBMs can incorporate additional factors like surface heat capacity and vertical heat diffusion through parameterizations (e.g. North, 1975; Guendelman et al., 2022), they still have limitations, such as assuming a grey atmosphere with no spectral dependence in radiative transfer and oversimplifying vertical heat transport. These factors are better addressed in more complex 1D models by explicitly incorporating radiative transfer and convective adjustment within the atmosphere.

1.2.3   1D Radiative-Convective Model

A 1D Radiative-Convective Model (RCM) is a climate model that focuses on the vertical structure of the atmosphere in a single column, balancing radiative transfer and convective processes to determine atmospheric temperature profiles. The simplest case assumes a single surface temperature with uniform longitudinal and latitudinal heat distribution. However, it can also be latitudinally dependent by considering a vertical profile for each latitudinal grid (e.g. Guendelman et al., 2022). 1D RCMs calculate how radiation is absorbed, emitted, and scattered by atmospheric gases and aerosols while also adjusting the vertical temperature gradient to prevent convective instability. RCMs are widely used to simulate Earth's atmosphere and in exoplanetary atmospheres, especially in exoplanet research (e.g. Kasting et al., 1993; Kopparapu et al., 2013).

In an RCM, the radiative transfer is calculated by solving the radiative transfer equation for each atmospheric layer. This includes accounting for the absorption, emission, and scattering of radiation by gases, clouds, and aerosols. The goal is to determine the temperature profile that results from radiative equilibrium, where the energy absorbed by the atmosphere and the Earth's surface is balanced by the energy emitted as longwave radiation. This process is described mathematically by the radiative transfer equation, which accounts for both absorption and emission of radiation.

The absorption cross-section σ_ν measures the probability that a single molecule or particle will absorb a photon of frequency ν. It represents the effective area that a molecule presents to incoming radiation for absorption.

The number density n is the number of particles per unit volume of the atmosphere. The product of the absorption cross-section and the number density gives the absorption coefficient α_ν, which quantifies the ability of the atmosphere to absorb radiation at a given frequency:

$$\alpha_\nu = n\sigma_\nu \tag{1.13}$$

The absorption mean free path s is the average distance a photon travels before being absorbed by the atmosphere. It is related to the absorption coefficient α_ν by:

$$s = \frac{1}{\alpha_\nu} \tag{1.14}$$

The radiative transfer equation for the change in specific intensity I_ν of radiation along the path l due to absorption is:

$$\frac{dI_\nu}{dl} = -\alpha_\nu I_\nu = -n\sigma_\nu I_\nu \tag{1.15}$$

Where I_ν is the specific intensity of the radiation. The solution to this differential equation, describing how the intensity changes along the path l, can be expressed in terms of the optical depth τ_ν:

$$I_\nu(l) = I_{\nu,0} \exp(-\tau_\nu) \tag{1.16}$$

Where $\tau_\nu = \alpha_\nu l$ is the optical depth along the path l. This equation shows that the intensity of radiation decreases exponentially as it travels through the atmosphere, with the rate of decrease determined by the optical properties of the atmosphere, specifically the optical depth. The equation 1.16 is known as the Lambert-Bouguer-Beer law of extinction.

When the optical depth $\tau_\nu \gg 1$, the atmosphere is optically thick, meaning that the radiation is almost entirely absorbed. Conversely, when $\tau_\nu \ll 1$, the atmosphere is optically thin, meaning that most of the radiation passes through unimpeded. For example, Earth's atmosphere is transparent in the visible wavelength, as most visible radiation from the Sun passes through the atmosphere because the atmosphere is optically thin at these wavelengths. Figure 1.8 provides a detailed illustration of the absorption features in Earth's atmosphere. It shows the absorption bands and their impact on both incoming solar radiation and outgoing thermal radiation. The individual absorption spectra for major greenhouse gases and the effects of Rayleigh scattering are also depicted.

In addition to absorption, radiation is also emitted by the atmosphere. The emission coefficient j_ν represents the amount of energy emitted per unit volume, per unit solid angle, per unit frequency interval. Including both absorption and emission, the radiative transfer equation becomes:

$$\frac{dI_\nu}{dl} = -\alpha_\nu I_\nu + j_\nu \tag{1.17}$$

Since τ_ν scales with atmospheric height, we can express this equation in terms of optical depth τ_ν, we use the relation $d\tau_\nu = \alpha_\nu dl$, giving:
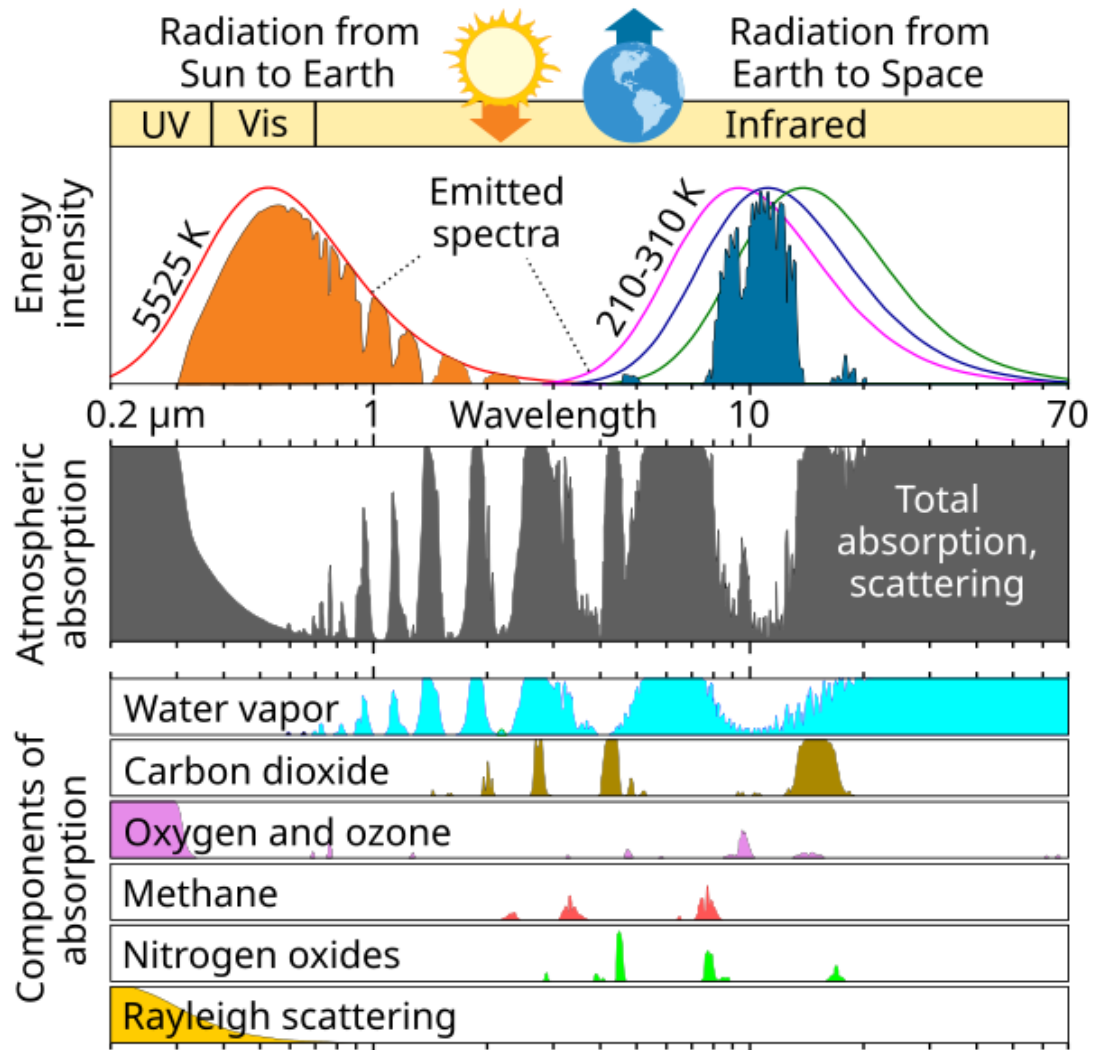
Figure 1.8: This figure illustrates the shortwave and longwave radiation from 0.2 to 70 microns for the Sun and Earth, assuming blackbody radiation for given temperatures (top panel), the bulk absorption spectrum in Earth's atmosphere (middle panel), and individual absorption features for major greenhouse gases along with Rayleigh scattering. *Image Credit: Robert A. Rohde for the Global Warming Art project. Licensed under CC BY-SA 3.0.*

$$\frac{dI_\nu}{d\tau_\nu} = -I_\nu + \frac{j_\nu}{\alpha_\nu} \tag{1.18}$$

Where $\frac{j_\nu}{\alpha_\nu}$ is often denoted as the source function S_ν, so the equation can be written as:

$$\frac{dI_\nu}{d\tau_\nu} = -I_\nu + S_\nu \tag{1.19}$$

This is the fundamental equation of radiative transfer in terms of optical depth. It describes how the specific intensity of radiation changes as it travels through an atmosphere, considering both absorption and emission along a specific direction.

This equation is solved to simulate the radiative transfer in climate models, often using the two-stream approximation method for computational efficiency. Instead of integrating beams over all incident angles, the method approximates beams in all directions into the upward and downward directions. The governing equations for two-stream approximation without considering scattering effects are known as the Schwarzschild equations:

$$\frac{dU_\nu}{d\tau_\nu} = -U_\nu + E(\nu, T(\tau_\nu)) \tag{1.20}$$

$$\frac{dD_\nu}{d\tau_\nu} = D_\nu - E(\nu, T(\tau_\nu)) \tag{1.21}$$

Where U_ν and D_ν are the specific intensities of the upward and downward beams at frequency ν, respectively. τ_ν is the optical depth at frequency ν, $E(\nu, T(\tau_\nu))$ is the blackbody emission at frequency ν and temperature $T(\tau_\nu)$, governed by the Planck function:

$$E(\nu, T) = \pi B(\nu, T) \tag{1.22}$$

The Planck function $B(\nu, T)$ is given by:

$$B(\nu, T) = \frac{2h\nu^3}{c^2} \frac{1}{\exp\left(\frac{h\nu}{kT}\right) - 1} \qquad (1.23)$$

Where h is Planck's constant $(6.626 \times 10^{-34} \, \mathrm{J\,s})$, c is the speed of light $(3.00 \times 10^8 \, \mathrm{m\,s^{-1}})$, k is the Boltzmann constant $(1.38 \times 10^{-23} \, \mathrm{J\,K^{-1}})$.

These equations describe the upward and downward beams attenuated by absorption (the first term) and augmented by emission assuming blackbody radiation (the second term) in each layer of the atmosphere. To consider the scattering effects for the two-stream approximation, the radiation from the host star can be split into a direct part, which goes upward at the same angle, and a diffuse part, which travels over all angles. The scattering from the direct beam acts as a source term for the diffuse radiation. The detailed formulation for two-stream approximation with scattering can be found in Pierrehumbert (2010).

Since the radiative transfer depends on the radiation frequency ν, and in particular, the absorption coefficient α_ν, climate models need to compute the wavelength-dependent absorption coefficient from each molecule present in an atmosphere, this is known as the line-by-line method. The line-by-line method provides good accuracy at the expense of computational cost. To address the computational demands of the line-by-line method while still maintaining accuracy in modeling, the correlated-k method offers a more efficient alternative. This method involves grouping absorption coefficients by strength within a given frequency interval covering a range of atmospheric pressure and temperature, leading to a statistic "k distribution" that requires significantly fewer frequency points to represent the spectral absorption effectively (Lacis et al., 1991). One of the potential challenges of the correlated-k method is handling overlapping gaseous absorption, where multiple gases absorb within the same spectral interval (e.g. Lacis et al., 1991; Amundsen et al., 2017). This issue arises because the relative strength of absorbers can change with variations in temperature and pressure, leading to significant overlap in the

absorption spectra of different gases. Refined methods have been developed to address these overlapping absorption bands in cases involving multiple gases (e.g. Mlawer et al., 1997). Informed by principles from radiative transfer theory and the implementation of the correlated-k method in atmospheric modeling, it is important to note that re-calibration of the correlated-k distribution may be necessary when conducting climate sensitivity analyses under different atmospheric compositions.

Radiative processes alone would lead to a temperature profile where the atmosphere cools rapidly with height, known as a radiative equilibrium profile. However, this is often unstable because it can produce a temperature gradient (lapse rate) that is steeper than the atmosphere can support without overturning due to convection. 1D RCMs use convection adjustment, which redistributes heat vertically to stabilize the temperature profile while maintaining the law of energy conservation (e.g. MacKay et al., 1991).

When the atmospheric lapse rate (the rate at which temperature decreases with altitude) becomes steeper than the adiabatic lapse rate, the atmosphere is considered convectively unstable. The adiabatic lapse rate describes how quickly the temperature of an air parcel changes when it moves vertically without exchanging heat with its surroundings. Under unstable conditions, the warmer and less dense air parcels near the surface tend to rise, and the cooler and denser air aloft tends to sink, resulting in convective overturning that redistributes heat and helps stabilize the atmosphere. In our Earth's troposphere, the actual lapse rate often lies between the dry and the moist adiabatic lapse rate. The dry lapse rate and the moist lapse rate refer to the temperature changes of a rising air parcel when it is unsaturated (dry) and when it has reached saturation (moist), respectively. When air parcels reach saturation, they release heat and follow the moist adiabatic lapse rate, which is lower than the dry adiabatic rate. If the environmental lapse rate is steeper than this moist rate, the saturated parcels will continue to rise, leading to convective conditions (i.e., clouds and storms).

To derive the adiabatic lapse rate of dry air, it's crucial to establish the concept of hy-

drostatic equilibrium. Hydrostatic equilibrium refers to the balance between the upward pressure gradient force (dF_p) and the downward gravitational force (dF_g) in a stationary atmosphere:

$$dPA = -\rho g A dz \tag{1.24}$$

where dP is the change in pressure, A is the cross-section area in which pressure acts on, dz is the change in height, ρ is the air density g is the acceleration due to gravity.

Simplifying Equation 1.24, we get the hydrostatic equation:

$$\frac{dP}{dz} = -\rho g \tag{1.25}$$

The dry adiabatic lapse rate is derived assuming no condensation occurs, meaning the air is unsaturated. The derivation begins with the ideal gas law:

$$PV = nRT \tag{1.26}$$

Where V is the volume of air, n is the number of moles, R is the universal gas constant, and T is the temperature.

By diving the mass of the air (M) in Equation 1.26, and substituting $n = \frac{M}{m}$ and $R_d = \frac{R}{m}$ where m is the molar mass and R_d is the specific gas constant for dry air, we can get an alternative form of the ideal gas law:

$$Pv = R_d T \tag{1.27}$$

where v is the specific volume (i.e., volume per unit mass), $R_d = \frac{R}{m}$ is the specific gas constant for dry air, and T is the gas temperature. The total derivative of Equation 1.27 is:

$$Pdv + vdP = R_d dT \tag{1.28}$$

The first law of thermodynamics for the adiabatic process is:

$$dQ = c_v dT + PdV = 0 \tag{1.29}$$

where dQ is the heat exchange and is zero in the adiabatic process, c_v is the specific heat capacity at constant volume, $c_v dT$ is the internal energy of the air parcel and PdV is the work done by air volume expansion.

By combining the first law of thermodynamics for the adiabatic process (see Equation 1.29) with the total derivative of the ideal gas law (see Equation 1.28) and Mayer's relation of $c_p = c_v + R_d$ where c_p is the specific heat capacity at constant pressure, we can get the dry adiabatic lapse rate Γ_d:

$$\Gamma_d = -\frac{dT}{dz} = \frac{g}{c_p} \tag{1.30}$$

For Earth's atmosphere, this value is approximately $9.8\,\mathrm{K/km}$.

The moist adiabatic lapse rate accounts for the latent heat released during condensation. Water vapor contains latent heat of vaporization, which is released when the air parcel cools and water vapor condenses. As a parcel of air rises and cools, it eventually becomes saturated. With further cooling, excess water vapor condenses, forming clouds and releasing latent heat. This release of latent heat slows the rate of cooling compared to dry air, resulting in the moist adiabatic lapse rate Γ_m [1]:

$$\Gamma_m = -\frac{dT}{dz} = \frac{g}{c_p}\left(\frac{1 + \frac{L_v r}{R_v T}}{1 + \frac{L_v^2 r}{c_p R_v T^2}}\right) \tag{1.31}$$

Where r is the mass mixing ratio of the water vapor to the dry air. For Earth's atmosphere, the moist adiabatic lapse rate typically ranges from $4\,\mathrm{K/km}$ to $7\,\mathrm{K/km}$, depending on the temperature and moisture content of the air.

In summary, 1D RCMs simulate planetary climates by solving the radiative transfer equations and applying convective adjustment to correct the vertical temperature profile within a single-column atmosphere. However, similar to EMB, 1D RCMs do not explicitly account for radiative, dynamic, and chemical processes across latitudinal and longitudinal dimensions. These aspects are addressed by 3D General Circulation Models, which we will briefly overview in the next subsection.

1.2.4   3D Global Circulation Models

Global Circulation Models (GCMs), also known as Global Climate Models, are toward the higher end of the model hierarchy in terms of their complexity and difficulty to fully understand. These models incorporate the three-dimensional nature of the atmosphere and/or ocean. GCMs can exist as fully coupled ocean-atmosphere models

---

[1]The derivation of the moist adiabatic lapse rate can be seen in Ambaum (2020)

(AOGCMs) or as independent circulation models for the atmosphere (AGCMs) and ocean (OGCMs). These models aim to simulate as many processes as possible and produce a three-dimensional picture of the time evolution of the state of the whole climate system.

Figure 1.9 shows an example of the grid structure of GCMs. GCMs compute the spatial average of various prognostic state variables, and the prognostic variables are updated sequentially by the "dynamics core" and then the "model physics". The dynamics core refers to the simulation of large-scale fluid motion using primitive equations [2], and "model physics" refers to the simulations of other sub-grid physical processes such as radiative transfer, cloud formation, and convection (Edwards, 2011).

GCMs simulate the Earth's climate by dividing the planet into a three-dimensional grid, where each grid cell is defined by specific longitude, latitude, and altitude (or pressure) coordinates. In atmospheric modelling, two common approaches are used to simulate the movement of air and other processes in the atmosphere: the Eulerian and Lagrangian methods.

In the Eulerian dynamical core, the model calculates how air and other quantities (like temperature and humidity) change at fixed points on a grid. This method is straightforward and aligns well with the way data is typically collected, but it can struggle with accurately capturing processes that involve rapid or complex movement, as it doesn't follow the actual path of air parcels. On the other hand, the Lagrangian dynamical core tracks individual parcels of air as they move through the atmosphere, allowing for a more detailed representation of air movement. The Finite-Volume (FV) dynamical core combines aspects of both the Eulerian and Lagrangian approaches. It operates with a fixed grid in the horizontal directions (like the Eulerian approach), ensuring that key quantities like mass and energy are conserved as air moves through the grid. Vertically, it adopts a quasi-Lagrangian discretization, following the movement of air parcels more

---

[2]The primitive equations refer to a set of nonlinear partial differential equations for approximating atmospheric/oceanic flow.

closely, which helps maintain accuracy in the model (NCAR, 2024).

The grid-based framework enables detailed computations within each cell, where key variables such as temperature, pressure, wind speed, and humidity are calculated. GCMs solve these variables incrementally over time, updating their values based on the exchange of energy, momentum, and mass between adjacent cells, a process known as forward modelling. To accurately simulate climate, GCMs require boundary conditions: upper boundary conditions such as top-of-atmosphere solar radiation and lower boundary conditions such as greenhouse gas concentrations, both of which are termed radiative forcings due to their impact on Earth's energy balance. The lower boundary also includes topography and orography (e.g., mountains). Additionally, initial conditions must be provided at the start of each simulation to initialize the model.

The dynamic core solves the governing equations, including the conservation of mass and momentum (known as the Navier-Stokes equation) and laws of thermodynamics. A list of the equations in its original form is given below for reference:

Conservation of Mass (Continuity Equation):

$$\frac{\partial \rho}{\partial t} + \nabla \cdot (\rho \mathbf{u}) = 0 \tag{1.32}$$

where ρ is the air density, $\mathbf{u}$ is the velocity vector and $\nabla \cdot$ is the divergence operator. This equation ensures that mass is conserved within the atmosphere.

Conservation of Momentum (Navier-Stokes Equation for a Rotating System):

$$\frac{\partial \mathbf{u}}{\partial t} + (\mathbf{u} \cdot \nabla)\mathbf{u} + 2\mathbf{\Omega} \times \mathbf{u} = -\frac{1}{\rho}\nabla p + \mathbf{g} + \mathbf{F}_{\text{friction}} \tag{1.33}$$

where $\mathbf{\Omega}$ is the Earth's rotation rate, p is the pressure, $\mathbf{g}$ is the gravitational acceleration, and $\mathbf{F}_{\text{friction}}$ represents frictional forces. This equation models the forces acting on air parcels, including Coriolis effects due to Earth's rotation.
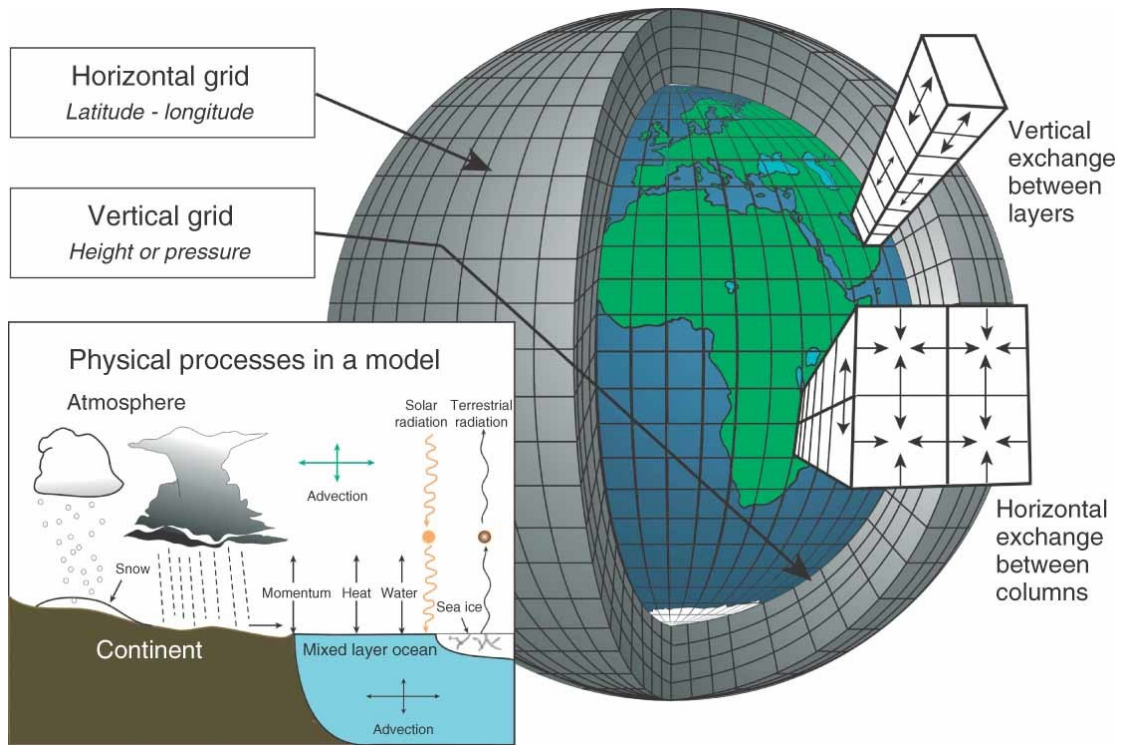
Figure 1.9: Adapted from Edwards (2011): This figure illustrates the structure of a GCM, showing how the planetary surface and atmosphere are divided into a grid of cells. Each cell contains information about the physical state of the atmosphere, including variables like temperature and pressure. The model computes vertical exchanges between layers and horizontal exchanges between columns, ensuring the conservation of mass, momentum, and energy across the entire system. The lower inset highlights some of the key physical processes, such as radiation, advection, and exchanges of momentum, heat, and water.

Conservation of Energy (First Law of Thermodynamics):

$$\frac{\partial T}{\partial t} + \mathbf{u} \cdot \nabla T = \frac{1}{c_p} \left(\frac{Q}{\rho} - \nabla \cdot \mathbf{F}_{\text{radiation}} \right) \tag{1.34}$$

where T is temperature, c_p is the specific heat at constant pressure, Q represents internal heating (such as latent heat release), and $\mathbf{F}_{\text{radiation}}$ is the radiative flux. This equation ensures that the total energy is conserved, accounting for both radiative processes and internal heat exchanges.

Equation of State (Ideal Gas Law):

$$P = \rho R T \tag{1.35}$$

where R is the specific gas constant. This equation links the thermodynamic properties of the atmosphere by relating pressure, temperature, and density.

For planets with thin atmospheres, the primitive equations can be simplified for an incompressible fluid under hydrostatic equilibrium, known as the shallow water approximation.

Overall, 3D GCMs offer a comprehensive and detailed approach to modelling the Earth's climate system. By solving the fundamental equations of fluid dynamics and thermodynamics and incorporating the effects of smaller-scale processes through parameterizations, GCMs enable the exploration and prediction of complex climate phenomena with a high degree of realism. However, this comes with the trade-off of greater complexity, which can make it more challenging to fully understand the underlying physical processes driving the model's behaviour.

1.3 Habitability

1.3.1 Definitions

Habitability refers to the ability of an environment to support the activity of at least one known organism, according to the binary classification: a planetary body is either habitable or uninhabitable at any given time in its geological history, depending on the location on, above, or underneath the planetary surface (Cockell et al., 2016). This concept of habitability can be divided into two categories: instantaneous habitability and continuous planetary habitability, and each suits for different types of studies (Cockell et al., 2016). Instantaneous habitability refers to microscopic scale habitable conditions in an instant in time on a planetary body that allows at least one organism to survive. It requires benign conditions for life, such as the presence of a solvent for biochemical reactions to occur (i.e., water), the range of temperature that allows metabolic activity, the source of energy for maintenance, growth, or reproduction of life, and the availability of six elements (C, H, N, O, P, and S) to build the basic structure of life. Contin-

uous planetary habitability is defined as the set of conditions that allow a planetary body to support habitable environments in at least part of the planet over geological timescales. This concept is particularly relevant for (exo)planetary science, where researchers are interested in understanding the long-term potential of a planet to maintain life-supporting conditions. In contrast, instantaneous habitability, which is more aligned with (astro)biological studies, focuses on the conditions that allow for life at specific moments in time (Cockell et al., 2016).

1.3.2 Habitable Zone

The habitable zone (HZ) concept was first proposed by Huang (1959). It is defined as a spherical shell around a star within which a planet can maintain liquid water on its surface, depending on the amount of stellar radiation it receives. The HZ definitions have been progressively refined as climate models have advanced, allowing for more precise estimations of habitability. Hart (1978) developed a 0D climate model with a wide range of parameterised processes to examine the Earth's climate evolution. Their results show a narrower HZ range for Earth from 0.95 to 1.01 AU than simple EMB predictions. The inner edge of the HZ (IHZ) is defined as the runaway greenhouse state, and the outer edge of the HZ (OHZ) is the point at which the runaway glaciation state (or snowballing state) takes place. The runaway greenhouse state (RGH) occurs when the planet's orbit is close enough such that high surface temperatures vaporize volatiles in the atmosphere, increasing the thermal re-emission from greenhouse gasses and creating a positive feedback loop for increasing surface temperature. The critical surface temperature is 70° Celsius, assuming an Earth-like atmosphere with 1 bar atmospheric pressure on the surface (Ingersoll, 1969). The runaway greenhouse effect also causes the water vapor to escape into space via irreversible thermal escape Catling et al. (e.g. 2017a).

In fact, the surface temperature required to render a planet too hot to be habitable is significantly lower than the runaway greenhouse (RGH) limit. The moist greenhouse state is associated with strong greenhouse effects, a wet stratosphere, and significant water loss,

requiring a lower surface temperature and exhibiting a longer water loss timescale than the RGH state (Kasting, 1988). The moist greenhouse state may eventually transition into an RGH state. Simulating the moist greenhouse effect can be challenging with 1D models, which often assume a fully saturated troposphere, but GCMs have proven capable of simulating these conditions more accurately by incorporating three-dimensional atmospheric dynamics, including horizontal and vertical transport of heat, moisture and cloud processes (Haqq-Misra et al., 2016). Wolf et al. (2014) used a 3D GCM to examine the timescale for Earth to enter a moist greenhouse state under a brightening sun. Their findings suggest that Earth's climate may remain safe from thermal runaway and significant water loss for at least another 1.5 billion years, even with a 15.5% increase in the solar constant. This indicates a greater resilience to water loss than previously predicted by 1D models, largely due to the more realistic 3D representation of atmospheric dynamics and cloud processes. Further studies using 3D GCMs show that on aqua-planets (planets with a large fraction of their surface covered by oceans, like Earth) in the moist greenhouse state, water loss can occur rapidly enough to preclude an RGH state. These models also suggest that a planet's climate could stabilize into a dry, desert-like state, allowing for habitable surface temperatures even under higher stellar radiation (Abe et al., 2011; Wolf et al., 2015).

On the other hand, the snowball state is associated with both positive and negative feedback loops. The positive feedback can drive the climate away from habitable conditions. This occurs when a planet's orbit is far enough from its star that more volatiles, such as H_2O and CO_2, condense, leading to H_2O and CO_2 cloud stabilizing effects by reflecting more stellar radiations and suppression of greenhouse effects by removing these greenhouse gasses from the atmosphere. The condensation of these volatiles can also increase the planet's surface albedo due to larger surface ice coverage, known as the ice-albedo effect (Jack J.Lissauer, 2017; Shields et al., 2013). Opposite to the positive feedback, when planets are farther away from the host star, CO_2 in the atmospheres begins accumulating due to the negative feedback between silicate weathering and surface temperature

(Walker et al., 1981). However, the increase in CO_2 concentrations can cause more CO_2 saturated air which enhances Rayleigh scattering and CO_2 condensation (Kasting et al., 1993; Shields et al., 2016b), which decreases the surface temperature. When a further increase in CO_2 cannot contribute to the overall warming, it is said that the "maximum greenhouse limit" is reached at the OHZ. This definition of OHZ is widely adopted in later studies with 1D and 3D models (e.g. Abe et al., 2011; Kopparapu et al., 2013).

In addition, the habitable zone of a planet may move outward as a star's luminosity increases over time as it evolves through the main sequence. The continuously habitable zone (CHZ), often a narrower band than the HZ, is defined as the zone that remains habitable around a star during a given period (Hart, 1978). Kasting et al. (1993) used a 1D radiative-convective climate model described in Kasting et al. (1984) to estimate the CHZ around our Sun and other main sequence stars. They found that the CHZ becomes wider for later spectral classes of main sequence stars. For instance, M and K dwarfs, due to their longer lifetimes, may have more extended CHZs compared to G and K dwarfs. This extended CHZ allows for potentially habitable conditions over more prolonged periods, which could be favourable for the maintenance and development of life. However, they also noted that the initial climate state of a planet influences the extent and stability of the CHZ. This concept addresses the evolution of planetary habitability over time. In our solar system, Venus and Mars serve as key examples of this evolution. Venus, currently a hot planet with a thick, dense atmosphere, may have had habitable conditions approximately 1 billion years ago if the planet transitioned from a water world to a dry land planet (Abe et al., 2011). These conditions could have persisted for nearly 3 billion years before the Sun's increasing brightness triggered a runaway greenhouse or moist greenhouse state, leading to its present inhospitable climate (Way et al., 2020). However, Turbet et al. (2021) argues that early Venus may never have had an ocean due to strong night-side clouds and greenhouse warming effects which prevent water vapor condensation. To date, the question of the existence of Venus' past habitability remains open and more observational data is required to further constrain

its past climate states (Westall et al., 2023). Similarly, Mars, now a cold planet with a thin atmosphere, likely had liquid water on its surface around 3 billion years ago. This is supported by geological evidence indicating the presence of surface water flow in Mars' past (Thomas et al., 2022; Jaumann et al., 2024). These examples highlight how planetary climates can evolve dramatically over geological timescale, influenced by factors such as the host stars' luminosity and orbital configurations.

1.3.3 Climate Bistability

Climate bistability refers to more than one climate steady state that can be reached from the same parameter space (i.e., external stellar radiation), depending on the planet's initial states (Boschi et al., 2013). An example of this is the bistability climate of Earth about 5 million years ago when Earth transitioned from a snowballing state to a warm state. Hoffman et al. (1998) used 0D EBM to explore the bistable climate on Earth and found that the bistability depends on the ice-albedo feedback (Zaliapin et al., 2010). Murante et al. (2020) used a 1D EMB to investigate the bistability of Earth-like exoplanets with varying orbital configurations and atmospheric pressure. Their study revealed that the planetary conditions necessary for climate bistability significantly overlap with those required to support complex life on a planet's surface. This suggests that the presence of climate bistability could be a critical factor in the habitability of exoplanets. Climate bistability has also been investigated using 3D GCMs, further supporting that the Earth's bistable climate states can exist in its past and present (e.g. Marotzke et al., 2007; Lucarini et al., 2019). The concept of climate bistability suggests that even planets currently in extreme climates, such as a snowball state, might still possess the underlying conditions necessary to support life, provided that their climate systems can transition to more temperate states.

1.3.4 Atmospheric Bistability

The habitability of Earth underwent significant changes before and after the Great Oxygenation Event (GOE) around 2.4 billion years ago due to the emergence of oxygenic photosynthesis. The GOE, also known as the Oxygen Catastrophe, marks the onset of the atmospheric bistability of oxygen, where Earth's atmosphere could maintain either a low oxygen steady state (10^{-5} PAL) or a high oxygen steady state ($> 5 \cdot 10^{-3}$ PAL). This transition took place long after oxygenic photosynthesis is thought to have evolved, and the delay arises because oxygen levels needed to exceed 10^{-5} PAL for UV shielding by ozone to become effective, which in turn increased the lifetime of atmospheric oxygen (Goldblatt et al., 2006).

Cooke et al. (2022) used an Earth System Model (ESM) and found that lower O_3 column densities than previously estimated allowed higher fluxes of biologically harmful UV radiation to reach the surface. This increased UV radiation enhanced the production of hydroxyl radicals (OH), significantly reducing the lifetime of methane (CH_4). These findings suggest that methane alone may not have provided sufficient greenhouse effect during the Mesoproterozoic (also known as the Middle Proterozoic Era) to resolve the faint young Sun paradox: a contradiction between geological evidence of a warm early Earth and model calculations suggesting the Sun's output was too weak to prevent Earth from freezing (Feulner, 2012). Charnay et al. (2020) argue that this paradox may have been resolved by higher CO_2 concentrations, which could have warmed Earth's surface sufficiently.

These studies highlight the necessity of considering planetary climate across geological timescales, considering the effects of varying stellar radiation and internal planetary changes. Thus, the CHZ concept should be considered when evaluating planetary habitability, as it offers a framework for assessing the long-term potential for life on planets both within our solar system and beyond.

1.3.5 Super-habitability

Super-habitability, a concept that allows for a comparative analysis of habitability, moves beyond the binary categorization of planets as simply habitable or uninhabitable, offering a more nuanced approach to quantifying the habitable conditions on a planetary body (Heller et al., 2014). Such studies often rely on 3D GCMs or at least latitudinal-dependent 1D models to capture the temporal and spatial variations in habitability.

Arguably, super habitable planets might not necessarily resemble Earth, yet the astrophysical conditions could permit planets to be even more suitable for life than our own (Schulze-Makuch et al., 2020). One approach to assessing the super-habitability of exoplanets relies on simulating Earth-analogues or Earth-like planets across a range of parameter spaces. This is because Earth is the planet we know best, and its habitable conditions can serve as a benchmark for comparative habitability studies under different parameters.

He et al. (2022) investigated the roles of obliquity and rotation period in the habitability of Earth-like exoplanets using a 3D GCM. They defined a habitability metric based on annual mean surface temperature and cumulative precipitation. Their simulations, covering obliquities from $0°$ to $90°$ and rotation periods from 1 to 128 days, found that the most habitable conditions occur at $45°$ obliquity with fast rotations (1 to 8 days). This configuration enhances habitability by up to 25% compared to Earth's current conditions through the spatial redistribution of clouds and water vapor. Additionally, the $45°$ obliquity leads to the highest sensitivity to the rotation period, allowing for a broader range of possible climate conditions compared to other obliquities.

While He et al. (2022) approached habitability from a climate perspective, considering temperature and precipitation, Jernigan et al. (2023) explored it from an astrobiological angle. They utilized a 3D marine biogeochemical model coupled with a GCM to examine the response of Earth-like marine life to a range of obliquities ($0°$ to $90°$) and eccentricities ($0 < e < 0.4$). Their findings indicate that marine biological activity and

the production of potential biosignatures, such as O_2 and CH_4, increase with higher obliquity and eccentricity. They argue that planets with these characteristics may be superhabitable and particularly favourable for detecting exoplanetary life.

1.3.6 Orbital Configurations

Recent observational statistics have shown that rocky planets with highly eccentric orbits ($e > 0.1$) are relatively common in the Universe. Figure 1.11 illustrates the distribution of exoplanets in the mass-eccentricity space, with rocky worlds highlighted by red circles, defined as having masses and radii less than 10 $M_\oplus$ and 1.6 $R_\oplus$ (Rogers, 2015; Lopez et al., 2019; Wordsworth et al., 2021). To date, the most eccentric rocky exoplanet identified is Kepler-127 b ($e = 0.47$) (Van Eylen et al., 2015). In total, 56 rocky exoplanets with $e > 0.1$ have been identified among 967 confirmed rocky exoplanets, indicating that less than 6% of rocky planets have $e > 0.1$, compared to over 22% for other exoplanet types. This discrepancy may suggest an observational bias, as smaller exoplanets with longer orbital periods are more difficult to detect (see Figure 1.10). Thus, the eccentricity distribution of rocky planets is arguably unknown.

A key question for planets in eccentric orbits is whether they could maintain habitability outside the traditional habitable zone, especially if they experience long-term eccentricity oscillations. To explore this, the eccentric habitable zone (EHZ) extends the concept of the habitable zone (HZ), defining it as a spherical shell around a star based on the average stellar flux a planet receives throughout its eccentric orbit (Barnes et al., 2008). Williams et al. (2002) introduced the mean flux approximation, suggesting that the climate of eccentric planets primarily depends on the annual mean stellar radiation they receive. However, it has been argued that the climatic effects of seasonality should also be considered, particularly for planets with highly eccentric orbits, where variations in stellar flux could have substantial impacts on climate (e.g., Bolmont et al., 2016; Palubski et al., 2020).

Orbital parameters like eccentricity and obliquity can oscillate over geological timescales
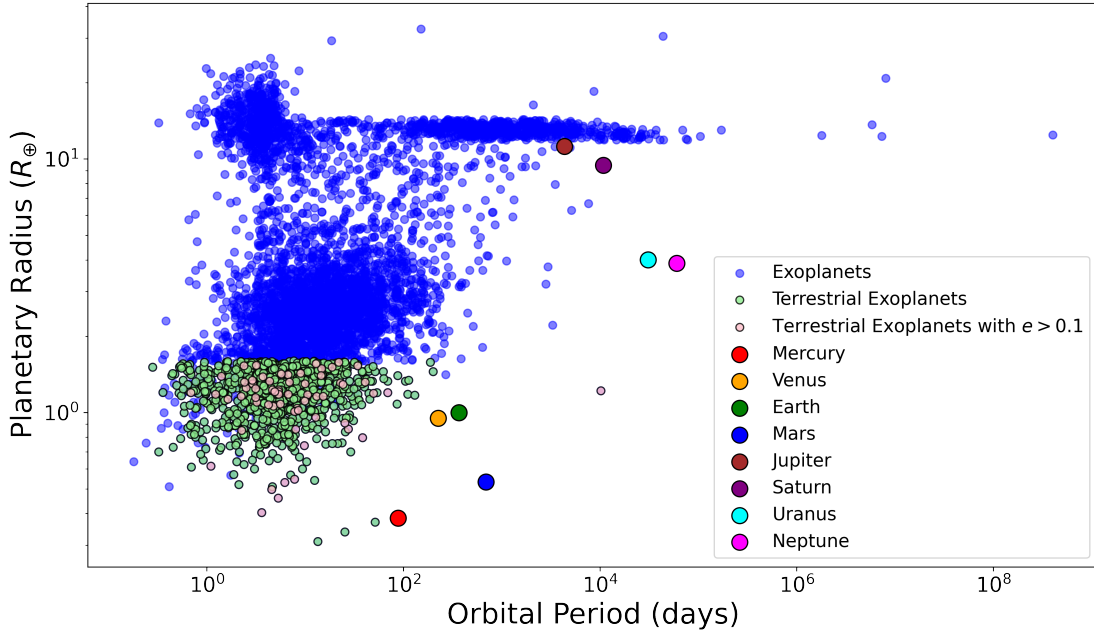
Figure 1.10: Distribution of confirmed exoplanets in planetary radius vs orbital period space. Blue circles represent all confirmed exoplanets, while green circles highlight terrestrial exoplanets. Terrestrial exoplanets with highly eccentric orbits ($e > 0.1$) are shown as pink circles. Solar system planets are represented by larger circles in different colors.

due to gravitational perturbations, akin to Earth's Milankovitch cycles (Berger, 1988). These cycles—encompassing changes in orbit shape (eccentricity), axial tilt (obliquity), and rotational axis orientation (precession)—affect stellar radiation distribution on the planetary surface, impacting climate stability and habitability. For instance, Way et al. (2023) used numerical simulations of full equations of motion and a 3D GCM to demonstrate that Earth's climate remains stable across a range of obliquity ($0°$, $23.5°$, $45°$) and eccentricity ($0 < e < 0.53$), with regional habitability varying over time and finding that a moist greenhouse state is only possible at the highest eccentricity. Similarly, Deitrick et al. (2018) employed an N-body model and a 1D latitudinal EBM to study Exo-Milankovitch cycles for Earth-like exoplanets, finding that climate instability leading to a snowball state can occur at obliquities greater than $35°$ or eccentricities exceeding 0.1. These studies highlight the critical role of long-term orbital evolution in determining climate states and potential habitability.

Eccentric orbits can be circularized by tidal effects from the host star acting on the planetary body (known as solid tide) as well as its atmosphere (known as atmospheric tides or thermal tides). These two have distinctively different effects. The former tends to circularize an eccentric orbit for close-in orbits, and the latter has the opposite effects for planets with longer orbital periods (e.g. Leconte et al., 2015; Auclair-Desrotour et al., 2017). The net torque from both solid tides and atmospheric tides determines the state of planetary rotation. The solar tidal effects on Earth have a negligible effect due to the long orbital distance to the Sun, but the effect can be much more significant for planets with close-in orbits around their host stars. Lower-mass stars can induce stronger tidal effects than higher-mass stars. For late M dwarfs, the orbits of potentially habitable planets are likely to be circularized within 1 billion years (Barnes, 2017). It is worth noting that, even with a thin atmosphere, the atmospheric tides can be enough to drive the planet out of synchronicity, so long-term stable eccentric orbits are possible (Leconte et al., 2015).

Tidal locking is common for rocky planets around M dwarfs due to their short orbital periods and the long lifetimes of M dwarfs, making tidal forces more effective at circularizing their orbits. However, planets in circular orbits can still experience other orbital resonances. Synchronous rotation is unlikely for planets with high eccentricities, like Mercury ($e \sim 0.21$), but it's not guaranteed even for circular orbits. This is because planets in circular orbits could pass through spin-orbit resonances, where the planet's rotational period aligns with its orbital period (e.g., Rodríguez et al., 2012). For instance, Mercury has a 3:2 spin-orbit resonance, and Proxima Centauri b may also exhibit a similar 3:2 resonance (Ribas et al., 2016).

Tidal locking causes permanent day and night-side hemispheres in circular orbits. With zero obliquity, there would be no seasonal variations in stellar radiation, leading to no seasonal climate changes. Studies indicate that non-zero obliquity is unlikely for tidally-locked planets due to tilt erosion (e.g. Heller et al., 2011). Tidal locking can impact habitability, as the planet's night side could freeze while the day side overheats. The

habitability of tidally-locked rocky planets has been debated. One of the concerns is about high XUV radiation and coronal mass ejection (CME) activity from M dwarfs, which could cause atmospheric erosion (e.g., Lammer et al., 2007). However, it has also been suggested that the magnetic fields of active M dwarfs may suppress CME activity, preventing atmospheric loss (e.g., Alvarado-Gómez et al., 2022). Other concerns include these long-lived stars' intense and prolonged stellar activity, which may lead to large amounts of harmful UV radiation reaching the surface. However, Ridgway et al. (2023) used 3D GCMs with an Earth-like atmosphere and showed that the increasing ozone formation due to stellar flares might reduce the impact of subsequent flares.

Earth-like planets around M dwarfs can exhibit either eyeball-shaped habitability (e.g., Pierrehumbert, 2011; Turbet et al., 2016; Wolf, 2017; Boutle et al., 2017; Turbet et al., 2018; Del Genio et al., 2019; Yang et al., 2020) or habitability restricted to terminator regions ("terminator habitability") (Lobo et al., 2022; Lobo et al., 2023) from model simulations, depending on the planetary water reservoir. In these studies, the eyeball-shaped habitability is characterized by a limited open ocean near the substellar point, typically found in water-rich worlds. In contrast, terminator habitability, often seen in drier planets, is confined to the ring-shaped region near the day-night boundary. Both configurations could support similar habitable areas under various constraints, but different observational strategies are favoured. For eyeball-shaped habitability, direct imaging such planets right before their secondary eclipse might reveal a water-rich atmosphere, potential biosignatures from the thermal emission spectrum and surface albedo from the reflection spectrum (Pierrehumbert, 2011), while terminator habitability is better studied through transmission spectroscopy. The terminator regions have limited precipitation, which reduces cloud coverage (Lobo et al., 2022), thus enhancing the detectability of absorption features of potential biosignatures during observations.
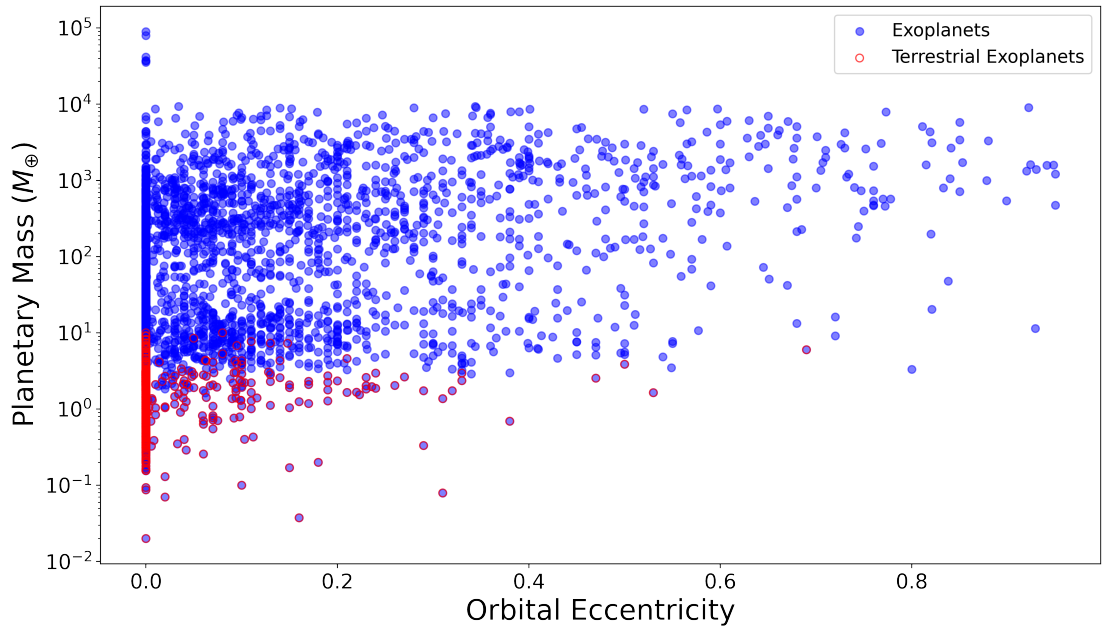
Figure 1.11: A scatter plot showing the relationship between planetary mass (in Earth masses) and orbital eccentricity for exoplanets. The blue dots represent all known exoplanets, while the red circles highlight terrestrial exoplanets (planets with masses comparable to Earth). Data is sourced from the NASA Exoplanet Archive.

1.3.7 Biosignatures

By definition, a habitable planet is not necessarily inhabited by life. Earth, the only known habitable planet, provides us with a fundamental understanding of environments supporting life. Thus, we can look for biosignatures derived from Earth's environment to find evidence of life outside the solar system. In the context of exoplanets, a biosignature is a remotely observable indication of living processes that influence a planet's atmosphere or surface (Schwieterman et al., 2024).

Biosignatures can include a suite of molecules, surface features (such as the "red edge" (Seager et al., 2005)), or time-dependent modulations of gases or surface characteristics linked to life. The "red edge" refers to a sharp increase in Earth's reflectance spectrum between 700 and 750 µm due to vegetation's reflectivity. Typical potential biosignatures include those that are prevalent on Earth today, such as O_2, O_3, CH_4, and N_2O (Schwieterman et al., 2024).

In this brief introduction, we focus on the biosignatures O_3, a chemical by-product of O_2, as it is among the most well-studied potential remote biosignatures (Schwieterman et al., 2024) and is particularly relevant to our study. The main absorption feature in the O_2 A-band at $0.76\,\mu m$ is often too narrow and weak to be detected, especially given the much larger flux from the star. However, O_3, a photochemical by-product of atmospheric O_2, can serve as an indicator of O_2 presence (e.g. Leger et al., 1993). Most of Earth's O_3 is formed in the stratosphere via the Chapman Cycle, resulting from the photolysis of O_2 (Chapman, 1930). The strongest mid-infrared feature for O_3 is at $9.65\,\mu m$, which has long been proposed as an indirect indicator of O_2 in the mid-infrared, where O_2 bands are too weak to detect (e.g. Leger et al., 1993). Recent studies suggest that detecting O_3 at a 3σ significance on TRAPPIST-1e, assuming it to be an Earth-like planet, would require around a few tens of transit observations with JWST's NIRSpec or MIRI instruments (e.g. Gialluca et al., 2021).

The UV absorption of O_3 in the Hartley band, centred near $0.25\,\mu m$ and extending from 0.2 to $0.31\,\mu m$, can shield Earth's surface from harmful UV radiation. This band could potentially be detected in reflected light by a future space-based telescope, such as the Habitable Worlds Observatory (HWO), via its absorption in the Hartley band (e.g. Damiano et al., 2023). Recent 3D modelling studies on ozone observability also predict that Earth-like planets around M dwarfs are sensitive to flare events (e.g. Tilley et al., 2019) and the input stellar spectra in the UV wavelength (e.g. Cooke et al., 2023b) and degenerate interpretations of O_3 are likely considering the uncertainties in the stellar activities.

Abiotic oxygen production could also lead to misinterpretation (false positive) of O_3. We use Figure 1.12 from Meadows et al. (2018b) to illustrate five possible scenarios where O_2 and O_3 could be discriminated between biotic and abiotic sources. The text at the bottom of the figure indicates the preferred bands for transmission and reflection observations, while the text at the top outlines the planetary types. For instance, in Earth's case, the abiotic source of O_2 and O_3 can be confirmed if CO (indicated by the red crossed circle)

is not detected. The green circles shown in other cases identify absorption species such as O_4 (O_2-O_2 collisionally induced absorption), which could help fingerprint the origin of O_2 and/or O_3 in various planetary context. Additionally, Ranjan et al. (2023), using a high-top photochemistry model, demonstrate that the upper atmospheric processes (i.e., escape mechanisms and photochemical reactions) can moderate or even prevent the runaway accumulation of O_2 from CO_2 photolysis alone. This updates the discussion in Meadows et al. (2018b) on the O_2 false positives by narrowing down the scenarios in which O_2 might appear abiotically, making future detections of O_2 signals from exoplanets more robust and hence less prone to misinterpretation as false positives.
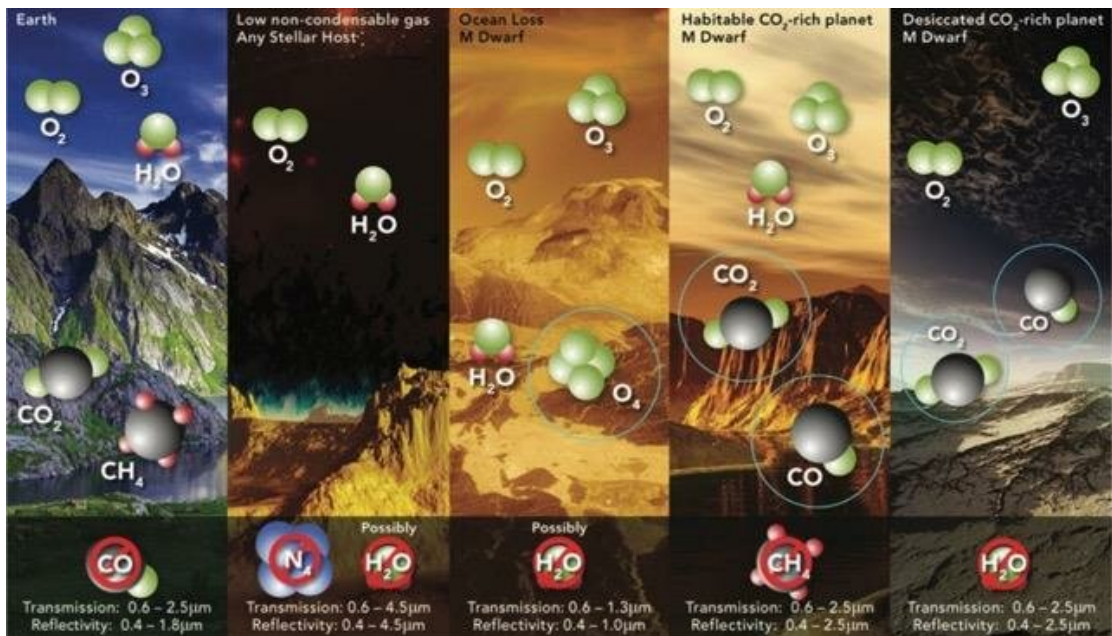
Figure 1.12: From Meadows et al. (2018b): Five possible false positive scenarios for O_2 and O_3 detections. The non-detections of forbidden molecules (crossed red circles), and detection of active molecules (green circles) can be used to separate biotic O_2 and O_3 from abiotic sources.

1.3.8 This thesis

Recent advances in telescope and observation techniques have made detecting and characterizing terrestrial planets orbiting nearby main-sequence stars increasingly promising. This progress has motivated simulations to explore the climates of these planets across a range of orbital parameters. This thesis uses WACCM6 to simulate an Earth-

analogue exoplanet in a highly eccentric orbit, benchmarking it against its circular orbit counterpart, and to simulate an Earth-like exoplanet, Proxima Centauri b, assuming a tidally-locked orbit. The next section introduces the models used to simulate planetary climates and synthetic spectroscopic observations of exoplanet atmospheres. Specific model configurations and their implementation are detailed in the method section of each science chapter. This thesis consists of three science chapters addressing the climate, atmospheric circulation, water vapor and ozone photochemistry, potential surface habitability, and observability of Earth-like exoplanets in eccentric orbits (Chapters 2 and 3) and Earth-analogue exoplanets in tidally-locked orbits (Chapter 4).

Orbital eccentricity introduces seasonally-varying stellar irradiation on the planet, and how it interacts with the planetary internal parameters and affects the planetary climate remains an area of ongoing research. This thesis quantifies the water and ocean loss rates due to a highly eccentric orbit for the first time using WACCM6 (see Chapter 2). I present idealized synthetic transmission spectra comparing the highly eccentric case and its circular equivalent, highlighting the annual mean and seasonal variations of H_2O, O_3, and CO_2 features. The results provide new insights for future observations of highly eccentric Earth-like worlds. My follow-up research focuses on detailed climate changes due to increased orbital eccentricity (see Chapter 3). I explain differences in surface temperature from albedo, cloud radiative effects, and atmospheric circulation patterns. Surface habitability is assessed using simplified metrics accounting for the diversity of lifeforms on Earth, and we demonstrate how increased orbital eccentricity contributes to land surface habitability, supplemental to the water loss rate analysis in the previous research.

Several potentially habitable terrestrial exoplanets so far are those orbiting M dwarfs, such as Proxima Centauri b, likely in a 3:2 resonance or tidally-locked orbit. In Chapter 4, I present the simulation configurations and the simulation results for Proxima Centauri b, assuming a tidally-locked orbit with the substellar point located over the Pacific Ocean. The climate, atmospheric circulation, O_3 chemistry, and surface habitability of

Proxima Centauri b are analyzed and compared to previous studies. While the overall climate state agrees with previous work, differences are found in many places. Idealized synthetic transmission, reflection, and emission spectra observations for Proxima Centauri b are shown to highlight potential observables assuming the best theoretical spectra possible. Finally, I summarize the thesis and propose future directions that may further contribute to understanding how orbital parameters affect the climate, habitability, and observability of terrestrial exoplanets.

1.3.9 Modelling Tools

WACCM6

Simulations are performed using WACCM6 (the Whole Atmosphere Community Climate Model version 6), which is a configuration in CESM2.1.3 (the Community Earth System Model version 2.2) (Gettelman et al., 2019). The Community Earth System Model (CESM) is an open-source, fully-coupled global climate model that provides state-of-the-art computer simulations of the Earth's past, present, and future climate states. WACCM6, an updated version from WACCM4 (Marsh et al., 2013), is a high-top 3D atmosphere model used primarily for studying the pre-industrial, present-day and potential future climates of Earth. As an Earth-system model, WACCM6 couples with the following models: the Community Land Model Version 5 (CLM5; Lawrence et al., 2019); the Los Alamos Sea Ice Model Version 5 (CICE5; Hunke et al., 2017); the - Parallel Ocean Program Version 2 (POP2; Smith et al., 2010); the Model for Scale Adaptive River Transport (MOSART; Tesfa et al., 2014) and the Community Ice Sheet Model Version 2 (CISM2; Lipscomb et al., 2013). A schematic representation of the model's capabilities is shown in Figure 1.14.

WACCM6 is capable of studying Earth's climate with whole atmosphere chemistry and dynamics, spanning from the surface (~ 1000 hPa) to the lower thermosphere (6×10^{-6} hPa). The model offers two horizontal resolution options, $\sim 1°$ and $\sim 2°$, allowing it to capture processes on scales of approximately 100 to 200 km, which is essential for

accurately representing atmospheric dynamics, such as jet streams and large-scale wave patterns. WACCM6 captures the complex vertical structure of Earth's atmosphere, which includes several distinct layers.

Figure 1.13 presents the vertical temperature profile of Earth's atmosphere as computed by the WACCM6 model. The temperature profile is plotted against pressure (in hPa) on the left y-axis and altitude (in km) on the right y-axis. Major atmospheric layers are identified: the troposphere, where temperature decreases with height and weather phenomena occur; the stratosphere, characterized by an increase in temperature with height due to the absorption of ultraviolet radiation by the ozone layer; the mesosphere, where temperatures again decrease with height and meteors burn up; and the thermosphere, where temperatures rise sharply due to the absorption of high-energy solar radiation, leading to the homopause, which marks the transition to a region where molecular diffusion dominates over turbulent mixing.

While approximately 80% of the atmospheric mass is concentrated in the troposphere, the middle atmosphere, which includes the stratosphere and the mesosphere (ranging from about 10 to 100 km), plays a crucial role in radiative, dynamic, and (photo)chemical processes that can affect the climate and surface habitability (Stolarski, 1986). Therefore, the coupling between different atmospheric layers and the surface in WACCM6 provides a more comprehensive view of the climate system than models considering just the lower atmosphere.

WACCM6 uses a Finite-Volume (FV) dynamic core, the same as in CAM6. WACCM6 is identical to CAM6 in the range of parameterized processes, with the only exception being the representation of parameterized gravity waves (Gettelman et al., 2019). Compared with low-top models, WACCM6 provides improvements in high-latitude climate variability at the surface and in sea ice extent, offering better alignment with observations (Gettelman et al., 2019).

The chemical mechanism selected for our simulations is the middle atmosphere chem-
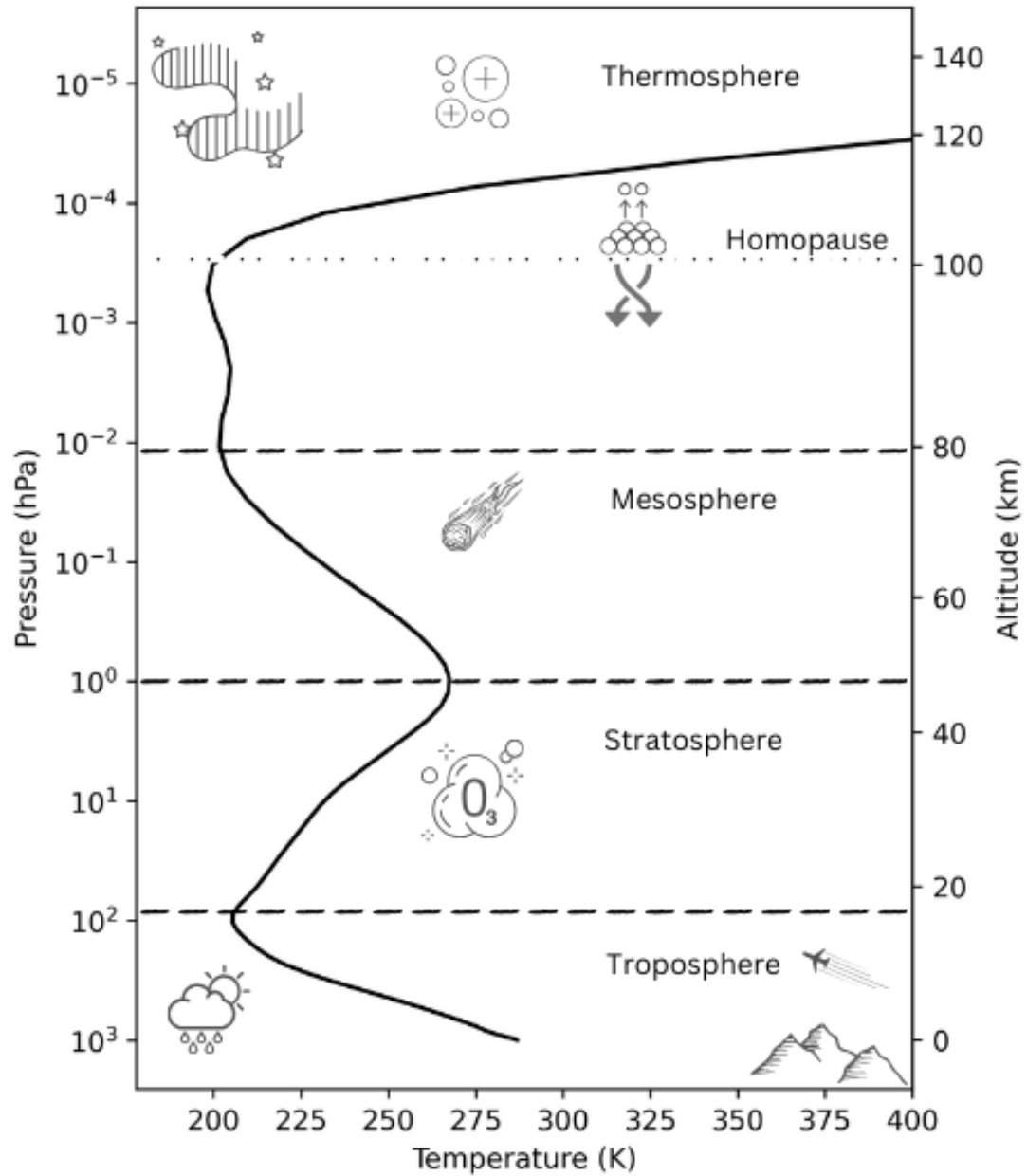
Figure 1.13: Vertical temperature profile of Earth's atmosphere as simulated by WACCM6. The left y-axis shows the pressure levels in hPa, while the right y-axis indicates the corresponding altitudes in km. The plot highlights the key atmospheric layers: the troposphere, stratosphere, mesosphere, and thermosphere, with their characteristic features. The homopause, above which molecular diffusion dominates over turbulent mixing, is marked at about 100 km. The temperature curve demonstrates the lapse rate, characterized by different governing processes in each atmospheric layer. Image credit. B. Liu.
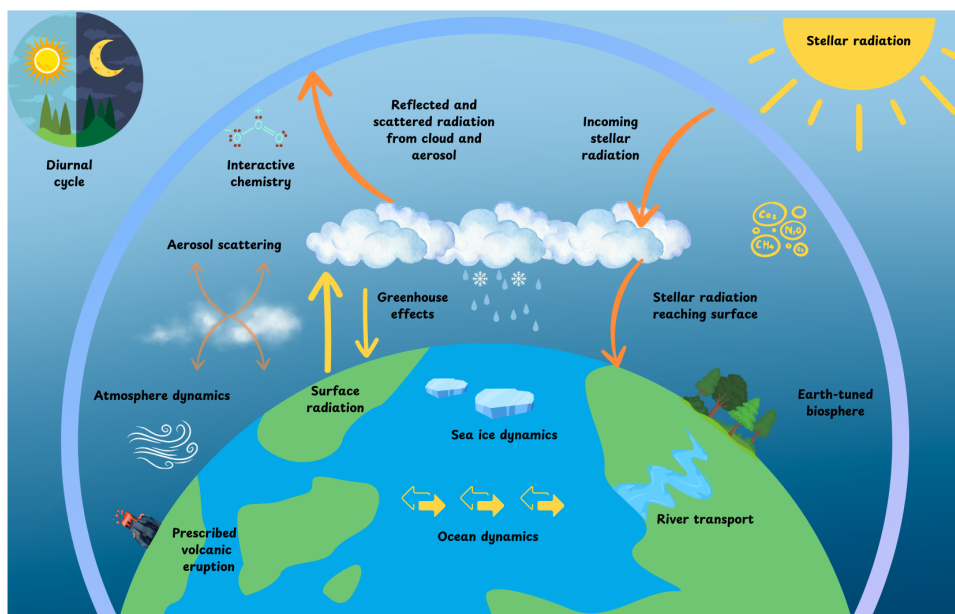
Figure 1.14: This cartoon illustrates some of the key features of WACCM6, including its fully interactive chemistry, coupled ocean, sea-ice, land, atmosphere, and chemistry components. Simplified radiative transfer processes are also depicted. These features highlight the model's comprehensive approach to simulating Earth's climate system. Image credit. B. Liu.

istry scheme (MA), which is a subset of the comprehensive troposphere-stratosphere-mesosphere-lower thermosphere chemistry scheme (TSMLT) (Gettelman et al., 2019; Emmons et al., 2020). This chemistry scheme is based on the Model of Ozone and Related Chemical Tracers (MOZART) (Emmons et al., 2020). The MA scheme includes 97 chemical species, 208 chemical reactions, and 90 photolysis reactions. Compared to TSMLT, the MA scheme requires significantly fewer computational resources due to a reduced set of tropospheric reactions (e.g., prescribed sulfate aerosols and the exclusion of non-methane hydrocarbons). Specifically, the scheme accounts for ozone (O_3) through the inclusion of the Chapman cycle, as well as HOx, NOx, SOx, BrOx, and ClOx species, which are involved in catalytic cycles that contribute to the destruction of O_3 in the stratosphere and mesosphere.

The radiative transfer code is the Rapid Radiative Transfer Model for GCMs (RRTMG) using the correlated-K approach (Mlawer et al., 1997; Iacono et al., 2008; Liu et al., 2012; Gettelman et al., 2019) in which the line integration over discrete wave number

is replaced by the integration over correlated continuous cumulative probability density function. RRTMG employs the two-stream approximation to calculate both shortwave radiation from the host star and longwave radiation from the surface and atmosphere, accounting for the effects of scattering, absorption, and emission by gases, clouds, and aerosols in the atmosphere. In WACCM6, shortwave is defined as the radiation from the Sun for wavelengths between 0.2 to 12 µm; longwave is defined as the radiation from the Earth for wavelength from 3 to 1000 µm.

The parameterizations for the boundary layer, shallow convection, and cloud macrophysics are unified and performed using the Cloud Layers Unified By Binormals (CLUBB) approach. In this method, small-scale variabilities are predicted by a multivariate probability density function (Larson et al., 2002; Bogenschutz et al., 2013; Li et al., 2022). Cloud microphysics is parameterized using the Morrison-Gettelman Version 2 microphysics (MG2), which explicitly predicts the mixing ratios and number concentrations of cloud water droplets and cloud ice for precipitation (Park et al., 2014; Gettelman et al., 2015). Aerosol processes are treated using the Modal Aerosol Model Version 4 (MAM4), where aerosol size distributions are represented by multiple lognormal functions (Liu et al., 2012; Liu et al., 2016; Mills et al., 2016).

All of the simulations in this thesis start with the pre-industrial case in 1850 (PI-control case). Typically, branching from the PI-control case means the simulation repeats the same boundary conditions from that year after we introduce the modifications. We modify a constant solar spectrum in the simulations for Earth-analogue exoplanets, excluding the 11-year solar cycle. The solar spectrum data is from the recommended dataset for the large model inter-comparison program—Coupled Model Intercomparison Project Phase 6 (CMIP6) (Matthes et al., 2017). The PI-control case has been run and scientifically validated for 300 years in CMIP6 (Eyring et al., 2016).

We use the model in a horizontal grid resolution of $1.9° \times 2.5°$ in latitude and longitude, respectively. Vertically, there are 70 pressure layers in the hybrid sigma-pressure

coordinate. The hybrid sigma-pressure coordinate is a vertical coordinate system that transitions smoothly from a terrain-following sigma coordinate near the surface to a pressure coordinate in the upper atmosphere. This allows for better representation of both surface and free-atmosphere processes. The model time step is set to 30 minutes, and the radiative transfer is calculated every other model time step. The coupling time step for the ocean and sea ice components is set to be the same as in the atmosphere component (i.e., 30 minutes).

Our methodology is based on the Earth system model, but our investigation has broader relevance to Earth-like exoplanets. WACCM6 has been extensively used to study Earth's climate from ancient geological eras to pre-industrial and modern times (e.g. Marsh et al., 2013; Pettit et al., 2018; Zeng et al., 2022; Richter et al., 2022; Dubé et al., 2022). Recently, the model has also been employed to explore the climate and potential habitability of Earth-like exoplanets (e.g. Chen et al., 2021; Cooke et al., 2022; Cooke et al., 2023a; Cooke et al., 2023b; Cooke et al., 2024).

Planetary Spectrum Generator

The Planetary Spectrum Generator (PSG) is a powerful radiative transfer tool that synthesizes and retrieves planetary spectra, covering a broad wavelength range from 50 nm to 100 mm. In PSG, the layer-by-layer radiative transfer is done by the Planetary and Universal Model of Atmospheric Scattering (PUMAS; Villanueva et al., 2018), and the line-by-line intensity calculation uses molecular cross sections from the latest HITRAN database (Gordon et al., 2022). PSG supports observations from a variety of platforms, including ground-based observatories like JWST and ALMA, conceptual telescopes like LIFE, and user-defined telescopes with customizable spectral resolving power, noise levels, and other parameters. The telescope resolving power (R) measures the number of wavelength bins for a given wavelength ($R = \frac{\lambda}{\Delta\lambda}$) where λ is the wavelength and $\Delta\lambda$ is the width of the wavelength bin. The telescope noises can be categorised into time-dependent random noises and a time-independent noise floor (i.e., systematic noise). The

random noise decreases with the square root of the observation time, while the noise floor remains unchanged with the observation time.

The Global Emission Spectra application (GlobES) in PSG can take climatological data from a variety of General Circulation Models (GCMs) and accurately synthesize transmission spectra along the planetary terminator and direct imaging spectra (i.e., reflection and emission spectra) over the observable planetary disk (Villanueva et al., 2022). Figure 1.15 shows how the processes for computing the transmission spectra and direct imaging spectra from 3D GCM data in GlobES. Once users convert their GCMs' 3D climatological data in netCDF format (i.e., temperature, pressure and chemical profiles, and surface properties and cloud properties) into PSG GCM binary files (the format which can be taken by GlobES) and upload the files to GlobES, the 3D data are then displayed graphically for the different variables. GlobES samples data along the terminator to generate transmission spectra, assigning equal weight to each point. For direct imaging spectra, it samples points across the observable planetary disk, applying weights based on the projected area of each point before integrating. Users can adjust the binning number to control the balance between calculation speed and accuracy. A higher binning number decreases the number of sample points for faster computation. For example, a binning number of 3 can group 9 data points, spanning 3 latitudinal and longitudinal grids, into a single sample. This results in a 9 times faster calculation while sacrificing a minor loss in accuracy.
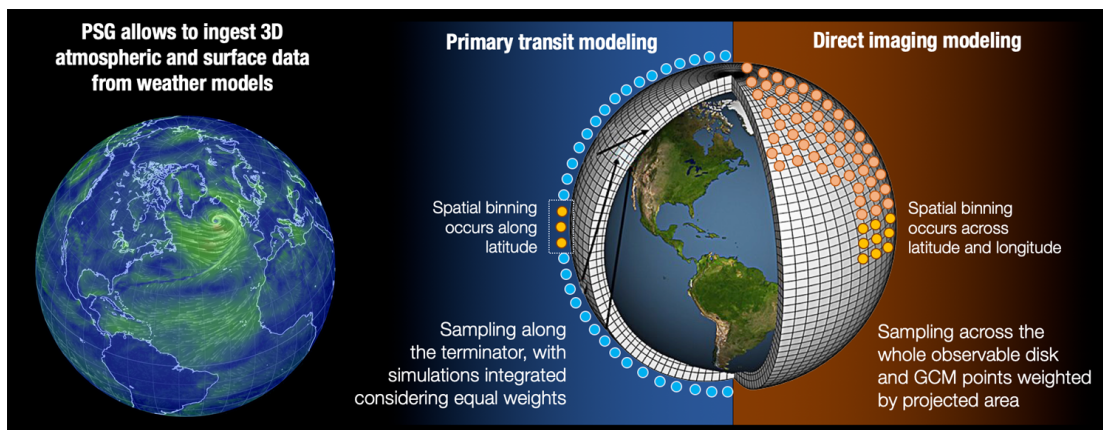
Figure 1.15: Figure adopted from Villanueva et al. (2022): The forward modelling capabilities of the Planetary Spectrum Generator (PSG; Villanueva et al., 2018) are displayed. 3D GCM data can be uploaded to the Global Emission Spectra application (GlobES) in PSG to compute transmission spectra (calculated from profiles at the terminator) or direct imaging spectra (calculated by integrating across the observable disk). Image credit: NASA.

Chapter 2

Earth as an Exoplanet in an Eccentric Orbit I: Temperature, Water and Observables

2.1 Introduction

The orbital parameters of a planet, such as eccentricity, play an important role in affecting the planetary climate. If we adopt 1.6 $R_\oplus$ (Earth radii) and 10 $M_\oplus$ (Earth masses) as the upper limits for defining rocky exoplanets, we find that among a total of 114 confirmed rocky exoplanets, 49 of them have measured eccentricities, and 9 of them have an eccentricity greater than 0.1[1]. For instance, TOI-1238 b has an eccentricity of 0.25, LTT 1445A c has an eccentricity of 0.223, and L 168-9 b has an eccentricity of 0.21 (González-Álvarez et al., 2022; Winters et al., 2022; Astudillo-Defru et al., 2020). To date, GJ 1061 d, a potentially rocky exoplanet (> 1.5 $M_\oplus$) detected by the radial velocity method, has the largest constrained eccentricity ($e < 0.54$) (Dreizler et al., 2020). The 10 $M_\oplus$ sets the boundary between super-Earth and ice/gas giant planets, and beyond 1.6 $R_\oplus$, the planet's density would be too low to be rocky (Rogers, 2015; Lopez et al., 2019; Wordsworth et al., 2021). Super-Earth and mini-Neptune exoplanets could vary largely in their planetary compositions, and the absence of their analogues in the Solar System

---

[1]The Extrasolar Planets Encyclopaedia: `http://exoplanet.eu/`

makes it difficult to fully characterize them and determine if they are predominantly rocky.

The climate response of rocky planets to changes in eccentricity has been investigated in previous work. Williams et al. (2002) examined the climate of the current Earth with elliptical orbits near the Sun's habitable zone (HZ). They pointed out that long-term climate stability primarily depends on the average stellar flux received over an entire orbit, known as the mean flux approximation. However, later Bolmont et al. (2016) demonstrated that the mean flux approximation becomes less reliable for tidally-locked Earth-like planets in highly-eccentric orbits ($e \geq 0.6$) with host star luminosities between 10^{-4} $L_{\odot}$ and 1 $L_{\odot}$ as surface liquid water may not persist for the entire course of an orbit as the planet moves in and out of the habitable zone. The seasonality effects induced by higher eccentricities were considered by Dressing et al. (2010), who found that Earth-like planets surrounding Sun-like stars do not necessarily suffer from long winters near aphelion due to thermal inertia if at least 10% of the surface is ocean-covered. In addition, Linsenmeier et al. (2015) showed that for Earth-like planets, eccentric orbits extend the habitable zone's outer edge and effectively limit the transition into snowball states.

The time it takes for the planetary atmosphere to adapt to changes in radiation, also known as the atmospheric radiative timescale, can be affected by the mass of the atmosphere, the equilibrium temperature and the surface thermal inertia (Donohoe et al., 2014; Guendelman et al., 2019; Ji et al., 2023). The seasonal response of temperature for rocky planets in eccentric orbits and with zero obliquity is strongly dependent on the interplay of the orbital period, rotation rate and radiative timescale (Adams et al., 2019; Guendelman et al., 2020; Guendelman et al., 2022; He et al., 2022). For example, the amplitude of the seasonal response decreases with decreasing rotation rate. For a constant rotation rate, longer orbital periods give the atmosphere more time to adjust to the changes in insolation, resulting in a stronger seasonal cycle. On the other hand, a longer radiative timescale means a weaker seasonal cycle because the atmosphere needs more time to respond to variations in insolation.

Ohno et al. (2019a) revealed that eccentricity might influence temperature patterns indirectly by affecting the radiative timescale; hence, a transition from a diurnal mean insolation-controlled climate to an annual mean insolation-controlled one is possible. Because equilibrium temperature increases with increasing eccentricity (Quirrenbach, 2022), we can deduce that the orbital eccentricity can modulate the seasonal temperature response for a given atmospheric mass and orbital period.

Eccentricity could also affect the habitability of rocky planets by affecting atmospheric loss rates. Originating near the planetary surface, hydrogen-bearing species in the form of H_2O, H_2, and CH_4 travel upward to the homopause through advection and turbulent mixing. In the upper homosphere, hydrogen-bearing molecules are dissociated by ultraviolet radiation, leaving hydrogen in atomic and molecular form only. Hunten (1973) showed that the diffusion-limited hydrogen escape flux (Φ_i), in units of molecules lost per unit time per unit area, is

$$\Phi_i = \frac{b_i f_i}{H_a} \tag{2.1}$$

where b_i is the binary diffusion parameter, f_i is the mixing ratio of the hydrogen-bearing species at the homopause in units of moles per mole of air, and H_a is the temperature-dependent atmospheric scale height at the homopause. The detailed derivation can be found in Catling et al., 2017b. The atmospheric water concentration due to the effect of eccentricity has been examined by Way et al., 2017b, in which they identify temperate climatic conditions when varying the eccentricity from 0 to 0.283. They found that the tropopause water vapor mixing ratio is the highest at $e = 0.283$. However, it is still nearly 15 times lower than the moist-greenhouse limit[2] at perihelion. In addition, Palubski et al. (2020) showed ocean worlds with higher eccentricity orbits are more likely to lose water and that if the eccentricity is greater than 0.55 for an Earth-like aqua-planet orbiting a G-type star, the whole water inventory will be lost owing to the runaway greenhouse

---

[2]The moist-greenhouse limit occurs when water vapor starts accumulating in the stratosphere with a mixing ratio $> 10^{-3}$.

effect.

The effects of eccentricity on water loss owing to an increased solar constant have been studied using both 1D radiative-convective models (RCMs) (e.g. Kasting et al., 1984; Kasting et al., 2015) and 3D general circulation models (GCMs) (e.g. Wolf et al., 2015; Linsenmeier et al., 2015; Kopparapu et al., 2017; Guendelman et al., 2020). They find a general trend that water loss increases with increasing solar constant. While there are a few papers which addressed the climate seasonality effect due to increasing eccentricity with the mean flux approximation for Earth-like exoplanets (e.g. Williams et al., 2002; Bolmont et al., 2016), they did not quantify the atmospheric water vapor abundance with varying eccentricity. In addition, the 3D GCMs used in Williams et al., 2002 and Bolmont et al., 2016 are not coupled with whole atmosphere chemistry, and the atmosphere's vertical extent does not reach the homopause at which the diffusion-limited escape of hydrogen can be estimated. This study quantifies the water abundance and estimates the water loss rate for a highly eccentric rocky exoplanet using the fully-coupled whole-atmosphere Earth-system model, WACCM 6 (1.3.9). We describe the WACCM6 simulation configurations in Section 2.2.1. The Planetary Spectrum Generator (PSG) generates synthetic transmission spectra using the WACCM6 outputs as inputs (1.3.9), and the model configurations are shown in Section 2.2.2. The simulation results are shown in Section 2.3. The impact of our results on the potential observability is included in the Discussion (Section 2.4). In Section 2.5, we summarize our findings.

2.2 Methods

2.2.1 WACCM6 Configurations

We use WACCM6 in the Middle Atmosphere chemistry (MA) configuration with a horizontal resolution of $1.875°$ in latitude and $2.5°$ in longitude to simulate an Earth-like planetary climate in a circular orbit ($e = 0$) and in a highly eccentric orbit ($e = 0.4$) to investigate the effects of increasing orbital eccentricity on the climate and habitability

in terms of water loss.

We initialize our simulations with equilibrated conditions on January 1st in the year 1850 (so-called pre-industrial era or PI) with a mean surface temperature of 287.2 K to isolate the climate response from those induced by human activities.

To focus on the climate response due to varying eccentricity only, we fix the total solar irradiance (TSI) of the $e = 0.4$ and the $e = 0$ cases to the same value as for the Earth's PI case (1360.75 W m^{-2}) by scaling their solar radiation spectra input accordingly. Using Eq. 2.2 and Eq. 2.3, the TSI is 1248.58 W m^{-2} for the $e = 0.4$ case, and 1360.94 W m^{-2} for the circular case.

$$TSI_{e=0.4} = TSI_{PI} \cdot \frac{F_{e=0.4}}{F_{e=0.0167}} \tag{2.2}$$

$$TSI_{e=0} = TSI_{PI} \cdot \frac{F_{e=0}}{F_{e=0.0167}} \tag{2.3}$$

The relationship between the orbital eccentricity and the TSI in WACCM6 follows the numerical computations of the Earth's orbital elements in Berger, 1978.

To avoid numerical instability caused by a sudden change in TSI due to the modifications of the eccentricity, we first run the PI case from January 1st for 101 days. This is when the TSI in the PI case approximately equals the TSI in the circular ($e = 0$) and in the highly-eccentric case ($e = 0.4$) on the same day in their orbits. This allows both the circular and the highly eccentric case to start with a TSI not far from the TSI in the PI case to avoid numerical instability caused by a sudden change in the solar forcing. In addition, we modified the planetary obliquity from the default $23.5°$ in the PI case to zero in a circular orbit case and a highly eccentric case to mute the effects of the seasonal variability caused by a non-zero obliquity.

The lower boundary conditions for the zonally symmetric surface chemical emissions in the PI-control case are cyclic, meaning they repeat annually with the same amplitudes and seasonal variations for each chemical species. For instance, the mixing ratios of the

greenhouse gases at the surface, such as CO_2, CH_4, and N_2O, have an annual global mean of 284 ppmv, 0.808 ppmv and 0.273 ppmv, respectively. These greenhouse gases have similar seasonal variations of 1%. Surface emissions from other H species, like H_2, are constant year-round at 0.5 ppmv and are assumed to be the same at all latitudes. The main atmospheric components are O_2 (21%) and N_2 (78%).

Two important modifications were made in the simulation configurations compared with a default PI run. Firstly, we mute the QBO (Quasi-biennial Oscillation in the stratosphere) forcing in the simulations [3]. This is because the QBO is not a prognostic variable but is parameterized in the atmosphere with a $\sim 2°$ horizontal resolution to reproduce the Earth's stratospheric water vapor distribution from observation. Secondly, we disable MARBL[4] (Marine Geo-biochemistry Library) in the model configurations to simplify the calculations and because it is also tailored to Earth's ecosystem, which we cannot assume is the same on other planets. Additionally, solutions to resolve model numerical instabilities associated with the $e = 0.4$ case involve adjusting the physical time steps in the atmosphere component and modifying sub-grid parameterizations, as described in Appendix A.

After running 30 simulation years for each case, we find that the inter-annual variability of the Earth Energy Imbalance becomes close to zero ($\Delta F = F_{S,D} - F_{L,U}$, where $F_{S,D}$ and $F_{L,U}$ are the downwelling shortwave radiation at the top of the model and the outgoing longwave radiation at the top of the model, respectively. ΔF can be approximated as the difference between the shortwave and longwave radiation at the top of the model because the host star is the only source of shortwave radiation, and the planet contributes all of the longwave radiation. Even though the ΔF in each case has not reached zero due to the long timescale of the deep ocean circulation, we can verify that the simulations have passed their spin-up phase and have reached the quasi-steady states as the inter-

---

[3]QBO is a regular variation of the winds in the Earth's tropical stratosphere, and the oscillation alternates between easterly and westerly wind phases, with each phase lasting approximately 28 to 29 months.

[4]MARBL is a sub-model that controls marine ecosystem dynamics and the coupled cycles of carbon, nitrogen, phosphorus, iron, silicon, and oxygen (Long et al., 2021).

annual variability of the surface temperature for both cases becomes sufficiently small (i.e., $\Delta T_S \sim 0.1K$). In addition, both cases ended with negative ΔF in the year 30, indicating ongoing cooling with further simulation time. However, the circular case has a more negative ΔF than the highly eccentric case ($\Delta F_{e=0} - \Delta F_{e=0.4} = -1.6\text{W m}^{-2}$), which indicates it would continue to cool down faster than the $e = 0.4$ case on the slow approach to the final steady state. To minimize inter-annual variability, we averaged over the monthly mean outputs in the last five simulation years for both cases for the climatology analysis.

2.2.2 PSG Configurations

To gain observational insights from our WACCM6 simulations, we adopt the Planetary Spectrum Generator (PSG;Villanueva et al., 2018) with an idealized telescope (i.e., no instrumental noise) and a constant spectral resolving power of 250. For all cases, we focus on one orbital scenario where the planet is in a transit orbit with $90°$ inclination angle (edge-on). The geometry of the observation is set such that the planet is in front of the host star at a phase of $180°$.

Model data from WACCM6 were re-binned to a resolution of $5.625°$ in latitude (i.e., a binning number equal to 3) to save costs for computing the radiative transfer in PSG. Hence, a total of 32 sample points in latitude on the terminator are averaged over instead of the original 96 latitudinal points from the WACCM6 runs. We also adjust the number of stream pairs (NMAX) and the Legendre terms (LMAX) in PSG and find that NMAX=3 and LMAX=41 can produce accurate simulations in relatively fast time (See Villanueva et al. (2022) for more details about the two parameters).

The atmospheric composition is assumed to be made of N_2, H_2O, O_2, O_3, CO_2, N_2O, CH_4 as they are the dominant absorbers expected over our chosen wavelength range. We feed PSG with the instantaneous WACCM6 output, which includes the pressure-temperature structure, the mixing ratios of the molecules in the atmosphere, cloud fraction, and cloud ice fraction. Using the WACCM6 outputs, PSG computes the layer-by-layer ra-

diative transfer in the atmosphere, including the line-by-line intensity calculation using molecular cross-sections from the latest HITRAN database.

We configure PSG to generate the transit spectrum between 0.2 to 20 μm covering the UV, visible and infrared regions to determine if the predicted water abundances for both cases lead to potentially observable differences. For the eccentric case, we take snapshots of the climate on April 16th and November 12th to represent the hottest and coldest days, respectively. The planet-star separation of the $e = 0.4$ case is 1.03 au on April 16th, and 1.2 au on November 12th. For the circular case, the planet-star separation is fixed at 1 au, and we take one snapshot on April 16th only for comparison since the climate experiences no seasonal variation (recall that both simulations assume zero obliquity). Note that we simulate spectra only at two distinct points in the orbit representative of two extreme cases (corresponding to the hottest and coldest day). We may expect simulated spectra from other orbital positions to lie within these two scenarios, but this should be tested with further simulations.

2.3 Results

2.3.1 Temperature and Water Vapor Profiles

Figure 2.1 shows the globally-averaged annual mean vertical temperature profiles for the circular case (blue) and the $e = 0.4$ case (red). The temperature decreases with increasing altitude in the troposphere up to the tropopause, at which a temperature inversion occurs. We show the globally-averaged monthly mean temperature profiles to demonstrate the range in temperature experienced by the eccentric planet in April (red dotted line) and November (pink dotted line) at which the highest and lowest surface temperatures are reached, respectively, and to compare with the annual means. The annual mean temperature profile for the $e = 0.4$ case has a slightly warmer troposphere with a 1.3 K higher surface temperature than the circular case. The tropopause is moved up in altitude in the $e = 0.4$ case but its tropopause temperature is lower than the
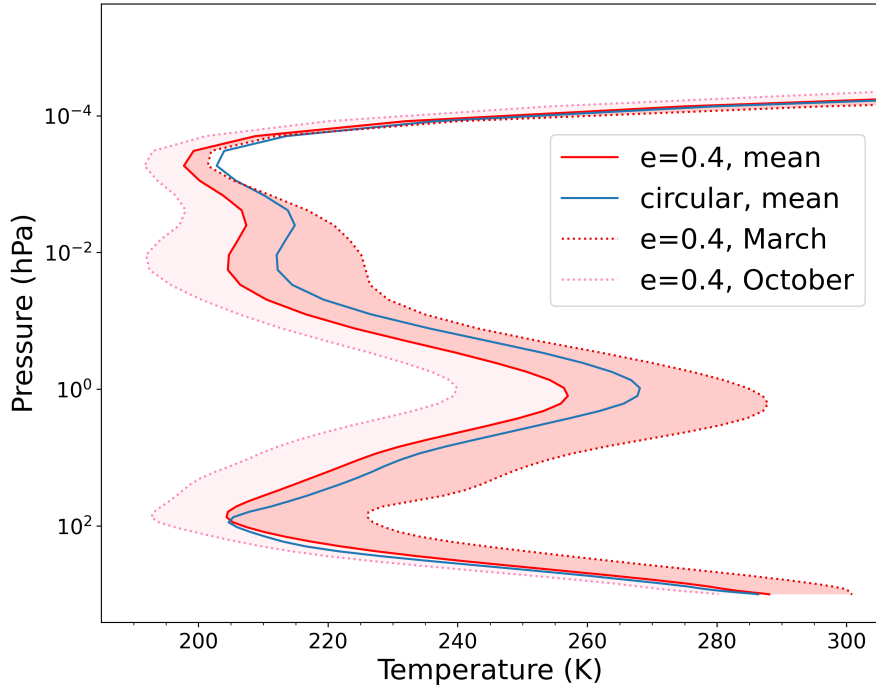
Figure 2.1: The annual mean atmospheric temperature profile for the $e = 0.4$ case (red) and the circular case (blue) from the surface to the homopause. The hot (red shaded area) and cold (pink shaded area) passages for the $e = 0.4$ case cover the time when the atmospheric temperature is higher than the mean and is lower than the mean, respectively. The temperature profiles for the hottest month (April) and the coldest month (November) are indicated by the dotted lines on the outer boundary of the shaded areas. For demonstration purposes, we give a secondary y-axis to indicate the altitude in km for the circular case. For the $e = 0.4$ case, the corresponding altitude in km does not deviate much from the secondary y-axis because they have similar atmospheric scale heights ($\delta H \sim 0.5$ km).

circular case by 1.2 K. In the upper atmosphere from the tropopause to the mesopause, the annual mean temperature in the $e = 0.4$ case is lower by 6.7 K on average than in the circular case, and the maximum temperature difference of 11.1 K occurs at the stratopause. That the stratosphere is colder may be due to a 3 % less annual mean ozone column due to increased production of OH radicals from increased water vapor photolysis (see Section 2.4 for more details). Less ozone means fewer UV absorbers, and hence they contribute less heating to the stratosphere. In addition, the increase in water vapor in the stratosphere could have a radiative cooling effect (Oinas et al., 2001).

Although the stratosphere and mesosphere are, on average, colder in the eccentric case, there is significant seasonal variation in the temperature profiles which reaches a max-

imum in April and a minimum in November due to the lagged response of surface and tropospheric temperature. It takes roughly two months for both the planetary surface and the atmosphere to respond to the highest insolation at perihelion, and three months to respond to the minimum insolation at aphelion (see Fig. 2.1). The lag may correspond to the radiative timescale of the coupling between the surface and the atmosphere (Cronin et al., 2013). A simplified approach from Guendelman et al. (2020) states that the radiative timescale, τ, can be approximated as

$$\tau \propto CQ^{-3/4}$$

where C is the atmospheric heat capacity and Q is the incoming insolation at the top of the atmosphere. Assuming that C remains approximately constant over the eccentric orbit, the radiative timescale should decrease with increasing Q. This is consistent with what we see here which is that the surface and tropospheric temperature lagged response at aphelion is longer than at perihelion. Furthermore, the surface temperature difference between the peak and the annual mean ($|\delta TS| = 12.8$ K) is significantly greater than the difference between the trough and the annual mean ($|\delta TS| = 7.8$ K). Thus, the lagged response of surface and tropospheric temperature for the $e = 0.4$ case is seasonally asymmetric in both the response time and the response magnitude.

The top panel of Fig. 2.2 shows the annual mean temperature (top panel) from the surface to the stratopause as a function of latitude for the $e = 0.4$ case, and the bottom two panels show the temperature difference at perihelion (middle panel) and aphelion (bottom panel) relative to the annual mean temperature profile. The mean temperature pattern reflects the fact that Earth's obliquity is set to zero such that the zonal mean surface temperature decreases between the tropics and the poles. Similar to Earth, the Arctic region is warmer at the surface than the Antarctic region because the former is ocean-covered and hence has a larger heat capacity mitigating the cold winters in the eccentric orbit. Unlike the whole atmospheric and surface warming and cooling during the

hottest month (April) and the coldest month (November) shown in the middle and bottom panel of Fig. 2.3, respectively, one feature in Fig. 2.2 is the atmospheric and surface lagged response to the change in insolation, as shown in the bottom panel. At perihelion where the planet receives 2.64 times its mean insolation, the troposphere ($< 10^2$ hPa) is colder than the annual mean temperature. However, the temperature pattern is reversed in the stratosphere between 10^2 to 1 hPa. We find that the stratospheric temperature is lagged by 1 month relative to perihelion, and 2 months relative to aphelion, whereas the tropospheric temperature is better coupled with the surface temperature. In addition to the ocean heat buffer at aphelion, that the troposphere and the surface are warmer in the $e = 0.4$ case can be attributed to a weaker cloud shortwave radiative effect, which contributes about 5 Wm^{-2} more into the system compared to the circular case. The cloud shortwave effect controls the transmitted radiation from the cloud layer down to the surface. The atmospheric and surface lagged response to insolation helps the climate to remain temperate in these two extreme scenarios.

During the hot orbital passage, more surface water can be evaporated and uplifted into the tropical troposphere as the surface temperature rises. Through condensation, the tropical tropopause, also known as the cold trap, confines most of the rising water vapor in the form of clouds, but a small amount of water vapor can escape into the stratosphere [5]. The stratospheric water vapor concentration oscillates seasonally at the same frequency as the tropical tropopause temperature, which is known as the 'tape recorder' signal. Here, we examine the 'tape recorder' signal in the circular and $e = 0.4$ cases. The upper panel in Fig. 2.4 shows the seasonal variation of tropical tropopause temperature for the $e = 0.4$ case (red) and the circular case (blue). The corresponding stratospheric water vapor mixing ratios in ppmv for these two cases are shown in the middle and bottom panels of Fig. 2.4. The tropical tropopause altitude is calculated for each month over the last five simulation years after steady state is reached since the tropopause can be lifted upward or downward depending on the surface temperature in the $e = 0.4$ case.

---

[5]Moist air could bypass the cold trap for high obliquity worlds (Kang, 2019)
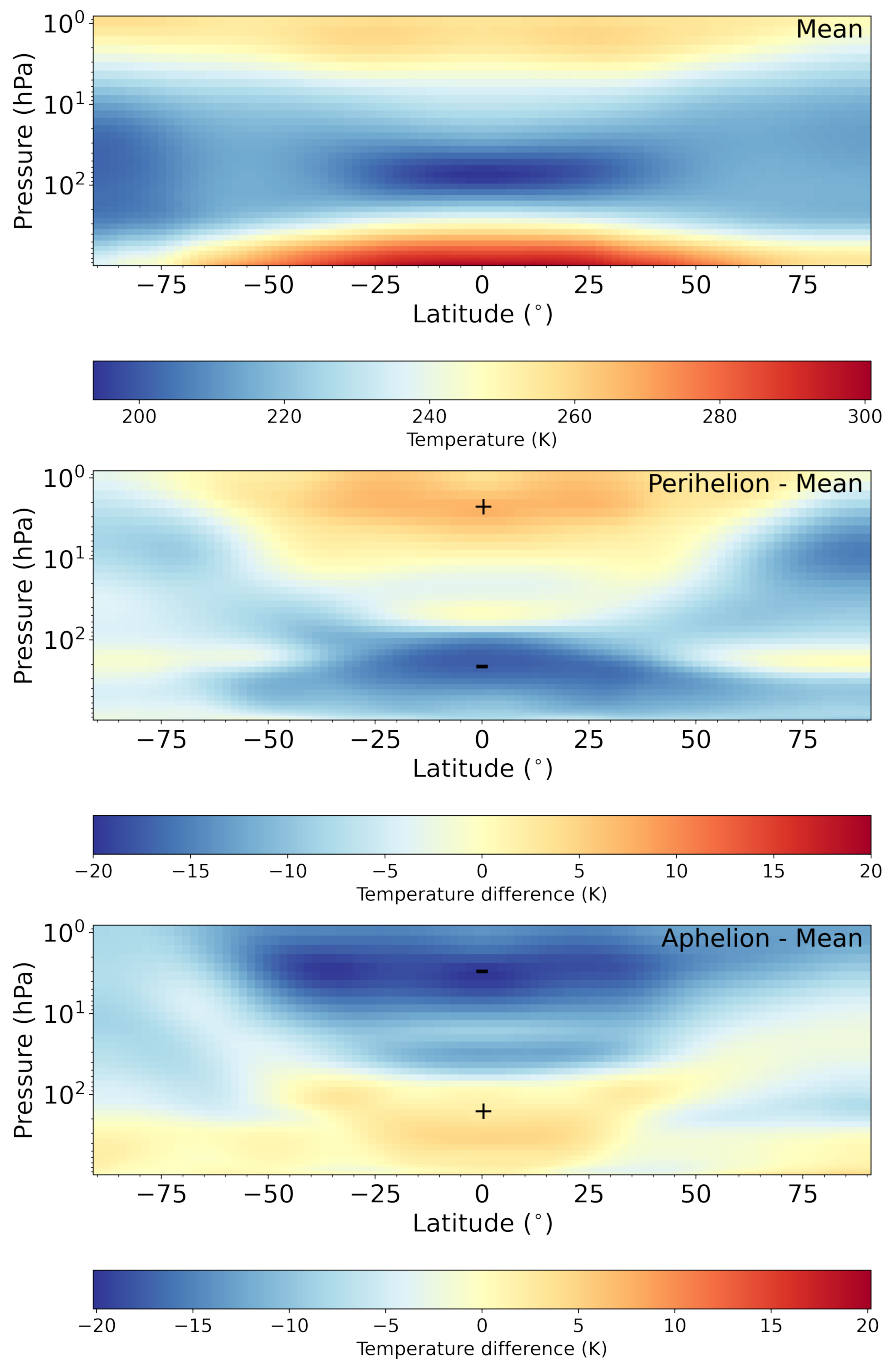
Figure 2.2: Upper panel: annual, zonal mean of air temperature from the surface to the stratopause over the last five simulation years after steady state is reached for the $e = 0.4$ case. Middle panel: the difference in air temperature between perihelion and the mean for the $e = 0.4$ case. Bottom panel: the difference in air temperature between aphelion and the mean for the $e = 0.4$ case. Note that the top panel has a different color scale than the middle and bottom panels. The plus and minus signs in the figure denote the positive and the negative temperature differences, respectively.
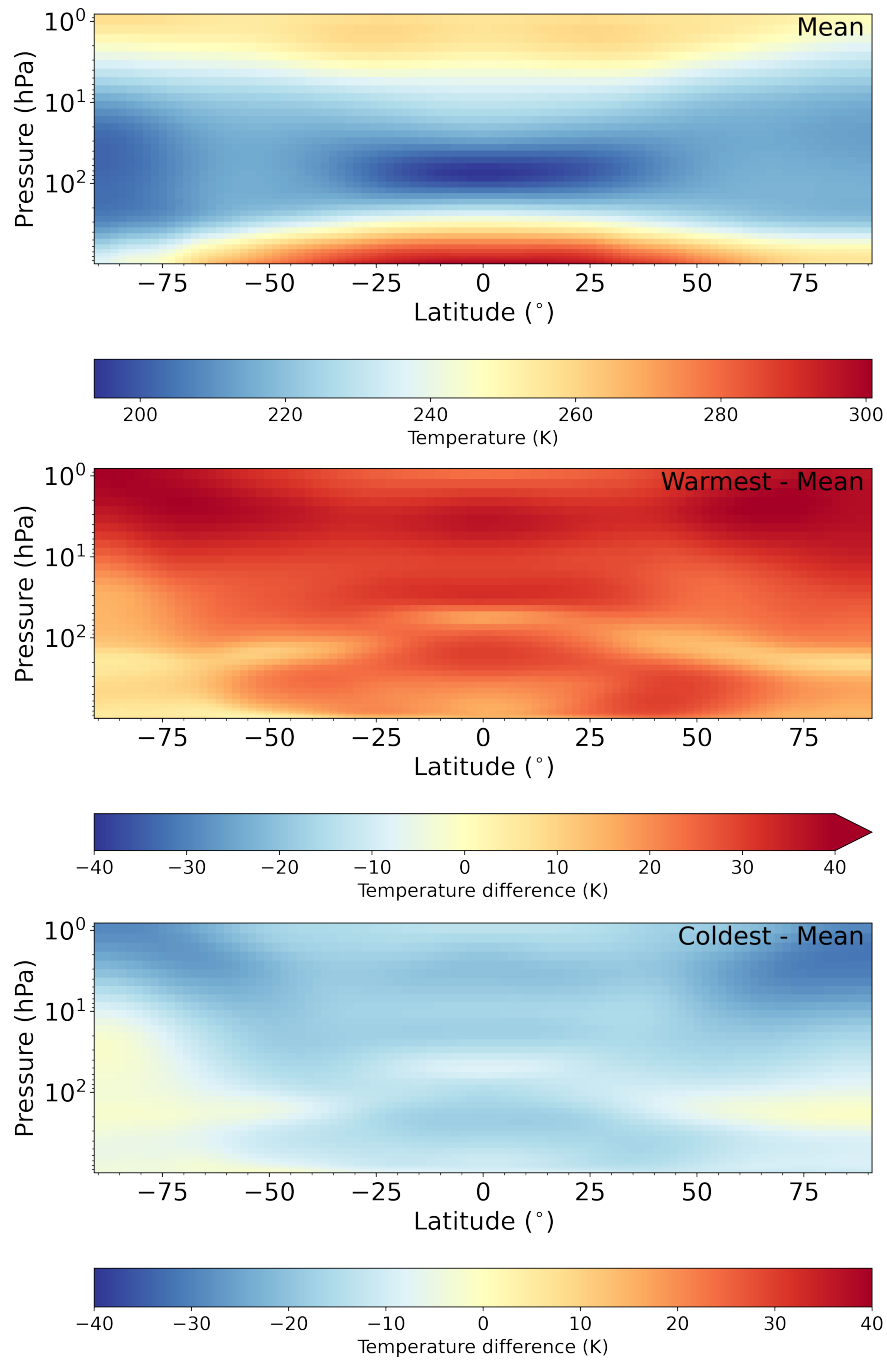
Figure 2.3: Upper panel: annual, zonal mean of air temperature from the surface to the stratopause over the last five simulation years after steady state is reached for the $e = 0.4$ case. Middle panel: the difference in air temperature between the warmest month (April) and the mean for the $e = 0.4$ case. Bottom panel: the difference in air temperature between the coldest month (November) and the mean for the $e = 0.4$ case. Note that the top panel has a different color scale than the middle and bottom panels.

As indicated by the dotted lines in the top panel of Fig. 2.4, the annual mean tropical tropopause temperatures are 194.27 K in the $e = 0.4$ case and 193.07 K in the circular case. Although the annual mean temperatures differ by ~ 1 K between these two cases, the seasonal variation of the tropical tropopause temperature in the $e = 0.4$ case is significantly higher than in the circular case. From the middle and the lower panels, the water vapor mixing ratios at the bottom of the stratosphere for both cases follow the same temporal pattern as shown in their tropical tropopause temperature profiles. This also indicates that the water vapor mixing ratios at the cold trap are in phase with the surface and tropospheric temperature. In April, the temperature is over ~ 215 K in the $e = 0.4$ case, in contrast to ~ 193 K in the circular case. The cold trap in April for the $e = 0.4$ case becomes less effective, allowing a larger amount of water vapor (up to 30 ppmv) to enter the stratosphere, producing a clear tape recorder signal.
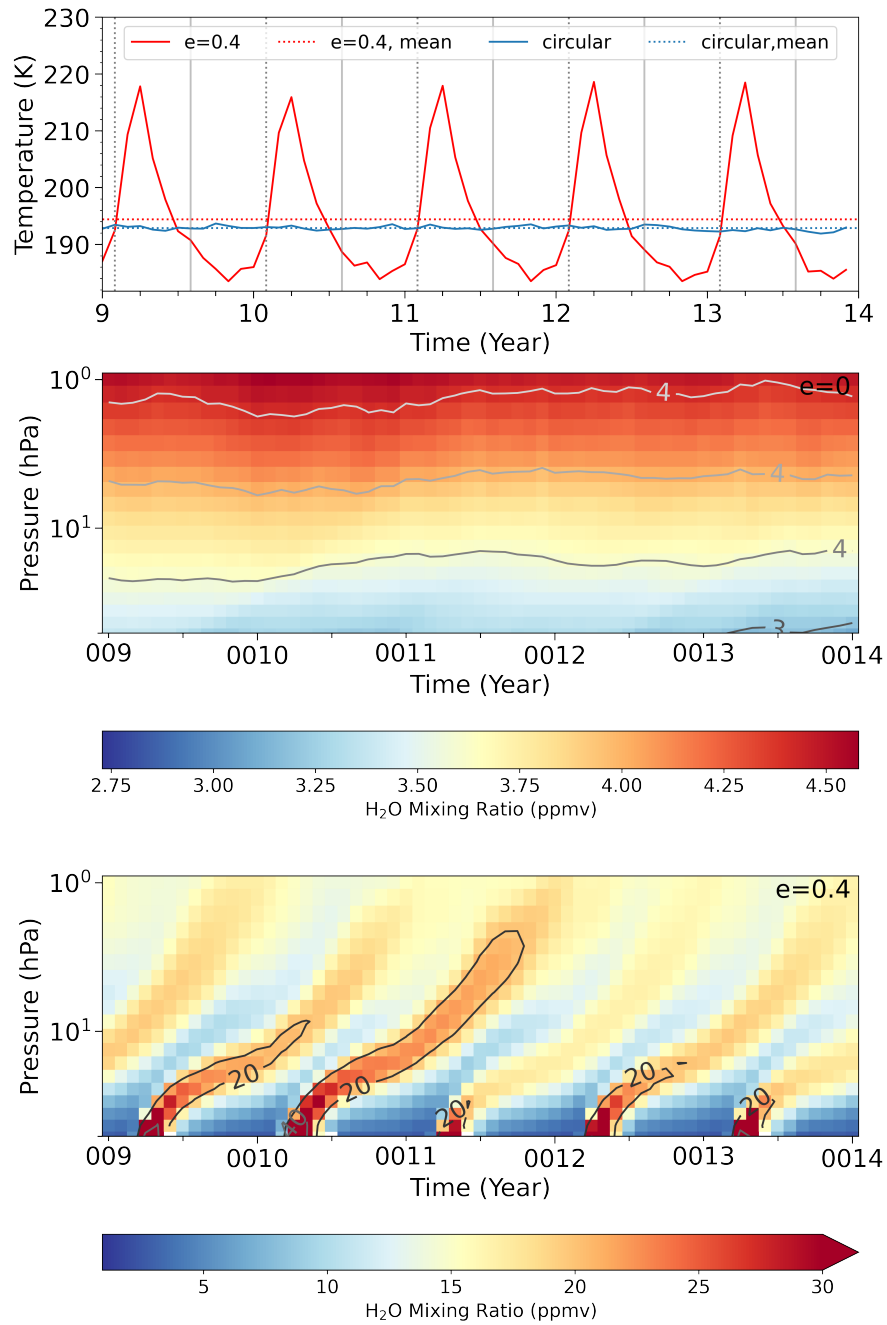
Figure 2.4: Upper panel: the seasonal variation in the tropical tropopause temperatures for the $e = 0.4$ case (red solid line) and the circular case (blue solid line). Also shown are the annual mean of the tropical tropopause temperatures for the $e = 0.4$ case (red dotted line) and the circular case (blue dotted line) over the last five consecutive years of the simulations. Perihelion takes place in February (grey dotted line), and aphelion takes place six months afterwards in August (grey solid line). Middle and lower panels: the H_2O mixing ratio in the stratosphere for the circular case and the $e = 0.4$ case over the last five consecutive years of the simulation, respectively. Note the presence of the 'tape recorder' signal in the bottom plot for the $e = 0.4$ case. The black contours highlight a constant mixing ratio of 20 ppmv and the 'tape recorder' signal is moving vertically upward in each case.

70

2.4 Discussion

2.4.1 Water Loss Rate and Ocean Loss Timescale

Figure 2.5 shows the H_2O and total H species ($H + 2 \cdot H_2 + 2 \cdot H_2O + 4 \cdot CH_4$) mixing ratios. For simplification, we assume that the total hydrogen species comprises only the four listed species, as these are the primary hydrogen carriers in the upper atmosphere of modern Earth. The annual mean mixing ratio of the tropical tropopause water vapor for the $e = 0.4$ case (red dotted line) is 11.3 ppmv and is about three times greater than that for the circular case (blue dotted line), though it is still about two orders of magnitude lower than the threshold of 3×10^3 ppmv needed to trigger moist greenhouse states (e.g. Kasting et al., 1984; Kasting, 1988).

To quantify how quickly water can escape into space, we compute the total loss rate at the homopause, in units of atoms $\text{cm}^{-2}\,\text{s}^{-1}$, as the sum of individual hydrogen-bearing species as follows:

$$\Phi_H = \frac{1}{H_a} \cdot (b_H f_H + 2 \cdot b_{H_2} f_{H_2} + 2 \cdot b_{H_2O} f_{H_2O} + 4 \cdot b_{CH_4} f_{CH_4}) \qquad (2.4)$$

where f is the mixing ratio of the selected hydrogen carrier in ppmv, b is the binary diffusion parameter in units of $\text{cm}^{-1}\,\text{s}^{-1}$, and H_a is the atmospheric scale height in cm. The scale height is $H_a = \frac{k_B T_{hp}}{mg}$ where k_B is Boltzmann's constant, T_{hp} is the globally averaged homopause temperature, m is the mean atmospheric molecular mass, and g is the surface gravity. The binary diffusion parameter formulas can be found in Hunten,
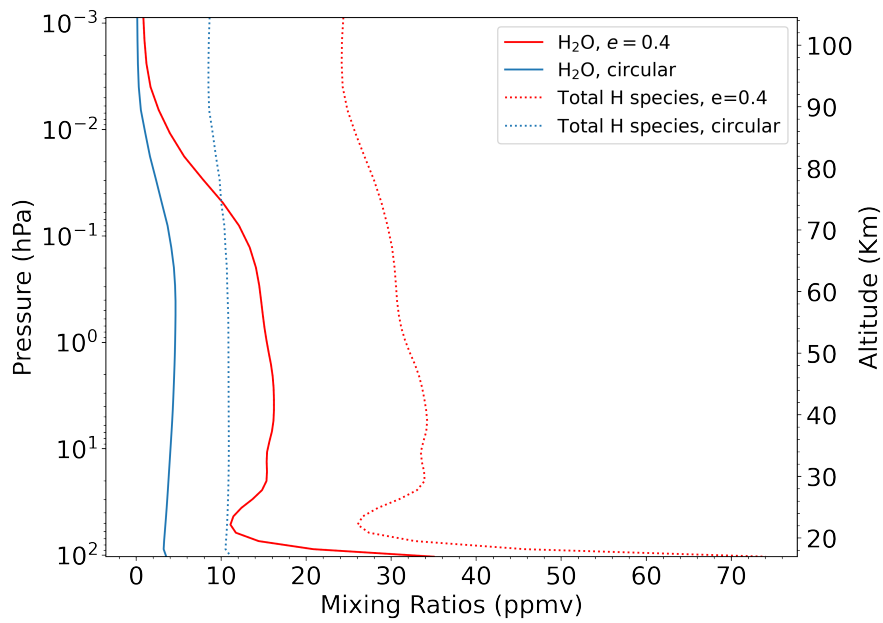
Figure 2.5: The global, annual mean H_2O and total H species mixing ratios in the stratosphere averaged over the last 5 simulation years for the $e = 0.4$ case (red solid and red dotted line, respectively) and the circular case (blue solid and blue dotted lines, respectively). The vertical scale in the plot is set to cover from the tropopause to the homopause for the circular case. For demonstration purposes, we give a secondary y-axis which is used to indicate the altitude in km for the circular case only. For the $e = 0.4$ case, the corresponding altitude in km does not deviate much from the secondary y-axis because both cases have similar atmospheric scale heights ($\delta H \sim 0.5$ km).

1973 for b_{H}, b_{H_2}, $b_{\mathrm{H}_2\mathrm{O}}$, and in Banks et al. (1973) for b_{CH_4}, and we reproduce them here:

$$b_H = 6.5 \times 10^{17} \cdot T_{hp}^{0.7}$$

$$b_{\mathrm{H}_2} = 2.67 \times 10^{17} \cdot T_{hp}^{0.75}$$

$$b_{\mathrm{H}_2\mathrm{O}} = 0.137 \times 10^{17} \cdot T_{hp}^{1.072}$$

$$b_{\mathrm{CH}_4} = 0.756 \times 10^{17} \cdot T_{hp}^{0.747}$$

$$(2.5)$$

where T_{hp} is the homopause temperature in K.

The homopause is taken to be at a pressure level of 1.458×10^{-3} hPa (~ 100 km), and the total hydrogen species mixing ratios at homopause in the $e = 0.4$ case (red dotted line in Fig. 2.5) is 24.2 ppmv. This is about three times larger than the 8.5 ppmv calculated for the circular case (blue dotted line). The escape fluxes calculated using the above equations are 6.33×10^8 and 2.31×10^8 atoms cm^{-2} s^{-1} for the $e = 0.4$ case and the circular case, respectively. Additionally, we have compared the escape fluxes from taking the global annual mean operator over the individual component on the right hand side of Eq. 2.4 against taking the global annual mean operator over the sum of all species, and we find a 0.3% difference in the escape flux. Thus, it can be confirmed that this uncertainty is not significant. To compare with previous estimates, the H escape flux in the circular case is lower than that Catling et al. (2017b) calculated for the Earth's eccentricity case (3.5×10^8 atoms cm^{-2} s^{-1}). This could be due to the obliquity and eccentricity differences, which result in a lower homopause temperature, a smaller scale height, and a lower total hydrogen species mixing ratio when calculating the escape flux. In addition, the hydrogen mixing ratio values in that work are taken from the lower stratosphere instead of the homopause. Thus, any bottlenecks that could exist above the lower stratosphere may not have been included in their calculations (see Fig. 2.5 for the differences in the total H mixing ratio at different altitudes).

We can use our calculated H escape fluxes to estimate the ocean survival timescale for

both cases. The total mass of water in Earth's ocean is 1.4×10^{24} g (e.g. Wolf et al., 2015; Kopparapu et al., 2017). We compute the corresponding total hydrogen reservoir to be about 9.36×10^{46} atoms so that the ocean loss timescale is 2,437 Gyr for the circular case and 891 Gyr for the $e = 0.4$ case. As a result, an Earth-like planet in an eccentric orbit ($e = 0.4$) around a Sun-like star loses its water inventory in approximately one third of the time it takes a planet in a circular orbit to lose its water inventory. Despite this higher ocean loss rate, our results suggest that a highly-eccentric Earth-like exoplanet could retain its oceans over the lifetime of the stellar system. Our result agrees with Palubski et al. (2020) who predict, using a 1D model, that an Earth-like exoplanet around a G-type star in an $e = 0.4$ orbit has a dry upper atmosphere (i.e., one that is far away from entering a runaway greenhouse state). However, it is worth noting that complete ocean water loss has been predicted to occur within 2 Gyr for our Earth under the brightening Sun due to its evolution through the main sequence stage (Wolf et al., 2015). Thus, the ocean loss timescale under a brightening host star should be much shorter than what we have estimated here for both the circular and the eccentric cases. How both orbital eccentricity and evolving host star luminosity together affect the water loss should be tested in future simulations. On the other hand, our water loss rate estimates are upper bounds under constant insolation as they are computed based on the mixing ratio of the total H species which can enter into the homopause (Hunten et al., 1974). So, the ocean loss timescales calculated in the two cases here could be longer depending on the efficiencies of active escape mechanisms (i.e., thermal escape, non-thermal escape, impact erosion). We note also that the water loss rate on an Earth-like exoplanet is also likely to be influenced by the stellar type of the host star (e.g. Wolf et al., 2017; Kaltenegger et al., 2021). Moreover, the ocean loss timescale also depends on the initial water inventory, and so it is possible for an Earth-like exoplanet with a much smaller initial water reservoir ($<1\%$) to lose all of its water content within the lifetime of its stellar system.

2.4.2 Implications for Observations

We use PSG (Planetary Spectrum Generator) to generate synthetic transit spectra for the $e = 0$ and $e = 0.4$ cases. The upper panel of Fig. 2.6 shows the synthetic transit spectra for the circular case (black), the snapshot on April 16th for the $e = 0.4$ case (red) and the snapshot on November 12th of the $e = 0.4$ case (blue). The lower panel shows the differences in transit depth between the circular case and the snapshot on April 16th of the $e = 0.4$ case (red) and between the circular case and the snapshot on November 12th of the $e = 0.4$ case (blue), and between the snapshots on April 16th and November 12th of the $e = 0.4$ case (green). Absorption signatures from H_2O, O_3, CO_2 and CH_4 are present in the synthetic spectra. The strong absorption feature near $4.8\,\mu m$ is due to CO_2 with a transit depth of $55\,km$. For water, the dominant feature is at $2.6\,\mu m$ with a ~ 37 km transit depth. The largest O_3 feature with a transit depth of $65\,km$ is at around $0.25\,\mu m$. The feature at $15\,\mu m$ has a transit depth of $50\,km$ and is due to both CO_2 and O_3. The baselines of the three cases are different due to a combined effect of differences in the planet-star separation, cloud coverage and temperature. In general, a larger planet-star separation, more cloud coverage and higher temperature all increase the baseline (Bétrémieux et al., 2014; Fauchez et al., 2019). The effect of clouds is important in the $e = 0.4$ case because there is more cloud than in the circular case, and the cloud extends vertically to the lower stratosphere below 20hPa. Thus, the cloud in the $e = 0.4$ case can, not only increase the transit depth of the baseline, but also decrease the depth of spectral features in the infrared.

In the lower panel of Fig. 2.6, the water features on April 16th are about 5 km deeper than on November 12th (green line), reflecting the largest seasonal difference in the water abundance in the $e = 0.4$ case. This is seen in the water absorption features present at $1.36\,\mu m$, $1.87\,\mu m$, $2.7\,\mu m$ and between $5.93\,\mu m$ and $6.64\,\mu m$. The difference in the depth of the water features between the April 16th snapshot in the $e = 0.4$ case and the circular case is 1 to 2 km larger (red line) than the maximum seasonal difference. The
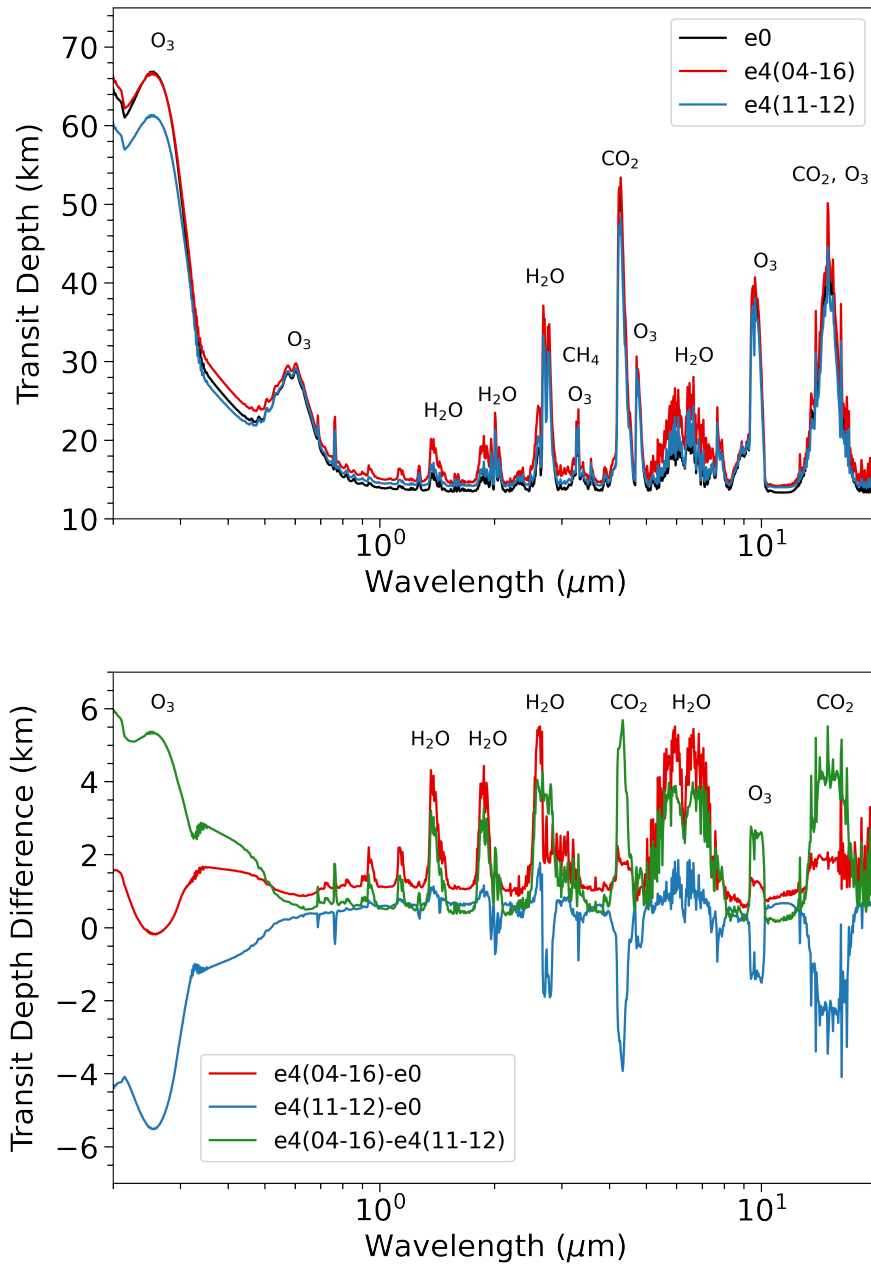
Figure 2.6: Upper panel: the transit spectra of the circular case (black), the snapshot on April 16th of the $e = 0.4$ case (red) and the snapshot on November 12th of the $e = 0.4$ case (blue) between 0.2 µm to 20 µm; Bottom panel: the transit depth difference between the snapshot on April 16th of the $e = 0.4$ case and the circular case (red), the transit depth difference between the snapshot on November 12th of the $e = 0.4$ case and the circular case (blue) and the transit depth difference between the snapshots on April 16th and November 12th of the $e = 0.4$ case (green).

76

differences in the depth of the water features between the November 12th snapshot in the $e = 0.4$ case and the circular case (blue line) is the smallest of our three comparisons; however, slightly stronger water absorption features are present even on the coldest day of the $e = 0.4$ case. The reason for this is related to the strong release of water vapor into the stratosphere during the warmest month (April in the $e = 0.4$ case) which slowly propagates upward in the stratosphere (see the bottom panel Fig. 2.4). Thus, the water vapor column above the baseline at a given time depends on both the current and the previous release of water vapor above the cold trap. This is essentially a result of the strong seasonality induced by the large eccentricity.

The stronger water features on April 16th compared to November 12th and the circular case can be explained by the higher temperature in the April 16th snapshot for the $e = 0.4$ case. A higher surface temperature increases the evaporation rate of H_2O, which increases the H_2O number density with altitude; more H_2O molecules mean stronger absorption in the infrared. Some secondary effects could also contribute to the transit depth difference. For example, the H_2O absorption cross-section positively correlates to the temperature at these wavelengths (Gordon et al., 2022). The higher temperature on April 16th also causes a more inflated atmosphere, and hence more water vapor molecules are present at a higher altitude.

Unlike the H_2O features which are always stronger in the highly-eccentric case than the circular case, the CO_2 transit depth features near $4.8\,\mu\text{m}$ and $15\,\mu\text{m}$ are 2 to 3 km deeper for the April 16th case than the circular case, but they are about 4 km deeper for the circular case than on November 12th. The seasonal variation of the CO_2 transit features is about 6 km between the April and the November cases. The reasons for these are the same as just described for the water. The atmosphere expands at higher temperatures, and the CO_2 density remains high at higher altitudes than if the atmosphere were cooler.

The ozone layer in the stratosphere is an important atmospheric constituent on Earth as it can prevent harmful UV radiation from reaching the surface. The ozone concentration

in the atmosphere does not vary as much as the water vapor in the highly eccentric system. The annual mean ozone column density decreases by about 3% in the $e = 0.4$ case compared to the circular case, and the seasonal ozone column density in the $e = 0.4$ case decreases up to about 13% in April compared to the circular case. This is affected by the water vapor abundance in the atmosphere: a higher water vapor abundance leads to more OH radicals formed in the atmosphere via photolysis, and hence more ozone is destroyed by the increasing amount of OH radicals. The seasonal variation of O_3 density in the stratospheric ozone layer for the $e = 0.4$ case ($\sim$ 16%) could impact the temporal surface habitability (Gómez-Leal et al., 2019). In the upper panel of Fig. 2.6, the most prominent ozone features of the transit spectrum peaks around 0.25 µm in the UV region, 0.6 µm in the visible, and around 9.6 µm in the infrared. There are small O_3 absorption depth differences between the April 16th snapshot case and the circular case, whilst there are noticeable O_3 absorption depth differences ($\sim$ 2 km) between the April 16th snapshot case and the November 12th snapshot case.

Contrary to expectations, the $e = 0.4$ case's ozone features are stronger on April 16th than on November 12th, as shown in the lower panel of Fig. 2.6, despite the former having a lower ozone column density than the latter. Similarly, when comparing the circular case and the November 12th snapshot case, we find that a higher ozone column density does not correspond to a more pronounced ozone feature. This is because a higher atmospheric temperature causes larger ozone absorption cross-sections (Serdyuchenko et al., 2014; Gordon et al., 2022), and the O_3 number density above 40 km is higher in both the April 16th snapshot case and the circular case than in the November 12th snapshot case. Therefore, future transmission spectra observations could result in degenerate interpretations for inferring the total ozone column density for Earth-like exoplanets.

2.5   Conclusions

Terrestrial exoplanets can have large orbital eccentricities up to values as high as 0.4 to 0.5 (Lopez et al., 2019). The climate response of rocky planets to changes in eccentricity has been studied in recent years using both 1D models and 3D general circulation models (GCMs). Previous work has examined water loss due to an increasing solar constant from both Earth and other potential exoplanet host stars. However, whether the eccentricity-induced seasonality effect alone has a critical impact on water loss had yet to be studied. Using the fully coupled 3D Earth climate model, WACCM6, we simulated the climate response of Earth-like rocky planets around a Sun-like star that have different orbital eccentricities. We compared the temperature structures and the water loss rates calculated for a circular orbit case and a highly-eccentric case ($e = 0.4$). We find that the water loss rate for a planet in the $e = 0.4$ orbit is about 3 times larger than if it were in a circular orbit under the same annual mean insolation. Consequently, the ocean loss timescale for an Earth-like exoplanet in such an eccentric orbit is about 3 times shorter than the circular orbit. Moreover, an Earth-like planet with an eccentricity of 0.4 spends half of its orbit outside of the Earth's habitable zone as traditionally defined by Kasting et al., 1993. Nevertheless, we find that the climate remains temperate and the planet can hold on to its water reservoir. In addition, Earth-like exoplanets with a high orbital eccentricity could have stronger H_2O and CO_2 absorption features in simulated transmission spectroscopy than for the same planet in a circular orbit. Hence, the climate response to eccentricity as indicated by a higher water abundance may be measurable with future observations. Stronger O_3 absorption features seen in future observations may not always imply a higher ozone column density for an Earth-like exoplanet with an ozone layer in its atmosphere. It is worth noting the limitations of this study. First of all, the model we adopted in the simulation uses numerous parameterizations that are tuned to Earth's climate and might be inappropriate to generalize to an exoplanetary climate with different conditions. Hence, these conclusions should be tested in future simulations

with more flexible chemistry, land and ocean coverage, and cloud and radiative transfer schemes. Secondly, a variety of effects such as QBO and ocean bio-geochemistry are excluded from the simulation, though they will not change our results qualitatively. In addition, the Earth-like exoplanet's atmosphere evolution over its geological history and the effects of space weather have been ignored because these factors are beyond the scope of this study. For a more comprehensive view of the habitability analysis of Earth-like exoplanets, future work should include a systemic climate study due to the change of eccentricity with more effects included and more inter-comparisons between different 1D and 3D model simulations.

Chapter 3

Earth as an Exoplanet in an Eccentric Orbit II: Energy Balance, Climate and Surface Habitability

3.1 Introduction

To assess surface habitable conditions on rocky planets, it is essential to consider the role of the planetary atmosphere, as it can mediate surface temperature through atmospheric radiative transfer and atmospheric circulation. Recent observations of tidally-locked planets, such as TRAPPIST-1 b (Greene et al., 2023) and TRAPPIST-1 c (Zieba et al., 2023), using the James Webb Space Telescope (JWST), have so far shown that these exoplanets may have no atmosphere. Looking ahead, future space missions like PLAnetary Transits and Oscillations of Stars (PLATO) will be able to find Earth-sized planets around Sun-like stars within the next decade (Heras et al., 2022). Concurrently, ground-based and space missions, such as the Extremely Large Telescope (ELT) (Padovani et al., 2023) and the Habitable Worlds Observatory (HWO) [1], will enable astronomers to study and characterize the atmospheres of rocky exoplanets with long orbital periods around Sun-like stars (Neichel et al., 2018; Vaughan et al., 2023).

Tidal evolution can circularize the eccentric orbits of exoplanets around low-mass ($\simeq$

---

[1]The Habitable Worlds Observatory: `https://science.nasa.gov/astrophysics/programs/habitable-worlds-observatory/`, accessed on 01/18/2024

$0.1 M_\odot$) to solar-mass stars ($\simeq 1 M_\odot$) well within the lifetime of the stellar system ($<$ 10 Gyr). Nevertheless, depending on the initial rotational period and possible tidal interactions between planets and moons in the stellar system, planets can also remain in, or evolve to, highly eccentric orbits (Barnes, 2017). To date, the total number of exoplanets detected and confirmed has reached approximately 6500 [2], of which 160 of them are potentially rocky exoplanets with masses and radii less than 10 $M_\oplus$ and 1.6 $R_\oplus$, respectively (Rogers, 2015; Lopez et al., 2019; Wordsworth et al., 2021). Among these 160 potentially rocky worlds, 89 have measured eccentricities, and 16 are in highly eccentric orbits ($e \geq 0.1$). It is worth mentioning that the eccentricity distribution of terrestrial planets around Sun-like stars is yet to be determined due to the lack of detection in this orbital regime, and the above statistics are biased towards close-in planets around M and K dwarfs that are both easier to detect and more likely to be circularized. As such, we expect more highly eccentric rocky planets to be detected in the future.

Understanding the potential climate outcome and surface habitability of highly eccentric ($e > 0.1$) rocky exoplanets is crucial for the future characterization of long-period exoplanets. Multiple studies using 1D and 3D simulations have found that increasing orbital eccentricity results in higher surface temperatures and stronger seasonal variations.(Williams et al., 2002; Way et al., 2017b; Dressing et al., 2010; Linsenmeier et al., 2015; Liu et al., 2023; Way et al., 2023; Biasiotti et al., 2024) and hence shifts the habitable zone farther out from the host star. These simulation results generally agree with what the analytical approach predicts (Quirrenbach, 2022; Ji et al., 2023). However, for tidally-locked Earth-like exoplanets around Sun-like host stars (1 $L_\odot$), the mean surface temperature decreases with increasing orbital eccentricity (Bolmont et al., 2016). Recent work on habitability analysis has focused on Earth-like exoplanets around Sun-like stars and M-dwarf stars. The former is often theoretical simulation cases investigating an Earth-twin planet with different sets of orbital parameters, host star types and ocean-

---

[2]The Extrasolar Planets Encyclopaedia: `http://exoplanet.eu/`, accessed on 27/06/2024

land distribution (e.g. Ozaki et al., 2021; Sproß et al., 2021; He et al., 2022; Höning et al., 2023); the latter, due to observability advances in recent years, have conducted habitability analysis for both theoretical and actual exoplanets cases covering a large set of parameter space (e.g. Valente et al., 2022; Macdonald et al., 2022a; Lobo et al., 2023; Braam et al., 2023a; Biasiotti et al., 2024). In these studies, the surface habitable conditions are often analyzed from the climate parameters, where surface temperature, precipitation and evaporation are usually the main variables of interest, and hence such studies necessitate 3D GCMs. In an aqua-planet (a planet with an ocean covering its entire surface) simulation, the nutrient uptake rate in the ocean-mixed layer has been used to determine the extent of habitability (Jernigan et al., 2023). Whether an exoplanet is habitable to the lifeforms adapted for Earth is challenging to answer with the limited information available from observations, and it depends on the definition of habitability and classification methods considered (e.g. Kane et al., 2012; Cockell et al., 2016; Safonova et al., 2021; Basak et al., 2021).

This study examines the radiative energy balance for a highly eccentric Earth-like planet and compares it with its circular orbit counterpart under the same annual mean irradiance. We define criteria to assess how orbital eccentricity can affect the habitable conditions on the land surface, and we explain our results considering the changes in the global radiative balance and atmospheric circulation. The model description is presented in Section 2.1; the simulation configurations are described in Section 2.2; the simulation results are shown in Section 3; the discussion, including the implications, caveats and possible future directions, is in Section 4, and we present our conclusions in Section 5.

3.2   Methods

Following the work in Chapter 2, which focuses on the water loss via hydrogen escape and potential observability, we use the same WACCM6 configurations to output an additional set of variables for a more detailed climate and habitability analysis for the $e = 0$ and

$e = 0.4$ cases.

To compare the habitability of a highly eccentric planet with its circular equivalent, we must define a metric. Since we are not simulating a completely exotic world and both cases stay relatively similar to our PI Earth configuration, we define our habitability metrics as a combination of the surface temperature and cumulative precipitation over land, similar to He et al. (2022).

We choose a lower limit for a habitable surface temperature to be the freezing point of water (273 K) at one standard atmospheric pressure. While we realize many lifeforms on Earth can exist in the ocean with various temperatures, pressures and salinities, we restrict the scope of this study only to land habitability based on the availability of liquid water. For the upper limit, the boiling point of water is not reasonable since the climate can enter the moist or runaway greenhouse state far below the boiling point temperature, during which the water will be irreversibly lost into space (e.g. Wolf et al., 2014). We choose a conservative temperature upper limit above which only thermophilic microorganisms can survive and reproduce (323 K), and beyond which the biodiversity on Earth significantly decreases (Clarke, 2014). In addition to the surface temperature limits, we define the accumulative precipitation limits in the same way as in He et al. (2022), which requires the annual total precipitation to be greater than 30 cm over land to separate the desert regions from those which can exhibit higher biodiversity and are potentially more habitable.

3.3 Results

3.3.1 Energy Balance

The annual global mean surface temperature in the $e = 0.4$ case is 289.6 K, which is 1.9 K higher than in the circular case due to a 6.3 W m^{-2} stronger average incoming radiation at the top of the model ($F_{S,D}$). If the global mean surface temperature were the only metric used, we might conclude that both configurations sit within the habitable

zone and are equally habitable (see the variables that describe the atmospheric energy balance in Table.3.1). For the $e = 0.4$ case, the higher surface temperature causes a 4.7 W m^{-2} increase in the outgoing longwave radiation at the top of the model ($F_{L,U}$) than in the circular case, resulting in a positive Earth Energy imbalance (ΔF) anomaly of 1.6 W m^{-2}. The positive 1.6 W m^{-2} ΔF anomaly indicates that the $e = 0.4$ case will become even warmer than the circular case ($\Delta T_S > 1.9$ K) as the model slowly approaches radiative equilibrium because it is cooling at a slower rate. As a result, the surface temperature anomaly of 1.9 K is a lower bound since the temperature difference will rise further, given more simulation time. The higher surface temperature in the $e = 0.4$ case is associated with a 0.5 % lower annual global mean planetary albedo. The planetary albedo is calculated from the ratio of the upwelling shortwave flux at the top of the model and the net total shortwave flux at the top of the model $\frac{F_{S,U}}{F_{S,U}+F_{S,D}}$). The diffuse surface albedo (A_S) and the cloud albedo (A_C) can both contribute to the planetary albedo (A_P) [3]. The cloud albedo is calculated based on the difference between the cloud-free and cloud-included cases. In a cloud-free case, we expect that the surface albedo and aerosol scattering only contribute to the planetary albedo. With the cloud included, the effects of the surface and the cloud are entangled. The planetary albedo can be roughly estimated by taking the arithmetic average of the cloud albedo and the surface albedo, scaled by the cloud coverage fraction and the fraction of the surface not covered by clouds, respectively. In the $e = 0.4$ case, the diffuse surface albedo is 0.5 % lower than the circular case, indicating that the surface is less reflective by 2.4 W m^{-2}, which is calculated by the difference of the reflected flux at the surface between the two cases.

Figure 3.1 shows the seasonal variations of the zonal mean total shortwave flux (excluding far-UV below 200 nm) at the top of the atmosphere (F_T, top panel), zonal mean surface temperature (T_S, middle panel) and zonal mean surface albedo (A_S, bottom panel). The latitudinal variation of the temporal mean and temporal variation of the global mean

---

[3]Other effects on planetary albedo such as the Rayleigh scattering are omitted here.

Table 3.1: Key variables that describe the energy balance of the circular case ($e = 0$), the highly eccentric case ($e = 0.4$), and their differences. $F_{S,D}$ and $F_{L,U}$ are the net downwelling shortwave and the net upwelling longwave at the model top, respectively; ΔF is the Earth Energy Imbalance calculated by $\Delta F = F_{S,D} - F_L$; $F_{S,U}$ is the upwelling shortwave flux at the model top; A_P is the planetary albedo and T_S is the surface temperature. For all variables, uncertainties are the standard deviation around their temporal mean, which reflects their 5-year inter-annual variability.

Variable	e=0	e=0.4	(e=0.4) - (e=0)
$F_{S,D}$ (W m^{-2})	237.2 ± 0.3	243.5 ± 0.3	6.3 ± 0.6
$F_{L,U}$ (W m^{-2})	239.7 ± 0.1	244.4 ± 0.2	4.7 ± 0.2
ΔF (W m^{-2})	-2.5 ± 0.3	-1.0 ± 0.3	1.6 ± 0.4
$F_{S,U}$ (W m^{-2})	103.0 ± 0.3	97.6 ± 0.3	-5.4 ± 0.4
A_P (%)	34.1 ± 0.1	33.6 ± 0.1	-0.5 ± 0.1
T_S (K)	287.7 ± 0.1	289.6 ± 0.1	1.9 ± 0.1

Table 3.2: Key variables that contribute to the surface albedo of the circular case (e=0), the highly eccentric case ($e = 0.4$), and their differences. The table includes the surface albedo (A_S), Sea-ice fraction, total land snow volume and the effective land snow coverage defined as the land surface fraction covered by at least 30 cm of snow layer. For all variables, uncertainties are the standard deviation around their temporal mean, which reflects their 5-year inter-annual variability.

Variable	e=0	e=0.4	(e=0.4) - (e=0)
Surface Albedo (A_S) (%)	59.30 ± 0.03	58.8 ± 0.1	-0.5 ± 0.1
Sea-ice Fraction (%)	5.6 ± 0.1	5.5 ± 0.1	-0.1 ± 0.1
Total Land Snow Volume (10^{12}m^3)	13.3 ± 0.4	1.31 ± 0.04	-11.9 ± 0.4
Effective Land Snow Coverage for Snow Depth > 30 cm (%)	24.1 ± 0.1	19.3 ± 0.5	-4.8 ± 0.7
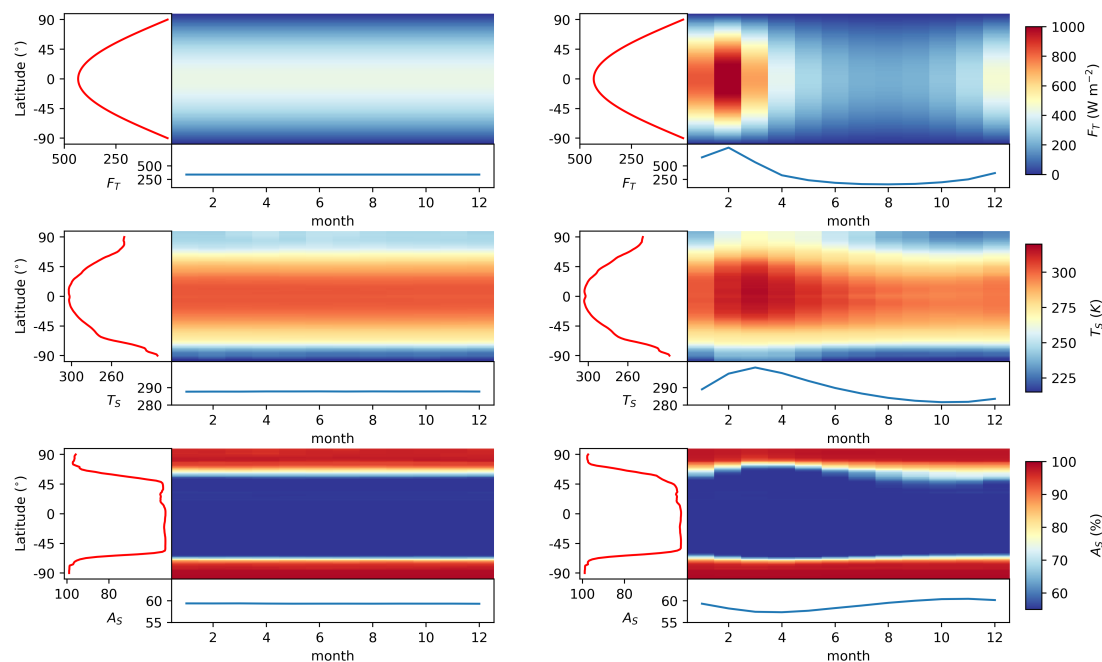
Figure 3.1: The seasonal variations of the zonal mean planetary insolation at the top of the atmosphere (F_T in units of W m^{-2}, top panel), zonal mean surface temperature (T_S in units of K, middle panel) and zonal mean surface albedo (A_S in %, bottom panel) for the circular case (left column) and the $e = 0.4$ case (right column). We take monthly mean outputs for the data analysis, and the peak at the perihelion highlights that the incoming radiation is the highest at this point. Two supplemental subplots are given to the left and the bottom axes of each 2D color map. The left subplots (red lines) show the latitudinal variation for the temporal mean of each variable, and the bottom ones (blue lines) show the temporal variation of the global mean for each variable.

Table 3.3: Key variables that describe the cloud radiative forcings of the circular case (e=0), the highly eccentric case ($e = 0.4$), and their differences. In the table, the cloud radiative forcing (C_{RF}) is the sum of the shortwave cloud forcing (C_{SWF}) and the longwave cloud forcing (C_{LWF}); The low-level cloud is defined to lie between 1000 and 680 hPa, and its area-weighted fraction is denoted as C_L in the table; the pressure of 440 hPa is the lower altitude bound for the high-level cloud, and its fraction is denoted as C_H; C_T represents the total cloud fraction; C_W stands for the total cloud liquid water path, which is the cloud's vertically integrated liquid water content; A_C, as shown in the last column of the table, is the cloud albedo calculated from the difference of surface shortwave flux in cloudy and cloud-free conditions. For all variables, uncertainties are the standard deviation around their temporal mean, which reflects their 5-year inter-annual variability.

Variable	e=0	e=0.4	(e=0.4) - (e=0)
C_{RF} (W m^{-2})	-26.0 ± 0.3	-21.0 ± 0.2	5.0 ± 0.4
C_{SWF} (W m^{-2})	-49.0 ± 0.4	-43.0 ± 0.3	6.0 ± 0.5
C_{LWF} (W m^{-2})	23.0 ± 0.1	22.0 ± 0.1	-1.0 ± 0.1
C_L (%)	44.0 ± 0.3	44.1 ± 0.3	0.1 ± 0.4
C_H (%)	43.5 ± 0.1	45.7 ± 0.2	2.2 ± 0.2
C_T (%)	70.7 ± 0.1	72.7 ± 0.3	2.0 ± 0.3
C_W (g m^{-2})	64.0 ± 0.8	67.9 ± 0.4	3.9 ± 0.9
A_C (%)	15.7 ± 0.1	17.6 ± 0.1	1.9 ± 0.2

variables are added to the left (red) and the bottom (blue) of the 2D maps, respectively. For F_T, its latitudinal variations for both cases are the same, which is consistent with our simulation setup in which two cases have the same annual flux and zero obliquity. However, unlike the circular case, the insolation in the $e = 0.4$ case shows a considerable seasonal variation. The seasonal variation of the insolation is nonlinear, which is up to 2.5 times more intense than the annual mean during the hot period of the eccentric orbit (February, March and April, hereafter referred to as the 'hot period') and is only about half of the annual mean during the rest of the orbital period. During the hot period, the surface temperature in the $e = 0.4$ case increases from an average of 289.6 K to a maximum of 340 K near the equator in March, approximately one month after perihelion (the planet's closest approach to the star) due to the Earth-like atmospheric radiative timescale. From Figure 3.1, the northern hemisphere (NH) experiences a much larger surface temperature swing throughout the orbit than the southern hemisphere (SH). This is likely because the NH has more land and less ocean than the SH, hence a lower heat capacity and shorter radiative timescale to the seasonally varying insolation.

The bottom panel of Figure 3.1 shows the corresponding changes in surface albedo due to the seasonal variation in surface temperature. The surface albedo in the $e = 0.4$ case decreases significantly in the NH during the hot period, whilst the SH has a much more stable surface albedo throughout the orbit.

Both changes in land snow and sea ice can contribute to the difference in the surface albedo between the two cases. The total land snow volume in the $e = 0.4$ case is lower than the circular case by a factor of 10 (see Table 3.2). The deeper land snow in the circular case is due to the zero-obliquity configuration, which mutes the seasons for the circular case and allows the snow layer to accumulate over a significant fraction of the high-latitude NH land area due to year-round sub-zero temperatures (see Figure 3.2). Based on the nonlinear relationship between snow depth and snow albedo, the effective land snow coverage is defined as the ratio of the snow-covered land area to the total land area for snow depths greater than 30 cm (Chen et al., 2014). Using the definition above, we find a 4.8% decrease in the effective land snow coverage in the NH for the eccentric case, contributing to a decrease in the surface albedo. Figure 3.2 shows the distributions of annual mean land snow depth and sea ice fraction. In both cases, the sea ice is restricted to the polar regions due to the zero-obliquity configuration, and only a small amount of radiation reaches the polar regions. We expect that the 0.1% difference in sea ice fraction between the two cases (see Table 3.2) is only significant in shaping the climate regionally rather than globally. The annual global mean sea-ice fraction is less in the $e = 0.4$ case, which corresponds to a decrease in sea ice in the Arctic and a slight increase in Antarctica, which is a result of the hemispheric surface temperature differences that we see in Figure 3.1. That the sea-ice extent in the SH increases in the $e = 0.4$ case is likely because of positive feedback triggered by the higher eccentricity. When the planet is far from the host star, sea ice forms in the Antarctic regions due to the sub-zero temperatures. This increases the surface albedo, reducing the incoming heat and the surface temperature, thereby preventing the sea ice from melting when the planet moves closer to the star.

Besides the decrease in surface albedo found in the $e = 0.4$ case, we find that the annual global mean cloud albedo is about 2 % lower in the $e = 0.4$ case compared with the circular case, despite the total cloud fraction (i.e., area-weighted total cloud coverage) increasing by roughly 2 % (see Table 3.3). This suggests that more cloud coverage does not necessarily lead to higher cloud albedo due to the interplay between insolation and cloud properties in different phases along the highly eccentric orbit. Figure 3.3 shows the seasonal variation of zonal mean cloud albedo (A_C), low cloud fraction (C_L) and total vertically-integrated cloud liquid water path (C_W). The latitudinal variation of the temporal mean variables and time variation of the global mean variables are added to the left and the bottom of the 2D maps, respectively. The top panel shows that cloud albedo decreases in the equatorial to mid-latitude regions in the $e = 0.4$ case during its hot period. This is associated with the decreased NH low cloud fraction during the hot period due to the higher NH surface temperature and lower tropospheric relative humidity. However, during the hot period and two months after, the cloud albedo around $60°$ south of the equator in the $e = 0.4$ case increases even though the cloud fraction is roughly the same as in the same region in the circular case. This is because a larger amount of water vapor can be evaporated into the atmosphere in the ocean-dominated latitudes during the hot period. Since cloud albedo increases with cloud liquid water path (Webster, 1994), the low cloud around $60°$ south of the equator becomes more reflective in the $e = 0.4$ case than in the circular counterpart, explaining the localized increase in A_C shown in Figure 3.3. Furthermore, the decrease of cloud albedo due to decreased cloud fraction in the lower latitudes outweighs the small increase in the higher latitudes in the $e = 0.4$ case, resulting in a net decrease of 2 % in the annual global mean cloud albedo in the $e = 0.4$ case, as compared with the circular case. Note that cloud albedo at lower latitudes has a greater impact on the global average because the uniform lat-lon grid in the model has larger grid cells toward the lower latitudes. With zero obliquity, lower latitude regions consistently receive more radiation than higher latitude regions, making clouds at lower latitudes more effective at reflecting radiation.

Clouds can not only cool the planet by reflecting stellar radiation into space, but also warm the surface by absorbing the outgoing longwave radiation from the surface. Figure 3.4 shows the seasonal variations of the longwave cloud forcing (C_{LWF}), the high cloud fraction (C_H) and the cloud vertical distribution (C) for both low-level cloud (between 1000 and 680 hPa) and high-level cloud (above the pressure level of 440 hPa). The first two color maps have supplemental subplots along the axes, similar to Figures 3.1 and 3.3. C_{LWF} represents the greenhouse effect of clouds due to absorption and re-emission of longwave radiation. In the $e = 0.4$ case, the seasonal variation of the longwave cloud forcing during the hot period is associated with the seasonal variation in the high cloud fraction in the equatorial to mid-latitude regions as the thin, cirrus-type high cloud has a strong warming effect (Zelinka et al., 2010). During the hot period, the tropical regions in the $e = 0.4$ case have a strong upward convective mass flux and a higher tropopause altitude associated with the higher surface temperature. This helps the vertical transport of water vapor to higher altitudes. However, due to the high tropospheric temperature in the equatorial region during the hot period, water vapor condensation and cloud formation can be suppressed, and a high cloud gap appears in the tropics in the $e = 0.4$ case. As the planet moves further away from the host star, the water vapor in the upper troposphere condenses into a wider band of high clouds due to the cooler tropospheric temperature. While the seasonal trend of tropopause temperature in the highly eccentric case closely follows the surface temperature with no lag (or a lag of less than one month throughout the year), the tropopause locations, determined by the vertical lapse rate, do not strictly correlate with surface temperature trends. This discrepancy arises from the complex interplay of various atmospheric processes, such as radiative heating and cooling rates and the Brewer-Dobson circulation in the stratosphere (Austin et al., 2008). In the highly eccentric case, the tropopause pressure varies from 35.9 hPa in July to 73.7 hPa in January/December, with the latter value matching that found at all times in the circular case. This variation in tropopause levels can affect the location of high cloud formation, causing high clouds in the $e = 0.4$ case to form higher in the upper troposphere compared

to the circular case, as illustrated in the bottom panel of Figure 3.4. The high cloud gap during the hot period reduces the cloud warming effect, and the wider high cloud band in the colder phases of the $e = 0.4$ orbit warms the planet. The net effect of the two opposing factors is a slight decrease (1W m^{-2}) in the annual global mean C_{LWF}, which indicates that the overall high cloud warming effect becomes slightly weaker in the $e = 0.4$ case than in the circular case.

The annual global mean cloud radiative forcing (C_{RF}) for both circular and highly eccentric cases are negative (see Table 3.3), meaning clouds have a net cooling effect on the planet, which is similar to our current Earth. The net cooling effect of clouds is because the shortwave cloud forcing (C_{SWF}) outweighs the longwave cloud forcing (C_{LWF}). Shortwave cloud forcing describes the net radiative effect of absorbing and reflecting shortwave radiation by clouds. It is important to note that shortwave cloud forcing differs from the cloud albedo effect as the latter only describes the reflected part of the C_{SWF}. Table 3.3 shows that C_{SWF} and C_{LWF} are weaker by 6 W m^{-2} and 1 W m^{-2} in the $e = 0.4$ case than in the circular case, respectively. The sum of the weaker C_{SWF} and C_{LWF} yields a 5 W m^{-2} weaker C_{RF} (cloud radiative forcing) in the $e = 0.4$ case. Overall, the change in the cloud radiative effects plays a more important role than the change in the radiative effects of surface albedo in shaping the energy budget and the climate of the $e = 0.4$ case.

3.3.2 Habitability Analysis

Using the land habitability criteria defined in Section 2.2 regarding the surface temperature and accumulative precipitation, we analyse and compare the number of months in which each of the two habitability conditions has been met. Figure 3.5 shows the precipitation habitability map (first row), the temperature habitability map (second row), and the combined habitability map (third row) in sequence. The precipitation habitability map adopts a binary criterion in which the land regions become uninhabitable if the annual accumulative precipitation is less than 30 cm/yr (hereafter referred to as
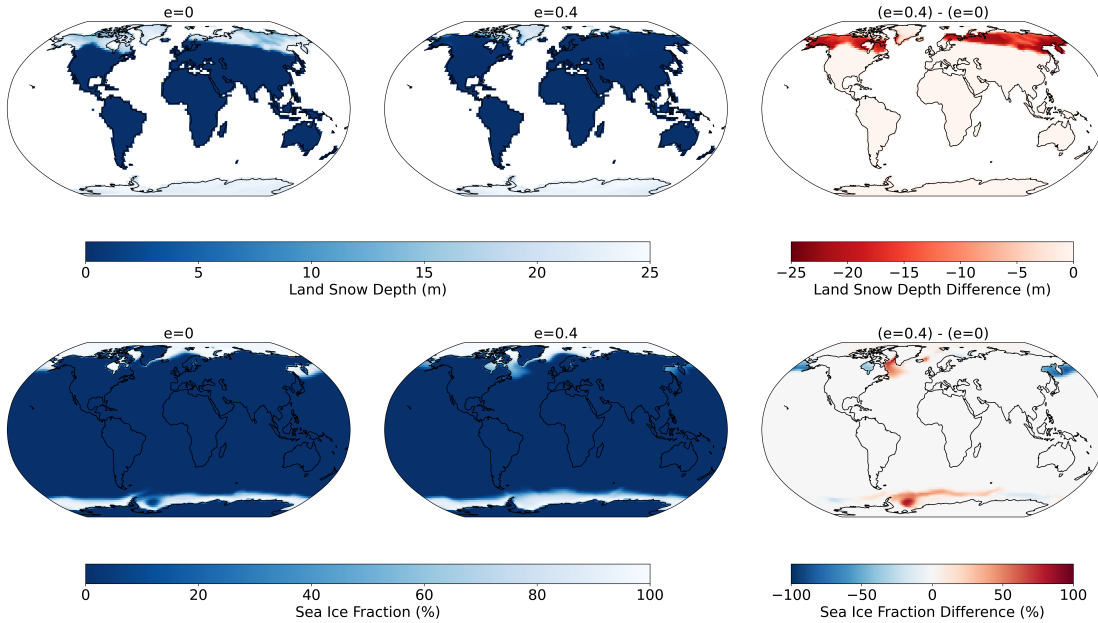
Figure 3.2: Top panel: annual mean land snow depth (m) for the circular case (left), the $e = 0.4$ case (middle) and their difference (right); Bottom panel: annual mean sea ice fraction (%) for the circular case (left), the $e = 0.4$ case (middle) and their difference (right).

the dry zone). Compared with the circular case, the dry zone decreases significantly in the $e = 0.4$ case, resulting in more habitable land regions according to the precipitation criterion. Figure 3.6 shows the latitudinal (upper panel) and seasonal variations (lower panel) of the total precipitation over land (P_T), convective precipitation over land (P_C), and large-scale precipitation over land (P_L). While convective precipitation is associated with localized, intense updrafts mainly within the convective cells in the lower latitudes, large-scale precipitation is linked to larger atmospheric circulation patterns that occur over larger geographic areas and can be less intense than convective precipitation. The lower panel in Figure 3.6 shows that the annual mean total precipitation is lower in the $e = 0.4$ case because of the lower annual mean convective precipitation. The annual mean large-scale precipitation is higher in the $e = 0.4$ due to a large spike in April, one month after the hottest month. This is due to the relative humidity, controlled by the temperature and water vapor mixing ratio in the troposphere, reaching its maximum in April. The upper panel in Figure 3.6 shows that the lower total precipitation in the $e = 0.4$ case results from the lower convective precipitation in the lower latitudes, and
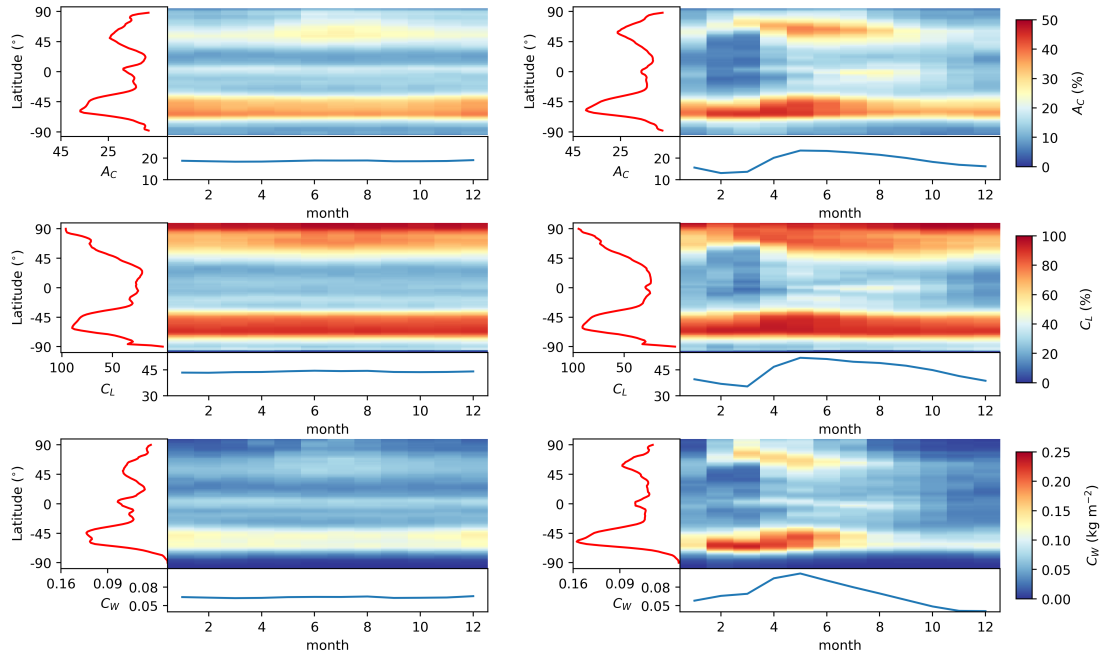
Figure 3.3: The seasonal variations of the zonal mean cloud albedo (A_C in %, top panel), zonal mean low-level cloud fraction (C_L in %, middle panel) and zonal mean vertically-integrated cloud liquid water path (C_W in units of kg m^{-2}, bottom panel) for the circular case (left column) and the $e = 0.4$ case (right column). Two supplemental subplots are given to the left and the bottom axes of each 2D color map. The left subplots (red lines) show the latitudinal variation for the temporal mean of each variable, and the bottom ones (blue lines) show the seasonal variation of the global mean for each variable.

94
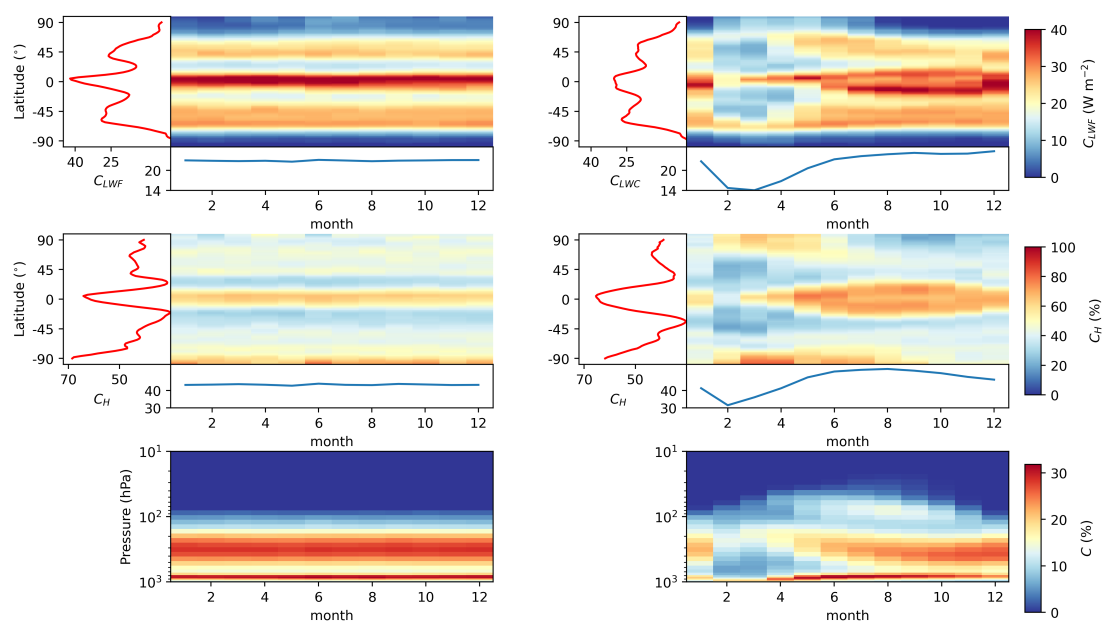
Figure 3.4: The seasonal variations of the zonal mean longwave cloud forcing (C_{LWF} in units of W m^{-2}, top panel), zonal mean high-level cloud fraction (C_H in %, middle panel) and global mean total cloud vertical distribution (C in %, bottom panel) for the $e = 0$ case (left column) and the $e = 0.4$ case (right column). Two supplemental subplots are given to the left and the bottom axes of the 2D color maps in the upper and middle panels. The left subplots (red lines) show the latitudinal variation for the temporal mean of each variable, and the bottom ones (blue lines) show the seasonal variation of the global mean for each variable.

it also shows a lower but more spread-out large-scale precipitation in the $e = 0.4$ case, which explains the reduced dry zone in the $e = 0.4$ case. For the highly eccentric case, it is worth mentioning that whilst the maximum tropospheric temperature in the $e = 0.4$ case has exceeded the lower limit (~ 320 K) required to trigger the hot-house climate regime [4] (Seeley et al., 2021; Spaulding-Astudillo et al., 2023; Song et al., 2023), the annual mean temperature at any latitude is still far below the threshold. Thus, the hot-house climate regime is not found in our simulation, except for the brief period in which the maximum temperature exceeds 320 K.

The temperature habitability map in the second row of Figure 3.5 assumes that land regions are only habitable if the monthly mean surface temperature is 0 to 50°C (see Section 2.2). Unlike the circular case, the equatorial regions in the $e = 0.4$ case become temporarily less habitable (< 12 months); however, the higher latitudes that are uninhabitable in the circular case become seasonally habitable (> 0 months) in the $e = 0.4$ case. This is due to the large surface temperature swings in the NH in the $e = 0.4$ case (see Figure 3.1). Compared with the SH, the NH is more sensitive to the seasonal variation of the insolation due to the lower surface heat capacity of the land-dominated surface. In addition, fewer clouds can form in the NH than in the SH during the hot period in the $e = 0.4$ case. The cloud fraction gap causes less insolation to be reflected and further increases the surface temperature in the NH. Furthermore, the deep land snow melts at high latitudes in the NH in the $e = 0.4$ case, and the land surface albedo decreases significantly during the hot period in the $e = 0.4$ case compared with the circular case. Consequently, the seasonally habitable land area expands to the Arctic, excluding the usually ice-sheet-covered Greenland.

A climate habitability metric that combines the previous temperature and precipitation habitability maps is shown in the last row of Figure 3.5. It shows that $\sim 75\%$ of land regions in the $e = 0.4$ case have seasonal habitability, which exceeds the $\sim 54\%$ of land

---

[4]The hot-house climate regime has a unique feature in precipitation: with a hot surface temperature, the moist static energy builds up to break the convection inhibition layer, and enormous precipitation would occur. This process is periodic and has a short timescale of a few days.

regions in the circular case that has year-round habitability. Specifically, for 10 out of 12 months, the $e = 0.4$ case has more land area (up to 25 % more) with the defined habitable conditions. The least habitable month in the $e = 0.4$ case is March, when the surface temperature reaches the highest, and the land precipitation is at a minimum. The changes in the precipitation distribution and the surface temperature are also associated with the change in the global circulation pattern in the $e = 0.4$ case. Figure 3.7 (top row) shows each case's annual mean mass stream function, representing the mass flow in the atmosphere at different latitudes. The mass stream function $\Phi_p(\phi, p)$ is defined as:

$$\Phi_p(\phi, p) = \frac{2\pi \cos \phi}{g} \int_p^{p_s} V \, dp \tag{3.1}$$

where $\Phi_p(\phi, p)$ is the mass stream function in terms of latitude ϕ, gravity g and pressure p, p_s is the surface pressure level and V is the meridional wind.

Both cases exhibit three-cell circulation patterns (sometimes referred to as the Hadley, Ferrel and Polar cells), similar to our Earth. On Earth, the Hadley cell is a low-latitude overturning circulation driven by convection, characterized by the ascent of warm, moist air near the equator, poleward movement in the upper atmosphere, and descent as drier air in the subtropical regions. The color maps represent the clockwise (northward) overturning circulations (red) and the counter-clockwise (southward) overturning circulations (blue). However, an abrupt change in the circulation pattern occurs during the hot period of the eccentric case (bottom row of Figure 3.7). Specifically, the polar cell vanishes due to the expansion of the Hadley cell towards 50° latitude. This results in a two-cell circulation pattern featuring the Hadley and Ferrel-like cells during the hot period. A weak polar cell remains visible in Antarctica in both cases due to the continent's unique geographical location, elevation, and temperature. Even during the warmest period of the orbit, katabatic winds—strong, persistent winds flowing from the dense, cold interior to the coast—continue to dominate the region's climate. The second plot of the bot-

tom panel in Figure 3.7 shows the difference in the annual mean mass stream function between the two cases, with green denoting a decrease in clockwise circulation and purple denoting an increase in counter-clockwise circulation. The expansion of the Hadley cell in the $e = 0.4$ case contributes to a weakened annual mean Hadley cell compared with the circular case. This weakening is particularly notable for the updrafts near the equator, implying a weaker convection strength and decreased convective precipitation on the annual average. The changing circulation pattern can also affect the distribution of clouds. For example, the cloud gap in the lower latitudes during the hot period of the $e = 0.4$ case is associated with the expanded Hadley cell (see Figure 3.3). The Hadley cell expansion can cause the re-distribution of the latent heat and precipitation by delivering more moist static energy from the equatorial oceanic regions to higher latitude land regions, enhancing the land temperature and precipitation habitability in the mid-to-high latitudes. Along with the expansion of the Hadley cell towards 50° latitudes in the $e = 0.4$ case, two stronger jet streams form at the edges of the Hadley cell, compared to the jet stream on Earth that forms at about 25° latitudes in the circular case. The stronger jet streams can drive the zonal water transport from the ocean to land around the 50° latitude, reducing the dry zone and further augmenting the precipitation habitability.

Our habitability metric indicates that the highly eccentric case exhibits greater land habitability than the circular case. This enhanced habitability is attributed to a combination of factors, including variations in albedo, cloud radiative effects, heat capacity contrast between hemispheres, and global circulation patterns. Together, these changes may create a more favorable environment for life to thrive on land in the highly eccentric case.
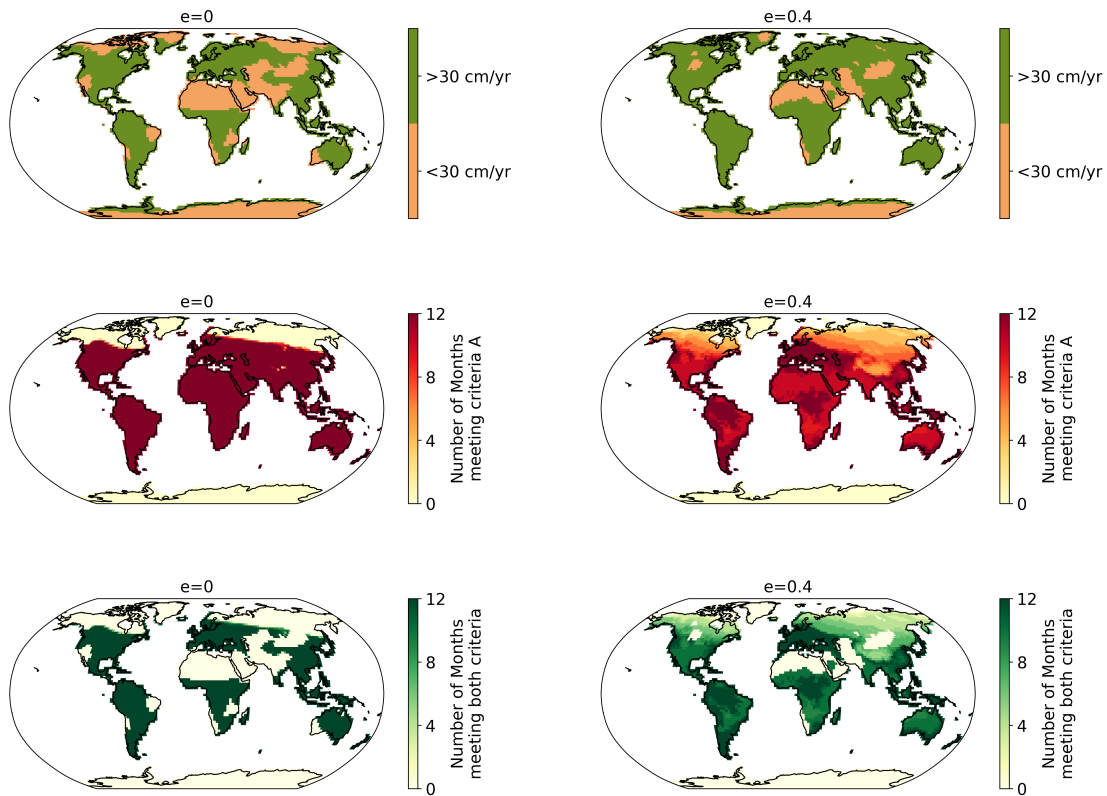
Figure 3.5: Top panel: Precipitation habitability, where brown marks the dry zone (desert-like regions), and green represents the land regions that meet the precipitation criterion. Middle panel: Temperature habitability, evaluated by the number of months in a year in which the land regions meet the habitable temperature range, with dark red indicating a full year and light yellow representing none. Bottom panel: Climate habitability, a combination of the precipitation and temperature maps. Dark green marks the land regions that meet the habitability criteria all year round.
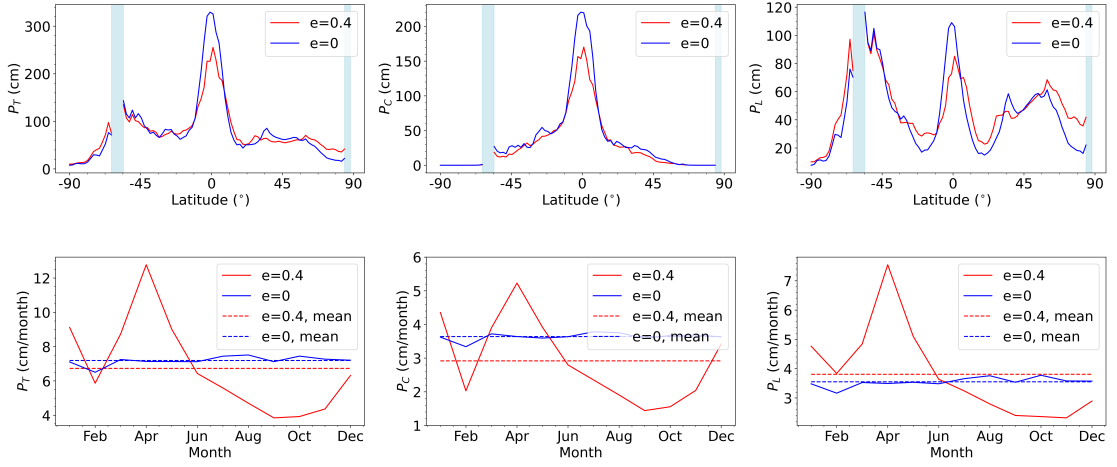
Figure 3.6: Top panel: Latitudinal variation of annual mean total precipitation (P_T, in units of cm), convective precipitation (P_C, in units of cm) and large scale precipitation (P_L, in units of cm) over land. Bottom panel: seasonal variation of global mean total precipitation (P_T, in units of cm/month), convective precipitation (P_C, in units of cm/month) and large-scale precipitation (P_L, in units of cm/month) over land. The red lines indicate the $e = 0.4$ case, whereas the blue lines represent the circular case. In the top panel, the light blue bars around $60°$ south and near the north pole highlight the ocean-exclusive latitudes and are excluded from the land habitability analysis. In the bottom panel, the dotted lines indicate the annual mean precipitation for each case.
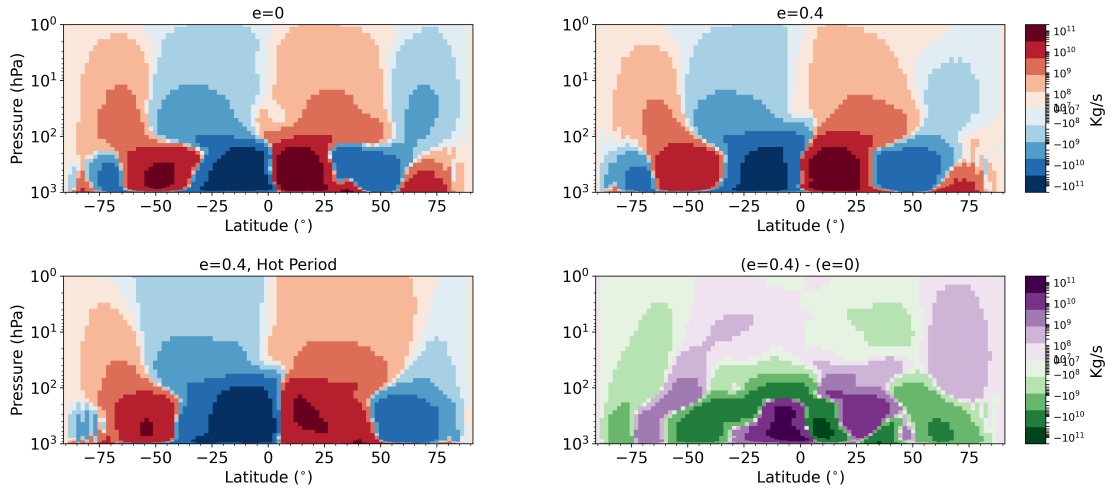
Figure 3.7: Top row: the annual mean mass stream function $\Phi_p(\phi, p)$ (vertically-integrated zonal mean meridional wind) for each case. Bottom row: the mass stream function for $e = 0.4$ during the hot period of the orbit, specifically, the average of February, March and April (left); and the difference in the annual mean between the two cases (right).

100

3.4   Discussion

In this study, we employed a fully-coupled 3D Earth system model to explore the impact of orbital eccentricity on climate and land habitability. We compare a highly eccentric Earth-like planet with its circular counterpart, both subjected to the same annual mean insolation. The orbital configuration in the model is set up such that the semi-major axis remains fixed whilst the semi-minor axis is reduced, leading to sinusoidal variations in insolation over time and an increased amplitude of the annual mean insolation. Notably, our approach disentangles the effects of seasonality from the annual mean insolation on the climate, which shows that an Earth-like planet with an eccentricity of 0.4 experiences a warmer climate compared with the circular case while remaining within a stable and temperate climate regime. This result generally agrees with the previous research in which both effects of seasonality and increased annual mean insolation are examined (e.g. Williams et al., 2002; Dressing et al., 2010; Linsenmeier et al., 2015; Palubski et al., 2020), and emphasizes the importance of the effects of seasonality on the climate and habitability. Our findings for the non-synchronously rotating Earth-like planet are consistent with Bolmont et al. (2016)'s predictions for tidally-locked planets, where orbital eccentricity causes significant climate deviations from the mean flux approximation proposed by Williams et al. (2002). This is due to the seasonally varying stellar flux received by the planet and the internal feedback loops in the climate of the planet. Unlike other studies that sweep a larger range in eccentricity, we specifically investigated and compared only two eccentricity cases. Specifically, the $e = 0.4$ case is an extreme case representing the upper limit of the eccentricity range for terrestrial exoplanets due to the current occurrence of highly eccentric rocky planets from observations. Therefore, we expect the simulated climate outcomes and habitable conditions on land to be upper limits.

For the highly eccentric case, the weaker cloud radiative effects significantly contribute to the annual global mean warming. Counter-intuitively, we find a lower cloud albedo

and a higher total cloud fraction in the $e = 0.4$ case. To explain this phenomenon, the temporal and latitudinal variations in the interactions between insolation and cloud optical properties must be considered. The hemispherical asymmetry in ocean and land distribution can also indirectly influence the cloud radiative effects by impacting surface temperature. Future work could focus on a sensitivity test of orbital eccentricity with different GCMs in which different cloud parameterizations are adopted and with high spatial resolution global cloud-resolving models (GCRM) or cloud-permitting models (CPM) which can offer more accuracy in representing cloud behaviours (Sergeev et al., 2020; Yang et al., 2023). Also, variations in cloud fraction during the hot/cold periods of the eccentric orbit can lead to potential decreases/increases in the baseline of transit spectra (e.g. Boutle et al., 2017; May et al., 2021) and hence, the transit depth of the molecules of interest such as H_2O, O_3 and CO_2 (e.g. Liu et al., 2023). This multi-dimensional analysis provides a more realistic representation of climate and is achievable only with 3D GCMs.

Compared with the circular case, the $e = 0.4$ case becomes 1.9 K warmer due to the lower annual global mean surface albedo and the cloud albedo. The greenhouse effects from higher water vapor abundance in the $e = 0.4$ case may also contribute to the warmer surface temperature. We estimate the total warming effect of all greenhouse gases between the two cases to approximate the impact of water vapor, as it shows the largest difference between the $e = 0.4$ and $e = 0$ cases, with a threefold increase in the $e = 0.4$ case. In contrast, other greenhouse gases, such as CH_4 and CO2, exhibit less than a 10 % difference in the troposphere and lower stratosphere between the two cases. The longwave radiation emitted by the surface should equal the longwave radiation at the top of the atmosphere if cloud and greenhouse gases are absent and the aerosol scattering is neglected. The difference in the longwave radiation emitted by the surface between the two cases is 10.3 W m^{-2}, and the difference in the net longwave flux at the top of the atmosphere between the two cases is 4.7 W m^{-2} ($\Delta F_{LW} = F_{LW,e=0.4} - F_{LW,e=0}$). So, the longwave radiation gap required to be filled by cloud and greenhouse gases is

5.6 W m^{-2}. Since the difference of the longwave cloud forcing is -1 W m^{-2} ($\Delta C_{LWF} = C_{LWF,e=0.4} - C_{LWF,e=0}$), shown in Table 3.3), which indicates longwave cooling from the cloud, this yields a difference in the total greenhouse gas warming between the two cases to be < 6.6 W m^{-2}. Although this increases the annual mean surface temperature in the $e = 0.4$ case, it does not necessarily mean that stronger greenhouse warming promotes greater land habitability. We must also consider the water vapor lifetime—the duration water vapor remains in the atmosphere before precipitating out, calculated using the column density of water vapor divided by the precipitation rate—and its location before precipitation. While most water vapor is concentrated in the tropics for both cases, the water vapor lifetime in the $e = 0.4$ case reaches a maximum of 37 days in the hottest and driest month (March), compared to 9 days in the circular case. Since the stronger water vapor greenhouse warming effect mainly occurs in the tropics during the hottest month, it likely buffers radiative warming near perihelion, potentially reducing the habitable land area around the equator during the hot period of the eccentric orbit.

The seasonally varying surface temperature and precipitation in the highly eccentric case create a more complex picture of land habitability than in the circular case. Using our habitability metric defined earlier in Section 2.2, we find more land areas are seasonally habitable in the $e = 0.4$ case (see Figure 3.5). On the other hand, our previous study (Liu et al., 2023) shows a 3% reduction in the annual mean ozone column density in the $e = 0.4$ case with the maximum decrease of 13% in March compared with the circular case. The seasonally weaker ozone layer may directly impact temporal habitability by increasing the amount of harmful UV radiation reaching the surface (e.g. Marshall et al., 2020; Cooke et al., 2022). The transient land habitability in the highly eccentric case may pose a stressor on living organisms (e.g. Dressing et al., 2010; Linsenmeier et al., 2015). Figure 3.8 shows the total habitable land area fraction (A_{Hab}) for the $e = 0.4$ case (bar charts) and the circular case (line plots) versus the number of months that meets the criteria (N), as a more straightforward view to Figure 3.5. Criterion I (dark green) and criterion II (coral) use our previously defined surface temperature
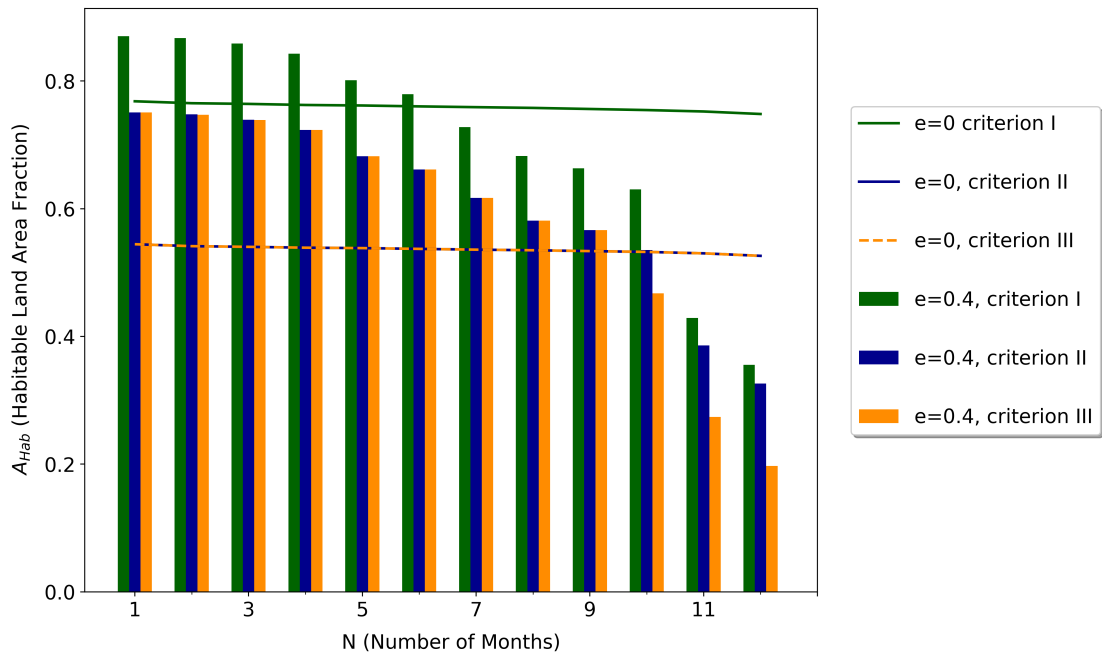
Figure 3.8: The habitable land area fraction for a given number of months that meet a criterion for the $e = 0.4$ case (bar charts) and $e = 0$ case (line plots) using three different criteria for habitability. Criterion I (dark green) uses only the surface temperature metric; criterion II (dark blue) uses the metric with both the surface temperature and precipitation constraints; criterion III (dark orange) uses the same precipitation constraint as criterion II but with a tighter wet-bulb temperature constraint. For the $e = 0$ case, criteria I and III yield the same values as denoted by the blue and orange dotted lines.

habitability and the combined habitability from the surface temperature and cumulative precipitation metrics, respectively. Criterion III adds the wet bulb temperature limit for humans as an additional constraint to Criterion II. The wet bulb temperature is the lowest temperature to which air can be cooled by the evaporation of water into the air at constant pressure. A wet-bulb temperature of 308 K (35° C) is commonly accepted as the threshold for human survivability. Beyond this temperature, the evaporative cooling mechanism through sweating becomes inefficient (Lu et al., 2023).

In all criteria, A_{Hab} decreases with increasing N (the number of months that meet the criteria) for the highly eccentric case, whereas A_{Hab} only decreases slightly with increasing N for the circular case. Note that the slight variations found in the circular case are associated with our use of monthly mean output, which can be affected by variations in the diurnal mean, which itself varies due to daily changes in temperature and climate.

104

Criterion II and III have the same A_{Hab} for N smaller than 10. However, the A_{Hab} decreases more in the tighter criterion III than criterion II for a larger N. This is because the wet bulb temperature, calculated from surface temperature and relative humidity, significantly increases during the hot period of the highly eccentric orbit. Also, criteria II and III have a much smaller A_{Hab} than criterion I for both cases. This suggests that the annual accumulative precipitation metric is crucial in shaping land habitability and that using the surface temperature metric alone would potentially overestimate land habitability for an Earth-like planet in a highly eccentric orbit. The $e = 0.4$ case is more habitable than the circular case only if N < 6, < 9 and < 10 for criteria I, II and III, respectively. Thus, whether the highly eccentric Earth-like planet is more habitable than its circular counterpart should be answered conditionally, depending on both the habitability metric adopted and the fraction of the orbital period when the conditions provided by the habitability metric hold. When averaged across all N, criteria II and III can yield 7% and 5% higher A_{Hab} in the $e = 0.4$ case than in the circular case, respectively; however, with the less constrained criterion I, the $e = 0.4$ case exhibits a 5% lower A_{Hab} than the $e = 0$ case.

Due to the numerous parameters tuned in WACCM6 to align with Earth's historical data, we exclude simulated land biomass and disable marine biogeochemistry. However, studies on ocean habitability have been conducted in recent years. For instance, Jernigan et al. (2023) employed a 3D marine biogeochemical model coupled with an atmospheric general circulation model (cGENIE-PlaSim) to study the response of an Earth-like biosphere to different eccentricity and obliquity in an aqua-planet configuration. Their findings indicated increased marine biological activity with increasing orbital eccentricity, attributed to a higher nutrient uptake rate in the ocean mixed layer. This supports the notion that Earth-like marine life can adapt well to the conditions of a highly eccentric aqua-planet, suggesting that such worlds might be potentially super-habitable[5] (Heller et al., 2014; Schulze-Makuch et al., 2020). For numerical efficiency, we only run

---

[5]Super-habitability or super-habitable conditions refer to the theoretical conditions that could support life even more effectively or sustainably than Earth.

the simulations to quasi-steady states. Running the deep ocean circulation to a steady state would require over 10^3 simulation years. However, the simulations suggest that the annual global mean surface temperature in the $e = 0.4$ case would become even higher than in the circular case. This can be inferred from the energy budget difference ($\Delta F = 1.6$ W m^{-2}) at the top of the atmosphere (see Table 3.1). The slightly higher surface temperature at the final steady state could buffer the hydrological cycle, leading to more atmospheric water vapor and stronger meridional heat transport from the equator to higher latitudes. Consequently, this may further increase land habitability at higher latitudes but decrease land habitability near the equatorial regions in highly eccentric cases. Additionally, we note that WACCM6 does not consider changes in tidal forcing due to increased orbital eccentricity. The tidal force, proportional to $1/r^3$ (with r being the distance from the planet to the host star), increases eight-fold when halving the Earth-Sun distance at perihelion. In the $e = 0.4$ configuration, the host star becomes a more dominant source of tidal effects than the moon, leading to an anticipated annual cycle of solar tides peaking around perihelion in the $e = 0.4$ orbit. The effects of eccentricity-induced stellar tides on climate and habitability are beyond the scope of this study but have been investigated for synchronously rotating planets around low mass stars (Colose et al., 2021). Colose et al. (2021) studied the climate states given different host star types and resonant states with and without tidal heating with increasing stellar radiation, and they found that tidal heating may increase the climate instability at the inner edge of the habitable zone due to the tidal warming effects. Potential future work aims to enhance the flexibility of complex Earth-system models like WACCM6, incorporating customized topography to explore potential climate, a less Earth-tuned biosphere model for changes in land and ocean bio-activities, and a refined representation of tidal forcing in highly eccentric orbits.

3.5 Conclusions

The detection of highly eccentric terrestrial exoplanets ($e > 0.1$) is low due to the limitation of the current observation techniques, which are biased toward close-in and thus, tidally-locked exoplanets in circular orbits. However, with the upcoming ground and space telescope missions such as PLATO, ELT and HWO, more highly eccentric Earth-like rocky exoplanets may be revealed and characterized. Understanding the potential climate outcomes and habitability of highly eccentric rocky exoplanets remains a challenging task. Recent 1D and 3D simulations suggest that increased orbital eccentricity can increase the surface temperature and potentially expand the habitable zone. In this work, we employed a 3D Earth-system model, WACCM6, to investigate and compare a highly eccentric Earth-like planet around a Sun-like star with its circular equivalent with zero obliquity and the same annual mean insolation. Overall, we find a > 1.9 K warmer surface temperature for the Earth-like planet in the $e = 0.4$ orbit than its circular orbit counterpart. The higher surface temperature results from a lower surface albedo and a weakened cloud radiative effect in the $e = 0.4$ case. Differences were found in many planetary attributes associated with the hydrological cycle (i.e., sea ice, land snow, cloud), and these were combined to explore a more nuanced view of land habitability than global mean surface temperature alone. Specifically, we adopt a habitability metric which uses both surface temperature and precipitation over land. A comparison of land habitability reveals distinct patterns between the two cases. In the $e = 0.4$ case, land surface temperature habitability increases at high latitudes but decreases in equatorial regions due to extreme temperatures following the perihelion and the aphelion in the orbit. Enhanced precipitation habitability in the $e = 0.4$ case results from a more evenly distributed large-scale accumulative precipitation over land. The circulation pattern undergoes a notable shift from an Earth-like three-cell to a two-cell configuration during the orbit's hot phase, marked by the Hadley cell expansion toward $50°$ in both hemispheres. The annual mean Hadley cell weakens in the $e = 0.4$ case, decreasing the total precipitation

in the tropics while increasing the accumulative large-scale precipitation in mid to high latitudes. Using the combined habitability metric reveals that the land habitability in the $e = 0.4$ case surpasses the circular case for over 80% of the orbital period, with an increase of $> 7\%$ averaged over all number of months that meet the habitability criteria. It is important to note that the habitability of land depends on the chosen metric and the duration of time during which the conditions are met for a specific metric. We conclude that, under the same annual mean stellar flux, an Earth-analogue planet with zero-obliquity in a highly eccentric orbit ($e = 0.4$) around a Sun-like star may have enhanced land habitability compared to its circular counterpart.

Chapter 4

Climate and Habitability of Tidally-locked Planets: A Case Study of Proxima Centauri b

4.1 Motivation for this study

Building on the investigation of orbital eccentricity effects on Earth-twin exoplanets in previous chapters, this chapter examines the climate and potential habitability of Proxima Centauri b (PC-b) assuming it is under a tidally-locked orbital configuration. As such, if PC-b were in a synchronous orbit around its M-dwarf host, it would experience a stark contrast in the received stellar flux between its permanent day and night-side. Using the state-of-the-art Earth System Model (WACCM6) with Earth-like atmospheric and surface conditions, this research evaluates surface temperature distributions, atmospheric circulations, ozone chemistry, and synthetic spectra. While the findings agree with previous research suggesting an overall snowball-like state with a limited habitable surface, the inclusion of the coupled chemistry, dynamic surface albedo scheme, ocean dynamics, and Earth's topography and orography in WACCM6 reveals subtle deviations in many aspects such as surface temperature distribution, cloud properties and cloud radiative effects, atmospheric circulation, and stratospheric ozone distribution.

4.2 Introduction

Recent advancements in observational astronomy, particularly with the James Webb Space Telescope (JWST), have enabled detailed studies of tidally-locked exoplanets. These planets, often orbiting M-dwarfs which comprise 70% of all stars (Bochanski et al., 2010), present a unique configuration where one hemisphere perpetually faces the star while the other remains in darkness, leading to temperature differences between day-side and night-side. Proxima Centauri b (PC-b), the closest exoplanet to our solar system (~ 1.3 parsecs), is a prime candidate for these studies, offering an unprecedented opportunity to investigate the nature of terrestrial planets orbiting M dwarfs.

PC-b is situated within its habitable zone (Anglada-Escudé et al., 2016), and is considered to be a candidate potentially habitable planet for future characterizations (Ribas et al., 2016; Barnes et al., 2016). Previous studies have employed 1D and 3D models to explore the climate and potential habitability of PC-b. For instance, Meadows et al. (2018a) used 1D coupled climate-photochemical models to simulate several potential atmospheres for PC-b, with different atmospheric compositions. In particular, they found that PC-b with a pre-industrial Earth atmosphere can be potentially habitable with a mean surface temperature of 273 K, suggesting a possible open ocean on the day-side hemisphere. 3D simulations (e.g. Turbet et al., 2016; Boutle et al., 2017; Lewis et al., 2018; Del Genio et al., 2019; Salazar et al., 2020b; Galuzzo et al., 2021) also predict that PC-b could be habitable, featuring an open ocean on the dayside hemisphere, across a range of orbital states (e.g., synchronously rotating or in 3:2 resonance with highly eccentric orbit (i.e., $e > 0.1$) (e.g. Anglada-Escudé et al., 2016)) and atmospheric compositions, including CO_2-dominated, N_2-dominated, and Earth-like atmospheres. These studies also emphasize the need for future detailed climate modeling using interactive chemistry and non-homogeneous surface conditions for climate and habitability assessments.

The ozone (O_3) chemistry on PC-b has also been a critical area of research due to its

impact on atmospheric dynamics and potential surface habitability. Using the Met Office Unified Model (UM), De Luca et al. (2024) found that simulations with interactive O_3 chemistry exhibit higher temperature and wind speed variability than those without, with stronger wind speeds and increased night-side trapping of O_3 in dynamically stable states. The spatial variation of O_3 was studied by Braam et al. (2023b), who attributed the O_3 accumulation on the nightside of PC-b to stratospheric circulation driven by the radiative heating and cooling contrast between the day and night sides. Further investigations using WACCM6 highlighted significant variations in O_3 columns under identical O_2 initial conditions due to differences in the strength and shape of the adopted UV spectrum, affecting the interpretation of the O_2 and O_3 abundance from the transmission and emission spectra (Cooke et al., 2023b). Additionally, Cooke et al. (2024) showed that surface O_3 concentrations on TRAPPIST-1 e and PC-b could exceed harmful levels, which should be considered alongside surface temperature and precipitation when evaluating land habitability.

Observational prospects for PC-b have also been extensively studied. Synthetic spectra and thermal phase curves have been generated to evaluate the capability of observational instruments to differentiate between climate states. For example, JWST observations beyond 10 µm could provide insights into atmospheric heat transport and molecular composition, while direct imaging spectra might detect key atmospheric features like O_4 (O_2-O_2 collisionally induced absorption), CO_2, and CO, making direct imaging the most effective method for assessing habitability (Meadows et al., 2018a). Thermal phase curves derived from the synthetic exoplanet's spectrum (assuming an Earth-like atmosphere) suggest that, using JWST, PC-b's thermal phase curve in the far-IR could be marginally distinguished with a signal-to-noise ratio (S/N) of approximately 1, requiring a minimal exposure time of 5 hours per orbital epoch (Galuzzo et al., 2021). It has been shown that JWST observations from 5-12 µm can test for the existence of an atmosphere and potentially detect the 9.8 µm ozone band, which could constrain the possibility of life around PC-b (Kreidberg et al., 2016). Snellen et al. (2017) found that CO_2 features at

15 μm are more prominent than O_3 at 9.6 μm and could be detected with a signal-to-noise ratio (S/N) of 2 with 20 days of JWST observing. While CO_2 is not a potential biosignature like O_3, detecting it can indicate the presence of an atmosphere and provide constraints on the planet's temperature structure (Snellen et al., 2017). Future missions aimed at detecting and characterizing PC-b's atmosphere, such as the Extremely Large Telescope (ELT) (e.g. Hawker et al., 2019; Galuzzo et al., 2021; Zhang et al., 2024) and the Large Interferometer for Exoplanets (LIFE) (e.g. Carrión-González et al., 2023), will further enhance our capability to characterize tidally-locked exoplanets.

The impact of surface conditions on the climate of PC-b and other tidally-locked exoplanets has also been a focus of 3D simulations. Using the EXOPLASIM model, Macdonald et al. (2022b) demonstrated that varying land configurations can alter global surface temperature by up to 20 K and atmospheric water vapor content by several orders of magnitude. Lewis et al. (2018) used the Met Office Unified Model (UM) with a land-surface model to investigate the climate effects of a continent at the substellar point of PC-b. They found that substellar land causes global cooling and increases day-night temperature contrasts by limiting heat redistribution. Introducing substellar land leads to a regime change in atmospheric circulation, forming two mid-latitude counter-rotating jets and weakening the equatorial super-rotating jet. These land-related climate differences highlight significant uncertainties in climate assessment through atmospheric observations alone, even if the atmospheric composition is known. Another study on TRAPPIST 1e using WACCM6 explored O_3 asymmetry in the atmosphere due to Earth-like orography, finding that land masses on the nightside cause drag in near-surface flows, leading to an asymmetric meridional overturning circulation and asymmetric ozone distribution over the poles (Sainsbury-Martinez et al., 2024).

Recent findings have revealed significant variability and complexity in the climate and atmospheric chemistry of Earth-like scenarios for PC-b, driven by factors such as surface conditions, atmospheric composition, stellar radiation and different climate models adopted (e.g. Turbet et al., 2016; Boutle et al., 2017; Lewis et al., 2018; Del Genio

et al., 2019; Salazar et al., 2020b; Galuzzo et al., 2021). Motivated by this, we used a fully-coupled Earth System Model - WACCM6 in this study to simulate the climate of PC-b with the substellar point over the ocean (PC-b) assuming Earth-like initial conditions and modified orbital and planetary parameters to match those of PC-b's. To understand the possible climate states of PC-b, we outline our methodology in Section 4.2 and present results for the PC-b case compared to a modern Earth case in Section 4.3. We focus on the primary climate diagnostics, analyzing surface temperature and its alignment with other PC-b studies (Section 4.3.1). I investigate atmospheric circulations and the stratospheric ozone layer in Sections 4.3.2 and 4.3.3, respectively. A brief analysis of the potential surface habitability and theoretical observables is presented in the discussion (Section 4.4). I conclude our findings in Section 4.5.

4.3 Methods

4.3.1 Simulation Configurations

PC-b is located within its host star's habitable zone with an equilibrium surface temperature of 234 K (Kopparapu et al., 2013; Anglada-Escudé et al., 2016). However, the planet's habitability depends on various factors, including its intrinsic planetary characteristics and environmental space conditions. Additionally, diverse evolutionary paths could lead to different climate states. These aspects can be addressed in 1D and 3D climate models. Here, we simulate the climate of PC-b with an Earth-like atmosphere using WACCM6, an Earth System Model. More details about the model specifications can be found in the previous chapters (see Chapters 1.3.9 and 2).

We start with a model configuration in the Earth's pre-industrial era in 1850, then, we modify the planetary parameters to match those of PC-b's. Table 4.1 shows the modified planetary parameters in the model setup. We adopt the stellar spectrum of Proxima Centauri (GJ 551) from the MUSCLES treasury survey (France et al., 2016;
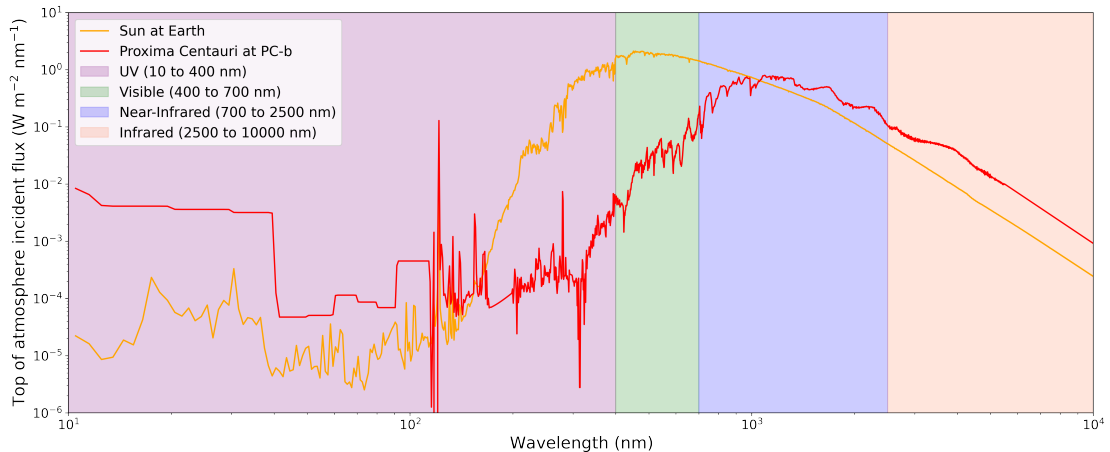
Figure 4.1: Spectral flux comparison between the Sun and Proxima Centauri. The plot shows the spectral flux distribution for the Sun (orange) and Proxima Centauri (red) across wavelengths ranging from UV to infrared incident on the top of atmospheres. The x-axis represents the wavelength in nm, and the y-axis shows the spectral flux in W m^{-2} nm^{-1}. The vertical line at 121.6 nm indicates the Lyman-α line. The flux in the wavelength bin to the left of the Lyman-α emission in the MUSCLES spectra is consistent with zero from the measurements. Shaded regions denote key spectral ranges: UV (100 to 400 nm, purple), visible (400 to 700 nm, green), near-infrared (700 to 2500 nm, blue), and infrared (2500 nm and beyond, coral). This comparison highlights the differences in emission characteristics between a G-type star (the Sun) and an M-type star (Proxima Centauri).

Youngblood et al., 2017) [1]. A comparison of the spectral flux between the Sun and Proxima Centauri is given in Figure 4.1.

Inspired by previous studies that suggest that different land/ocean distribution can lead to the variability of climate and chemistry, we choose to tidally lock the planet so that the sub-stellar point is over the 180° longitude and the 0° latitude (i.e., over the Pacific Ocean), and keeping the Earth's atmosphere composition, topography and orography (the PC-b case). Currently, the PC-b case has been running for 320 years since the benchmarked Earth case. The PC-b case has reached a quasi-steady state, with a top-of-atmosphere (TOA) energy imbalance of approximately -1 W m^{-2}. For climatology analysis, we take the annual mean of $\sim$ 30 orbits for the PC-b case. For the benchmarked

---

[1]This can be found at: `https://archive.stsci.edu/prepds/muscles/`

Table 4.1: Modified planetary parameters for PC-b simulations

Parameter	Value	Unit
Radius R	1.07	$R_{\oplus}$
Orbital Period P_{orb}	11.18	days
Peak Insolation I	840	W m^{-2}
Surface Gravity g	12.2	m s^{-2}
Obliquity ϵ	0	radian
Eccentricity e	0	radian

Earth case, we averaged over the monthly mean outputs for five simulation years (i.e., 5 Earth's orbits).

Similar to that done in Chapters 2 and 3, we have muted the QBO forcings and the marine geobiochemistry since they are tuned parameters to match the Earth's observation. The QBO forcing is muted in our 2-degree resolution simulation (i.e., $1.9° \times 2.5°$ in latitude and longitude) to save computational resources, such that wave dissipation in the stratosphere will not align with Earth's observation, but similar inter-annual oscillation features can exist and can potentially affect the climate. One caveat in the model setup is that the dynamic ocean component model has the Earth's rotation rate instead of that for the PC-b's, which might cause inaccuracy regarding ocean heat transport and sea ice dynamics.

The data produced by WACCM6-CESM2.1.3 was branched from the original datasets (credits to Greg Cooke and the ARC4 HPC facilities at the University of Leeds) [2].

4.3.2 Tidally-locked Coordinates

It is important to note that throughout the scientific analysis in this chapter, we occasionally switch to tidally-locked coordinates from geographic coordinates, particularly when variables of interest are influenced by wind patterns and day-to-night circulations. This shift allows for a more appropriate representation of the unique dynamics of tidally-locked

---

[2]Detailed description of the datasets can be found in the GitHub repository, available on GitHub: `https://github.com/exo-cesm/CESM2.1.3/tree/main/Tidally_locked_exoplanets`.

exoplanets compared to geographic coordinates, highlighting the hemispheric differences between the day- and the night-side.

Compared with geographic coordinates, the tidally-locked (TL) coordinates have their own advantage when analysing the climate outcomes of tidally-locked planets with longer orbital periods (Koll et al., 2015; Hammond et al., 2021) due to their climate symmetry connecting the substellar and the anti-stellar points. In the tidally-locked coordinates, the 90/-90-degree latitude is set to be the substellar/anti-stellar point, with the 0-degree latitude marking the terminator separating the day and the night side hemispheres [3]. Figure 4.2 shows how the TL coordinates are visually connected to the geographic coordinate for the PC-b case, to aid our understanding of the TL coordinates. The left panel shows half of the globe with the substellar point over the Pacific Ocean at the longitude of 180° and the latitude of 0° with Antarctica in the centre. The right panel shows the full projected map in the TL coordinates, in which the TL longitude between 90° and 270° corresponds to the half of the globe in the left panel.

---

[3]To transform the geographic coordinates to TL coordinates, one can follow the detailed steps in Koll et al., 2015, and an example code is documented in GitHub at `https://github.com/danielkoll/tidally-locked-coordinates/tree/master/TL_coordinates`.
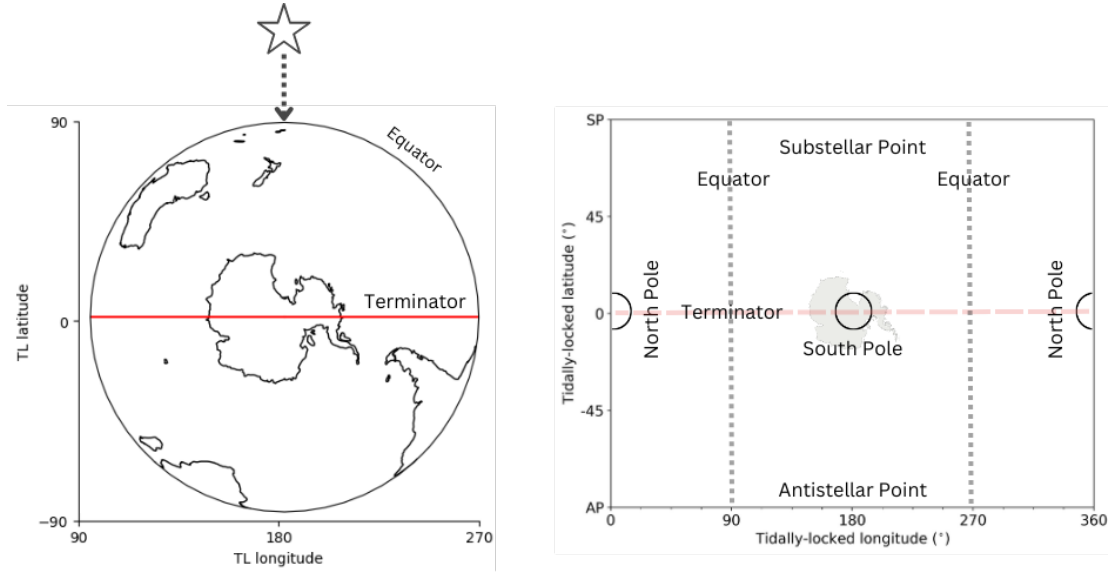
Figure 4.2: Illustration of the tidally-locked coordinate system for the PC-b case. Left: A view of half the globe oriented in TL coordinates, with the substellar point located over the Pacific Ocean at 180° longitude and 0° latitude. The red line indicates the terminator, separating the day side from the night side hemisphere. Right: The entire globe is projected onto the TL coordinates. Vertical black dashed lines represent the equator, while the horizontal red dashed line marks the terminator. The positions of the south pole, north pole, substellar point (SP), and antistellar point (AP) are labelled according to their locations in TL coordinates.

4.4 Results

4.4.1 Primary Climate Diagnostics

Table 4.2 shows the annual global mean surface temperature, the total stellar irradiance (TSI), the planetary albedo (A_P), the surface albedo (A_S), the cloud albedo (A_C) and the top-of-atmosphere energy imbalance (ΔF) for the Earth case and the PC-b case. The Earth case is the default pre-industrial Earth case (with the solar spectrum) simulating the climate in the year 1850 and can be compared to the tidally-locked cases to aid our understanding of how the change in orbital configuration and stellar spectrum has affected the climate. The PC-b case has essentially reached a quasi-steady state since $|\Delta F| \sim 1\mathrm{W\ m^{-2}}$, and the surface temperature variance in successive orbits is small ($\Delta T < 0.24$ K).

The PC-b case has a colder annual global mean surface temperature of 220.5 K, compared

117

Table 4.2: Energy balance: annual global mean variables

Variables	Earth	PC-b
T_S (K)	288.2	220.5
TSI (W m^{-2})	341.8	220.9
A_P (%)	31.6	40.1
A_S (%)	14.9	56.3
A_C (%)	18.0	18.8
ΔF (W m^{-2})	0.41	-1.1

to 288.2 K in the Earth case. The PC-b case receives less stellar radiation ($TSI_{PC-b} \sim$ 0.65 $TSI_{\oplus}$), so the surface temperature is inevitably colder. The planetary albedo is higher ($\Delta A_P = 8.5\%$) in the PC-b case because of a much higher surface albedo ($\Delta A_S = 41.4\%$) and a slightly higher cloud albedo ($\Delta A_C = 0.8\%$).

Figure 4.3 shows the surface temperature maps in geographic coordinates for both cases, with the white contours highlighting the regions where the surface temperature is above the freezing point of typical saline water on Earth. The freezing point of saline water depends on the salinity and ocean layer pressure (e.g. Fujino et al., 1974). For simplicity, we adopt the constant freezing point temperature ($-1.8°$ or 271.35 K), which is parameterised in the sea ice model (CICE5) (Hunke et al., 2013) for demonstrating the open ocean area in our simulations. The ocean surface albedo decreases with increasing wavelength from the visible to the infrared band due to the differences in the optical properties of water, snow and ice (e.g. Briegleb et al., 2007), and the fact that PC-b receives more near-infrared radiation compared to Earth (see Figure 4.1) can cause the ocean surface to be less reflective. However, the larger sea ice coverage in the PC-b case appears to be a stronger effect. In the PC-b case, about 65% of the day-side surface is covered or partially covered by sea ice, which is significantly higher than the global mean sea ice fraction of 3.9% in the Earth case.

Despite the below-freezing global mean surface temperature (220.5 K), an open ocean is always retained in the PC-b case. This aligns well with the previous Earth-like PC-b simulations regardless of the inclusion of ocean dynamics (e.g. Turbet et al., 2016;
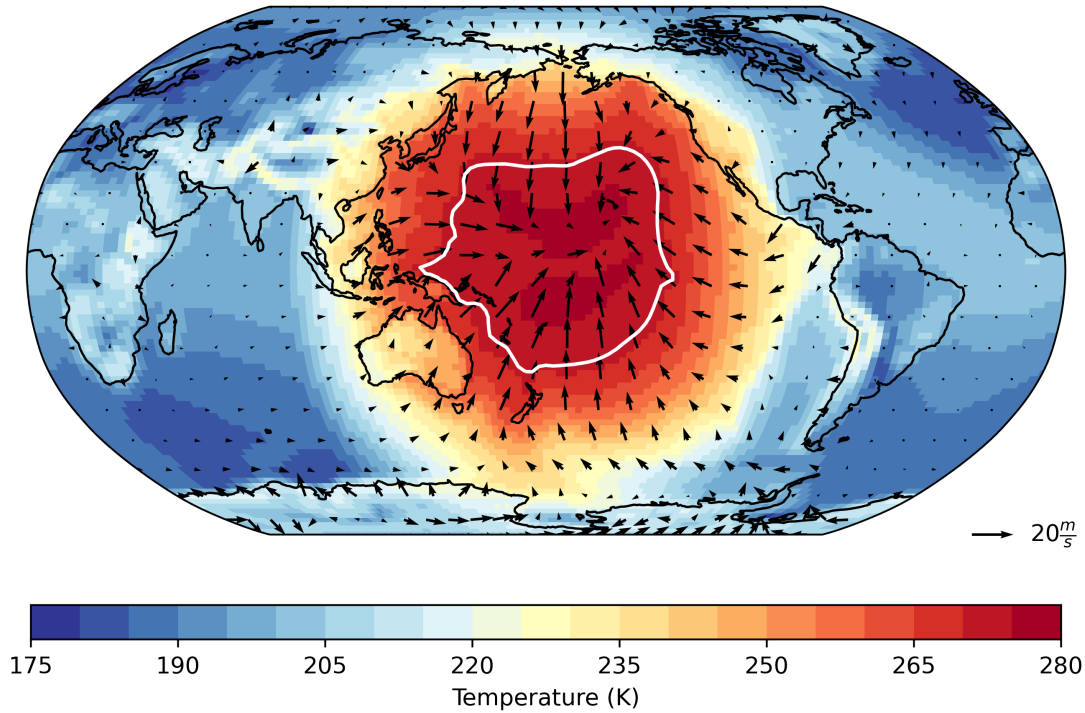
Figure 4.3: The surface temperatures for the PC-b case. The black contour highlights the boundary of land continents, and the white contour indicates the open ocean area where the surface temperature > 271.35 K. The wind vectors at the surface are shown in black arrows.

Boutle et al., 2017; Lewis et al., 2018; Del Genio et al., 2019; Salazar et al., 2020b; Galuzzo et al., 2021). Del Genio et al. (2019) explored the impact of ocean dynamics on an Earth-like PC-b's climate and discovered a "lobster-shaped" open ocean region formed by wind-driven currents. This pattern emerges due to Rossby wave-induced cyclones resembling the "claws of a lobster" on each side of the equator and an elongated equatorial "tail" driven by a tropical eastward Kelvin wave [4] (Hu et al., 2014). When continents are included, they can block zonal heat transport, shifting the pattern to an "eyeball-shape" ocean, similar to the scenarios that exclude ocean dynamics (Del Genio et al., 2019; Salazar et al., 2020a). This explains the eyeball-shaped open ocean in the PC-b case from our simulations, in which both ocean dynamics and the Earth's ocean/land distribution are included.

---

[4]Equatorially trapped waves that propagate eastward without any meridional component due to a balance between the Coriolis force and pressure gradients

Figure 4.3 shows the temperature distribution across the day-side and night-side hemi-spheres, with a maximum surface temperature of 278 K on the day-side and a minimum of 177 K on the night-side. The maximum day-side surface temperature is not located at the substellar point. Instead, we notice an eastward shift from the substellar point (180° in longitude) to a longitude of 195°. This eastward shift of the maximum sur-face temperature may be explained by the tropospheric super-rotating jet stream in the equatorial region for the PC-b case (see Figure 4.9). Compared to Boutle et al. (2017), which used the UM model to simulate PC-b with an Earth-like atmosphere and a slab ocean (2.4 m mixed layer), our simulations show a colder day-side surface temperature (278 K vs. 290 K) but a warmer night-side (177 K vs. 150 K). The higher day-side albedo in our case (40% vs. 35%) likely explains the cooler day-side, while enhanced heat transport from ocean dynamics may account for the warmer night-side temperature by more effectively distributing heat across the planet. Our results for the maximum and minimum surface temperatures are significantly lower than those reported by Del Genio et al. (2019), who used the ROCKE-3D GCM (Resolving Orbital and Climate Keys of Earth and Extraterrestrial Environments with Dynamics; Way et al. (2017a)) to simulate PC-b with an Earth-like atmosphere and land-ocean configuration with ocean dynamics. Their simulation found a day-side maximum surface temperature of 291 K and a night-side minimum of 196 K. Among a variety of different parameterizations em-ployed in our model (WACCM6) and in ROCKE-3D, a key difference that may explain the temperature differences is the treatment of land surface albedo. Way et al. (2017a) assume a constant land surface albedo of 0.2 (typical of a terrestrial desert), while the Community Land Model Version 5 (CLM5; Lawrence et al., 2019) coupled to WACCM6 calculates the land surface albedo dynamically, varying spatially and temporally based on surface characteristics. In the Earth case, our simulations show that the global mean land surface albedo is ~ 0.23, only slightly higher than that used in Way et al. (2017a). However, the PC-b case evolves from the Earth case, the land surface albedo increases significantly to ~ 0.67, as the surface albedo is largely influenced by land snow and ice

120

accumulations due to the cold temperatures.

Apart from the albedo effects, surface temperature can be affected by the cloud radiative effects and warming from greenhouse gases. As shown in Boutle et al. (2017), cloud representation in GCMs is crucial to determine the mean surface temperature and explain the day-night temperature contrast for PC-b. Figure 4.4 shows the spatial distributions of the low-level (1000 to 680 hPa), mid-level (680 to 440 hPa) and high-level ($<$ 440 hPa) effective cloud fractions, in which their morphologies are driven by the wind at the atmospheric pressures of 850 hPa, 500 hPa and 250 hPa, respectively. In Figure 4.4, the low-level cloud blankets nearly the entire planet, covering both the day-side and night-side hemispheres. On the day-side, these clouds are driven by upwelling moist convergent winds in the lower troposphere, similar to the cloud formation processes in Earth's Intertropical Convergence Zone (ITCZ). The day-side low-level cloud are optically thicker than other cloud types and effectively block a significant portion of stellar radiation from reaching the surface. In contrast, the night-side low-level cloud does not form locally due to the colder temperatures and limited atmospheric water vapor. Instead, it results from the tropospheric overturning divergent circulation (similar to the Hadley cell on Earth) and the tropospheric eastward equatorial jet stream (e.g. Hammond et al., 2021), where moist air is transported from the day-side to the night-side at higher atmospheric level (i.e., from the high-level cloud), condensing as it descends to the lower level on the night-side atmosphere (e.g. Boutle et al., 2017).

While the low-level cloud is formed in the rising branch of the convergence zone around the substellar point through "shallow convection", the high-level cloud is formed in the divergent upper branch through "deep convection" and does not cover the night-side except in the polar regions of the lower stratosphere (see Figure 4.5). Similar to the formation of Polar Stratospheric Clouds (PSCs) during the Antarctic winter on Earth, the polar clouds can form in the very dry stratosphere with extremely cold temperatures ($\sim$ 200 K) in the PC-b case. Positioned between the low-level and high-level clouds, the mid-level cloud primarily covers the substellar regions and shifts toward the northern
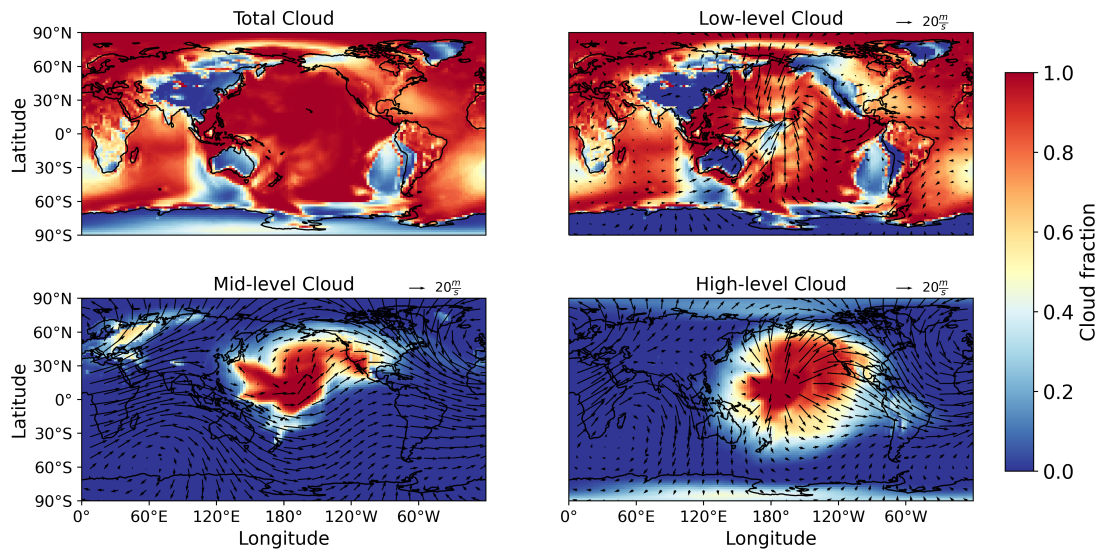
Figure 4.4: The total cloud fraction (upper left), the low-level cloud fraction (upper right), the mid-level cloud fraction (bottom left) and the high-level cloud fraction (bottom right). Wind vectors are plotted as black arrows at each corresponding pressure level at 850 hPa, 500 hPa and 250 hPa for low-level, mid-level and high-level clouds, respectively.
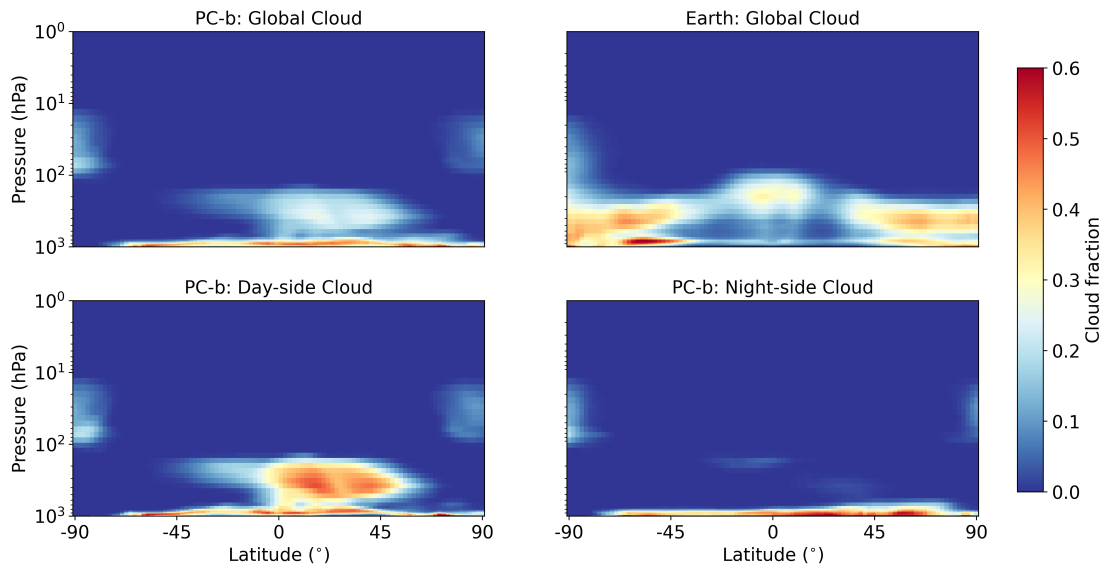
Figure 4.5: Vertical cloud distributions from the surface (1000 hPa) to 1 hPa for the PC-b case (top-left) and the Earth case (top-right). The bottom panels show cloud distributions in the PC-b case across day-side longitudes (bottom left) and across night-side longitudes (bottom right).

hemisphere on the day-side. Its spatial distribution is influenced by both the meridional overturning circulation and the equatorial jet stream in the mid-level troposphere. As

shown in Figure 4.8, the overturning circulation is slightly tilted northward, enhancing

the northward wind flow, while the equatorial jet stream drives the cloud eastward (see

Figure 4.9).
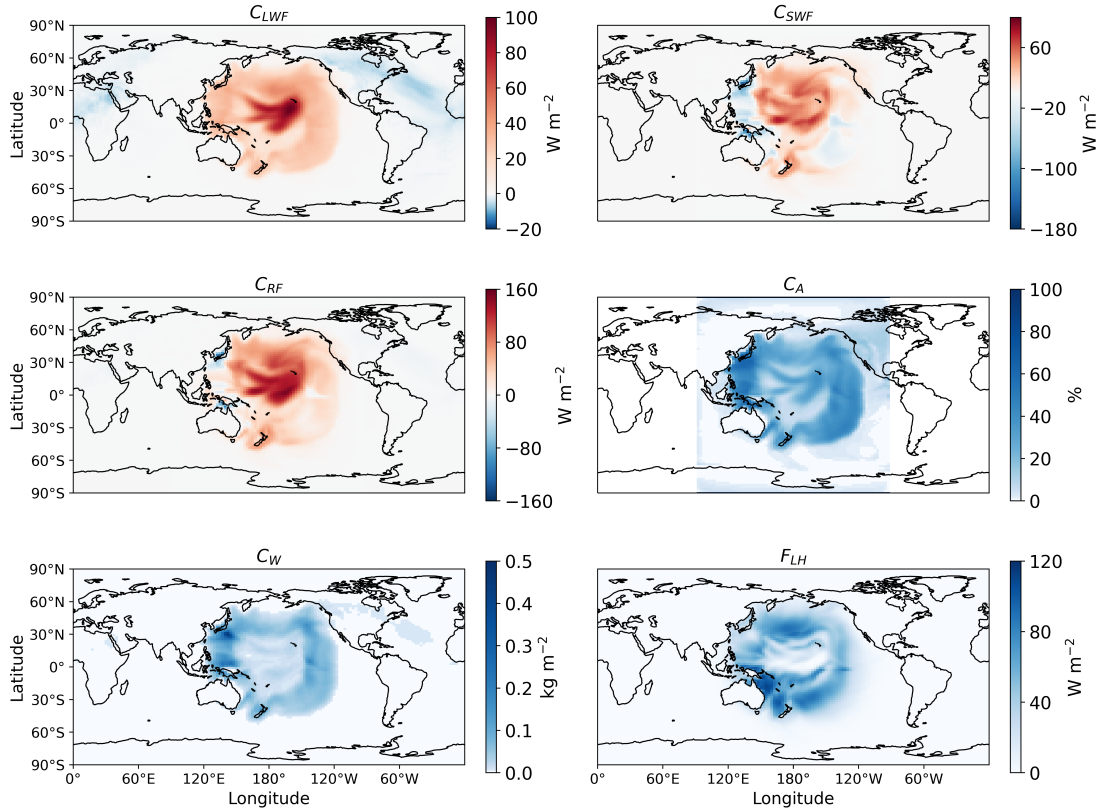
Figure 4.6: A multi-panel figure showing cloud radiative effects, cloud properties, and surface latent heat. The first row presents the longwave cloud radiative forcing (C_{LWF}) on the left and the shortwave cloud radiative forcing (C_{SWF}) on the right. The second row displays the net cloud radiative forcing (C_{RF}) on the left and the cloud albedo (C_A) on the right. The third row includes the vertically integrated total cloud water path (C_W) on the left and the latent heat flux (F_{LH}) on the right. Colorbars for C_{LWF}, C_A, and C_W are adjusted to emphasize lower values, enhancing the visibility in their corresponding colormaps.

Table 4.3 shows that the global mean C_{RF} in the PC-b case is 10 W m^{-2}, compared to

the -25 W m^{-2} in the Earth case. The positive C_{RF} indicates overall cloud radiative

warming in contrast to the net cloud cooling effect on Earth. In other words, the cloud

in PC-b regulates the climate in an opposite way compared to Earth on a global scale.

To explain this, we can split the C_{RF} into C_{SWF} and C_{LWF}. As described previously in

Chapter 3, C_{SWF} refers to the combination of cloud shortwave absorption and reflection,

Table 4.3: Cloud properties and surface latent heat flux: annual global mean variables

Variables	Earth	PC-b
C_{RF} (W m^{-2})	-25.0	10.0
C_{SWF} (W m^{-2})	-47.7	3.4
C_{LWF} (W m^{-2})	22.6	6.7
C_W (g m^{-2})	63.4	11.4
F_{LH} (W m^{-2})	85.9	10.8

while the reflection part is often shown as cloud albedo. The positive W m^{-2} C_{SWF} in the PC-b case indicates that the shortwave absorption is strong enough to outweigh the reflection. This is mainly because of the differences in the stellar spectrum between Proxima Centauri and the Sun. As seen in Figure 4.1, Proxima Centauri's spectrum has significantly less radiation in the visible range, which explains the weaker cloud shortwave reflection, while the stronger near-infrared radiation in the spectrum enhances absorption by water cloud. The global mean C_{SWF} (3.4 W m^{-2}) and C_{LWF} (6.7 W m^{-2}) in our simulations differ from those reported by Del Genio et al. (2019), in which C_{SWF} and C_{LWF} are -32 W m^{-2} and 13 W m^{-2}, respectively. This could be due to the different cloud parameterizations adopted between the models.

Figure 4.6 shows the spatial distribution of cloud shortwave (C_{SWF}), longwave (C_{LWF}) and net radiative effects (C_{RF}), together with the cloud albedo (C_A), cloud water content (C_W [5]) and surface latent heat flux (F_{LH}). C_{SWF} (right panel in the first row) is only present on the day-side hemisphere due to the absence of stellar irradiation on the night-side, similar to the cloud representation in Boutle et al. (2017). C_{SWF} is predominantly positive around the substellar point, except for a negative annular region where the high-level cloud is absent. The high-level cloud acts as a warming layer by absorbing near-infrared radiation, situated above the more reflective low-level cloud (right panel in the second row).

C_{LWF} (left panel in the first row) is predominantly positive on the day-side hemisphere,

---

[5]C_W is the total amount of water (liquid and ice) per unit area in the column of air from cloud base to top.

where the high-level cloud is present. The high-level cloud exerts a strong longwave warming effect by absorbing upwelling longwave radiation and re-emitting it at its colder temperature. However, there is no longwave cloud warming on the night-side hemisphere. The night-side cloud is optically thin due to its limited cloud water (C_W). C_W originates from surface latent heat flux (F_{LH}) in an annular region of the substellar point on the day-side hemisphere, where strong surface convergent winds can enhance the rate of liquid water evaporation, similar to the findings in Boutle et al. (2017). In addition, the lack of longwave cloud warming is associated with the vertical temperature inversion on the night-side hemisphere. In the lower troposphere, the temperature inversion causes the cloud top to be warmer than the surface (see Figure 4.13), switching off the cloud's longwave warming effect (i.e., cloud greenhouse warming effect) and turning on the longwave cloud cooling effect. This phenomenon is described as the "radiator fin" analogy for effective night-side cooling (Yang et al., 2014). This "radiator fin" is evident in the "arm-shaped" region with a negative C_{LWF}, where the cloud water content is higher than the rest of the night-side hemisphere (left panel in the third row). The increased cloud water is driven by the tropospheric overturning circulation and the equatorial super-rotating jet stream in the PC-b case.

In addition to surface albedo and cloud radiative effects, the clear-sky greenhouse effect (CGE) plays an important role in explaining the lower surface temperature in the PC-b case. Compared to the Earth case, which exhibits a strong global mean CGE of 135 Wm^{-2}, the PC-b case has a significantly lower global mean CGE of only 9 Wm^{-2} (not shown). This reduction in CGE is primarily due to lower water vapor concentrations in the PC-b case (see Figure 4.13), which weakens the trapping of outgoing longwave radiation. Similar to the cloud greenhouse effect in the PC-b case, the CGE shows opposite effects between the day-side and night-side hemispheres. The day-side has a positive CGE of 38 Wm^{-2}, driven by the presence of water vapor and warmer surface temperatures, which lead to longwave absorption and re-emission. On the other hand, the night-side shows a negative CGE of -20 Wm^{-2}. This negative value arises because the

night-side surface, being much colder and drier than the overlying atmosphere, inverts the greenhouse effect.

4.4.2 Atmospheric Circulation

In section 4.4.1, we have demonstrated that the surface temperature differences between the PC-b case and the Earth case are controlled by the variables such as the surface albedo, cloud radiative effects and clear-sky greenhouse effects. As briefly discussed earlier, differences in atmospheric circulation are also crucial to understanding the spatial distributions of these variables.

On a tidally-locked exoplanet such as PC-b, the large day-to-night temperature and pressure gradients can induce strong atmospheric circulation, modified by the horizontal temperature gradients and the Coriolis force due to the slower planetary rotation rate. Based on the rotation period of tidally-locked planets, Haqq-Misra et al. (2018) defined three dynamical regimes (i.e., slow rotation, fast rotation and Rhines rotation) evaluated in terms of the equatorial Rossby deformation radius (λ_R) and the Rhines length (L_R). For tidally-locked planets, λ_R refers to the maximum extent of the mean zonal circulation from the day to the night side, and L_R indicates the latitudinal scale at which turbulent flow can organize into zonal jets (e.g. Haqq-Misra et al., 2018).

The following dimensionless equations for λ_R evaluated at the equator and L_R shown in Haqq-Misra et al. (2018) are:

$$\lambda_R/a = (\frac{\sqrt{gH}}{2\beta a^2})^{\frac{1}{2}} \tag{4.1}$$

$$L_R/a = \frac{\pi}{a}\sqrt{\frac{U}{\beta}} \tag{4.2}$$

where a is the radius of the planet; g is the gravitational constant; $H = \frac{\overline{T_S} R}{m_{air} g}$ is the atmospheric scale height in terms of the area-weighted mean surface temperature $\overline{T_S}$, universal gas constant R, air density and gravitational constant g; $\beta = 2\Omega$ is the Coriolis parameter in terms of the rotational angular velocity Ω, U is the area-weighted mean surface wind.

Applying the parameters value of PC-B in Table 4.1 and $\overline{T_S} = 220.45K$ and $U = 5.33$ m s^{-1} from our model outputs, we find that $\lambda_R/a = 1.19$ and $L_R/a = 0.77$. These values of PC-b align with the Rhines rotator regime in which $\lambda_R/a > 1$ and $L_R/a < 1$. In other words, we expect that PC-b can have a day-to-night overturning circulation from a planetary-scale Rossby wave, with the presence of turbulence-driven jet streams. This agrees with what Haqq-Misra et al. (2018) predicts that planets around stars with a rotation period of 5 to 20 days are Rhines rotators.

To gain a more detailed view of the large-scale atmospheric circulation patterns in PC-b, we show the mass stream function for the meridional overturning circulation (see Figure 4.8) and the zonal mean zonal wind for the jet streams (see Figure 4.9). Figure 4.8 shows the mass stream function $\Phi_p(\phi, p)$ as a function of latitude (ϕ) and vertical pressure (p) for the PC-b case (see Equation 4.1 in Chapter 3 for details on the mass stream function). The panels compare the geographic coordinate system (top-left) with the tidally-locked (TL) coordinate system (top-right), representing the mean meridional circulation in the troposphere and stratosphere (1000 hPa to 1 hPa). The top-left panel shows $\Phi_p(\phi, p)$ averaged over all longitudes, while the bottom-left and bottom-right panels highlight the day-side and night-side hemispheres, respectively. In geographic coordinates, a northward clockwise circulation (red) is observed in the northern hemisphere, and a southward counterclockwise circulation (blue) in the southern hemisphere, resembling Earth's Hadley cells but extending from the equator to the poles. When examined separately for the day-side and night-side, however, the circulation patterns reverse, with the night-side exhibiting a pole-to-equator flow. While the circulation patterns are opposite on the day-side and night-side hemispheres in geographic coordinates,

the TL coordinates can capture the day-to-night circulation as a whole (top-right panel). Notably, a spatially small night-to-day circulation appears between the antistellar point (AP) and approximately $-30°$ TL latitude, driven by the surface temperature gradient and horizontal winds flowing from the AP to the coldest region around $-30°$ TL latitude. This temperature gradient can be seen in Figure 4.7, which highlights the hemispherically asymmetric cold temperatures on the night-side.

Similar to the PC-b simulation in Braam et al. (2023b), we find that the PC-b case has a single thermally driven cell that transports heat from the day-side to the night-side seen in the TL coordinates. However, the maximum circulation strength in our case is two orders of magnitude lower than found in that work (10^{12} kg s^{-1} vs. 10^{14} kg s^{-1}), and this is related to the smaller meridional surface temperature gradient in our case possibly due to the finer model horizontal resolution and the inclusion of ocean dynamics. However, in Braam et al. (2023b), the night-side downwelling circulation takes place in the Rossby gyre location [6] at $-30°$ TL latitude but does not reach the antistellar point (AP). This is different from our case; we find a weaker downwelling circulation occurs at the AP and a stronger downwelling wind in the gyre location. In addition, the wind speed (around 400 hPa) in the gyre location is much weaker (25 m s^{-1}) compared to Braam et al. (2023b) (50 m s^{-1}).

Figure 4.9 shows the zonal mean zonal wind in the whole atmosphere between 1000 hPa to $6 \cdot 10^{-6}$ hPa for the PC-b case (panel) and the Earth case (right panel). For the Earth case, we can see a pair of mid-latitude zonal wind jets in the troposphere and asymmetric polar wind jets in the stratosphere. The polar jets are part of the Brewer-Dobson circulation and are associated with tropical upwelling and polar downwelling on Earth, both driven by extratropical Rossby waves originated in the troposphere and that propagate upwards and break in the stratosphere (e.g. Carone et al., 2018). For the PC-b case, we find a single super-rotating jet stream in the equatorial region in the troposphere.

---

[6]On a tidally-locked planet, the Rossby gyre is a large-scale atmospheric vortex on the night-side formed due to the interaction of planetary-scale Rossby and Kelvin waves generated by the strong day-night thermal contrast and influenced by the planet's rotation (e.g. Sainsbury-Martinez et al., 2024).

The super-rotation criterion for a planetary atmosphere can be obtained by allowing the atmospheric axial angular momentum $(r_p \cos\theta(\omega r_p \cos\theta + U))$ to be greater than the equatorial angular momentum (ωr_p^2) (e.g. Galuzzo et al., 2021), and the resulting zonal wind threshold is $U = \frac{\omega r_p \sin\theta^2}{\cos\theta}$ where ω is the angular velocity of the planetary rotation, r_p is the planetary radius and θ is the planetary latitude. At the equator, any positive (eastward) wind velocity is considered super-rotating since $\sin 90° = 0$.

Interestingly, our simulation results, which show the formation of a pair of polar super-rotating jets in the stratosphere, differ from the predictions of Carone et al. (2018) for exoplanets with intermediate rotation periods (4 days < P < 25 days). According to their results, exoplanets with $P_{\mathrm{orb}} \leq 25$ days are expected to have circulation dominated by standing tropical Rossby waves in both the troposphere and stratosphere, which leads to either a strong equatorial eastward super-rotating jet or no equatorial jet in the stratosphere, depending on the assumptions for the stratosphere wind breaking. The lack of stratospheric polar jets for slow rotators in Carone et al. (2018) may be because their study focuses on the jet formation from the tropical Rossby waves and does not incorporate other mechanisms like extratropical waves, gravity waves, or turbulence-driven processes that can contribute to jet formation. As we will discuss later, atmospheric circulation patterns are important to determine the spatial distribution of ozone (O_3) and its impact on surface habitability.
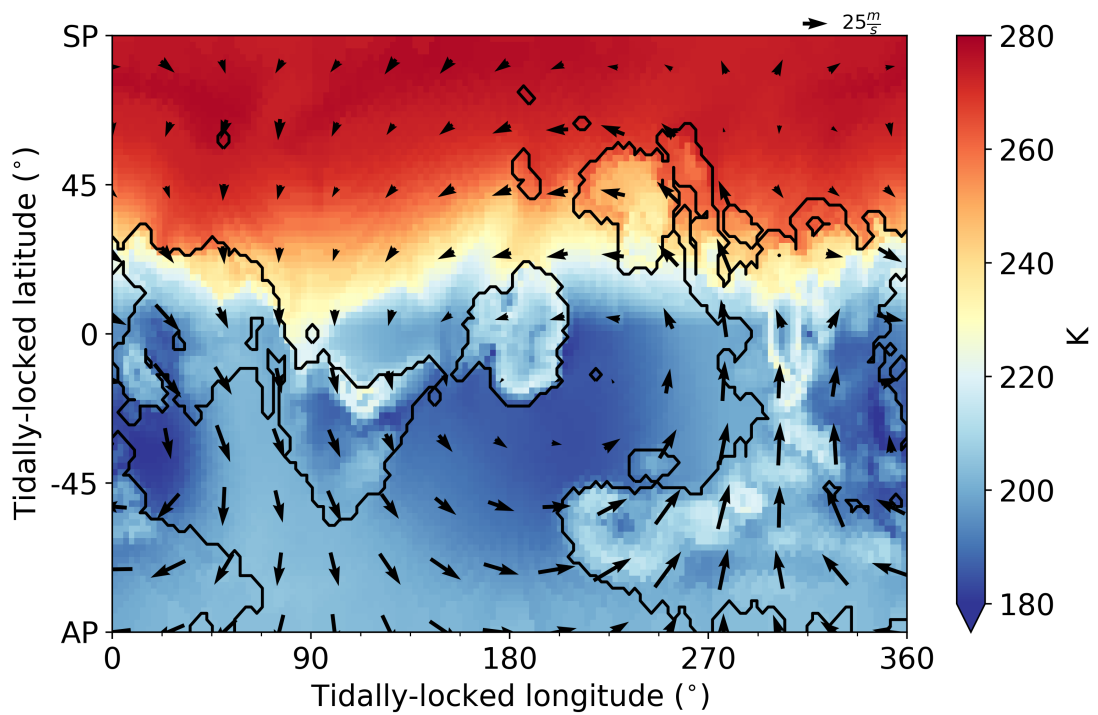
Figure 4.7: Surface temperature for the PC-b case in TL coordinates, where the substellar point is denoted as SP and the antistellar point is denoted as AP. Tropospheric wind vectors at about 400 hPa are shown on the plot.
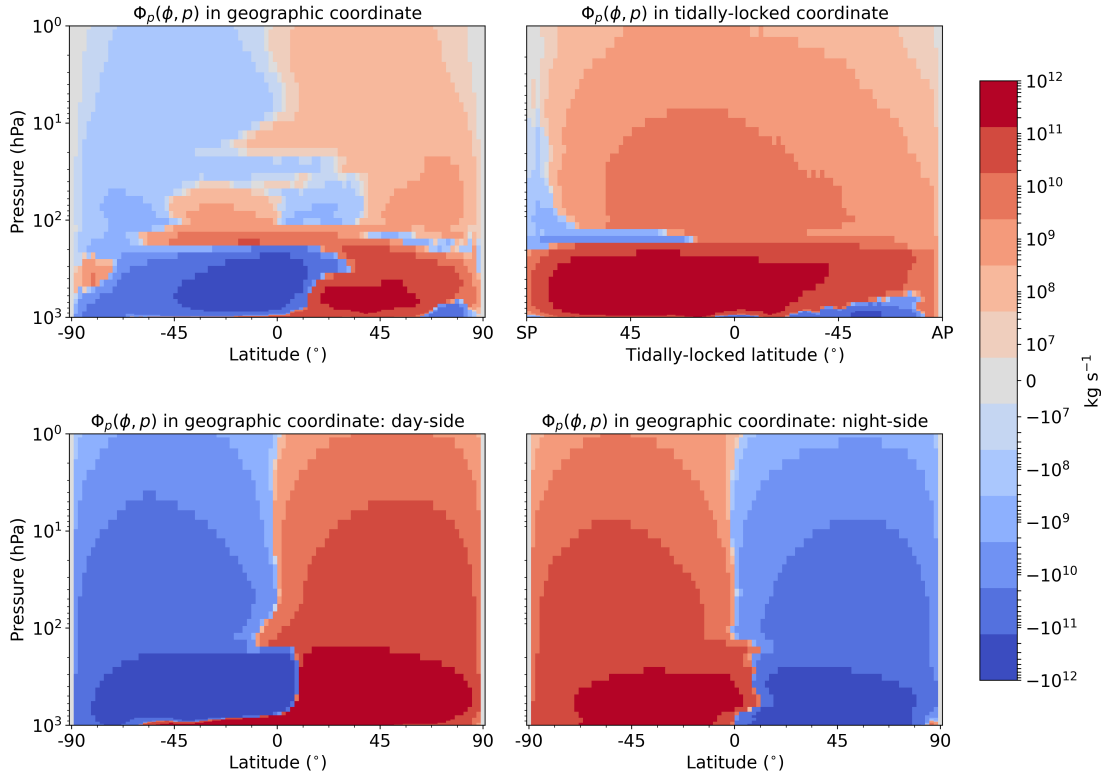
Figure 4.8: The top-left panel depicts the global mean mass stream function $\Phi_p(\phi, p)$ (vertically integrated zonal mean meridional wind) in geographic coordinates for the PC-b case, while the top-right panel shows it in tidally-locked coordinates. To understand the global mean $\Phi_p(\phi, p)$ in geographic coordinates, we split it into the day-side (lower left) and night-side mean (lower right). In geographic coordinates, clockwise (northward) overturning circulations are indicated in red, and counterclockwise (southward) circulations are shown in blue. In the tidally-locked coordinate system, the day-to-night overturning circulation is shown in red, and the night-to-day circulation is in blue.
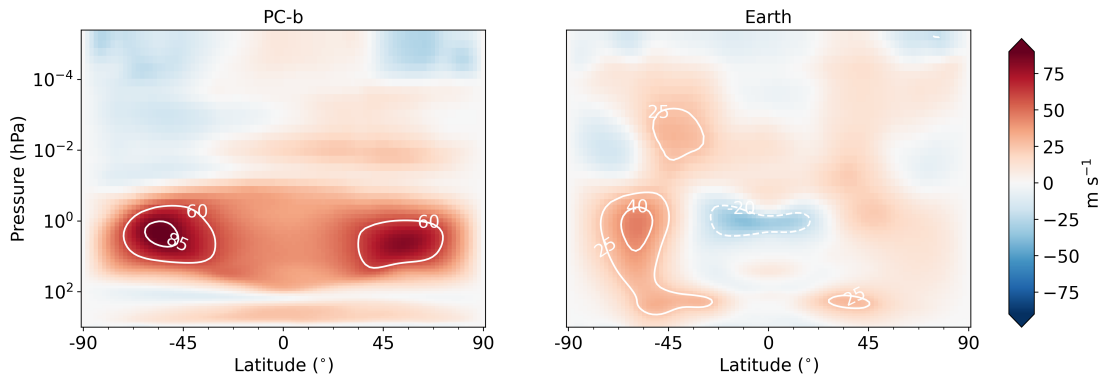
Figure 4.9: Zonal mean zonal wind for the PC-b case (left panel) and the Earth case (right panel). For the PC-b case, an equatorial superrotating jet stream in the troposphere flows eastward at about 25 m s^{-1}, and a pair of stratospheric superrotating jet streams flows eastward at about 70 m s^{-1}, in contrast to the Earth case.

4.4.3 Stratospheric Ozone Layer

O_3 in the stratosphere plays a crucial role in protecting life on Earth by absorbing harmful ultraviolet (UV) radiation. The formation and maintenance of the ozone layer are primarily explained by the Chapman cycle. The Chapman cycle involves a series of photochemical reactions. The cycle begins with the photodissociation of molecular oxygen (O_2) by short-wavelength UV radiation (< 240 nm), producing atomic oxygen (O), $O_2 + h\nu \rightarrow 2O$. Next, an oxygen atom O reacts with another O_2 molecule to form O_3, $O + O_2 + M \rightarrow O_3 + M$. Here, M represents a third body, typically molecular nitrogen or oxygen, that carries away excess energy from the reaction. O_3 can absorb UV radiation, leading to its photodissociation back into an oxygen molecule and an oxygen atom, $O_3 + h\nu \rightarrow O_2 + O$. Additionally, O_3 can react with O to regenerate O_2, $O_3 + O \rightarrow 2O_2$. In addition, it is necessary to consider the catalytic loss cycles of O_3 (Brasseur et al., 2005). For example, catalysts such as nitrogen oxide radicals ($NO_x = NO + NO_2$), hydrogen oxide radicals ($HO_x = H + OH + HO_2 + H_2O_2$) and chlorine and bromine oxide radicals ($ClO_x = Cl + ClO$ and $BrO_x = Br + BrO$) can destroy O_3 but are not consumed in the reactions. These reactions create a dynamic equilibrium that maintains the O_3 concentration in the stratosphere. O_3 can absorb ultraviolet (UV) radiation across three primary bands: the Hartley (200 to 310 nm), Huggins (310 to 340 nm), and Chappuis (400 to 650 nm) bands. The absorption in the Hartley and Huggins bands can block the most harmful UV-C and UV-B radiation from reaching the surface.

To understand the differences in O_3 chemistry between the PC-b case and the Earth case, we compare the global mean O_3 column density and analyze the spatial distribution of O_3. The global mean O_3 column density in the PC-b case is 188 Dobson Units (DU; 1 DU $= 2.687 \times 10^{20}$ molecules m^{-2}), which is significantly lower than in the Earth case (275 DU). The lower stellar UV radiation from Proxima Centauri (see Figure 4.1) reduces the production rate of O_3, which can explain the lower O_3 in the PC-b case. In addition, we find that a lower O mixing ratio in the PC-b case compared to the Earth case (see

Figure 4.13). This reduction is related to the colder surface temperatures in the PC-b case, which result in decreased evaporation of water vapor into the troposphere, and the colder tropopause that acts as a "cold trap", preventing water vapor from entering the stratosphere. Consequently, the stratospheric H_2O mixing ratio is lower in the PC-b case (see Figure 4.13). Since O can be produced through the photolysis of H_2O, the reduced H_2O abundance leads to lower O concentrations in the PC-b case. However, the H_2O mixing ratio is not the limiting factor for the decreased global mean O_3 column density in the PC-b case as O is mainly generated via O_2 photolysis (see Figure 4.10). The lower O production rate seen in the PC-b case is due to the lower photolysis rate of O_2, which is caused by the weaker UV radiation of Proxima Centauri compared to the Sun-like host star.

Moreover, we find that the stratospheric temperature is colder in the PC-b case, which can increase the three-body reaction rate in $O + O_2 + M \rightarrow O_3 + M$ (Atkinson et al., 2004). Notice that the lower stratospheric temperature also indicates lower reaction rates from the catalytic cycles, which decreases the rate of O_3 loss. Additionally, the mixing ratios of catalysts such as HO_x and NO_x in the PC-b are lower than in the Earth case (see Figure 4.13). In the upper atmosphere, NO_x undergoes continuous production via energetic particle precipitation and absorption of high-energy photons and is destroyed primarily via photolysis. The observed NO_x profile is the result of a balance between photochemistry and transport. However, the increased three-body reaction rate and the weaker catalytic cycles are insufficient to counterbalance the effects of the increased O productions from O_2 photolysis.

Figure 4.11 and Figure 4.12 show the spatial distribution of O_3 column density in the geographic coordinates and in the TL coordinates, respectively. In geographic coordinates, O_3 column density in the PC-b case concentrates toward the higher latitude of the southern hemisphere around Antarctica, with a maximum O_3 column density of 295 DU. However, the O_3 column density in the PC-b case is low elsewhere, particularly in the poles (25 DU). Compared to the Earth case, we find similar stratospheric polar
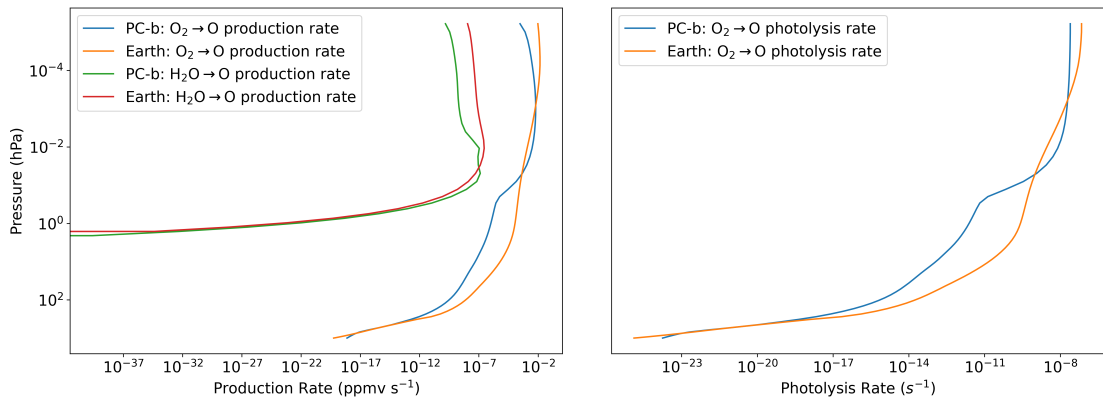
Figure 4.10: Vertical profiles of O production rates from H_2O and O_2 photolysis for the PC-b case and the Earth case. The left panel shows the production rates (ppmv s^{-1}) for H_2O and O_2 photolysis resulting in O production, while the right panel displays the O_2 photolysis rates (s^{-1}). The solid lines represent the global mean variables, with black indicating the Earth case and green indicating the PC-b case.
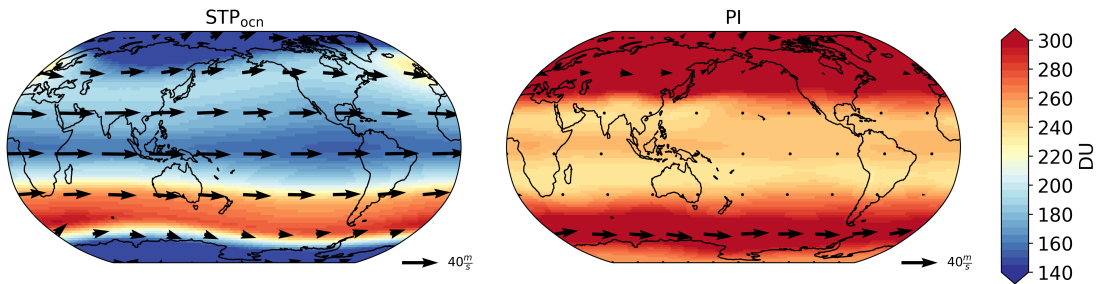
Figure 4.11: O_3 column density spatial distribution in geographic coordinates for the PC-b case (left panel) and the Earth case (right panel), with wind vectors (~ 40 hPa) in the stratosphere.
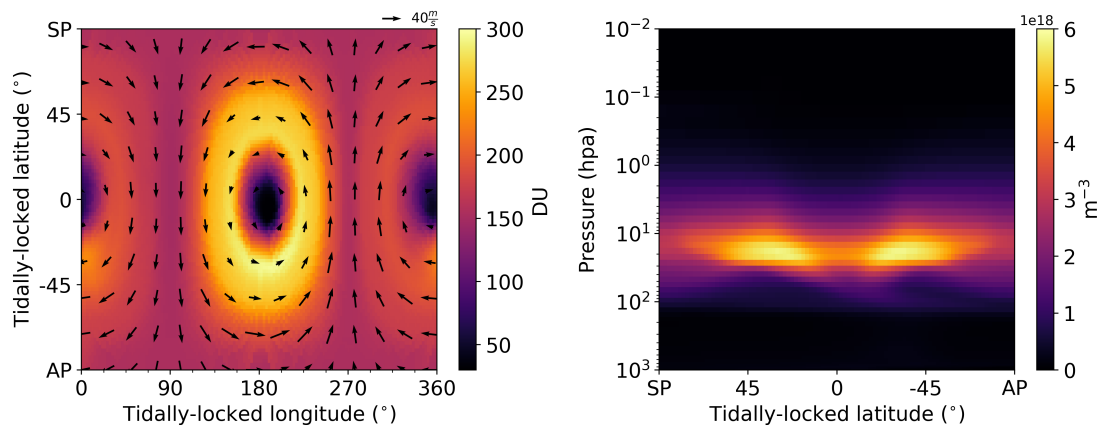
Figure 4.12: For the PC-b case, O_3 column density spatial distribution in TL coordinates (left panel), and zonal mean O_3 number density in TL coordinate (right panel), with wind vectors (~ 40 hPa) in the stratosphere.

vortices (i.e., high-speed, cyclonically rotating winds, characterized by the zonal mean zonal winds around the polar regions) that limit O_3 meridional transport to the polar regions. Another factor that may further reduce the lower O_3 column density in the poles is the presence of the polar stratospheric clouds (PSCs) in our simulations (see Figure 4.5). On Earth, these clouds provide surfaces that promote the production of chlorine radicals that destroy ozone catalytically (e.g. Tritscher et al., 2021).

One interesting finding is that the O_3 column density is hemispherically asymmetric in the PC-b case, and the O_3 column density in the northern hemisphere is much lower than that in the southern hemisphere. Since ozone is a long-lived species (i.e., the chemical lifetime exceeds the dynamical lifetime) (e.g. Proedrou et al., 2016; Braam et al., 2023a), the spatial distribution of O_3 is controlled by the atmospheric dynamics instead of the gain/loss from the chemical reactions on site. Sainsbury-Martinez et al. (2024) used the same model (WACCM6) and model configurations as ours to study the climate of TRAPPIST-1e, and they attribute the north-south O_3 asymmetry to the difference in the polar vortex strength, in which the stronger stratospheric jet streams in the southern hemisphere act as a more effective O_3 trap than in the northern hemisphere. In contrast to Braam et al. (2023a), who found that O_3 accumulates exclusively on the night-side hemisphere at Rossby gyre locations, our simulations demonstrate a symmetric O_3 column density around the terminator (see Figure 4.12). This symmetry is likely due to the presence of two high-latitude stratospheric super-rotating jet streams in our simulations (see Figure 4.9), which limits the stratospheric downwelling branch of the day-to-night circulation from reaching the gyre locations (see Figure 4.8). In comparison, Braam et al. (2023a) found a single equatorial jet stream in the troposphere and the stratosphere so that the descending air can reach the gyre location. This discrepancy in the stratospheric dynamics of PC-b may result from the inclusion of Earth's topography (i.e., land/ocean distribution) and Earth's orography, as similar studies suggest (e.g. Sainsbury-Martinez et al., 2024).
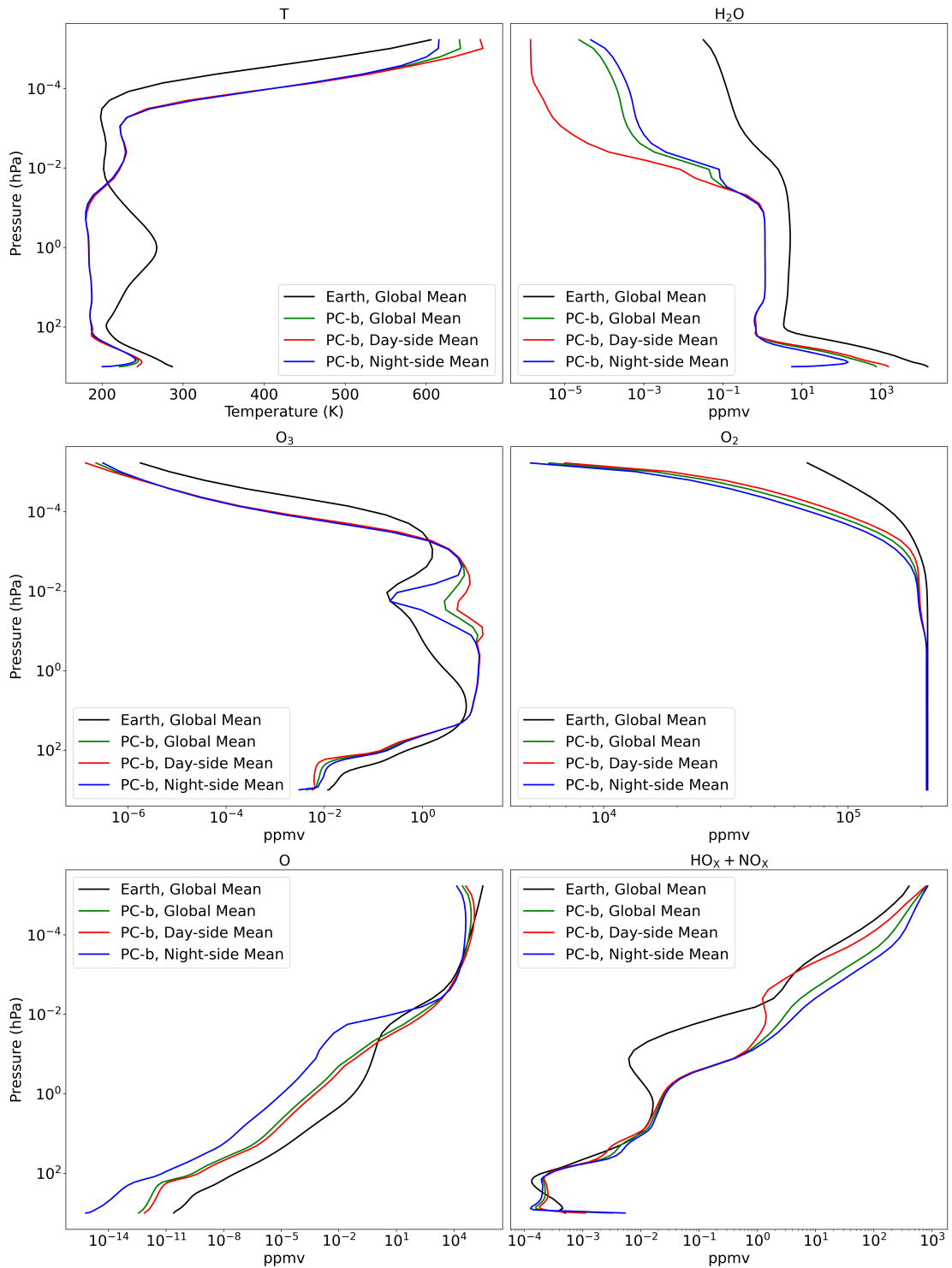
Figure 4.13: Vertical profiles of global mean, day-side mean and night-side mean temperature and atmospheric chemical mixing ratios for the PC-b case and the Earth case. The top-left panel displays the temperature profile, while the remaining subplots show mixing ratios (in ppmv) for H_2O, O_3, O_2, O, and $HO_X + NO_X$. Black and green lines represent the global mean variables for the Earth case and the PC-b case, respectively. Red and blue lines denote the day-side and night-side mean variables, respectively.

136

4.5 Discussion

4.5.1 Surface Habitability

There are a variety of factors that could affect the habitability of PC-b. These factors are overviewed in Meadows et al. (2018a). In this work, we briefly assess the surface habitability of PC-b using only two metrics: surface temperature and surface O_3 concentrations. We excluded the precipitation metric, which was adopted in Chapter 3 for a highly-eccentric Earth-analogue planet, as the land continent area with the surface temperature above the freezing point in the PC-b case is negligible. While an understanding of the habitability under the ocean surface requires a coupled marine biogeochemistry model, we have disabled this in our model (similar to the simulations in Chapter 2 and Chapter 3) because it is tuned to match Earth's observation and we cannot assume it is the same for exoplanets. Other factors that may affect the surface habitability of PC-b, such as the UV radiation at the surface and in the ocean mixed layer and the stellar flares, are beyond the scope of this work but are important to consider for future studies. While the O_3 layer is an important shield from harmful UV radiation in the Earth's stratosphere, O_3 is considered a pollutant at the surface and in the troposphere due to its ability to cause molecular and biological damage to life from its oxidative properties (e.g. Cooke et al., 2024). Cooke et al. (2024) have shown that a lethal amount of surface O_3 (> 40 ppbv) is possible for exoplanets with a variety of atmospheric compositions, and they suggested that surface O_3 concentrations should be incorporated into frameworks that aim to determine planetary habitability. Following this suggestion, we added the surface O_3 concentration as a new metric in addition to the surface temperature for analyzing the surface habitability of PC-b.
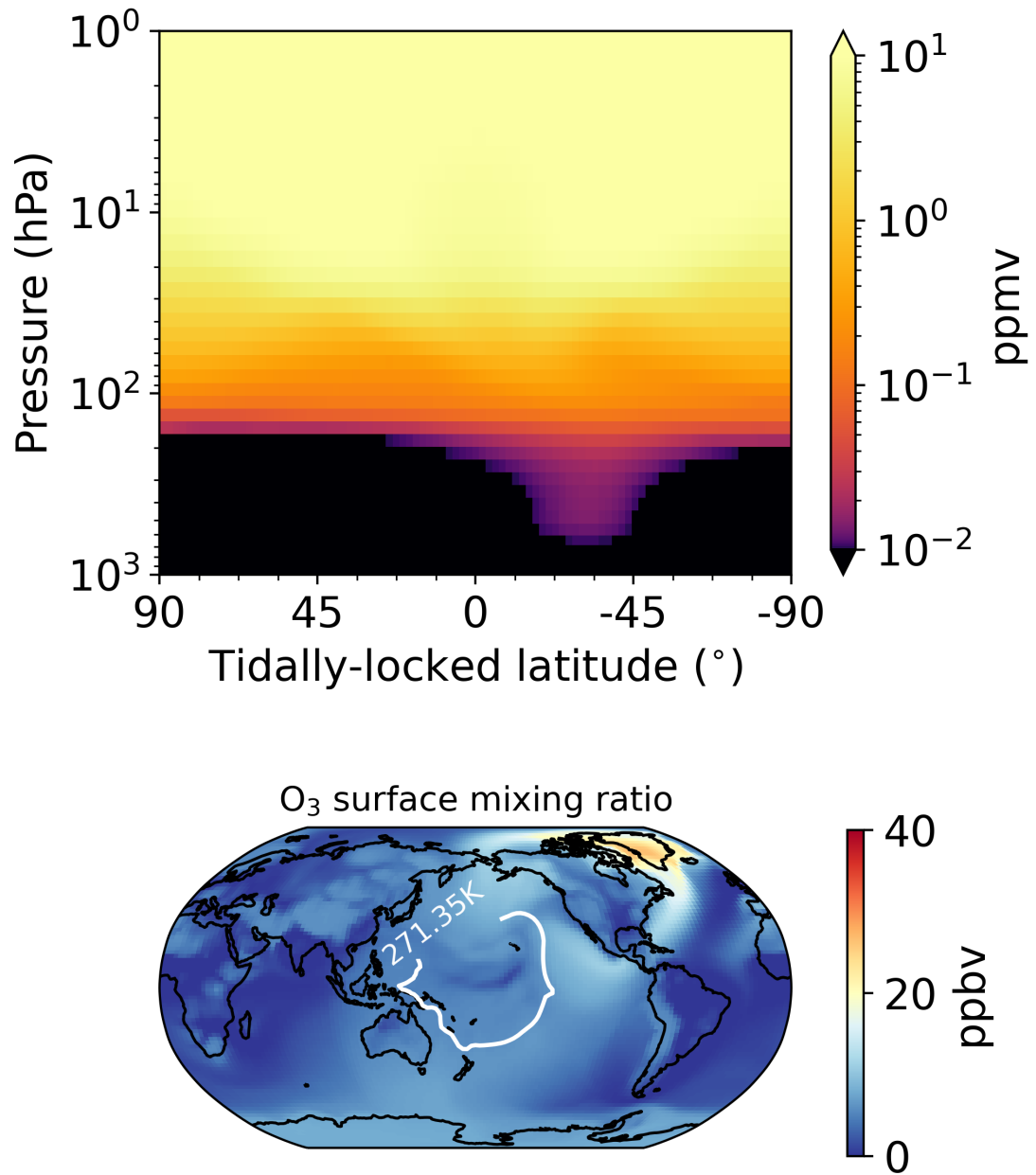
Figure 4.14: The top panel shows the O$_3$ transport from the stratosphere to the troposphere in the night-side gyre location in the TL coordinates. The bottom panel shows the surface ozone mixing ratio in parts per billion (ppb) in geographic coordinates, with a white contour highlighting the surface temperature above the freezing point.

Figure 4.14 shows the stratospheric and tropospheric O$_3$ mixing ratio (ppmv) in TL coordinates (top panel) and the surface O$_3$ mixing ratio in geographic coordinates (bottom panel). Compared to Braam et al. (2023b), we find a lower amount of O$_3$ ($\sim 10^{-2}$

ppmv) transported from the stratosphere to troposphere in the night-side Rossby gyre locations, and such transport can only occur in the northern hemisphere in our simulations. This discrepancy is likely due to the symmetry-breaking effect of including the Earth's topography and orography discussed in section 4.4.3 and in Sainsbury-Martinez et al. (2024). The bottom panel of Figure 4.14 shows the resulting surface O_3 mixing ratio is the highest in Greenland (26 ppbv), corresponding to the gyre location where the stratosphere-to-troposphere O_3 transport occurs in the northern hemisphere. The O_3 mixing ratio is < 40 ppbv anywhere on the surface, and hence the surface is exempt from the O_3 oxidizing stress according to our habitability metrics. Based on our results, if PC-b has a substellar point over the ocean, with a similar land-ocean distribution and atmospheric composition to Earth's, its day-side surface is likely to be partially habitable over the open ocean area.

4.5.2   Synthetic Spectra

In this study, we assume that PC-b is an Earth-like exoplanet with a radius of 6816.9 km and a surface gravity of 12.2 m s^{-2} (Table 4.1). This corresponds to a planetary mass of 1.425 $M_\oplus$, assuming the same density as Earth. The minimum estimated mass for PC-b is approximately 1.07 $M_\oplus$, based on an edge-on inclination orbit (Faria et al., 2022). Our assumed mass yields an inclination angle of 48.84°. However, the actual inclination angle of PC-b is unknown, and it is likely to orbit at a lower inclination, making its transit undetectable. PC-b may also have a highly eccentric orbit ($e > 0.1$) and be in a 3:2 orbital resonance, possibly due to gravitational interactions with other undetected planets in the system and with Alpha Centauri—the triple-star system that includes Proxima Centauri (Ribas et al., 2016). If the planet is not tidally-locked and has a non-zero eccentricity, tidal heating could play a significant role in its climate evolution and stability, further complicating the scenario (e.g. Driscoll et al., 2015; Colose et al., 2021). For simplicity, we assume that PC-b is in a tidally-locked orbit with an inclination angle of 90°, an eccentricity of 0, and an obliquity of 0°.

To demonstrate potential observables in the atmosphere of the PC-b case, we use the Global Emission Spectra application (GlobES) within the Planetary Spectrum Generator (PSG) to generate synthetic spectra based on WACCM6 3D outputs (more details about GlobES are provided in Chapter 1.3.9). In the PSG simulations, synthetic spectra are generated assuming an idealized telescope configured as a single-dish instrument with a resolving power of 250 over the wavelength range of 0.1 to 20 μm, covering the UV, visible, and infrared bands. For computational efficiency, we averaged our WACCM6 output data in the longitude by a factor of 4 (i.e., 36 longitudinal points instead of 144) before feeding it into PSG for radiative transfer calculations. To generate the synthetic transit spectra, we set the binning number to 10, which yields a total of 20 samples uniformly distributed over the terminator, and each sample has 70 vertical atmospheric layers. For the direct imaging spectra, we additionally averaged the latitude by a factor of 2 (i.e., 48 latitudinal points instead of 98), and with the same binning number, we have 15 samples over the observational disk. These modifications allow PSG radiative-transfer calculations to be faster without sacrificing too much accuracy.

There are a few other assumptions made in the PSG simulations. Firstly, we do not consider the Doppler effect in our analysis. Although the effect may be small for PC-b, given its proximity at 1.3 parsecs, it becomes relevant for high-resolution spectroscopic simulations and high-contrast imaging (HCI). Additionally, we do not account for stellar contamination in our models. In practice, high-contrast imaging (HCI) observations usually require a coronagraph to suppress starlight and isolate the planetary signal. Moreover, we treat the observation (transit spectroscopy and direct imaging) as a snapshot rather than continuous observations of the planet orbiting the star at different orbital phases. This means we do not compute the full ephemeris, which describes the planet's continuous motion in its orbit relative to the observer on Earth over time. Since we use an instantaneous snapshot, the planet's atmospheric and climatic conditions are assumed to be constant during the observation period, neglecting any temporal variations that may occur due to possible interannual oscillations similar to the Quasi-Biennial

Oscillation (QBO) as seen on Earth. Therefore, the synthetic spectra we present in this work are synthetic spectra in their simplest forms and can only represent the theoretical circumstances.

Figure 4.15 presents the synthetic transmission spectrum (0.1 to $25\,\mu m$) for the PC-b case, based on snapshot data from WACCM6 output on 2024/01-01 00:00 UT. We compared PC-b's spectrum to an Earth-Sun analogue positioned at the same distance (i.e., 1.3 parsec away). Seasonal variability in transit depth due to Earth's non-zero obliquity was verified to be minimal (less than 1 km); thus, we used a single snapshot to represent the Earth case. The upper panel displays the full spectrum for each case (solid lines), accounting for contributions from seven atmospheric molecules (N_2, H_2O, O_2, O_3, CO_2, N_2O, and CH_4), as well as effects from cloud liquid and ice droplets, Rayleigh scattering, and collision-induced absorption (CIA). Major absorption features are labelled at their corresponding wavelengths. The most prominent absorption feature in the PC-b case, exceeding 50 km in transit depth, is from O_3 around $0.25\,\mu m$ in the Hartley band, amplified by the Rayleigh scattering effect in the baseline. At longer wavelengths, where Rayleigh scattering becomes weaker and nearly constant, the O_3 feature at $9.8\,\mu m$ shows a smaller transit depth (~ 25 km). CO_2 absorption features at $4.2\,\mu m$ and $15\,\mu m$ are the second largest, with depths of ~ 35 km. The contribution of H_2O to the full spectrum is minor due to PC-b's cold surface temperature, which limits atmospheric water vapor. The H_2O infrared band between 5 and $7\,\mu m$ has a transit depth of about 5 km, comparable to the CH_4 features at 3.3 and $7.5\,\mu m$. Vertical gray bars in the upper panel indicate transit depths in ppm (10, 20, and 30 ppm). Considering the James Webb Space Telescope's (JWST) optimistic noise floor of 5–10 ppm (i.e., 3.5–7 km) (e.g. Schlawin et al., 2020), all absorption features in the PC-b case are within the theoretical detection limit, with O_3 at $0.25\,\mu m$ providing the strongest signal.

The dashed lines in the upper panel represent baselines from Rayleigh scattering and CIA (notably between 4 and $5\,\mu m$). PC-b's baseline is lower (~ 7 km) compared to Earth's, primarily due to PC-b's colder temperature and higher surface gravity, which reduces the

141

atmospheric scale height and compresses its atmosphere. The middle panel decomposes the full spectrum into individual contributions from key atmospheric constituents for each case, while the bottom panel highlights the differences between PC-b and Earth. Despite PC-b's lower baseline, its O_3, CO_2, and H_2O absorption features are weaker than Earth's. The largest differences occur for O_3 between 0.2 and 0.3 µm (~ 12 km) and CO_2 between 4 and 5 µm (~ 10 km). While the weaker CO_2 absorption is attributed to temperature differences, the reduced O_3 and H_2O features are due to lower mixing ratios in PC-b's atmosphere. As a result, the absorption features in the PC-b's transit spectrum are more challenging to observe compared to Earth's, despite the smaller planet-star radius contrast enabling deeper probing of its atmosphere.

Figure 4.16 presents the synthetic reflection spectra (0.1 to 3 µm) and emission spectra (3 to 20 µm) for the PC-b case, compared against the Earth case at three orbital phases: $\phi = 90°$, $270°$, and $350°$. The first two phases ($90°$ and $270°$) correspond to quadrature, where half of the planet's surface along the line of sight is illuminated by the host star, while the other half remains in darkness. The phase $\phi = 350°$ occurs just before the planet enters its secondary eclipse, when the entire illuminated dayside hemisphere is visible from an observer on Earth. Key absorption features are labelled using the same decomposition method as in Figure 4.15.

The direct imaging spectra of PC-b exhibit baselines approximately three orders of magnitude higher than those of the Earth case, primarily due to differences in the stellar luminosity. As an M dwarf, Proxima Centauri has a much lower bolometric luminosity than the Sun ($L_{\text{star}} \approx 0.0015 L_{\odot}$) (e.g. Ribas et al., 2017), and in practice, a coronagraph would be necessary to enhance the planet-to-star contrast for directly imaging Earth-like exoplanets around Sun-like stars. For the idealized reflection spectra, the most prominent absorption features, along with the largest planet-to-star contrast, arise from O_3 in the Hartley band between 290 and 350 nm, as well as H_2O and CO_2 between 2.5–3 µm at $\phi = 350°$. Due to the small variations in surface temperature on PC-b, the emission spectrum shows minimal differences between orbital phases, except for a slightly elevated
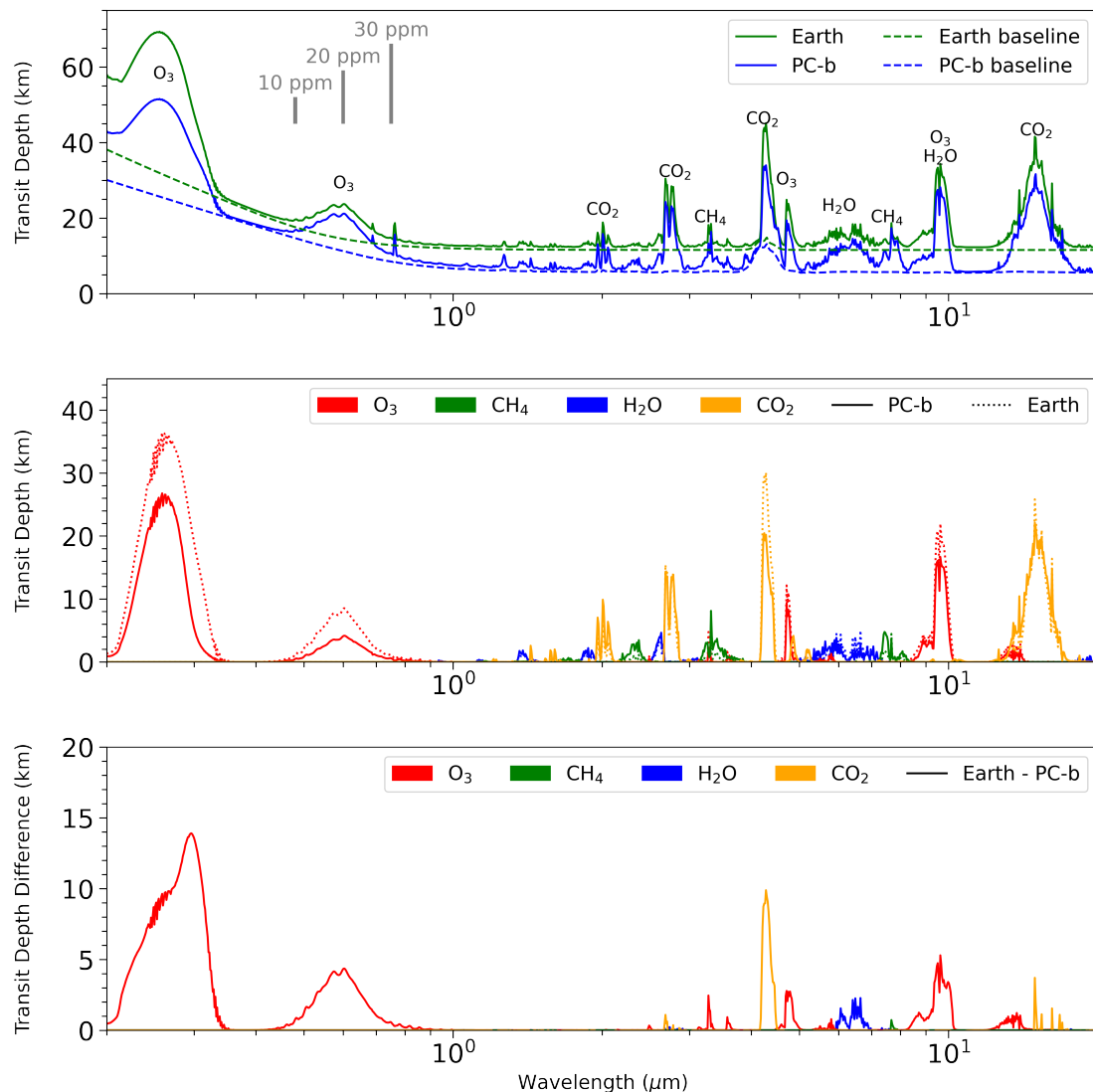
Figure 4.15: Idealized transit spectra for the PC-b case compared against the Earth case. The upper panel displays the full spectra, which includes contributions from seven molecules (N_2, H_2O, O_2, O_3, CO_2, N_2O, CH_4), cloud liquid and ice droplets, and the effect of Rayleigh scattering and collision-induced absorption (CIA). Major absorption features are labelled at their corresponding wavelengths. The dashed lines indicate the baselines due to Rayleigh scattering and CIA for both cases. The vertical grey bars indicate the corresponding transit depths in units of ppm, with values marked at 10 ppm, 20 ppm, and 30 ppm. The middle panel decomposes the full spectra into individual key atmospheric constituents for both cases, highlighting the contribution of each to the overall absorption features. The bottom panel shows the transit depth difference of the key atmospheric constituents between the PC-b case and the Earth case.
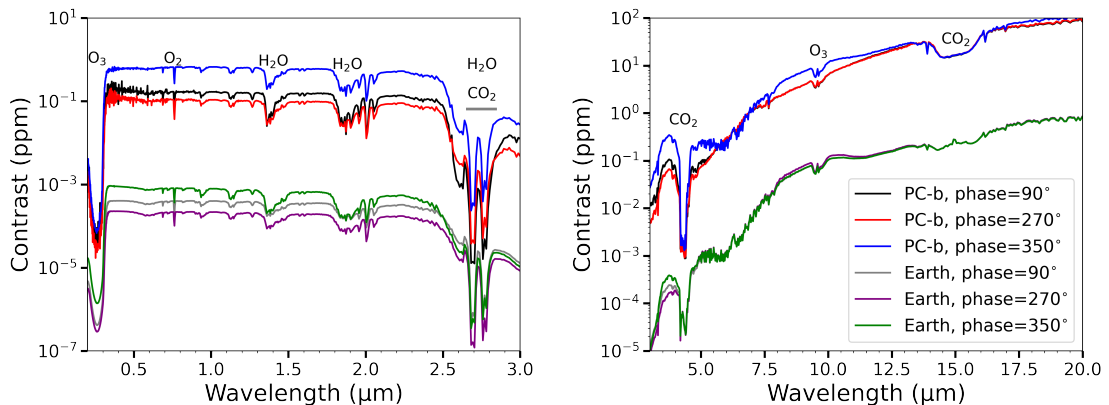
Figure 4.16: Synthetic reflection spectra (left panel) and emission spectra (right panel) for the PC-b case compared against the Earth case in three orbital phases (i.e., 90, 270 and 350 degrees). The y-axis represents the relative flux contrast between the planet and its host star in parts per million (ppm). Major absorption features are labelled with their corresponding molecules.

baseline at $\phi = 350°$, attributed to a larger portion of the planet's illuminated hemisphere facing the observer. CO_2 dominates the absorption features between 14–16 µm, while the O_3 absorption feature at 9.6 µm is relatively weak. Compared to the Earth case, the CO_2 absorption features in the emission spectra exhibit noticeable differences. The PC-b case lacks the characteristic spikes at approximately 4.3 and 15 µm associated with CO_2 absorption, indicating an absence of sufficient O_3 to heat the stratosphere (e.g. Rugheimer et al., 2018).

4.6 Conclusions

In this study, we utilized the Whole Atmosphere Community Climate Model Version 6 (WACCM6) to simulate Proxima Centauri b (PC-b) in a tidally-locked orbit with the substellar point over an ocean surface, assuming an Earth-like atmosphere, topography, and orography. Specifically, we analyzed the climate, atmospheric circulation, ozone chemistry, surface habitability, and observability for this specific case of PC-b (PC-b). Our findings indicate that the PC-b case exhibits a significantly colder climate than the pre-industrial Earth case. This difference can be attributed to lower stellar irradiance, higher surface albedo, weaker cloud radiative effects, and reduced greenhouse

effects compared to the Earth case. Our results agree with similar work that PC-b can retain a dayside open ocean despite the global mean freezing temperature. We find that the stratospheric O_3 layer in the PC-b case is substantially weaker than in the Earth case due to the lower atomic oxygen produced by the weaker photolysis of O_2 and the weaker UV radiation of Proxima Centauri. The spatial distribution of the stratospheric O_3 layer is driven by the asymmetric stratospheric polar jets between the north and south hemispheres, which trap more O_3 around the south pole. For assessing surface habitability, we considered surface O_3 levels as an additional metric and found that no lethal O_3 concentration is present at the surface. We also noticed some deviations from other studies of PC-b in terms of surface temperature, cloud coverage, greenhouse gas concentrations, and atmospheric circulations. These discrepancies are likely attributable to differences in surface albedo and cloud parameterizations and the inclusion of ocean dynamics and Earth's topography in our model.

To investigate the observability of PC-b, we employed the Planetary Spectrum Generator (PSG) to compute correlated-k radiative transfer using the climate outputs from WACCM6. However, our approach includes several caveats, including the assumption of an idealized telescope and the use of only single-snapshot climate data, which excludes potential temporal variability in climate and atmospheric dynamics. Overall, we find that O_3, centred at 0.25 μm, dominates the absorption features in the synthetic transit spectrum (exceeding 71 ppm), largely due to the overlapping H_2O absorption band and the effects of Rayleigh scattering. H_2O primarily influences the synthetic reflection spectrum in the near-infrared, particularly between 1.3–1.5 μm and 1.8–1.95 μm. However, because of the relatively low planet-to-star irradiance contrast at these wavelengths, all features remain well below 1 ppm. In the synthetic emission spectrum, CO_2, centred at 15 μm, produces the largest feature for direct imaging, exceeding 15 ppm.

We encourage future follow-up studies to examine the detectability of PC-b using existing state-of-the-art telescopes like the James Webb Space Telescope (JWST) (e.g. Kreidberg et al., 2016; Snellen et al., 2017; Meadows et al., 2017) and the Extremely Large Tele-

scope (ELT) (e.g. Vaughan et al., 2024), as well as conceptual telescopes such as HWO (e.g. Meadows et al., 2017) and LIFE (e.g. Angerhausen et al., 2024), making direct comparisons with these studies. Additionally, inferring the presence of dayside open oceans from the gradual reduction in albedo as the open ocean comes into view may be plausible using thermal emission spectra and thermal phase curves (e.g., Pierrehumbert, 2011), warranting further investigation. Moreover, this study does not consider alternative atmospheric compositions, land/ocean distributions, or orbital configurations that could induce different climate, dynamics, and chemistry and potentially affect observable features compared to the case we focused on here.

Chapter 5

Conclusion

5.1 Summary

In this thesis, I use WACCM6, a fully coupled Earth system model, to perform climate simulations for planets in different orbital configurations, and PSG, a radiative transfer model, to synthesize theoretical spectra based on the outputs from WACCM6. This thesis consists of three science chapters that address the climate, chemistry, potential surface habitability and observability of Earth-like and Earth-analogue exoplanets with varying orbital parameters. In this summary, we can divide the research into two major parts. The first part focuses on the effects of the orbital eccentricity of Earth-analogue exoplanets around Sun-like stars, covered in Chapters 2 and 3 of the thesis, while the second part focuses on a case study of the exoplanet-Proxima Centauri (PC-b) in a tidally-locked orbit Chapter 4.

5.1.1 Eccentric orbits

Climate and implications on habitability

Terrestrial exoplanets around Sun-like stars (i.e., G-type stars) are expected to have an occurrence rate of approximately 0.01 to 2 according to data from the Kepler mission (e.g.

Burke et al., 2015; Bryson et al., 2021). The large uncertainty is due to the limited sample size of detected planets and the challenge of constraining the planet radii and stellar parameters from measurements. Recent observational statistics from Kepler and TESS space telescopes have shown that terrestrial planets with highly eccentric orbits ($e > 0.1$) are relatively common outside our solar system. The most eccentric terrestrial exoplanet identified to date is Kepler-409 b (Bonomo et al., 2023), with $e < 0.69$, $R_p = 1.199 R_\oplus$ and $M_p < 6 M_\oplus$. Among 967 confirmed terrestrial exoplanets, 56 have highly eccentric orbits, indicating $\sim 6\%$ of terrestrial planets have $e > 0.1$. While the occurrence rate of the highly eccentric terrestrial worlds is low ($\sim 6\%$) compared to other exoplanet types ($\sim 22\%$) for other exoplanet types, it is likely to be an observational bias caused by the current detection limits.

Previous studies using 1D climate models suggest that the long-term climate states of a highly eccentric Earth-like exoplanet primarily depend on the average stellar flux received over an entire elliptical orbit, known as the mean flux approximation (Williams et al., 2002). The mean flux approximation means that the seasonal temperature variations caused by a highly eccentric orbit are unlikely to be strong enough to drive a stable temperate climate state to another (e.g., snowballing or runaway greenhouse state). Multiple studies using 1D and 3D simulations have found that increasing orbital eccentricity will not transform an Earth-like exoplanet to a different climate state, but the higher eccentricity can result in higher global mean surface temperatures and stronger seasonal variations which extend the outer edge of the habitable zone (Williams et al., 2002; Way et al., 2017b; Dressing et al., 2010; Linsenmeier et al., 2015; Liu et al., 2023; Way et al., 2023; Biasiotti et al., 2024). These simulation results generally agree with what the analytical approach predicts (Quirrenbach, 2022; Ji et al., 2023). However, it is important to note that the mean flux approximation becomes less reliable for tidally-locked Earth-like planets as surface liquid water may not persist for the entire course of a highly eccentric orbit (Bolmont et al., 2016), though the tidal-locking effect can circularize the eccentric orbits of exoplanets around low-mass ($\simeq 0.1 M_\odot$) to solar-mass stars ($\simeq 1 M_\odot$)

well within the lifetime of the stellar system (< 10 Gyr).

The climate response to a temporally varying stellar irradiance (i.e., seasonality) is not instantaneous. The time it takes for the planetary atmosphere to adapt to changes in radiation, known as the atmospheric radiative timescale, can be influenced by many factors such as the planet's equilibrium temperature, the atmosphere mass, the surface thermal inertia, the orbital period, the rotation rate and orbital eccentricity (Donohoe et al., 2014; Guendelman et al., 2019; Adams et al., 2019; Ohno et al., 2019a; Guendelman et al., 2020; Guendelman et al., 2022; He et al., 2022; Ji et al., 2023). To gain insights into how eccentricity itself can affect the annual mean climate and the seasonality for Earth-like exoplanets around Sun-like stars, we fix the stellar irradiation received at the top of the planetary atmosphere in our simulations. For this purpose, we set up two simulation cases: one with an eccentricity of 0.4 ($e = 0.4$) and one with a circular orbit ($e = 0$), both with zero obliquity. The choice of an eccentricity of 0.4 represents an upper limit for terrestrial exoplanets, and we expect that an eccentricity smaller than this value will induce less pronounced seasonality.

Using the Earth System Model (WACCM6), we investigated the spatial and temporal variations in many planetary attributes associated with the hydrological cycle (e.g., sea ice, land snow, and cloud) to explore a more nuanced view of land habitability than global mean surface temperature alone. The eccentric case has a small increase in the annual global mean surface temperature (> 1.9 K) compared to its circular counterpart. If the global mean surface temperature were the only metric used, we might conclude that both configurations sit within the habitable zone and are equally habitable. However, the temporal variation of stellar irradiance is nonlinear, which is up to 2.5 times more intense than the annual mean during the hot period of the eccentric orbit (February, March and April, hereafter referred to as the 'hot period') and is only about half of the annual mean during the rest of the orbital period. The temporally varying stellar irradiance has more pronounced effects in the northern hemisphere than in the southern hemisphere. During the hot period, a sharp increase in surface temperature is found in the northern

hemisphere. Since the exoplanet we simulate has the same land and ocean distribution as Earth's, the northern hemisphere (NH) is land-dominated and has a lower heat capacity than the ocean-dominated southern (SH). The increased surface temperature in NH triggers a positive feedback loop of sea ice and land snow coverage, in which a significant reduction of effective land snow coverage (4.8%) results in a subsequent decrease in surface albedo and further increases the temperature.

In addition, we find that NH also experiences a larger decrease in the low-level cloud coverage during the hot period due to the higher NH temperature and hence lower water vapor condensation rates. The higher tropospheric temperature in NH also indicates a higher water vapor mixing ratio and a longer water vapor lifetime, which enhances the water vapor greenhouse effects in the NH equatorial to mid-latitudes. In the SH, the surface temperature is colder than in NH during the hot period, and an increased mid-latitude cloud albedo due to a higher amount of cloud water is found to further contrast the hemispherical temperature difference. Clouds can not only cool the planet by reflecting stellar radiation into space but also warm the surface by absorbing the outgoing longwave radiation from the surface. During the hot period, a tropical cloud gap appears due to the higher temperature. As the planet moves further away from the host star, the water vapor in the upper troposphere condenses into a wider band of high clouds due to the cooler tropospheric temperature. The high-level cloud gap during the hot period reduces the cloud warming effect, and the wider high-level cloud band in the colder phases of the $e = 0.4$ orbit warms the planet. The two opposing effects are also not linear due to the nonlinear temporal variation of the stellar irradiance, which the net effect is a slight decrease (1W m^{-2}) in the annual global mean longwave cloud warming. However, the reduced longwave cloud warming effect is small in the global energy budget and outweighed by the increased shortwave cloud cooling effect associated with low-level cloud reduction in the NH. Overall, the warmer global annual mean surface temperature in the $e = 0.4$ case is due to the temporally varying stellar irradiance and a larger NH climate sensitivity described by the feedback loops in the hydrological cycles (i.e., surface

albedo, cloud radiative effects and greenhouse effects).

Assessing the habitability of an exoplanet is a complex process involving multiple factors and varying definitions (e.g. Cockell et al., 2016). In this study, we employ a simplified Earth-centric habitability metric that focuses solely on two key parameters: surface temperature and precipitation over land. For the surface temperature criterion, we set the lower limit to 273 K, corresponding to the freezing point of water at 1 bar atmospheric pressure, and the upper limit to 323 K, representing the threshold above which Earth's biodiversity significantly decreases (Clarke, 2014). Similarly, to account for biodiversity, we adopt the accumulative precipitation limits defined by He et al. (2022), requiring annual precipitation over land to exceed 30 cm. A comparison of land habitability reveals distinct patterns in the $e = 0.4$ case. The land surface temperature habitability increases at high latitudes but decreases in equatorial regions due to extreme temperatures following perihelion and aphelion in the orbit. Enhanced precipitation habitability in the $e = 0.4$ case results from a more evenly distributed large-scale accumulative precipitation over land. Using the combined habitability metric reveals that the land habitability in the $e = 0.4$ case surpasses the circular case for over 80% of the orbital period, with an increase of $> 7\%$ averaged over all number of months that meet the habitability criteria. These changes are closely tied to the shift in meridional circulation patterns in the $e = 0.4$ case. During the orbit's hot phase, the circulation transitions from an Earth-like three-cell structure to a two-cell configuration, with the Hadley cell expanding toward $50°$ in both hemispheres. The annual mean Hadley cell weakens in this case, leading to reduced total precipitation in the tropics but increased large-scale precipitation accumulation in mid to high latitudes.

The significantly higher surface temperatures during the hot period raise concerns about the timescale for water loss and its impact on long-term habitability. In the $e = 0.4$ case, the annual global mean water vapor mixing ratio in the stratosphere exceeds 20 ppmv—about five times higher than the 4 ppmv observed in the circular orbit—due to increased photolysis during the hot period. Assuming water loss occurs mainly through

thermal escape and disregarding other mechanisms like non-thermal escape and impact erosion, the ocean loss rate in the $e = 0.4$ case is approximately three times faster than in the circular orbit. However, this loss rate suggests that such a highly eccentric Earth-like planet could retain its water reservoir over the system's lifetime, suggesting that long-term habitability is unaffected by the higher water loss. We conclude that, under the same annual mean stellar flux, an Earth-analogue planet with zero-obliquity in a highly eccentric orbit ($e = 0.4$) around a Sun-like star may have enhanced land habitability compared to its circular counterpart and can retain its atmosphere despite the higher water loss rates.

Synthetic transmission spectra

Using the Planetary Spectrum Generator (PSG) with an idealized telescope and a constant spectral resolving power of 250, we calculated the transit spectra in the UV, visible, and infrared regions (0.2 to 20 µm) to determine observable differences in water abundances between two cases: one with an eccentricity of 0.4 and one with a circular orbit. For the eccentric case, climate snapshots were taken on April 16 and November 12 to represent the hottest and coldest days, respectively, with varying planet-star separations (1.03 au and 1.2 au). For the circular case, a snapshot was taken on April 16 at a fixed 1 au separation. The atmospheric composition included N_2, H_2O, O_2, O_3, CO_2, N_2O, and CH_4. The spectra revealed significant absorption features, particularly for H_2O, CO_2, and O_3, with notable differences in transit depths due to seasonal and orbital variations.

The most prominent H_2O absorption feature was observed at 2.6 µm with a transit depth of approximately 37 km. Additional water absorption features were noted at 1.36 µm, 1.87 µm, 2.7 µm, and between 5.93 µm and 6.64 µm. For CO_2, the major absorption features were found at 4.8 µm and 15 µm, with transit depths of 55 km and 50 km, respectively. The largest O_3 absorption feature appeared at 0.25 µm in the UV region, with a transit depth of 65 km, and other significant features at 0.6 µm in the visible

region and around 9.6 µm in the infrared region.

Seasonal variations in the eccentric orbit significantly influenced the absorption features. On April 16, the higher temperatures led to increased H_2O) evaporation and a more inflated atmosphere, resulting in stronger water absorption features. The presence of seasonally varying clouds in the eccentric case also affected the baseline transit depths, although their effect was smaller than that of changes in temperature. Compared with the circular case, the eccentric case showed more pronounced changes in absorption features. The H_2O features were generally stronger on April 16 in the eccentric case compared to November 12 and the circular case due to higher temperatures and increased H_2O vapor abundance. Even on the coldest day (November 12), slightly stronger H_2O absorption features were observed in the eccentric case compared to the circular case. This is because the large amount of water vapor evaporated on April 16th can travel upward and remain in the stratosphere and mesosphere due to the slow advection speed.

The O_3 column density showed a 3% annual mean decrease in the eccentric case compared to the circular case, with up to 13% seasonal variation. Despite this decrease, stronger O_3 features are observed on April 16 in the eccentric case due to higher atmospheric temperatures, which increase O_3 absorption cross-sections. This resulted in stronger O_3 absorption features despite a lower O_3 column density compared to other periods, indicating a possible degenerate interpretation from future observations.

The analysis of the transit spectra revealed significant CO_2 absorption features at 4.8 µm and 15 µm. These features exhibited more notable seasonal differences in the eccentric orbit than the differences between the eccentric and circular orbit cases. The seasonal variation in the CO_2 transit features was approximately 6 km between the hottest (April 16) and coldest (November 12) days in the eccentric case. Unlike H_2O and O_3, CO_2 absorption features in the transmission spectra correlate better with temperature.

This study investigates and quantifies the climate differences between highly eccentric and circular orbits for an Earth-analogue planet orbiting a Sun-like star. We showed

and explained the surface temperature differences between the two cases by offering a comprehensive view into the surface albedo, cloud radiative effects and meridional circulation patterns. Adopting the surface temperature and the land precipitation criteria for assessing land surface habitability, we found that eccentric orbits can be super-habitable compared to circular orbits. Our synthetic transmission spectra highlight the theoretical observables at different orbital phases, suggesting that planets in eccentric orbits could be prime targets for future transmission spectroscopy observations to confirm or refute the presence of atmospheric water vapor. These insights contribute to the current understanding of the climate and habitability of highly eccentric rocky exoplanets.

5.1.2   Case study of PC-b

M dwarfs are believed to be the most common type of stars in our Galaxy due to their long lifespans (Adams et al., 1997; Bochanski et al., 2010). There is currently no statistical evidence from Kepler's data for more Earth-sized exoplanets in the habitable zone of M dwarfs than FGK dwarfs (Bergsten et al., 2023). However, the habitable zones of M dwarfs are closer to the star, increasing the probability and frequency of transits, as well as the amplitude of the induced radial-velocity variation, making these planets ideal targets for detection and characterization (e.g. Wunderlich et al., 2019). Due to the proximity of the habitable zone around M dwarfs, the terrestrial exoplanets around M dwarfs are likely to be in tidally-locked orbits (e.g. Barnes, 2017). A tidally-locked orbit causes one hemisphere of the planet to always face the star while the other hemisphere remains in permanent darkness. This unique configuration can lead to extreme variations in climate, atmospheric circulations and chemistry. Proxima Centauri b (PC-b), the closest exoplanet to our solar system (~ 1.3 parsecs), is a prime candidate for studying the effects of the tidally-locked orbits.

In this work, we simulated a specific case for PC-b using a fully-coupled Earth System Model-WACCM6. Details for the model configurations can be seen in the Methods section in Chapter 1. Overall, we performed a comparative analysis for the PC-b case

with the sub-stellar point over ocean (STP$_{ocn}$) with the pre-industrial Earth case (PI) to highlight how the climate of PC-b deviates from the world that we are familiar with. Specifically, we analyzed the climate, atmospheric circulation, ozone chemistry, surface habitability, and observability for the STP$_{ocn}$ case. We find that understanding the atmospheric circulation is important to explain the climate behaviours in the tidally-locked STP$_{ocn}$ case.

Primary climate diagnostics

The STP$_{ocn}$ case exhibits a significantly colder climate than the pre-industrial Earth case (PI), which can be attributed to lower stellar irradiance, higher surface albedo, weaker cloud radiative effects, and reduced greenhouse effects compared to the PI case. We find that an "eyeball-shaped" open ocean is possible on the day-side hemisphere despite the global mean cold temperature, which is similar to the findings in previous work (Turbet et al., 2016; Boutle et al., 2017; Lewis et al., 2018; Del Genio et al., 2019; Salazar et al., 2020b; Galuzzo et al., 2021). We notice an eastward shift of the maximum day-side surface temperature (278 K) from the substellar point due to the tropospheric super-rotating jet stream in the equatorial region for the STP$_{ocn}$ case. Differences in the simulated day-side and night-side surface temperatures are found compared to other work with a similar model setup (Boutle et al., 2017; Del Genio et al., 2019). For example, the lower day-side and night-side surface temperature compared to Del Genio et al. (2019) arises from the different land surface albedo treatments, and the lower day-to-night surface temperature contrast compared to Boutle et al. (2017) is likely due to the inclusion of ocean dynamics.

In addition to the surface albedo, we analysed and compared the cloud radiative effects and the clear-sky greenhouse warming effect in the STP$_{ocn}$ case with the PI case and the literature. We specifically demonstrated the low-level, mid-level and high-level clouds regarding their spatial distribution and radiative effects. The low-level cloud blankets almost the entire planet, covering both the day-side and night-side hemispheres because

of the strong day-to-night overturning circulation in the lower troposphere. The day-side low-level cloud contributes to a large portion of the reflected shortwave radiation because of its high water content, originating from wind-driven evaporation in the annular region around the substellar point. Conversely, the night-side low-level cloud does not form locally due to the colder temperatures and limited atmospheric water vapor. Instead, It comes from the tropospheric overturning divergent circulation and the tropospheric eastward equatorial jet stream, where water vapor is transported from the day-side to the night-side at higher atmospheric level. Hence, the night-side cloud is optically thin due to limited water content, and it is radiatively inactive due to the absence of stellar irradiation in the night-side hemisphere. The day-side and night-side cloud spatial distribution is similar to the findings in Boutle et al. (2017).

Clouds on PC-b can not only reflect shortwave from the host star but also absorb it. The increased shortwave cloud absorption in the STP_{ocn} case is due to the enhanced cloud water absorption from the stronger near-infrared radiation emitted by the M dwarf - Proxima Centauri. The net effect of the global mean reflection and absorption in shortwave (C_{SWF}) is positive (3.4 W m^{-2}), which differs from the largely negative shortwave cloud forcing (-32 W m^{-2}) in Del Genio et al. (2019). This could be due to the different cloud parameterizations adopted between the models. Considering the longwave cloud warming effect, the STP_{ocn} case has a global mean C_{LWF} of 6.7 W m^{-2}. C_{LWF} is predominantly positive in the day-side hemisphere, where the high-level cloud is present due to the deep convection of the upwelling overturning circulation around the substellar point. The high-level cloud exerts a strong longwave warming effect by absorbing the upwelling longwave radiation from the surface and emitting it at its colder temperature. Interestingly, we find that the greenhouse warming effects of the night-side cloud can be reversed due to the vertical temperature inversion in the night-side hemisphere. The cloud layer in the night-side hemisphere is warmer than the surface and hence acts as a "radiator fin" for effective night-side cooling, which is similar in Yang et al. (2014) and Del Genio et al. (2019). Additionally, we find that the "radiator fin" is active in a spe-

cific region in the night-side hemisphere following the path of day-to-night water vapor transport. The clear-sky greenhouse effect for the STP_{ocn} case is only 9 W m^{-2}, which is significantly lower than that for the PI case (135 W m^{-2}). The reduced clear-sky greenhouse effect is mainly due to lower water vapor concentrations in the STP_{ocn} case from the colder surface temperature. Similar to the night-side reversed cloud longwave forcing, there is an anti-greenhouse effect of -20 Wm^{-2} from water vapor due to the night-side temperature inversion.

Atmospheric circulation

As we concluded above, the spatial variations in the surface temperature, cloud coverage, cloud radiative effects and greenhouse effects are significantly influenced by the unique atmospheric circulation of PC-b. Thus, it is necessary for us to look more closely at the circulation patterns. On a tidally-locked exoplanet such as PC-b, the large day-to-night temperature and pressure gradients can induce strong atmospheric circulation, modified by the horizontal temperature gradients and the Coriolis force due to the slower planetary rotation rate. We find that the STP_{ocn} case belongs to the Rhines rotation dynamical regime according to the definition given in Haqq-Misra et al. (2018). The Rhines rotation regime is a transition between the fast and slow rotation regimes, characterized by the temperature-driven day-to-night global circulation and the emergence of turbulence-driven zonal jet streams. For the day-to-night overturning circulation, we show the meridional mass stream function in the geographic coordinates and in the tidally-locked (TL) coordinates. Unlike in geographic coordinates, in which the circulation can only be accurately represented by showing separately in the northern and southern hemispheres and the day-side and night-side hemispheres, the TL coordinates can represent the day-to-night overturning circulation in a single cell. Compared with Braam et al. (2023b), the maximum circulation strength in our case is two orders of magnitude lower (10^{12} kg s^{-1} vs. 10^{14} kg s^{-1}). Additional differences between our case and Braam et al. (2023b) are found for the location where the night-side downwelling

circulation occurs. Braam et al. (2023b) shows that the downwelling branch occurs in the Rossby gyre location at $-30°$ TL latitude but not in the anti-substellar point. However, we find a weaker downwelling circulation occurs at the AP and a stronger downwelling wind in the gyre location. The weaker circulation strength in our case can result from a smaller meridional surface temperature gradient, possibly due to the finer model horizontal resolution and the inclusion of ocean dynamics. The locations of the downwelling circulation branch are related to the symmetry-breaking effect (Sainsbury-Martinez et al., 2024) from including the ocean/land distribution in our case compared to the slab ocean model adopted in Braam et al. (2023b).

Besides the meridional stream function, we also analysed the jet streams from the zonal mean zonal wind. For the PI case, a pair of mid-latitude zonal wind jets are found in the troposphere, and asymmetric polar wind jets are found in the stratosphere. For the STP_{ocn} case, we found a single super-rotating jet stream in the equatorial region in the troposphere and another super-rotating jet in the mid-latitudes in the stratosphere. This differs from Carone et al. (2018), in which they show exoplanets with $P_{orb} \leq 25$ days can have either a strong equatorial eastward super-rotating jet or no equatorial jet in the stratosphere depending on the assumptions for the stratosphere wind breaking. This is likely due to the exclusion of the stratospheric wave breaking from the weaker extratropical Rossby waves, the gravity waves from the Earth's orography, and/or turbulence-driven processes that can contribute to the stratospheric jet formation.

Stratospheric ozone layer and surface habitability

In this study, we find that the atmospheric circulation patterns and the photochemistry are important to determine the spatial distribution of ozone (O_3) concentrations in the stratosphere. The global mean O_3 column density in the STP_{ocn} case is 188 DU which is significantly lower than in the PI case (275 DU). The difference is mainly due to a lower photolysis rate from the lower stellar UV radiation of Proxima Centauri, a lower

O mixing ratio resulting from the photolysis of less stratospheric water vapor in the STP_{ocn} case. Additional factors that contribute to the lower stratospheric O_3 in the STP_{ocn} case are the lower stratospheric temperature which slows the reaction rate of O_3 production and lower mixing ratios of the catalysts such as HO_x and NO_x. The spatial distribution of the stratospheric O_3 layer is driven by the asymmetric stratospheric polar jets between the north and south hemispheres, which trap more O_3 around the south pole. The driver of the North-South hemispherical asymmetry is explained in more detail in Sainsbury-Martinez et al. (2024). We found that the stratospheric O_3 can transport to the troposphere through the Rossby gyre in the night side at about $-30°$ latitude in the TL coordinates, similar to the findings in Braam et al. (2023b).

For assessing surface habitability, we considered surface O_3 levels as an additional metric (Cooke et al., 2024) and found that no lethal O_3 concentration (40 ppbv) is present at the surface. The highest surface O_3 is found in Greenland (26 ppbv), corresponding to the gyre location where the stratosphere-to-troposphere O_3 transport occurs in the northern hemisphere. Thus, the planetary surface is safe from the O_3 oxidizing stress. Together with the day-side open ocean, we concluded that the sub-stellar point of PC-b is likely to be habitable given the simplified habitability metric.

Synthetic spectra

To investigate the observability of PC-b, we employed the Planetary Spectrum Generator (PSG) to compute line-by-line radiative transfer using the climate outputs from WACCM6. Similar to the eccentricity studies in Chapter 2 and Chapter 3, we assumed an idealized telescope and used a single snapshot of climate data. Overall, we find that O_3, centred at 0.25 µm, dominates the absorption features in the synthetic transit spectrum (> 50 km or 71 ppm). This is because of the overlapping H_2O absorption band and the effects of Rayleigh scattering. H_2O features are dominant in the near-infrared of the synthetic reflection spectrum, particularly between 1.3–1.5 µm and 1.8–1.95 µm. However, because of the relatively low planet-to-star irradiance contrast at these wave-

lengths, all absorption features are less than 1 ppm in the reflection spectrum. In the synthetic emission spectrum, CO_2, centred at 15 µm, produces the largest feature for direct imaging, exceeding 15 ppm.

5.2 Future work

Building on the findings presented in my thesis, several promising avenues of research remain to be explored. In this section, I propose future directions that may further contribute to understanding how orbital parameters affect the climate, habitability, and observability of terrestrial exoplanets. Additionally, I suggest future directions for model development to better address these questions.

1. For our eccentricity studies, we specifically examined two cases: zero obliquity with eccentricities of 0.4 and 0. These cases are upper and lower bounds for climate outcomes across other potential eccentricities (e < 0.4). The upper eccentricity limit is conservative and based on current observational data. It would be valuable to explore higher eccentricities (i.e., e>0.6) to understand whether an Earth-like planet can sustain a stable climate, enter a snowball state, or transition to a runaway greenhouse effect, given the complex interaction between external solar forcing and internal feedback mechanisms.

2. Eccentricity is not the only factor that can induce seasonality; other orbital parameters, such as obliquity and the longitude of perihelion, can also significantly affect climate. These factors can modulate the distribution of stellar radiation across the planetary surface, influencing the intensity and duration of seasons and impacting the climate and potential habitability (Linsenmeier et al., 2015; Ohno et al., 2019b; Kang, 2019; Colose et al., 2019; He et al., 2022; Jernigan et al., 2023). Future research should investigate the effects of these factors using fully coupled GCMs. Such studies could be compared with previous research to better assess the diversity of climates on Earth-like terrestrial exoplanets and refine the predictions

of their potential to support life.

3. Our work on the effects of eccentricity does not account for the evolution of a planet's atmosphere, topography, and stellar radiation over geological timescales. For instance, Earth's topography has evolved dramatically due to plate tectonics and volcanic activity, leading to different configurations such as large supercontinents surrounded by oceans (e.g. Nance, 2022). Additionally, stellar luminosity increases as a star evolves along the main sequence, which can significantly impact planetary climate and habitability (e.g. Wolf et al., 2015). Orbital elements such as eccentricity, obliquity, and precession can also oscillate over geological timescales, as evidenced by Earth's Milankovitch cycles (e.g. Deitrick et al., 2018). Considering these factors would provide a more comprehensive understanding of the evolution of long-term climate and habitability.

4. Our research for the case study of PC-b has many assumptions. One key assumption is that we assume the substellar point is over the centre of the Pacific Ocean (STP_{ocn}). The substellar point ocean/land size is an important factor affecting the planetary climate and atmospheric circulations (Lewis et al., 2018; Macdonald et al., 2022b). Thus, it would be interesting to investigate how the substellar point location over the Earth's topography can affect our results by comparing the STP_{ocn} case with another case in which the substellar point is over the land continent (STP_{lnd}). This is a work in progress as we have simulated the STP_{lnd} case for about 170 years. However, we did not present and compare the results for the STP_{lnd} case with the STP_{ocn} case described in Chapter 4. This is because the STP_{ocn} case has a top-of-atmosphere radiative energy imbalance of about -4 W m^{-2}, which indicates that it has not reached a quasi-steady state and the surface temperature would decrease faster than that in the STP_{ocn} case. We expect that the STP_{lnd} case requires another 40 to 50 years of simulation to reach quasi-steady and ongoing efforts are in place to solve the problem of numerical instabilities and to push the model across crashes.

5. While our model configurations assume that PC-b is in a tidally-locked orbit with zero eccentricity, it is possible for PC-b to be in a 3:2 resonance state with a highly eccentric orbit (Anglada-Escudé et al., 2016). To understand PC-b's climate under this alternative orbital configuration and to enable direct comparisons with previous studies that have explored this scenario (Turbet et al., 2016; Boutle et al., 2017; Lewis et al., 2018; Del Genio et al., 2019; Salazar et al., 2020b; Galuzzo et al., 2021), future research can focus on conducting simulations for the 3:2 resonance orbit with WACCM6.

6. Cloud and haze radiative effects introduce significant uncertainties in climate simulations. Conducting sensitivity tests on orbital eccentricity using various GCMs with different cloud parametrizations and employing high-resolution global cloud-resolving models (GCRMs) or cloud-permitting models (CPMs) would likely yield more accurate cloud behaviour simulations.

7. For assessing the theoretical observables, we setup PSG simulations using an ideal telescope with many simplifications. For future research, we should examine the observability assuming real telescopes such as JWST and ELT and future concept telescopes such as HWO and LIFE. This would involve considering different telescope resolving powers and more realistic noise estimates. In our PSG simulations, we treat the observation (transit spectroscopy and direct imaging) as a snapshot rather than continuous observations of the planet orbiting the star at different orbital phases. Future work should compute the thermal phase curve using a full ephemeris. The Quasi-Biennial Oscillation (QBO) forcing was excluded from our simulations due to the model's 2-degree resolution, as it is a tuning parameter used to match the Earth's observation. Exploring the QBO-like interannual oscillation in the stratosphere may reveal time variability in the synthetic spectra and affect the observation strategy.

8. In the highly eccentric case, the host star can exert a more significant tidal effect

than the moon, making it interesting to study the impact of solar tides on the climate and habitability of an eccentric exo-Earth. WACCM6 does not account for changes in tidal forcing due to increased orbital eccentricity, and we suggest future model development to incorporate such effects.

9. We anticipate that simulating exoplanets with non-Earth-like atmospheres, such as those similar to Martian or Venusian atmospheres, would yield different climate outcomes. While other general circulation models (GCMs) offer flexibility for such simulations, the Earth-system model we used provides greater accuracy and detail, though it is specifically designed for Earth's conditions. Modifications could include implementing a more adaptable correlated-k radiative transfer scheme to better simulate Earth-like exoplanets, as the current model's absorption coefficients are optimized for Earth's atmosphere and may not be valid for different gas compositions.

10. The exclusion of ocean biogeochemistry, specifically developed for Earth, limited our study to land surface habitability. Future work can incorporate a more flexible biogeochemistry model to explore both land and ocean habitability.

11. One caveat in the model setup for PC-b simulations is that the dynamic ocean component model has the Earth's rotation rate instead of that for the PC-b's, which might cause inaccuracy regarding ocean heat transport and sea ice dynamics. Even though we expect that atmospheric dynamics play a more important role in heat transport and the inaccuracy in the wind-driven ocean current is small because of the largely frozen ocean surface, it would be more accurate to make the dynamic ocean component consistent with other parts in the model. This is part of the model development suggestions for making an Earth system model more feasible for studying Earth-like exoplanets with different orbital configurations.

12. The ocean/land distribution of Earth is a crucial factor that shapes the climate and atmospheric dynamics. To study and compare the effects of different ocean/-

land distributions on climate, habitability, and potential observability with other more flexible models, ongoing efforts are being made to allow WACCM6 to have customized topography.

5.3 Conclusion

Understanding the climate and habitability of terrestrial exoplanets is a fundamental question in exoplanetary science, as it addresses the potential for life beyond our Solar System and enriches our knowledge of planetary diversity in the Universe. My research contributes to this overarching goal by investigating how different orbital parameters, specifically orbital eccentricity and tidal locking, affect the climate, atmospheric chemistry, potential habitability, and observability of Earth-like exoplanets. Utilizing a fully-coupled Earth System model (WACCM6), I explored scenarios such as highly eccentric, circular and tidally-locked terrestrial exoplanets. Our findings contribute to previous work that habitable conditions may exist across a range of orbital parameters.

Based on my research, future work should investigate a broader range of eccentricities and obliquities using more flexible 3D climate models that incorporate additional physical processes. Model intercomparisons within the climate model hierarchy are necessary, as they can refine our interpretations of the underlying physics in the climate systems of terrestrial exoplanets. Integrating space weather, geological processes and biological components into 3D climate models will further contribute to the interdisciplinary field. Future missions equipped with next-generation telescopes and instruments could provide the necessary sensitivity and resolution to observe key atmospheric constituents, confirming or refuting the predictions by climate modeling and thereby stepping forward to answer the profound questions about the prevalence of life in the Universe.

Appendix A

Appendix Chapter

A.1 Common Errors in WACCM6 Simulations

Simulating Earth-analogue exoplanets with different eccentricity and obliquity, as discussed in Chapters 2 and 3, may seem straightforward, but it involves several modifications to the source code in WACCM6. More importantly, we had to resolve crashes caused by numerical instabilities, also encountered when simulating Earth-like exoplanets orbiting M dwarfs, as covered in Chapter 4.

In this chapter, we outline two common simulation errors encountered during these simulations, including those related to the changes in eccentricity and obliquity and M dwarf environments, and provide general methods for resolving/mitigating them.

A.1.1 Lagrangian Crossing Error

In the FV dynamical core, while the vertical movement of air is treated in a quasi-Lagrangian manner, there are strict numerical checks to ensure that the model remains stable and physically realistic. One such check is related to the Lagrangian crossing error:

What is Lagrangian Crossing?

The model calculates the pressure at different vertical levels. For the model to be stable, these pressure levels must not "cross" each other. That is, the pressure at a higher level (say level k) must always be greater than the pressure at the level below it (say level $k - 1$). If the pressure difference between two adjacent levels becomes too small (less than a critical threshold), the model detects a Lagrangian crossing. This indicates that the layers are too close, which can cause numerical instability.

Error Condition:

The error is triggered if the difference between the pressure at level k and the pressure at level $k - 1$ falls below a critical threshold:

$$P(k) - P(k - 1) < 10^{-11} \tag{A.1}$$

Here, $P(k)$ is the pressure at level k, and $P(k-1)$ is the pressure at the level just below it.

Why This Happens:

Changing Radiative Forcings: When modifying the model, such as changing the orbital eccentricity, it can lead to seasonal variations in the solar forcing and, hence, larger vertical temperature gradients. This, in turn, causes the air parcels to move more rapidly in the vertical direction, increasing the chance of Lagrangian levels crossing.

Solution: When this error occurs, the model may suggest increasing the variable `NSPLTVRM`, which controls how often the model's vertical remapping is performed. More frequent remapping can help prevent the layers from crossing and maintain stability.

A.1.2 CFL Violation

The Courant-Friedrichs-Lewy (CFL) condition is a fundamental criterion for ensuring the numerical stability of simulations that use explicit time-stepping methods, such as

those employed in the Finite Volume (FV) dynamic core of models like WACCM6.

Understanding CFL Violation

The CFL condition ensures that the numerical domain of dependence encompasses the physical domain of dependence. In practical terms, this means that the time step Δt used in the simulation must be small enough to prevent a signal (e.g., a wave or flow feature) from traveling across more than one grid cell in a single time step. The CFL condition is mathematically expressed as:

$$\frac{u\Delta t}{\Delta x} \leq C \tag{A.2}$$

where u is the flow speed, Δx is the grid spacing, and C is the CFL number, typically set to be less than 1 to maintain numerical stability.

CFL Violation in the Sea Ice Component (CICE)

CFL violations can occur not only in the atmospheric component but also in the sea ice component of WACCM6, known as CICE. In high-resolution sea ice simulations, rapid changes in sea ice velocity can lead to a violation of the CFL condition. When this happens, the model may output an error related to "bad departure points," indicating that the calculated positions of fluid parcels have moved too far in one-time step, leading to numerical instability.

The error is triggered if the displacement of the departure points falls outside the bounds defined by the grid cell dimensions. Specifically, the condition in the model is:

```
if (dpx(i,j) < -HTN(i,j) .or.  dpx(i,j) > HTN(i+1,j) .or.

        dpy(i,j) < -HTE(i,j) .or.  dpy(i,j) > HTE(i,j+1))        (A.3)
```

Here, `dpx(i,j)` and `dpy(i,j)` are the displacements of sea ice in the x and y directions, respectively, while `HTN(i,j)` and `HTE(i,j)` are the grid cell dimensions in the north-south and east-west directions. The simulation crashes if these conditions are met.

Possible Solutions

- **Increase the Coupling Frequency:** For high-resolution simulations, increasing the coupling frequency between the atmosphere and sea ice components can help reduce the likelihood of CFL violations by ensuring that the model updates more frequently. However, this adjustment is typically only feasible in initial or hybrid runs, not in branch runs. Branch runs require bit-for-bit reproducibility, so a potential solution is to convert branch cases into hybrid cases and then adjust the coupling timesteps. This requires closely checking the simulation outputs before and after the modification, which can only be valid if they largely agree.

- **Tune CLUBB Parameters:** The parameterizations for the boundary layer, shallow convection, and cloud macrophysics in WACCM6 are unified under the Cloud Layers Unified By Binormals (CLUBB) framework. Adjusting CLUBB parameters, particularly those related to the damping of horizontal wind speed, may help mitigate CFL violations by reducing excessive wind speeds that can lead to instability.

- **Sub-Stepping in CICE:** Increasing the thermodynamic time-stepping within the CICE component can help the model better handle rapid changes in sea ice velocity, thereby reducing the risk of CFL violations.

References

Abe, Yutaka, Abe-Ouchi, Ayako, Sleep, Norman H., and Zahnle, Kevin J. (June 2011). "Habitable Zone Limits for Dry Planets". In: *Astrobiology* 11.5, pp. 443–460. DOI: `10.1089/ast.2010.0545`.

Adams, Arthur D., Boos, William R., and Wolf, Eric T. (May 2019). "Aquaplanet Models on Eccentric Orbits: Effects of the Rotation Rate on Observables". In: *Astronomical Journal* 157.5, 189. DOI: `10.3847/1538-3881/ab107f`. arXiv: `1903.06216 [astro-ph.EP]`.

Adams, Fred C. and Laughlin, Gregory (Apr. 1997). "A dying universe: the long-term fate and evolutionof astrophysical objects". In: *Reviews of Modern Physics* 69.2, pp. 337–372. DOI: `10.1103/RevModPhys.69.337`. arXiv: `astro-ph/9701131 [astro-ph]`.

Alvarado-Gómez, Julián. D., Drake, Jeremy J., Cohen, Ofer, Fraschetti, Federico, Garraffo, Cecilia, and Poppenhäger, Katja (May 2022). "Coronal mass ejections and exoplanets: A numerical perspective". In: *Astronomische Nachrichten* 343.4, e10100. DOI: `10.1002/asna.20210100`. arXiv: `2111.09704 [astro-ph.SR]`.

Ambaum, Maarten H. P. (2020). *Thermal Physics of the Atmosphere (Second Edition)*. ISBN: 978-0-12-824498-2: Royal Meteorological Society – Elsevier.

Amundsen, David S., Tremblin, Pascal, Manners, James, Baraffe, Isabelle, and Mayne, Nathan J. (Feb. 2017). "Treatment of overlapping gaseous absorption with the correlated-k method in hot Jupiter and brown dwarf atmosphere models". In: *Astronomy and*

Astrophysics 598, A97. DOI: 10.1051/0004-6361/201629322. arXiv: 1610.01389
[astro-ph.EP].

Angerhausen, Daniel, Pidhorodetska, Daria, Leung, Michaela, Hansen, Janina, Alei, Eleonora, Dannert, Felix, Kammerer, Jens, Quanz, Sascha P., Schwieterman, Edward W., and The LIFE initiative (Mar. 2024). "Large Interferometer For Exoplanets (LIFE). XII. The Detectability of Capstone Biosignatures in the Mid-infrared—Sniffing Exoplanetary Laughing Gas and Methylated Halogens". In: *Astronomical Journal* 167.3, 128. DOI: 10.3847/1538-3881/ad1f4b.

Anglada-Escudé, Guillem, Amado, Pedro J., Barnes, John, Berdiñas, Zaira M., Butler, R. Paul, Coleman, Gavin A. L., de La Cueva, Ignacio, Dreizler, Stefan, Endl, Michael, Giesers, Benjamin, Jeffers, Sandra V., Jenkins, James S., Jones, Hugh R. A., Kiraga, Marcin, Kürster, Martin, López-González, María J., Marvin, Christopher J., Morales, Nicolás, Morin, Julien, Nelson, Richard P., Ortiz, José L., Ofir, Aviv, Paardekooper, Sijme-Jan, Reiners, Ansgar, Rodríguez, Eloy, Rodríguez-López, Cristina, Sarmiento, Luis F., Strachan, John P., Tsapras, Yiannis, Tuomi, Mikko, and Zechmeister, Mathias (Aug. 2016). "A terrestrial planet candidate in a temperate orbit around Proxima Centauri". In: *Nature* 536.7617, pp. 437–440. DOI: 10.1038/nature19106. arXiv: 1609.03449 [astro-ph.EP].

Astudillo-Defru, N., Cloutier, R., Wang, S. X., Teske, J., Brahm, R., Hellier, C., Ricker, G., Vanderspek, R., Latham, D., Seager, S., Winn, J. N., Jenkins, J. M., Collins, K. A., Stassun, K. G., Ziegler, C., Almenara, J. M., Anderson, D. R., Artigau, E., Bonfils, X., Bouchy, F., Briceño, C., Butler, R. P., Charbonneau, D., Conti, D. M., Crane, J., Crossfield, I. J. M., Davies, M., Delfosse, X., Díaz, R. F., Doyon, R., Dragomir, D., Eastman, J. D., Espinoza, N., Essack, Z., Feng, F., Figueira, P., Forveille, T., Gan, T., Glidden, A., Guerrero, N., Hart, R., Henning, Th., Horch, E. P., Isopi, G., Jenkins, J. S., Jordán, A., Kielkopf, J. F., Law, N., Lovis, C., Mallia, F., Mann, A. W., de Medeiros, J. R., Melo, C., Mennickent, R. E., Mignon, L., Murgas, F., Nusdeo, D. A.,

Pepe, F., Relles, H. M., Rose, M., Santos, N. C., Ségransan, D., Shectman, S., Shporer, A., Smith, J. C., Torres, P., Udry, S., Villasenor, J., Winters, J. G., and Zhou, G. (Apr. 2020). "A hot terrestrial planet orbiting the bright M dwarf L 168-9 unveiled by TESS". In: *Astronomy and Astrophysics* 636, A58. DOI: 10.1051/0004-6361/201937179. arXiv: 2001.09175 [astro-ph.EP].

Atkinson, R., Baulch, D. L., Cox, R. A., Crowley, J. N., Hampson, R. F., Hynes, R. G., Jenkin, M. E., Rossi, M. J., and Troe, J. (Sept. 2004). "Evaluated kinetic and photochemical data for atmospheric chemistry: Volume I - gas phase reactions of O_x, HO_x, NO_x and SO_x species". In: *Atmospheric Chemistry & Physics* 4.6, pp. 1461–1738. DOI: 10.5194/acp-4-1461-200410.5194/acpd-3-6179-2003.

Auclair-Desrotour, P., Laskar, J., Mathis, S., and Correia, A. C. M. (July 2017). "The rotation of planets hosting atmospheric tides: from Venus to habitable super-Earths". In: *Astronomy and Astrophysics* 603, A108. DOI: 10.1051/0004-6361/201628701. arXiv: 1611.05678 [astro-ph.EP].

Austin, John and Reichler, Thomas J. (Apr. 2008). "Long-term evolution of the cold point tropical tropopause: Simulation results and attribution analysis". In: *Journal of Geophysical Research (Atmospheres)* 113.D7, D00B10. DOI: 10.1029/2007JD009768.

Banks, P. M. and Kockarts, G. (1973). *Aeronomy.*

Barnes, Rory (Dec. 2017). "Tidal locking of habitable exoplanets". In: *Celestial Mechanics and Dynamical Astronomy* 129.4, pp. 509–536. DOI: 10.1007/s10569-017-9783-7. arXiv: 1708.02981 [astro-ph.EP].

Barnes, Rory, Deitrick, Russell, Luger, Rodrigo, Driscoll, Peter E., Quinn, Thomas R., Fleming, David P., Guyer, Benjamin, McDonald, Diego V., Meadows, Victoria S., Arney, Giada, Crisp, David, Domagal-Goldman, Shawn D., Foreman-Mackey, Daniel, Kaib, Nathan A., Lincowski, Andrew, Lustig-Yaeger, Jacob, and Schwieterman, Eddie

(Aug. 2016). "The Habitability of Proxima Centauri b I: Evolutionary Scenarios". In: *arXiv e-prints*, arXiv:1608.06919. DOI: `10.48550/arXiv.1608.06919`. arXiv: `1608.06919 [astro-ph.EP]`.

Barnes, Rory, Raymond, Sean N., Jackson, Brian, and Greenberg, Richard (June 2008). "Tides and the Evolution of Planetary Habitability". In: *Astrobiology* 8.3, pp. 557–568. DOI: `10.1089/ast.2007.0204`. arXiv: `0807.0680 [astro-ph]`.

Basak, Suryoday, Mathur, Archana, Theophilus, Abhijit Jeremiel, Deshpande, Gouri, and Murthy, Jayant (May 2021). "Habitability classification of exoplanets: a machine learning insight". In: *European Physical Journal Special Topics* 230.10, pp. 2221–2251. DOI: `10.1140/epjs/s11734-021-00203-z`.

Benneke, Björn, Roy, Pierre-Alexis, Coulombe, Louis-Philippe, Radica, Michael, Piaulet, Caroline, Ahrer, Eva-Maria, Pierrehumbert, Raymond, Krissansen-Totton, Joshua, Schlichting, Hilke E., Hu, Renyu, Yang, Jeehyun, Christie, Duncan, Thorngren, Daniel, Young, Edward D., Pelletier, Stefan, Knutson, Heather A., Miguel, Yamila, Evans-Soma, Thomas M., Dorn, Caroline, Gagnebin, Anna, Fortney, Jonathan J., Komacek, Thaddeus, MacDonald, Ryan, Raul, Eshan, Cloutier, Ryan, Acuna, Lorena, Lafrenière, David, Cadieux, Charles, Doyon, René, Welbanks, Luis, and Allart, Romain (Mar. 2024). "JWST Reveals CH_4, CO_2, and H_2O in a Metal-rich Miscible Atmosphere on a Two-Earth-Radius Exoplanet". In: *arXiv e-prints*, arXiv:2403.03325. DOI: `10.48550/arXiv.2403.03325`. arXiv: `2403.03325 [astro-ph.EP]`.

Berger, A. (Nov. 1988). "Milankovitch Theory and climate". In: *Reviews of Geophysics* 26.4, pp. 624–657. DOI: `10.1029/RG026i004p00624`.

Berger, André L. (Dec. 1978). "Long-Term Variations of Daily Insolation and Quaternary Climatic Changes." In: *Journal of Atmospheric Sciences* 35.12, pp. 2362–2367. DOI: `10.1175/1520-0469(1978)035<2362:LTVODI>2.0.CO;2`.

Bergsten, Galen J., Pascucci, Ilaria, Hardegree-Ullman, Kevin K., Fernandes, Rachel B., Christiansen, Jessie L., and Mulders, Gijs D. (Dec. 2023). "No Evidence for More Earth-sized Planets in the Habitable Zone of Kepler's M versus FGK Stars". In: *Astronomical Journal* 166.6, 234. DOI: `10.3847/1538-3881/ad03ea`. arXiv: `2310.11613 [astro-ph.EP]`.

Bétrémieux, Yan and Kaltenegger, Lisa (Aug. 2014). "Impact of Atmospheric Refraction: How Deeply can We Probe Exo-Earth's Atmospheres during Primary Eclipse Observations?" In: *Astrophysical Journal* 791.1, 7. DOI: `10.1088/0004-637X/791/1/7`. arXiv: `1312.6625 [astro-ph.EP]`.

Biasiotti, L., Simonetti, P., Vladilo, G., Ivanovski, S., Damasso, M., Sozzetti, A., and Monai, S. (June 2024). "Potential climates and habitability on Gl 514 b: a super-Earth exoplanet with high eccentricity". In: *Monthly Notices of the Royal Astronomical Society* 530.4, pp. 4300–4316. DOI: `10.1093/mnras/stae1124`.

Bochanski, John J., Hawley, Suzanne L., Covey, Kevin R., West, Andrew A., Reid, I. Neill, Golimowski, David A., and Ivezić, Željko (June 2010). "The Luminosity and Mass Functions of Low-mass Stars in the Galactic Disk. II. The Field". In: *Astronomical Journal* 139.6, pp. 2679–2699. DOI: `10.1088/0004-6256/139/6/2679`. arXiv: `1004.4002 [astro-ph.SR]`.

Bogenschutz, Peter A., Gettelman, Andrew, Morrison, Hugh, Larson, Vincent E., Craig, Cheryl, and Schanen, David P. (Dec. 2013). "Higher-Order Turbulence Closure and Its Impact on Climate Simulations in the Community Atmosphere Model". In: *Journal of Climate* 26.23, pp. 9655–9676. DOI: `10.1175/JCLI-D-13-00075.1`.

Bolmont, Emeline, Libert, Anne-Sophie, Leconte, Jeremy, and Selsis, Franck (June 2016). "Habitability of planets on eccentric orbits: Limits of the mean flux approximation". In: *Astronomy and Astrophysics* 591, A106. DOI: `10.1051/0004-6361/201628073`. arXiv: `1604.06091 [astro-ph.EP]`.

Bonomo, A. S., Dumusque, X., Massa, A., Mortier, A., Bongiolatti, R., Malavolta, L., Sozzetti, A., Buchhave, L. A., Damasso, M., Haywood, R. D., Morbidelli, A., Latham, D. W., Molinari, E., Pepe, F., Poretti, E., Udry, S., Affer, L., Boschin, W., Charbonneau, D., Cosentino, R., Cretignier, M., Ghedina, A., Lega, E., López-Morales, M., Margini, M., Martínez Fiorenzano, A. F., Mayor, M., Micela, G., Pedani, M., Pinamonti, M., Rice, K., Sasselov, D., Tronsgaard, R., and Vanderburg, A. (Sept. 2023). "Cold Jupiters and improved masses in 38 Kepler and K2 small planet systems from 3661 HARPS-N radial velocities. No excess of cold Jupiters in small planet systems". In: *Astronomy and Astrophysics* 677, A33. DOI: 10.1051/0004-6361/202346211. arXiv: 2304.05773 [astro-ph.EP].

Bony, Sandrine, Stevens, Bjorn, Held, Isaac H, Mitchell, John F, Dufresne, Jean-Louis, Emanuel, Kerry A, Friedlingstein, Pierre, Griffies, Stephen, and Senior, Catherine (2013). "Carbon dioxide and climate: Perspectives on a scientific assessment". In: *Climate science for serving society: Research, modeling and prediction priorities*, pp. 391–413.

Boschi, Robert, Lucarini, Valerio, and Pascale, Salvatore (Nov. 2013). "Bistability of the climate around the habitable zone: A thermodynamic investigation". In: *Icarus* 226.2, pp. 1724–1742. DOI: 10.1016/j.icarus.2013.03.017. arXiv: 1207.1254 [physics.ao-ph].

Boutle, Ian A., Mayne, Nathan J., Drummond, Benjamin, Manners, James, Goyal, Jayesh, Hugo Lambert, F., Acreman, David M., and Earnshaw, Paul D. (May 2017). "Exploring the climate of Proxima B with the Met Office Unified Model". In: *Astronomy and Astrophysics* 601, A120. DOI: 10.1051/0004-6361/201630020. arXiv: 1702.08463 [astro-ph.EP].

Box, George EP (1979). "Robustness in the strategy of scientific model building". In: *Robustness in statistics*. Elsevier, pp. 201–236.

Braam, Marrick, Palmer, Paul I., Decin, Leen, Cohen, Maureen, and Mayne, Nathan J. (June 2023a). "Stratospheric dayside-to-nightside circulation drives the 3-D ozone distribution on synchronously rotating rocky exoplanets". In: *arXiv e-prints*, arXiv:2306.03004. DOI: 10.48550/arXiv.2306.03004. arXiv: 2306.03004 [astro-ph.EP].

– (Nov. 2023b). "Stratospheric dayside-to-nightside circulation drives the 3D ozone distribution on synchronously rotating rocky exoplanets". In: *Monthly Notices of the Royal Astronomical Society* 526.1, pp. 263–278. DOI: 10.1093/mnras/stad2704. arXiv: 2306.03004 [astro-ph.EP].

Brasseur, Guy and Solomon, Susan (2005). *Aeronomy of the Middle Atmosphere: Chemistry and Physics of the Stratosphere and Mesosphere.* 3rd. Dordrecht: Springer.

Briegleb, Philip A. and Light, Bonnie (2007). "A Delta-Eddington Mutiple Scattering Parameterization for Solar Radiation in the Sea Ice Component of the Community Climate System Model". In: URL: https://api.semanticscholar.org/CorpusID: 128734394.

Bryson, Steve, Kunimoto, Michelle, Kopparapu, Ravi K., Coughlin, Jeffrey L., Borucki, William J., Koch, David, Aguirre, Victor Silva, Allen, Christopher, Barentsen, Geert, Batalha, Natalie M., Berger, Travis, Boss, Alan, Buchhave, Lars A., Burke, Christopher J., Caldwell, Douglas A., Campbell, Jennifer R., Catanzarite, Joseph, Chandrasekaran, Hema, Chaplin, William J., Christiansen, Jessie L., Christensen-Dalsgaard, Jørgen, Ciardi, David R., Clarke, Bruce D., Cochran, William D., Dotson, Jessie L., Doyle, Laurance R., Duarte, Eduardo Seperuelo, Dunham, Edward W., Dupree, Andrea K., Endl, Michael, Fanson, James L., Ford, Eric B., Fujieh, Maura, Gautier Thomas N., III, Geary, John C., Gilliland, Ronald L., Girouard, Forrest R., Gould, Alan, Haas, Michael R., Henze, Christopher E., Holman, Matthew J., Howard, Andrew W., Howell, Steve B., Huber, Daniel, Hunter, Roger C., Jenkins, Jon M., Kjeldsen, Hans, Kolodziejczak, Jeffery, Larson, Kipp, Latham, David W., Li, Jie, Mathur, Savita, Meibom, Søren, Mid-

dour, Chris, Morris, Robert L., Morton, Timothy D., Mullally, Fergal, Mullally, Susan E., Pletcher, David, Prsa, Andrej, Quinn, Samuel N., Quintana, Elisa V., Ragozzine, Darin, Ramirez, Solange V., Sanderfer, Dwight T., Sasselov, Dimitar, Seader, Shawn E., Shabram, Megan, Shporer, Avi, Smith, Jeffrey C., Steffen, Jason H., Still, Martin, Torres, Guillermo, Troeltzsch, John, Twicken, Joseph D., Uddin, Akm Kamal, Van Cleve, Jeffrey E., Voss, Janice, Weiss, Lauren M., Welsh, William F., Wohler, Bill, and Zamudio, Khadeejah A. (Jan. 2021). "The Occurrence of Rocky Habitable-zone Planets around Solar-like Stars from Kepler Data". In: *Astronomical Journal* 161.1, 36. DOI: 10.3847/1538-3881/abc418. arXiv: 2010.14812 [astro-ph.EP].

Burke, Christopher J., Christiansen, Jessie L., Mullally, F., Seader, Shawn, Huber, Daniel, Rowe, Jason F., Coughlin, Jeffrey L., Thompson, Susan E., Catanzarite, Joseph, Clarke, Bruce D., Morton, Timothy D., Caldwell, Douglas A., Bryson, Stephen T., Haas, Michael R., Batalha, Natalie M., Jenkins, Jon M., Tenenbaum, Peter, Twicken, Joseph D., Li, Jie, Quintana, Elisa, Barclay, Thomas, Henze, Christopher E., Borucki, William J., Howell, Steve B., and Still, Martin (Aug. 2015). "Terrestrial Planet Occurrence Rates for the Kepler GK Dwarf Sample". In: *Astrophysical Journal* 809.1, 8. DOI: 10.1088/0004-637X/809/1/8. arXiv: 1506.04175 [astro-ph.EP].

Cadieux, Charles, Doyon, René, MacDonald, Ryan J., Turbet, Martin, Artigau, Étienne, Lim, Olivia, Radica, Michael, Fauchez, Thomas J., Salhi, Salma, Dang, Lisa, Albert, Loíc, Coulombe, Louis-Philippe, Cowan, Nicolas B., Lafrenière, David, L'Heureux, Alexandrine, Piaulet-Ghorayeb, Caroline, Benneke, Björn, Cloutier, Ryan, Charnay, Benjamin, Cook, Neil J., Fournier-Tondreau, Marylou, Plotnykov, Mykhaylo, and Valencia, Diana (July 2024a). "Transmission Spectroscopy of the Habitable Zone Exoplanet LHS 1140 b with JWST/NIRISS". In: *Astrophysical Journal Letters* 970.1, L2. DOI: 10.3847/2041-8213/ad5afa. arXiv: 2406.15136 [astro-ph.EP].

Cadieux, Charles, Plotnykov, Mykhaylo, Doyon, René, Valencia, Diana, Jahandar, Farbod, Dang, Lisa, Turbet, Martin, Fauchez, Thomas J., Cloutier, Ryan, Cherubim,

Collin, Artigau, Étienne, Cook, Neil J., Edwards, Billy, Hallatt, Tim, Charnay, Benjamin, Bouchy, François, Allart, Romain, Mignon, Lucile, Baron, Frédérique, Barros, Susana C. C., Benneke, Björn, Canto Martins, B. L., Cowan, Nicolas B., De Medeiros, J. R., Delfosse, Xavier, Delgado-Mena, Elisa, Dumusque, Xavier, Ehrenreich, David, Frensch, Yolanda G. C., González Hernández, J. I., Hara, Nathan C., Lafrenière, David, Lo Curto, Gaspare, Malo, Lison, Melo, Claudio, Mounzer, Dany, Passeger, Vera Maria, Pepe, Francesco, Poulin-Girard, Anne-Sophie, Santos, Nuno C., Sosnowska, Danuta, Suárez Mascareño, Alejandro, Thibault, Simon, Vaulato, Valentina, Wade, Gregg A., and Wildi, François (Jan. 2024b). "New Mass and Radius Constraints on the LHS 1140 Planets: LHS 1140 b Is either a Temperate Mini-Neptune or a Water World". In: *Astrophysical Journal Letters* 960.1, L3. DOI: 10.3847/2041-8213/ad1691. arXiv: 2310.15490 [astro-ph.EP].

Carone, L., Keppens, R., Decin, L., and Henning, Th. (Feb. 2018). "Stratosphere circulation on tidally locked ExoEarths". In: *Monthly Notices of the Royal Astronomical Society* 473.4, pp. 4672–4685. DOI: 10.1093/mnras/stx2732. arXiv: 1711.11446 [physics.ao-ph].

Carrión-González, Óscar, Kammerer, Jens, Angerhausen, Daniel, Dannert, Felix, García Muñoz, Antonio, Quanz, Sascha P., Absil, Olivier, Beichman, Charles A., Girard, Julien H., Mennesson, Bertrand, Meyer, Michael R., Stapelfeldt, Karl R., and LIFE Collaboration (Oct. 2023). "Large Interferometer For Exoplanets (LIFE). X. Detectability of currently known exoplanets and synergies with future IR/O/UV reflected-starlight imaging missions". In: *Astronomy and Astrophysics* 678, A96. DOI: 10.1051/0004-6361/202347027. arXiv: 2308.09646 [astro-ph.EP].

Carslaw, Ken S. (2022). "Chapter 2 - Aerosol in the climate system". In: *Aerosols and Climate*. Ed. by Ken S. Carslaw. Elsevier, pp. 9–52. ISBN: 978-0-12-819766-0. DOI: https://doi.org/10.1016/B978-0-12-819766-0.00008-0. URL: https://www.sciencedirect.com/science/article/pii/B9780128197660000080.

Catling, David C. and Kasting, James F. (2017a). *Atmospheric Evolution on Inhabited and Lifeless Worlds.*

Catling and Kasting (2017b). *Atmospheric Evolution on Inhabited and Lifeless Worlds.* ISBN 9781139020558: Cambridge University Press.

Chapman, S. (1930). "XXXV. On ozone and atomic oxygen in the upper atmosphere". In: *The London, Edinburgh, and Dublin Philosophical Magazine and Journal of Science* 10.64, pp. 369–383. DOI: 10.1080/14786443009461588. eprint: https://doi.org/10.1080/14786443009461588. URL: https://doi.org/10.1080/14786443009461588.

Charnay, Benjamin, Wolf, Eric T., Marty, Bernard, and Forget, François (July 2020). "Is the Faint Young Sun Problem for Earth Solved?" In: *Space Science Reviews* 216.5, 90. DOI: 10.1007/s11214-020-00711-9. arXiv: 2006.06265 [astro-ph.EP].

Chen, Ajiao, Li, Weiping, Li, Weijing, and Liu, Xin (Dec. 2014). "An observational study of snow aging and the seasonal variation of snow albedo by using data from Col de Porte, France". In: *Chinese Science Bulletin* 59. DOI: 10.1007/s11434-014-0429-9.

Chen, Howard, Zhan, Zhuchang, Youngblood, Allison, Wolf, Eric T., Feinstein, Adina D., and Horton, Daniel E. (Jan. 2021). "Persistence of flare-driven atmospheric chemistry on rocky habitable zone worlds". In: *Nature Astronomy* 5, pp. 298–310. DOI: 10.1038/s41550-020-01264-1. arXiv: 2101.04507 [astro-ph.EP].

Christ, Callista N., Montet, Benjamin T., and Fabrycky, Daniel C. (June 2019). "Observations of the Kepler Field with TESS: Predictions for Planet Yield and Observable Features". In: *Astronomical Journal* 157.6, 235. DOI: 10.3847/1538-3881/ab1aae. arXiv: 1810.02826 [astro-ph.EP].

Clarke, Andrew (Apr. 2014). "The thermal limits to life on Earth". In: *International Journal of Astrobiology* 13.2, pp. 141–154. DOI: 10.1017/S1473550413000438.

Cockell, C. S., Bush, T., Bryce, C., Direito, S., Fox-Powell, M., Harrison, J. P., Lammer, H., Landenmark, H., Martin-Torres, J., Nicholson, N., Noack, L., O'Malley-James, J., Payler, S. J., Rushby, A., Samuels, T., Schwendner, P., Wadsworth, J., and Zorzano, M. P. (Jan. 2016). "Habitability: A Review". In: *Astrobiology* 16.1, pp. 89–117. DOI: `10.1089/ast.2015.1295`.

Colose, Christopher M., Del Genio, Anthony D., and Way, M. J. (Oct. 2019). "Enhanced Habitability on High Obliquity Bodies near the Outer Edge of the Habitable Zone of Sun-like Stars". In: *Astrophysical Journal* 884.2, 138. DOI: `10.3847/1538-4357/ab4131`. arXiv: `1905.09398 [astro-ph.EP]`.

Colose, Christopher M., Haqq-Misra, Jacob, Wolf, Eric T., Del Genio, Anthony D., Barnes, Rory, Way, Michael J., and Ruedy, Reto (Nov. 2021). "Effects of Spin-Orbit Resonances and Tidal Heating on the Inner Edge of the Habitable Zone". In: *Astrophysical Journal* 921.1, 25. DOI: `10.3847/1538-4357/ac135c`. arXiv: `2012.07996 [astro-ph.EP]`.

Cooke, G. J., Marsh, D. R., Walsh, C., Black, B., and Lamarque, J. -F. (Jan. 2022). "A revised lower estimate of ozone columns during Earth's oxygenated history". In: *Royal Society Open Science* 9.1, 211165. DOI: `10.1098/rsos.211165`. arXiv: `2102.11675 [astro-ph.EP]`.

Cooke, G. J., Marsh, D. R., Walsh, C., Rugheimer, S., and Villanueva, G. L. (Jan. 2023a). "Variability due to climate and chemistry in observations of oxygenated Earth-analogue exoplanets". In: *Monthly Notices of the Royal Astronomical Society* 518.1, pp. 206–219. DOI: `10.1093/mnras/stac2604`. arXiv: `2209.07566 [astro-ph.EP]`.

Cooke, G. J., Marsh, D. R., Walsh, C., and Sainsbury-Martinez, F. (July 2024). "Lethal Surface Ozone Concentrations Are Possible on Habitable Zone Exoplanets". In: *The Planetary Science Journal* 5.7, 168. DOI: `10.3847/PSJ/ad53c3`. arXiv: `2405.20167 [astro-ph.EP]`.

Cooke, G. J., Marsh, D. R., Walsh, C., and Youngblood, A. (Dec. 2023b). "Degenerate Interpretations of O_3 Spectral Features in Exoplanet Atmosphere Observations Due to Stellar UV Uncertainties: A 3D Case Study with TRAPPIST-1 e". In: *Astrophysical Journal* 959.1, 45. DOI: 10.3847/1538-4357/ad0381. arXiv: 2309.15239 [astro-ph.EP].

Cronin, Timothy W. and Emanuel, Kerry A. (Dec. 2013). "The climate time scale in the approach to radiative-convective equilibrium". In: *Journal of Advances in Modeling Earth Systems* 5.4, pp. 843–849. DOI: 10.1002/jame.20049.

Crossfield, Ian J. M., Malik, Matej, Hill, Michelle L., Kane, Stephen R., Foley, Bradford, Polanski, Alex S., Coria, David, Brande, Jonathan, Zhang, Yanzhe, Wienke, Katherine, Kreidberg, Laura, Cowan, Nicolas B., Dragomir, Diana, Gorjian, Varoujan, Mikal-Evans, Thomas, Benneke, Björn, Christiansen, Jessie L., Deming, Drake, and Morales, Farisa Y. (Sept. 2022). "GJ 1252b: A Hot Terrestrial Super-Earth with No Atmosphere". In: *Astrophysical Journal Letters* 937.1, L17. DOI: 10.3847/2041-8213/ac886b. arXiv: 2208.09479 [astro-ph.EP].

Currie, T., Biller, B., Lagrange, A., Marois, C., Guyon, O., Nielsen, E. L., Bonnefoy, M., and De Rosa, R. J. (July 2023). "Direct Imaging and Spectroscopy of Extrasolar Planets". In: *Protostars and Planets VII*. Ed. by S. Inutsuka, Y. Aikawa, T. Muto, K. Tomida, and M. Tamura. Vol. 534. Astronomical Society of the Pacific Conference Series, p. 799. DOI: 10.48550/arXiv.2205.05696. arXiv: 2205.05696 [astro-ph.EP].

Damiano, Mario, Bello-Arufe, Aaron, Yang, Jeehyun, and Hu, Renyu (June 2024). "LHS 1140 b Is a Potentially Habitable Water World". In: *Astrophysical Journal Letters* 968.2, L22. DOI: 10.3847/2041-8213/ad5204. arXiv: 2403.13265 [astro-ph.EP].

Damiano, Mario, Hu, Renyu, and Mennesson, Bertrand (Oct. 2023). "Reflected Spectroscopy of Small Exoplanets. III. Probing the UV Band to Measure Biosignature

Gases". In: *Astronomical Journal* 166.4, 157. DOI: 10.3847/1538-3881/acefd3. arXiv: 2308.08490 [astro-ph.EP].

De Luca, P., Braam, M., Komacek, T. D., and Hochman, A. (June 2024). "The impact of ozone on Earth-like exoplanet climate dynamics: the case of Proxima Centauri b". In: *Monthly Notices of the Royal Astronomical Society* 531.1, pp. 1471–1482. DOI: 10.1093/mnras/stae1199. arXiv: 2404.17972 [astro-ph.EP].

Deitrick, Russell, Barnes, Rory, Bitz, Cecilia, Fleming, David, Charnay, Benjamin, Meadows, Victoria, Wilhelm, Caitlyn, Armstrong, John, and Quinn, Thomas R. (June 2018). "Exo-Milankovitch Cycles. II. Climates of G-dwarf Planets in Dynamically Hot Systems". In: *Astronomical Journal* 155.6, 266. DOI: 10.3847/1538-3881/aac214. arXiv: 1805.00283 [astro-ph.EP].

Del Genio, Anthony D., Way, Michael J., Amundsen, David S., Aleinov, Igor, Kelley, Maxwell, Kiang, Nancy Y., and Clune, Thomas L. (Jan. 2019). "Habitable Climate Scenarios for Proxima Centauri b with a Dynamic Ocean". In: *Astrobiology* 19.1, pp. 99–125. DOI: 10.1089/ast.2017.1760.

Diamond-Lowe, H., King, G. W., Youngblood, A., Brown, A., Howard, W. S., Winters, J. G., Wilson, D. J., France, K., Mendonça, J. M., Buchhave, L. A., Corrales, L., Kreidberg, L., Medina, A. A., Bean, J. L., Berta-Thompson, Z. K., Evans-Soma, T. M., Froning, C., Duvvuri, G. M., Kempton, E. M. -R., Miguel, Y., Pineda, J. S., and Schneider, C. (Sept. 2024). "High-energy spectra of LTT 1445A and GJ 486 reveal flares and activity". In: *Astronomy and Astrophysics* 689, A48. DOI: 10.1051/0004-6361/202450107. arXiv: 2407.00165 [astro-ph.EP].

Donohoe, Aaron, Frierson, Dargan M. W., and Battisti, David S. (Aug. 2014). "The effect of ocean mixed layer depth on climate in slab ocean aquaplanet experiments". In: *Climate Dynamics* 43.3-4, pp. 1041–1055. DOI: 10.1007/s00382-013-1843-4.

Dreizler, S., Jeffers, S. V., Rodríguez, E., Zechmeister, M., Barnes, J. R., Haswell, C. A., Coleman, G. A. L., Lalitha, S., Hidalgo Soto, D., Strachan, J. B. P., Hambsch, F. -J., López-González, M. J., Morales, N., Rodríguez López, C., Berdiñas, Z. M., Ribas, I., Pallé, E., Reiners, A., and Anglada-Escudé, G. (Mar. 2020). "RedDots: a temperate 1.5 Earth-mass planet candidate in a compact multiterrestrial planet system around GJ 1061". In: *Monthly Notices of the Royal Astronomical Society* 493.1, pp. 536–550. DOI: `10.1093/mnras/staa248`. arXiv: `1908.04717 [astro-ph.EP]`.

Dressing, Courtney D., Spiegel, David S., Scharf, Caleb A., Menou, Kristen, and Raymond, Sean N. (Oct. 2010). "Habitable Climates: The Influence of Eccentricity". In: *Astrophysical Journal* 721.2, pp. 1295–1307. DOI: `10.1088/0004-637X/721/2/1295`. arXiv: `1002.4875 [astro-ph.EP]`.

Driscoll, P. E. and Barnes, R. (Sept. 2015). "Tidal Heating of Earth-like Exoplanets around M Stars: Thermal, Magnetic, and Orbital Evolutions". In: *Astrobiology* 15.9, pp. 739–760. DOI: `10.1089/ast.2015.1325`. arXiv: `1509.07452 [astro-ph.EP]`.

Dubé, Kimberlee, Randel, William, Bourassa, Adam, and Degenstein, Doug (Sept. 2022). "Tropopause-Level NO_x in the Asian Summer Monsoon". In: *Geophysical Research Letters* 49.18, e99848. DOI: `10.1029/2022GL099848`.

Edwards, Paul N. (Jan. 2011). "History of climate modeling". In: *WIREs Climate Change* 2.1, pp. 128–139. DOI: `10.1002/wcc.95`.

Ehrenreich, D., Tinetti, G., Lecavelier Des Etangs, A., Vidal-Madjar, A., and Selsis, F. (Mar. 2006). "The transmission spectrum of Earth-size transiting planets". In: *Astronomy and Astrophysics* 448.1, pp. 379–393. DOI: `10.1051/0004-6361:20053861`. arXiv: `astro-ph/0510215 [astro-ph]`.

Emmons, Louisa K., Schwantes, Rebecca H., Orlando, John J., Tyndall, Geoff, Kinnison, Douglas, Lamarque, Jean-François, Marsh, Daniel, Mills, Michael J., Tilmes, Si-

mone, Bardeen, Charles, Buchholz, Rebecca R., Conley, Andrew, Gettelman, Andrew, Garcia, Rolando, Simpson, Isobel, Blake, Donald R., Meinardi, Simone, and Pétron, Gabrielle (Apr. 2020). "The Chemistry Mechanism in the Community Earth System Model Version 2 (CESM2)". In: *Journal of Advances in Modeling Earth Systems* 12.4, e2019MS001882. DOI: `10.1029/2019MS001882`.

Eyring, Veronika, Bony, Sandrine, Meehl, Gerald A., Senior, Catherine A., Stevens, Bjorn, Stouffer, Ronald J., and Taylor, Karl E. (May 2016). "Overview of the Coupled Model Intercomparison Project Phase 6 (CMIP6) experimental design and organization". In: *Geoscientific Model Development* 9.5, pp. 1937–1958. DOI: `10.5194/gmd-9-1937-2016`.

Faria, J. P., Suárez Mascareño, A., Figueira, P., Silva, A. M., Damasso, M., Demangeon, O., Pepe, F., Santos, N. C., Rebolo, R., Cristiani, S., Adibekyan, V., Alibert, Y., Allart, R., Barros, S. C. C., Cabral, A., D'Odorico, V., Di Marcantonio, P., Dumusque, X., Ehrenreich, D., González Hernández, J. I., Hara, N., Lillo-Box, J., Lo Curto, G., Lovis, C., Martins, C. J. A. P., Mégevand, D., Mehner, A., Micela, G., Molaro, P., Nunes, N. J., Pallé, E., Poretti, E., Sousa, S. G., Sozzetti, A., Tabernero, H., Udry, S., and Zapatero Osorio, M. R. (Feb. 2022). "A candidate short-period sub-Earth orbiting Proxima Centauri". In: *Astronomy and Astrophysics* 658, A115. DOI: `10.1051/0004-6361/202142337`. arXiv: `2202.05188 [astro-ph.EP]`.

Fauchez, Thomas J., Turbet, Martin, Villanueva, Geronimo L., Wolf, Eric T., Arney, Giada, Kopparapu, Ravi K., Lincowski, Andrew, Mandell, Avi, de Wit, Julien, Pidhorodetska, Daria, Domagal-Goldman, Shawn D., and Stevenson, Kevin B. (Dec. 2019). "Impact of Clouds and Hazes on the Simulated JWST Transmission Spectra of Habitable Zone Planets in the TRAPPIST-1 System". In: *Astrophysical Journal* 887.2, 194. DOI: `10.3847/1538-4357/ab5862`. arXiv: `1911.08596 [astro-ph.EP]`.

Feulner, Georg (May 2012). "The faint young Sun problem". In: *Reviews of Geophysics* 50.2, RG2006. DOI: 10.1029/2011RG000375. arXiv: 1204.4449 [astro-ph.EP].

France, Kevin, Loyd, R. O. Parke, Youngblood, Allison, Brown, Alexander, Schneider, P. Christian, Hawley, Suzanne L., Froning, Cynthia S., Linsky, Jeffrey L., Roberge, Aki, Buccino, Andrea P., Davenport, James R. A., Fontenla, Juan M., Kaltenegger, Lisa, Kowalski, Adam F., Mauas, Pablo J. D., Miguel, Yamila, Redfield, Seth, Rugheimer, Sarah, Tian, Feng, Vieytes, Mariela C., Walkowicz, Lucianne M., and Weisenburger, Kolby L. (Apr. 2016). "The MUSCLES Treasury Survey. I. Motivation and Overview". In: *Astrophysical Journal* 820.2, 89. DOI: 10.3847/0004-637X/820/2/89. arXiv: 1602.09142 [astro-ph.SR].

Fujino, K., Lewis, E. L., and Perkin, R. G. (Apr. 1974). "The freezing point of seawater at pressures up to 100 bars". In: *Journal of Geophysical Research* 79.12, pp. 1792–1797. DOI: 10.1029/JC079i012p01792.

Fulton, Benjamin J., Petigura, Erik A., Howard, Andrew W., Isaacson, Howard, Marcy, Geoffrey W., Cargile, Phillip A., Hebb, Leslie, Weiss, Lauren M., Johnson, John Asher, Morton, Timothy D., Sinukoff, Evan, Crossfield, Ian J. M., and Hirsch, Lea A. (Sept. 2017). "The California-Kepler Survey. III. A Gap in the Radius Distribution of Small Planets". In: *Astronomical Journal* 154.3, 109. DOI: 10.3847/1538-3881/aa80eb. arXiv: 1703.10375 [astro-ph.EP].

Galuzzo, Daniele, Cagnazzo, Chiara, Berrilli, Francesco, Fierli, Federico, and Giovannelli, Luca (Mar. 2021). "Three-dimensional Climate Simulations for the Detectability of Proxima Centauri b". In: *Astrophysical Journal* 909.2, 191. DOI: 10.3847/1538-4357/abdeb4. arXiv: 2102.03255 [astro-ph.EP].

Gettelman, A., Mills, M. J., Kinnison, D. E., Garcia, R. R., Smith, A. K., Marsh, D. R., Tilmes, S., Vitt, F., Bardeen, C. G., McInerny, J., Liu, H. -L., Solomon, S. C., Polvani, L. M., Emmons, L. K., Lamarque, J. -F., Richter, J. H., Glanville, A. S., Bacmeister,

J. T., Phillips, A. S., Neale, R. B., Simpson, I. R., DuVivier, A. K., Hodzic, A., and Randel, W. J. (Dec. 2019). "The Whole Atmosphere Community Climate Model Version 6 (WACCM6)". In: *Journal of Geophysical Research (Atmospheres)* 124.23, pp. 12, 380–12, 403. DOI: 10.1029/2019JD030943.

Gettelman, A. and Morrison, H. (Feb. 2015). "Advanced Two-Moment Bulk Microphysics for Global Models. Part I: Off-Line Tests and Comparison with Other Schemes". In: *Journal of Climate* 28.3, pp. 1268–1287. DOI: 10.1175/JCLI-D-14-00102.1.

Gialluca, Megan T., Robinson, Tyler D., Rugheimer, Sarah, and Wunderlich, Fabian (May 2021). "Characterizing Atmospheres of Transiting Earth-like Exoplanets Orbiting M Dwarfs with James Webb Space Telescope". In: *Publications of the Astronomical Society of the Pacific* 133.1023, 054401. DOI: 10.1088/1538-3873/abf367. arXiv: 2101.04139 [astro-ph.EP].

Gilmozzi, R. and Spyromilio, J. (Mar. 2007). "The European Extremely Large Telescope (E-ELT)". In: *The Messenger* 127, p. 11.

Goldblatt, Colin, Lenton, Timothy M., and Watson, Andrew J. (Oct. 2006). "Bistability of atmospheric oxygen and the Great Oxidation". In: *Nature* 443.7112, pp. 683–686. DOI: 10.1038/nature05169.

Gómez-Leal, Illeana, Kaltenegger, Lisa, Lucarini, Valerio, and Lunkeit, Frank (Mar. 2019). "Climate sensitivity to ozone and its relevance on the habitability of Earth-like planets". In: *Icarus* 321, pp. 608–618. DOI: 10.1016/j.icarus.2018.11.019. arXiv: 1901.02897 [astro-ph.EP].

González-Álvarez, E., Zapatero Osorio, M. R., Sanz-Forcada, J., Caballero, J. A., Reffert, S., Béjar, V. J. S., Hatzes, A. P., Herrero, E., Jeffers, S. V., Kemmer, J., López-González, M. J., Luque, R., Molaverdikhani, K., Morello, G., Nagel, E., Quirrenbach, A., Rodríguez, E., Rodríguez-López, C., Schlecker, M., Schweitzer, A., Stock,

S., Passegger, V. M., Trifonov, T., Amado, P. J., Baker, D., Boyd, P. T., Cadieux, C., Charbonneau, D., Collins, K. A., Doyon, R., Dreizler, S., Espinoza, N., Fűrész, G., Furlan, E., Hesse, K., Howell, S. B., Jenkins, J. M., Kidwell, R. C., Latham, D. W., McLeod, K. K., Montes, D., Morales, J. C., O'Dwyer, T., Pallé, E., Pedraz, S., Reiners, A., Ribas, I., Quinn, S. N., Schnaible, C., Seager, S., Skinner, B., Smith, J. C., Schwarz, R. P., Shporer, A., Vanderspek, R., and Winn, J. N. (Feb. 2022). "A multi-planetary system orbiting the early-M dwarf TOI-1238". In: *Astronomy and Astrophysics* 658, A138. DOI: `10.1051/0004-6361/202142128`. arXiv: `2111.14602 [astro-ph.EP]`.

Gordon, I. E., Rothman, L. S., Hargreaves, R. J., Hashemi, R., Karlovets, E. V., Skinner, F. M., Conway, E. K., Hill, C., Kochanov, R. V., Tan, Y., Wcisło, P., Finenko, A. A., Nelson, K., Bernath, P. F., Birk, M., Boudon, V., Campargue, A., Chance, K. V., Coustenis, A., Drouin, B. J., Flaud, J. -M., Gamache, R. R., Hodges, J. T., Jacquemart, D., Mlawer, E. J., Nikitin, A. V., Perevalov, V. I., Rotger, M., Tennyson, J., Toon, G. C., Tran, H., Tyuterev, V. G., Adkins, E. M., Baker, A., Barbe, A., Canè, E., Császár, A. G., Dudaryonok, A., Egorov, O., Fleisher, A. J., Fleurbaey, H., Foltynowicz, A., Furtenbacher, T., Harrison, J. J., Hartmann, J. -M., Horneman, V. -M., Huang, X., Karman, T., Karns, J., Kassi, S., Kleiner, I., Kofman, V., Kwabia-Tchana, F., Lavrentieva, N. N., Lee, T. J., Long, D. A., Lukashevskaya, A. A., Lyulin, O. M., Makhnev, V. Yu., Matt, W., Massie, S. T., Melosso, M., Mikhailenko, S. N., Mondelain, D., Müller, H. S. P., Naumenko, O. V., Perrin, A., Polyansky, O. L., Raddaoui, E., Raston, P. L., Reed, Z. D., Rey, M., Richard, C., Tóbiás, R., Sadiek, I., Schwenke, D. W., Starikova, E., Sung, K., Tamassia, F., Tashkun, S. A., Vander Auwera, J., Vasilenko, I. A., Vigasin, A. A., Villanueva, G. L., Vispoel, B., Wagner, G., Yachmenev, A., and Yurchenko, S. N. (Jan. 2022). "The HITRAN2020 molecular spectroscopic database". In: *Journal of Quantitative Spectroscopy and Radiative Transfer* 277, 107949. DOI: `10.1016/j.jqsrt.2021.107949`.

Greene, Thomas P., Bell, Taylor J., Ducrot, Elsa, Dyrek, Achrène, Lagage, Pierre-Olivier, and Fortney, Jonathan J. (June 2023). "Thermal emission from the Earth-sized exoplanet TRAPPIST-1 b using JWST". In: *Nature* 618.7963, pp. 39–42. DOI: `10.1038/s41586-023-05951-7`. arXiv: `2303.14849 [astro-ph.EP]`.

Guendelman, Ilai and Kaspi, Yohai (Aug. 2019). "Atmospheric Dynamics on Terrestrial Planets: The Seasonal Response to Changes in Orbital, Rotational, and Radiative Timescales". In: *Astrophysical Journal* 881.1, 67. DOI: `10.3847/1538-4357/ab2a06`. arXiv: `1906.05748 [astro-ph.EP]`.

– (Sept. 2020). "Atmospheric Dynamics on Terrestrial Planets with Eccentric Orbits". In: *Astrophysical Journal* 901.1, 46. DOI: `10.3847/1538-4357/abaef8`. arXiv: `2004.14673 [astro-ph.EP]`.

– (Oct. 2022). "The Key Factors Controlling the Seasonality of Planetary Climate". In: *AGU Advances* 3.5, e2022AV000684. DOI: `10.1029/2022AV000684`. arXiv: `2210.11357 [physics.ao-ph]`.

Hammond, Mark and Lewis, Neil T. (Mar. 2021). "The rotational and divergent components of atmospheric circulation on tidally locked planets". In: *Proceedings of the National Academy of Science* 118.13, e2022705118. DOI: `10.1073/pnas.2022705118`. arXiv: `2102.11760 [astro-ph.EP]`.

Haqq-Misra, J. D., Kopparapu, R., Batalha, N. E., Harman, C., and Kasting, J. F. (Dec. 2016). "Limit cycles at the outer edge of the habitable zone". In: *AGU Fall Meeting Abstracts*. Vol. 2016, PP23C-2335, PP23C–2335.

Haqq-Misra, Jacob, Wolf, Eric. T., Joshi, Manoj, Zhang, Xi, and Kopparapu, Ravi Kumar (Jan. 2018). "Demarcating Circulation Regimes of Synchronously Rotating Terrestrial Planets within the Habitable Zone". In: *Astrophysical Journal* 852.2, 67. DOI: `10.3847/1538-4357/aa9f1f`. arXiv: `1710.00435 [astro-ph.EP]`.

Hart, M. H. (Jan. 1978). "The evolution of the atmosphere of the earth". In: *Icarus* 33.1, pp. 23–39. DOI: 10.1016/0019-1035(78)90021-0.

Hawker, George A. and Parry, Ian R. (Apr. 2019). "High-resolution spectroscopy and high contrast imaging with the ELT: looking for O_2 in Proxima b". In: *Monthly Notices of the Royal Astronomical Society* 484.4, pp. 4855–4864. DOI: 10.1093/mnras/stz323. arXiv: 1901.10833 [astro-ph.EP].

He, Feng, Merrelli, Aronne, L'Ecuyer, Tristan S., and Turnbull, Margaret C. (July 2022). "Climate Outcomes of Earth-similar Worlds as a Function of Obliquity and Rotation Rate". In: *Astrophysical Journal* 933.1, 62. DOI: 10.3847/1538-4357/ac6951.

Heller, R., Leconte, J., and Barnes, R. (Apr. 2011). "Tidal obliquity evolution of potentially habitable planets". In: *Astronomy and Astrophysics* 528, A27. DOI: 10.1051/0004-6361/201015809. arXiv: 1101.2156 [astro-ph.EP].

Heller, René and Armstrong, John (Jan. 2014). "Superhabitable Worlds". In: *Astrobiology* 14.1, pp. 50–66. DOI: 10.1089/ast.2013.1088. arXiv: 1401.2392 [astro-ph.EP].

Heras, Ana María, Rauer, Heike, Aerts, Conny, Deleuil, Magali, Gizon, Laurent, Goupil, Marie-Jo, Mas-Hesse, Miguel, Pagano, Isabella, Piotto, Giampaolo, Pollacco, Don, Ragazzoni, Roberto, Ramsay, Gavin, and Udry, Stephane (June 2022). "ESA's PLATO mission: Development status and upcoming milestones". In: *Bulletin of the American Astronomical Society*. Vol. 54, 504.01.

Hippler, Stefan (Jan. 2019). "Adaptive Optics for Extremely Large Telescopes". In: *Journal of Astronomical Instrumentation* 8.2, 1950001-322, pp. 1950001–322. DOI: 10.1142/S2251171719500016. arXiv: 1808.02693 [astro-ph.IM].

Hoffman, Paul F., Kaufman, Alan J., Halverson, Galen P., and Schrag, Daniel P. (Aug. 1998). "A Neoproterozoic Snowball Earth". In: *Science* 281, p. 1342. DOI: 10.1126/science.281.5381.1342.

Höning, Dennis and Spohn, Tilman (Apr. 2023). "Land Fraction Diversity on Earth-like Planets and Implications for Their Habitability". In: *Astrobiology* 23.4, pp. 372–394. DOI: 10.1089/ast.2022.0070. arXiv: 2211.09473 [astro-ph.EP].

Hu, Yongyun and Yang, Jun (Jan. 2014). "Role of ocean heat transport in climates of tidally locked exoplanets around M dwarf stars". In: *Proceedings of the National Academy of Science* 111.2, pp. 629–634. DOI: 10.1073/pnas.1315215111.

Huang, Su-Shu (Sept. 1959). "Occurrence of Life in the Universe". In: *American Scientist* 47.3, pp. 397–402.

Hunke, Elizabeth, Lipscomb, William, Jones, Philip, Turner, Adrian, Jeffery, Nicole, and Elliott, Scott (May 2017). *CICE, The Los Alamos Sea Ice Model, Version 00*. URL: https://www.osti.gov/biblio/1364126.

Hunke, Elizabeth C., Lipscomb, William H., Turner, Adrian K., Jeffery, Nicole, and Elliott, Scott (2013). *CICE: The Los Alamos Sea Ice Model Documentation and Software User's Manual Version 5.0*. Tech. rep. LA-CC-06-012. Los Alamos National Laboratory. URL: https://citeseerx.ist.psu.edu/document?repid=rep1&type=pdf&doi=5eca93a8fbc716474f8fd80c804319b630f90316.

Hunten, Donald M. (Nov. 1973). "The Escape of Light Gases from Planetary Atmospheres." In: *Journal of Atmospheric Sciences* 30.8, pp. 1481–1494. DOI: 10.1175/1520-0469(1973)030\textless{}1481:TEOLGF\textgreater{}2.0.CO;2.

Hunten, Donald M. and Strobel, Darrell F. (Mar. 1974). "Production and Escape of Terrestrial Hydrogen." In: *Journal of Atmospheric Sciences* 31.2, pp. 305–317. DOI: 10.1175/1520-0469(1974)031<0305:PAEOTH>2.0.CO;2.

Iacono, Michael J., Delamere, Jennifer S., Mlawer, Eli J., Shephard, Mark W., Clough, Shepard A., and Collins, William D. (July 2008). "Radiative forcing by long-lived

greenhouse gases: Calculations with the AER radiative transfer models". In: *Journal of Geophysical Research (Atmospheres)* 113.D13, D13103. DOI: 10.1029/2008JD009944.

Ingersoll, Andrew P. (Nov. 1969). "The Runaway Greenhouse: A History of Water on Venus." In: *Journal of Atmospheric Sciences* 26.6, pp. 1191–1198. DOI: 10.1175/1520-0469(1969)026\textless{}1191:TRGAHO\textgreater{}2.0.CO;2.

Intergovernmental Panel on Climate Change (IPCC) (2023). "Annex VII: Glossary". In: *Climate Change 2021 – The Physical Science Basis: Working Group I Contribution to the Sixth Assessment Report of the Intergovernmental Panel on Climate Change.* Cambridge University Press, pp. 2215–2256.

Jack J.Lissauer, lmke de Pater (2017). *Fundamental Planetary Science.* ISBN 978-0-521-85330-9: Cambridge University Press.

Jaumann, R., Tirsch, D., Adeli, S., Bahia, R., Michael, G., Le Deit, L., Grau Galofre, A., Head, J., Bohacek, E., Gross, C., Walter, S. G. H., and Hiesinger, H. (June 2024). "Geological Record of Water and Wind Processes on Mars as Observed by the Mars Express High Resolution Stereo Camera". In: *Space Science Reviews* 220.4, 45. DOI: 10.1007/s11214-024-01076-z.

Jernigan, Jonathan, Laflèche, Émilie, Burke, Angela, and Olson, Stephanie (Feb. 2023). "Superhabitability of High-obliquity and High-eccentricity Planets". In: *Astrophysical Journal* 944.2, 205. DOI: 10.3847/1538-4357/acb81c. arXiv: 2303.02188 [astro-ph.EP].

Ji, Xuan, Bailey, Nora, Fabrycky, Daniel, Kite, Edwin S., Jiang, Jonathan H., and Abbot, Dorian S. (Jan. 2023). "Inner Habitable Zone Boundary for Eccentric Exoplanets". In: *Astrophysical Journal Letters* 943.1, L1. DOI: 10.3847/2041-8213/acaf62. arXiv: 2211.07883 [astro-ph.EP].

Kaltenegger, Lisa and Lin, Zifan (Mar. 2021). "Finding Signs of Life in Transits: High-resolution Transmission Spectra of Earth-line Planets around FGKM Host Stars". In: *Astrophysical Journal Letters* 909.1, L2. DOI: `10.3847/2041-8213/abe634`. arXiv: `2102.12011 [astro-ph.EP]`.

Kane, Stephen R., Bean, Jacob L., Campante, Tiago L., Dalba, Paul A., Fetherolf, Tara, Mocnik, Teo, Ostberg, Colby, Pepper, Joshua, Simpson, Emilie R., Turnbull, Margaret C., Ricker, George R., Vanderspek, Roland, Latham, David W., Seager, Sara, Winn, Joshua N., Jenkins, Jon M., Huber, Daniel, and Chaplin, William J. (Jan. 2021). "Science Extraction from TESS Observations of Known Exoplanet Hosts". In: *Publications of the Astronomical Society of the Pacific* 133.1019, 014402. DOI: `10.1088/1538-3873/abc610`. arXiv: `2010.15164 [astro-ph.EP]`.

Kane, Stephen R. and Gelino, Dawn M. (Oct. 2012). "The Habitable Zone and Extreme Planetary Orbits". In: *Astrobiology* 12.10, pp. 940–945. DOI: `10.1089/ast.2011.0798`. arXiv: `1205.2429 [astro-ph.EP]`.

Kang, Wanying (May 2019). "Wetter Stratospheres on High-obliquity Planets". In: *Astrophysical Journal Letters* 877.1, L6. DOI: `10.3847/2041-8213/ab1f79`. arXiv: `1904.04740 [astro-ph.EP]`.

Kasting, J. F. (June 1988). "Runaway and moist greenhouse atmospheres and the evolution of Earth and Venus". In: *Icarus* 74.3, pp. 472–494. DOI: `10.1016/0019-1035(88)90116-9`.

Kasting, J. F., Pollack, J. B., and Ackerman, T. P. (Mar. 1984). "Response of Earth's atmosphere to increases in solar flux and implications for loss of water from Venus". In: *Icarus* 57.3, pp. 335–355. DOI: `10.1016/0019-1035(84)90122-2`.

Kasting, James F., Chen, Howard, and Kopparapu, Ravi K. (Nov. 2015). "Stratospheric Temperatures and Water Loss from Moist Greenhouse Atmospheres of Earth-like Plan-

ets". In: *Astrophysical Journal Letters* 813.1, L3. DOI: 10.1088/2041-8205/813/1/L3. arXiv: 1510.03527 [astro-ph.EP].

Kasting, James F., Whitmire, Daniel P., and Reynolds, Ray T. (Jan. 1993). "Habitable Zones around Main Sequence Stars". In: *Icarus* 101.1, pp. 108–128. DOI: 10.1006/icar.1993.1010.

Kipping, David M., Cameron, Chris, Hartman, Joel D., Davenport, James R. A., Matthews, Jaymie M., Sasselov, Dimitar, Rowe, Jason, Siverd, Robert J., Chen, Jingjing, Sandford, Emily, Bakos, Gáspár Á., Jordán, Andrés, Bayliss, Daniel, Henning, Thomas, Mancini, Luigi, Penev, Kaloyan, Csubry, Zoltan, Bhatti, Waqas, Da Silva Bento, Joao, Guenther, David B., Kuschnig, Rainer, Moffat, Anthony F. J., Rucinski, Slavek M., and Weiss, Werner W. (Mar. 2017). "No Conclusive Evidence for Transits of Proxima b in MOST Photometry". In: *Astronomical Journal* 153.3, 93. DOI: 10.3847/1538-3881/153/3/93. arXiv: 1609.08718 [astro-ph.EP].

Kirk, James, Stevenson, Kevin B., Fu, Guangwei, Lustig-Yaeger, Jacob, Moran, Sarah E., Peacock, Sarah, Alam, Munazza K., Batalha, Natasha E., Bennett, Katherine A., Gonzalez-Quiles, Junellie, López-Morales, Mercedes, Lothringer, Joshua D., MacDonald, Ryan J., May, E. M., Mayorga, L. C., Rustamkulov, Zafar, Sing, David K., Sotzen, Kristin S., Valenti, Jeff A., and Wakeford, Hannah R. (Mar. 2024). "JWST/NIRCam Transmission Spectroscopy of the Nearby Sub-Earth GJ 341b". In: *Astronomical Journal* 167.3, 90. DOI: 10.3847/1538-3881/ad19df. arXiv: 2401.06043 [astro-ph.EP].

Koll, Daniel D. B. and Abbot, Dorian S. (Mar. 2015). "Deciphering Thermal Phase Curves of Dry, Tidally Locked Terrestrial Planets". In: *Astrophysical Journal* 802.1, 21. DOI: 10.1088/0004-637X/802/1/21. arXiv: 1412.8216 [astro-ph.EP].

Kopparapu, Ravi Kumar, Ramirez, Ramses, Kasting, James F., Eymet, Vincent, Robinson, Tyler D., Mahadevan, Suvrath, Terrien, Ryan C., Domagal-Goldman, Shawn, Meadows, Victoria, and Deshpande, Rohit (Mar. 2013). "Habitable Zones around

Main-sequence Stars: New Estimates". In: *Astrophysical Journal* 765.2, 131. DOI: 10.1088/0004-637X/765/2/131. arXiv: `1301.6674 [astro-ph.EP]`.

Kopparapu, Ravi kumar, Wolf, Eric T., Arney, Giada, Batalha, Natasha E., Haqq-Misra, Jacob, Grimm, Simon L., and Heng, Kevin (Aug. 2017). "Habitable Moist Atmospheres on Terrestrial Planets near the Inner Edge of the Habitable Zone around M Dwarfs". In: *Astrophysical Journal* 845.1, 5. DOI: `10.3847/1538-4357/aa7cf9`. arXiv: `1705.10362 [astro-ph.EP]`.

Kreidberg, Laura, Koll, Daniel D. B., Morley, Caroline, Hu, Renyu, Schaefer, Laura, Deming, Drake, Stevenson, Kevin B., Dittmann, Jason, Vanderburg, Andrew, Berardo, David, Guo, Xueying, Stassun, Keivan, Crossfield, Ian, Charbonneau, David, Latham, David W., Loeb, Abraham, Ricker, George, Seager, Sara, and Vanderspek, Roland (Aug. 2019). "Absence of a thick atmosphere on the terrestrial exoplanet LHS 3844b". In: *Nature* 573.7772, pp. 87–90. DOI: `10.1038/s41586-019-1497-4`. arXiv: `1908.06834 [astro-ph.EP]`.

Kreidberg, Laura and Loeb, Abraham (Nov. 2016). "Prospects for Characterizing the Atmosphere of Proxima Centauri b". In: *Astrophysical Journal Letters* 832.1, L12. DOI: `10.3847/2041-8205/832/1/L12`. arXiv: `1608.07345 [astro-ph.EP]`.

Kroupa, Pavel (Jan. 2002). "The Initial Mass Function of Stars: Evidence for Uniformity in Variable Systems". In: *Science* 295.5552, pp. 82–91. DOI: `10.1126/science.1067524`. arXiv: `astro-ph/0201098 [astro-ph]`.

Lacis, A. A. and Oinas, V. (May 1991). "A description of the correlated-k distribution method for modelling nongray gaseous absorption, thermal emission, and multiple scattering in vertically inhomogeneous atmospheres". In: *Journal of Geophysical Research* 96, pp. 9027–9064. DOI: `10.1029/90JD01945`.

Lammer, Helmut, Lichtenegger, Herbert I. M., Kulikov, Yuri N., Grießmeier, Jean-Mathias, Terada, N., Erkaev, Nikolai V., Biernat, Helfried K., Khodachenko, Maxim L., Ribas, Ignasi, Penz, Thomas, and Selsis, Franck (Feb. 2007). "Coronal Mass Ejection (CME) Activity of Low Mass M Stars as An Important Factor for The Habitability of Terrestrial Exoplanets. II. CME-Induced Ion Pick Up of Earth-like Exoplanets in Close-In Habitable Zones". In: *Astrobiology* 7.1, pp. 185–207. DOI: 10.1089/ast.2006.0128.

Larson, Vincent E., Golaz, Jean-Christophe, and Cotton, William R. (Dec. 2002). "Small-Scale and Mesoscale Variability in Cloudy Boundary Layers: Joint Probability Density Functions." In: *Journal of Atmospheric Sciences* 59.24, pp. 3519–3539. DOI: 10.1175/1520-0469(2002)059<3519:SSAMVI>2.0.CO;2.

Laughlin, Gregory, Bodenheimer, Peter, and Adams, Fred C. (June 1997). "The End of the Main Sequence". In: *Astrophysical Journal* 482.1, pp. 420–432. DOI: 10.1086/304125.

Lawrence, David M., Fisher, Rosie A., Koven, Charles D., Oleson, Keith W., Swenson, Sean C., Bonan, Gordon, Collier, Nathan, Ghimire, Bardan, van Kampenhout, Leo, Kennedy, Daniel, Kluzek, Erik, Lawrence, Peter J., Li, Fang, Li, Hongyi, Lombardozzi, Danica, Riley, William J., Sacks, William J., Shi, Mingjie, Vertenstein, Mariana, Wieder, William R., Xu, Chonggang, Ali, Ashehad A., Badger, Andrew M., Bisht, Gautam, van den Broeke, Michiel, Brunke, Michael A., Burns, Sean P., Buzan, Jonathan, Clark, Martyn, Craig, Anthony, Dahlin, Kyla, Drewniak, Beth, Fisher, Joshua B., Flanner, Mark, Fox, Andrew M., Gentine, Pierre, Hoffman, Forrest, Keppel-Aleks, Gretchen, Knox, Ryan, Kumar, Sanjiv, Lenaerts, Jan, Leung, L. Ruby, Lipscomb, William H., Lu, Yaqiong, Pandey, Ashutosh, Pelletier, Jon D., Perket, Justin, Randerson, James T., Ricciuto, Daniel M., Sanderson, Benjamin M., Slater, Andrew, Subin, Zachary M., Tang, Jinyun, Thomas, R. Quinn, Val Martin, Maria, and Zeng, Xubin (Dec. 2019). "The Community Land Model Version 5: Description of New Features,

Benchmarking, and Impact of Forcing Uncertainty". In: *Journal of Advances in Modeling Earth Systems* 11.12, pp. 4245–4287. DOI: `10.1029/2018MS001583`.

Leconte, Jérémy, Wu, Hanbo, Menou, Kristen, and Murray, Norman (Feb. 2015). "Asynchronous rotation of Earth-mass planets in the habitable zone of lower-mass stars". In: *Science* 347.6222, pp. 632–635. DOI: `10.1126/science.1258686`. arXiv: `1502.01952` `[astro-ph.EP]`.

Leger, A., Pirre, M., and Marceau, F. J. (Sept. 1993). "Search for primitive life on a distant planet: relevance of 02 and 03 detections". In: *Astronomy and Astrophysics* 277, p. 309.

Lewis, Neil T., Lambert, F. Hugo, Boutle, Ian A., Mayne, Nathan J., Manners, James, and Acreman, David M. (Feb. 2018). "The Influence of a Substellar Continent on the Climate of a Tidally Locked Exoplanet". In: *Astrophysical Journal* 854.2, 171. DOI: `10.3847/1538-4357/aaad0a`. arXiv: `1802.00378 [astro-ph.EP]`.

Li, Jiadong, Liu, Chao, Zhang, Zhi-Yu, Tian, Hao, Fu, Xiaoting, Li, Jiao, and Yan, Zhi-Qiang (Jan. 2023). "Stellar initial mass function varies with metallicity and time". In: *Nature* 613.7944, pp. 460–462. DOI: `10.1038/s41586-022-05488-1`. arXiv: `2301.07029 [astro-ph.GA]`.

Li, Te, Wang, Minghuai, Guo, Zhun, Yang, Ben, Xu, Yifei, Han, Xiaomen, and Sun, Jianning (Dec. 2022). "An Updated CLUBB PDF Closure Scheme to Improve Low Cloud Simulation in CAM6". In: *Journal of Advances in Modeling Earth Systems* 14.12, e2022MS003127. DOI: `10.1029/2022MS003127`.

Limbach, Mary Anne, Lustig-Yaeger, Jacob, Vanderburg, Andrew, Vos, Johanna M., Heller, René, and Robinson, Tyler D. (Aug. 2024). "Exomoons and Exorings with the Habitable Worlds Observatory. I. On the Detection of Earth–Moon Analog Shadows

and Eclipses". In: *Astronomical Journal* 168.2, 57. DOI: 10.3847/1538-3881/ad4a75. arXiv: 2405.02408 [astro-ph.EP].

Lincowski, Andrew P., Meadows, Victoria S., Zieba, Sebastian, Kreidberg, Laura, Morley, Caroline, Gillon, Michaël, Selsis, Franck, Agol, Eric, Bolmont, Emeline, Ducrot, Elsa, Hu, Renyu, Koll, Daniel D. B., Lyu, Xintong, Mandell, Avi, Suissa, Gabrielle, and Tamburo, Patrick (Sept. 2023). "Potential Atmospheric Compositions of TRAPPIST-1 c Constrained by JWST/MIRI Observations at 15 µm". In: *Astrophysical Journal Letters* 955.1, L7. DOI: 10.3847/2041-8213/acee02. arXiv: 2308.05899 [astro-ph.EP].

Linsenmeier, Manuel, Pascale, Salvatore, and Lucarini, Valerio (Jan. 2015). "Climate of Earth-like planets with high obliquity and eccentric orbits: Implications for habitability conditions". In: *Planetary and Space Science* 105, pp. 43–59. DOI: 10.1016/j.pss.2014.11.003. arXiv: 1401.5323 [astro-ph.EP].

Lipscomb, William H., Fyke, Jeremy G., Vizcaíno, Miren, Sacks, William J., Wolfe, Jon, Vertenstein, Mariana, Craig, Anthony, Kluzek, Erik, and Lawrence, David M. (Oct. 2013). "Implementation and Initial Evaluation of the Glimmer Community Ice Sheet Model in the Community Earth System Model". In: *Journal of Climate* 26.19, pp. 7352–7371. DOI: 10.1175/JCLI-D-12-00557.1.

Liu, Binghan, Marsh, Daniel R., Walsh, Catherine, and Cooke, Greg (Sept. 2023). "Higher water loss on Earth-like exoplanets in eccentric orbits". In: *Monthly Notices of the Royal Astronomical Society* 524.1, pp. 1491–1502. DOI: 10.1093/mnras/stad1828. arXiv: 2306.10958 [astro-ph.EP].

Liu, X., Easter, R. C., Ghan, S. J., Zaveri, R., Rasch, P., Shi, X., Lamarque, J. -F., Gettelman, A., Morrison, H., Vitt, F., Conley, A., Park, S., Neale, R., Hannay, C., Ekman, A. M. L., Hess, P., Mahowald, N., Collins, W., Iacono, M. J., Bretherton, C. S., Flanner, M. G., and Mitchell, D. (May 2012). "Toward a minimal representation of aerosols in climate models: description and evaluation in the Community Atmosphere

Model CAM5". In: *Geoscientific Model Development* 5.3, pp. 709–739. DOI: 10.5194/gmd-5-709-2012.

Liu, X., Ma, P. -L., Wang, H., Tilmes, S., Singh, B., Easter, R. C., Ghan, S. J., and Rasch, P. J. (Feb. 2016). "Description and evaluation of a new four-mode version of the Modal Aerosol Module (MAM4) within version 5.3 of the Community Atmosphere Model". In: *Geoscientific Model Development* 9.2, pp. 505–522. DOI: 10.5194/gmd-9-505-2016.

Lobo, Ana, Shields, Aomawa, Palubski, Igor, and Wolf, Eric (June 2022). "Terminator Habitability on M-Dwarf Planets". In: *American Astronomical Society Meeting #240*. Vol. 240. American Astronomical Society Meeting Abstracts, 402.06.

Lobo, Ana H., Shields, Aomawa L., Palubski, Igor Z., and Wolf, Eric (Mar. 2023). "Terminator Habitability: The Case for Limited Water Availability on M-dwarf Planets". In: *Astrophysical Journal* 945.2, 161. DOI: 10.3847/1538-4357/aca970. arXiv: 2212.06185 [astro-ph.EP].

Long, Matthew C., Moore, J. Keith, Lindsay, Keith, Levy, Michael, Doney, Scott C., Luo, Jessica Y., Krumhardt, Kristen M., Letscher, Robert T., Grover, Maxwell, and Sylvester, Zephyr T. (Dec. 2021). "Simulations With the Marine Biogeochemistry Library (MARBL)". In: *Journal of Advances in Modeling Earth Systems* 13.12, e02647. DOI: 10.1029/2021MS002647.

Lopez, T. A., Barros, S. C. C., Santerne, A., Deleuil, M., Adibekyan, V., Almenara, J. -M., Armstrong, D. J., Brugger, B., Barrado, D., Bayliss, D., Boisse, I., Bonomo, A. S., Bouchy, F., Brown, D. J. A., Carli, E., Demangeon, O., Dumusque, X., Díaz, R. F., Faria, J. P., Figueira, P., Foxell, E., Giles, H., Hébrard, G., Hojjatpanah, S., Kirk, J., Lillo-Box, J., Lovis, C., Mousis, O., da Nóbrega, H. J., Nielsen, L. D., Neal, J. J., Osborn, H. P., Pepe, F., Pollacco, D., Santos, N. C., Sousa, S. G., Udry, S., Vigan, A., and Wheatley, P. J. (Nov. 2019). "Exoplanet characterisation in the longest known

resonant chain: the K2-138 system seen by HARPS". In: *Astronomy and Astrophysics* 631, A90. DOI: 10.1051/0004-6361/201936267. arXiv: 1909.13527 [astro-ph.EP].

Lu, Yi-Chuan and Romps, David M. (Sept. 2023). "Is a wet-bulb temperature of 35 °C the correct threshold for human survivability?" In: *Environmental Research Letters* 18.9, 094021. DOI: 10.1088/1748-9326/ace83c.

Lucarini, Valerio and Bódai, Tamás (Apr. 2019). "Transitions across Melancholia States in a Climate Model: Reconciling the Deterministic and Stochastic Points of View". In: *Physical Review Letters* 122.15, 158701. DOI: 10.1103/PhysRevLett.122.158701. arXiv: 1808.05098 [physics.ao-ph].

Lustig-Yaeger, Jacob, Fu, Guangwei, May, E. M., Ceballos, Kevin N. Ortiz, Moran, Sarah E., Peacock, Sarah, Stevenson, Kevin B., Kirk, James, López-Morales, Mercedes, MacDonald, Ryan J., Mayorga, L. C., Sing, David K., Sotzen, Kristin S., Valenti, Jeff A., Redai, Jéa I. Adams, Alam, Munazza K., Batalha, Natasha E., Bennett, Katherine A., Gonzalez-Quiles, Junellie, Kruse, Ethan, Lothringer, Joshua D., Rustamkulov, Zafar, and Wakeford, Hannah R. (Nov. 2023). "A JWST transmission spectrum of the nearby Earth-sized exoplanet LHS 475 b". In: *Nature Astronomy* 7, pp. 1317–1328. DOI: 10.1038/s41550-023-02064-z. arXiv: 2301.04191 [astro-ph.EP].

Macdonald, Evelyn, Menou, Kristen, Paradise, Adiv, and Lee, Christopher (Dec. 2022a). "Influence of Dayside Land on Climates and Transit Spectra of Synchronously Rotating Rocky Planets". In: *AGU Fall Meeting Abstracts*. Vol. 2022, P44A-02, P44A–02.

Macdonald, Evelyn, Paradise, Adiv, Menou, Kristen, and Lee, Christopher (June 2022b). "Climate uncertainties caused by unknown land distribution on habitable M-Earths". In: *Monthly Notices of the Royal Astronomical Society* 513.2, pp. 2761–2769. DOI: 10.1093/mnras/stac1040. arXiv: 2110.04310 [astro-ph.EP].

MacKay, R.M. and Khalil, M.A.K. (1991). "Theory and development of a one dimensional time dependent radiative convective climate model". In: *Chemosphere* 22.3, pp. 383–417. ISSN: 0045-6535. DOI: `https://doi.org/10.1016/0045-6535(91)90326-9`. URL: `https://www.sciencedirect.com/science/article/pii/0045653591903269`.

Madhusudhan, Nikku (2018). "Atmospheric Retrieval of Exoplanets". In: *Handbook of Exoplanets*. Ed. by Hans J. Deeg and Juan Antonio Belmonte, 104. DOI: `10.1007/978-3-319-55333-7_104`.

Madhusudhan, Nikku, Agúndez, Marcelino, Moses, Julianne I., and Hu, Yongyun (Dec. 2016). "Exoplanetary Atmospheres—Chemistry, Formation Conditions, and Habitability". In: *Space Science Reviews* 205.1-4, pp. 285–348. DOI: `10.1007/s11214-016-0254-3`. arXiv: `1604.06092 [astro-ph.EP]`.

Madhusudhan, Nikku, Sarkar, Subhajit, Constantinou, Savvas, Holmberg, Måns, Piette, Anjali A. A., and Moses, Julianne I. (Oct. 2023). "Carbon-bearing Molecules in a Possible Hycean Atmosphere". In: *Astrophysical Journal Letters* 956.1, L13. DOI: `10.3847/2041-8213/acf577`. arXiv: `2309.05566 [astro-ph.EP]`.

Maher, Penelope, Gerber, Edwin P., Medeiros, Brian, Merlis, Timothy M., Sherwood, Steven, Sheshadri, Aditi, Sobel, Adam H., Vallis, Geoffrey K., Voigt, Aiko, and Zurita-Gotor, Pablo (June 2019). "Model Hierarchies for Understanding Atmospheric Circulation". In: *Reviews of Geophysics* 57.2, pp. 250–280. DOI: `10.1029/2018RG000607`.

Mansfield, Laura A., Gupta, Aman, Burnett, Adam C., Green, Brian, Wilka, Catherine, and Sheshadri, Aditi (Oct. 2023). "Updates on Model Hierarchies for Understanding and Simulating the Climate System: A Focus on Data-Informed Methods and Climate Change Impacts". In: *Journal of Advances in Modeling Earth Systems* 15.10, e2023MS003715. DOI: `10.1029/2023MS003715`.

Marotzke, Jochem and Botzet, Michael (Aug. 2007). "Present-day and ice-covered equilibrium states in a comprehensive climate model". In: *Geophysical Research Letters* 34.16, L16704. DOI: 10.1029/2006GL028880.

Marsh, Daniel R., Mills, Michael J., Kinnison, Douglas E., Lamarque, Jean-Francois, Calvo, Natalia, and Polvani, Lorenzo M. (Oct. 2013). "Climate Change from 1850 to 2005 Simulated in CESM1(WACCM)". In: *Journal of Climate* 26.19, pp. 7372–7391. DOI: 10.1175/JCLI-D-12-00558.1.

Marshall, John E. A., Lakin, Jon, Troth, Ian, and Wallace-Johnson, Sarah M. (May 2020). "UV-B radiation was the Devonian-Carboniferous boundary terrestrial extinction kill mechanism". In: *Science Advances* 6.22, eaba0768. DOI: 10.1126/sciadv.aba0768.

Matthes, Katja, Funke, Bernd, Andersson, Monika E., Barnard, Luke, Beer, Jürg, Charbonneau, Paul, Clilverd, Mark A., Dudok de Wit, Thierry, Haberreiter, Margit, Hendry, Aaron, Jackman, Charles H., Kretzschmar, Matthieu, Kruschke, Tim, Kunze, Markus, Langematz, Ulrike, Marsh, Daniel R., Maycock, Amanda C., Misios, Stergios, Rodger, Craig J., Scaife, Adam A., Seppälä, Annika, Shangguan, Ming, Sinnhuber, Miriam, Tourpali, Kleareti, Usoskin, Ilya, van de Kamp, Max, Verronen, Pekka T., and Versick, Stefan (June 2017). "Solar forcing for CMIP6 (v3.2)". In: *Geoscientific Model Development* 10.6, pp. 2247–2302. DOI: 10.5194/gmd-10-2247-2017.

May, E. M., MacDonald, Ryan J., Bennett, Katherine A., Moran, Sarah E., Wakeford, Hannah R., Peacock, Sarah, Lustig-Yaeger, Jacob, Highland, Alicia N., Stevenson, Kevin B., Sing, David K., Mayorga, L. C., Batalha, Natasha E., Kirk, James, López-Morales, Mercedes, Valenti, Jeff A., Alam, Munazza K., Alderson, Lili, Fu, Guangwei, Gonzalez-Quiles, Junellie, Lothringer, Joshua D., Rustamkulov, Zafar, and Sotzen, Kristin S. (Dec. 2023). "Double Trouble: Two Transits of the Super-Earth GJ 1132 b Observed with JWST NIRSpec G395H". In: *Astrophysical Journal Letters* 959.1, L9. DOI: 10.3847/2041-8213/ad054f. arXiv: 2310.10711 [astro-ph.EP].

May, E. M., Taylor, J., Komacek, T. D., Line, M. R., and Parmentier, V. (Apr. 2021). "Water Ice Cloud Variability and Multi-epoch Transmission Spectra of TRAPPIST-1e". In: *Astrophysical Journal Letters* 911.2, L30. DOI: 10.3847/2041-8213/abeeff. arXiv: 2103.09313 [astro-ph.EP].

Mayor, Michel and Queloz, Didier (Nov. 1995). "A Jupiter-mass companion to a solar-type star". In: *Nature* 378.6555, pp. 355–359. DOI: 10.1038/378355a0.

Meadows, Victoria, Arney, Giada, Schwieterman, Edward, Lustig-Yaeger, Jacob A., Lincowski, Andrew, Robinson, Tyler D., Domagal-Goldman, Shawn, Barnes, Rory, Fleming, David P., Deitrick, Russell, Luger, Rodrigo, Driscoll, Peter E., Quinn, Thomas R., and Crisp, David (Jan. 2017). "Proxima Centauri b: Environmental States and Observational Discriminants". In: *American Astronomical Society Meeting Abstracts #229*. Vol. 229. American Astronomical Society Meeting Abstracts, 120.03.

Meadows, Victoria S., Arney, Giada N., Schwieterman, Edward W., Lustig-Yaeger, Jacob, Lincowski, Andrew P., Robinson, Tyler, Domagal-Goldman, Shawn D., Deitrick, Russell, Barnes, Rory K., Fleming, David P., Luger, Rodrigo, Driscoll, Peter E., Quinn, Thomas R., and Crisp, David (Feb. 2018a). "The Habitability of Proxima Centauri b: Environmental States and Observational Discriminants". In: *Astrobiology* 18.2, pp. 133–189. DOI: 10.1089/ast.2016.1589. arXiv: 1608.08620 [astro-ph.EP].

Meadows, Victoria S., Reinhard, Christopher T., Arney, Giada N., Parenteau, Mary N., Schwieterman, Edward W., Domagal-Goldman, Shawn D., Lincowski, Andrew P., Stapelfeldt, Karl R., Rauer, Heike, DasSarma, Shiladitya, Hegde, Siddharth, Narita, Norio, Deitrick, Russell, Lustig-Yaeger, Jacob, Lyons, Timothy W., Siegler, Nicholas, and Grenfell, J. Lee (June 2018b). "Exoplanet Biosignatures: Understanding Oxygen as a Biosignature in the Context of Its Environment". In: *Astrobiology* 18.6, pp. 630–662. DOI: 10.1089/ast.2017.1727. arXiv: 1705.07560 [astro-ph.EP].

Mills, Michael J., Schmidt, Anja, Easter, Richard, Solomon, Susan, Kinnison, Douglas E., Ghan, Steven J., Neely, Ryan R., Marsh, Daniel R., Conley, Andrew, Bardeen, Charles G., and Gettelman, Andrew (Mar. 2016). "Global volcanic aerosol properties derived from emissions, 1990-2014, using CESM1(WACCM)". In: *Journal of Geophysical Research (Atmospheres)* 121.5, pp. 2332–2348. DOI: 10.1002/2015JD024290.

Mlawer, Eli J., Taubman, Steven J., Brown, Patrick D., Iacono, Michael J., and Clough, Shepard A. (July 1997). "Radiative transfer for inhomogeneous atmospheres: RRTM, a validated correlated-k model for the longwave". In: *Journal of Geophysical Research* 102.D14, pp. 16, 663–16, 682. DOI: 10.1029/97JD00237.

Moran, Sarah E., Stevenson, Kevin B., Sing, David K., MacDonald, Ryan J., Kirk, James, Lustig-Yaeger, Jacob, Peacock, Sarah, Mayorga, L. C., Bennett, Katherine A., López-Morales, Mercedes, May, E. M., Rustamkulov, Zafar, Valenti, Jeff A., Adams Redai, Jéa I., Alam, Munazza K., Batalha, Natasha E., Fu, Guangwei, Gonzalez-Quiles, Junellie, Highland, Alicia N., Kruse, Ethan, Lothringer, Joshua D., Ortiz Ceballos, Kevin N., Sotzen, Kristin S., and Wakeford, Hannah R. (May 2023). "High Tide or Riptide on the Cosmic Shoreline? A Water-rich Atmosphere or Stellar Contamination for the Warm Super-Earth GJ 486b from JWST Observations". In: *Astrophysical Journal Letters* 948.1, L11. DOI: 10.3847/2041-8213/accb9c. arXiv: 2305.00868 [astro-ph.EP].

Murante, Giuseppe, Provenzale, Antonello, Vladilo, Giovanni, Taffoni, Giuliano, Silva, Laura, Palazzi, Elisa, Hardenberg, Jost von, Maris, Michele, Londero, Elisa, Knapic, Cristina, and Zorba, Sonia (Feb. 2020). "Climate bistability of Earth-like exoplanets". In: *Monthly Notices of the Royal Astronomical Society* 492.2, pp. 2638–2650. DOI: 10.1093/mnras/stz3529. arXiv: 1912.05392 [astro-ph.EP].

Nance, R. Damian (Sept. 2022). "The supercontinent cycle and Earth's long-term climate". In: *Annals of the New York Academy of Sciences* 1515.1, pp. 33–49. DOI: 10.1111/nyas.14849.

REFERENCES

NASA Exoplanet Science Institute (2024). *Exoplanet and Candidates Statistics.* URL: https://exoplanetarchive.ipac.caltech.edu/docs/counts_detail.html (visited on 08/18/2024).

NCAR (2024). *Community Atmosphere Model (CAM) Documentation.* Accessed: August 30, 2024. URL: https://ncar.github.io/CAM/doc/build/html/index.html.

Neichel, B., Mouillet, D., Gendron, E., Correia, C., Sauvage, J. F., and Fusco, T. (Dec. 2018). "Overview of the European Extremely Large Telescope and its instrument suite". In: *SF2A-2018: Proceedings of the Annual meeting of the French Society of Astronomy and Astrophysics.* Ed. by P. Di Matteo, F. Billebaud, F. Herpin, N. Lagarde, J. -B. Marquette, A. Robin, and O. Venot, p. Di. DOI: 10.48550/arXiv.1812.06639. arXiv: 1812.06639 [astro-ph.IM].

North, Gerald R. (Nov. 1975). "Theory of Energy-Balance Climate Models." In: *Journal of the Atmospheric Sciences* 32.11, pp. 2033–2043. DOI: 10.1175/1520-0469(1975) 032<2033:TOEBCM>2.0.CO;2.

Ohno, Kazumasa and Zhang, Xi (Mar. 2019a). "Atmospheres on Nonsynchronized Eccentric-tilted Exoplanets. I. Dynamical Regimes". In: *Astrophysical Journal* 874.1, 1. DOI: 10.3847/1538-4357/ab06cc. arXiv: 1903.00907 [astro-ph.EP].

– (Mar. 2019b). "Atmospheres on Nonsynchronized Eccentric-tilted Exoplanets. II. Thermal Light Curves". In: *Astrophysical Journal* 874.1, 2. DOI: 10.3847/1538-4357/ab06ca. arXiv: 1903.00908 [astro-ph.EP].

Oinas, V., Lacis, A. A., Rind, D., Shindell, D. T., and Hansen, J. E. (July 2001). "Radiative cooling by stratospheric water vapor: Big differences in GCM results". In: *Geophysical Research Letters* 28.14, pp. 2791–2794. DOI: 10.1029/2001GL013137.

Ozaki, Kazumi and Reinhard, Christopher T. (Jan. 2021). "The future lifespan of Earth's oxygenated atmosphere". In: *Nature Geoscience* 14.3, pp. 138–142. DOI: 10.1038/s41561-021-00693-5. arXiv: 2103.02694 [astro-ph.EP].

Padovani, Paolo and Cirasuolo, Michele (Jan. 2023). "The Extremely Large Telescope". In: *Contemporary Physics* 64.1, pp. 47–64. DOI: 10.1080/00107514.2023.2266921. arXiv: 2312.04299 [astro-ph.IM].

Palubski, Igor Z., Shields, Aomawa L., and Deitrick, Russell (Feb. 2020). "Habitability and Water Loss Limits on Eccentric Planets Orbiting Main-sequence Stars". In: *Astrophysical Journal* 890.1, 30. DOI: 10.3847/1538-4357/ab66b2. arXiv: 2001.02228 [astro-ph.EP].

Park, Sungsu, Bretherton, Christopher S., and Rasch, Philip J. (Sept. 2014). "Integrating Cloud Processes in the Community Atmosphere Model, Version 5". In: *Journal of Climate* 27.18, pp. 6821–6856. DOI: 10.1175/JCLI-D-14-00087.1.

Pettit, J., Randall, C. E., Marsh, D. R., Bardeen, C. G., Qian, L., Jackman, C. H., Woods, T. N., Coster, A., and Harvey, V. L. (July 2018). "Effects of the September 2005 Solar Flares and Solar Proton Events on the Middle Atmosphere in WACCM". In: *Journal of Geophysical Research (Space Physics)* 123.7, pp. 5747–5763. DOI: 10.1029/2018JA025294.

Pierrehumbert, R. T. (Jan. 2011). "A Palette of Climates for Gliese 581g". In: *Astrophysical Journal Letters* 726.1, L8. DOI: 10.1088/2041-8205/726/1/L8.

Pierrehumbert, Raymond T. (2010). *Principles of Planetary Climate*. Cambridge University Press.

Polvani, LM, Clement, AC, Medeiros, B, Benedict, JJ, and Simpson, IR (2017). "When less is more: Opening the door to simpler climate models, Eos, 98". In: *Eos, Transactions American Geophysical Union* 99.3, pp. 15–16.

Proedrou, Elisavet and Hocke, Klemens (June 2016). "Characterising the three-dimensional ozone distribution of a tidally locked Earth-like planet". In: *Earth, Planets and Space* 68.1, 96. DOI: `10.1186/s40623-016-0461-x`.

Quanz, S. P., Ottiger, M., Fontanet, E., Kammerer, J., Menti, F., Dannert, F., Gheorghe, A., Absil, O., Airapetian, V. S., Alei, E., Allart, R., Angerhausen, D., Blumenthal, S., Buchhave, L. A., Cabrera, J., Carrión-González, Ó., Chauvin, G., Danchi, W. C., Dandumont, C., Defrére, D., Dorn, C., Ehrenreich, D., Ertel, S., Fridlund, M., García Muñoz, A., Gascón, C., Girard, J. H., Glauser, A., Grenfell, J. L., Guidi, G., Hagelberg, J., Helled, R., Ireland, M. J., Janson, M., Kopparapu, R. K., Korth, J., Kozakis, T., Kraus, S., Léger, A., Leedjärv, L., Lichtenberg, T., Lillo-Box, J., Linz, H., Liseau, R., Loicq, J., Mahendra, V., Malbet, F., Mathew, J., Mennesson, B., Meyer, M. R., Mishra, L., Molaverdikhani, K., Noack, L., Oza, A. V., Pallé, E., Parviainen, H., Quirrenbach, A., Rauer, H., Ribas, I., Rice, M., Romagnolo, A., Rugheimer, S., Schwieterman, E. W., Serabyn, E., Sharma, S., Stassun, K. G., Szulágyi, J., Wang, H. S., Wunderlich, F., Wyatt, M. C., and LIFE Collaboration (Aug. 2022). "Large Interferometer For Exoplanets (LIFE). I. Improved exoplanet detection yield estimates for a large mid-infrared space-interferometer mission". In: *Astronomy and Astrophysics* 664, A21. DOI: `10.1051/0004-6361/202140366`. arXiv: `2101.07500 [astro-ph.EP]`.

Quirrenbach, Andreas (Mar. 2022). "The Equilibrium Temperature of Planets on Eccentric Orbits: Time Scales and Averages". In: *Research Notes of the American Astronomical Society* 6.3, 56. DOI: `10.3847/2515-5172/ac5f0d`. arXiv: `2203.11723 [astro-ph.EP]`.

Ramirez, Solange, Akeson, R. L., Ciardi, D., Kane, S. R., Plavchan, P., von Braun, K., and NASA Exoplanet Archive Team (Jan. 2013). "The NASA Exoplanet Archive". In: *American Astronomical Society Meeting Abstracts #221*. Vol. 221. American Astronomical Society Meeting Abstracts, 334.01.

Ranjan, Sukrit, Schwieterman, Edward W., Leung, Michaela, Harman, Chester E., and Hu, Renyu (Nov. 2023). "The Importance of the Upper Atmosphere to CO/O_2 Runaway on Habitable Planets Orbiting Low-mass Stars". In: *Astrophysical Journal Letters* 958.1, L15. DOI: 10.3847/2041-8213/ad037c. arXiv: 2307.08752 [astro-ph.EP].

Rauer, H., Aerts, C., Cabrera, J., and PLATO Team (Sept. 2016). "The PLATO Mission". In: *Astronomische Nachrichten* 337.8-9, p. 961. DOI: 10.1002/asna.201612408.

Ribas, Ignasi, Bolmont, Emeline, Selsis, Franck, Reiners, Ansgar, Leconte, Jérémy, Raymond, Sean N., Engle, Scott G., Guinan, Edward F., Morin, Julien, Turbet, Martin, Forget, François, and Anglada-Escudé, Guillem (Dec. 2016). "The habitability of Proxima Centauri b. I. Irradiation, rotation and volatile inventory from formation to the present". In: *Astronomy and Astrophysics* 596, A111. DOI: 10.1051/0004-6361/201629576. arXiv: 1608.06813 [astro-ph.EP].

Ribas, Ignasi, Gregg, Michael D., Boyajian, Tabetha S., and Bolmont, Emeline (July 2017). "The full spectral radiative properties of Proxima Centauri". In: *Astronomy and Astrophysics* 603, A58. DOI: 10.1051/0004-6361/201730582. arXiv: 1704.08449 [astro-ph.SR].

Richter, Jadwiga H., Glanville, Anne A., Edwards, James, Kauffman, Brian, Davis, Nicholas A., Jaye, Abigail, Kim, Hyemi, Pedatella, Nicholas M., Sun, Lantao, Berner, Judith, Kim, Who M., Yeager, Stephen G., Danabasoglu, Gokhan, Caron, Julie M., and Oleson, Keith W. (June 2022). "Subseasonal Earth System Prediction with CESM2". In: *Weather and Forecasting* 37.6, pp. 797–815. DOI: 10.1175/WAF-D-21-0163.1.

Ridgway, R. J., Zamyatina, M., Mayne, N. J., Manners, J., Lambert, F. H., Braam, M., Drummond, B., Hébrard, E., Palmer, P. I., and Kohary, K. (Jan. 2023). "3D modelling of the impact of stellar activity on tidally locked terrestrial exoplanets: atmospheric composition and habitability". In: *Monthly Notices of the Royal Astronomical*

Society 518.2, pp. 2472–2496. DOI: 10.1093/mnras/stac3105. arXiv: 2210.13257 [astro-ph.EP].

Rodríguez, A., Callegari, N., Michtchenko, T. A., and Hussmann, H. (Dec. 2012). "Spin-orbit coupling for tidally evolving super-Earths". In: *Monthly Notices of the Royal Astronomical Society* 427.3, pp. 2239–2250. DOI: 10.1111/j.1365-2966.2012.22084.x. arXiv: 1209.1580 [astro-ph.EP].

Roettenbacher, Rachael M. and Kane, Stephen R. (Dec. 2017). "The Stellar Activity of TRAPPIST-1 and Consequences for the Planetary Atmospheres". In: *Astrophysical Journal* 851.2, 77. DOI: 10.3847/1538-4357/aa991e. arXiv: 1711.02676 [astro-ph.SR].

Rogers, Leslie A. (Mar. 2015). "Most 1.6 Earth-radius Planets are Not Rocky". In: *Astrophysical Journal* 801.1, 41. DOI: 10.1088/0004-637X/801/1/41. arXiv: 1407.4457 [astro-ph.EP].

Rugheimer, S. and Kaltenegger, L. (Feb. 2018). "Spectra of Earth-like Planets through Geological Evolution around FGKM Stars". In: *Astrophysical Journal* 854.1, 19. DOI: 10.3847/1538-4357/aaa47a. arXiv: 1712.10027 [astro-ph.EP].

Safonova, Margarita, Mathur, Archana, Basak, Suryoday, Bora, Kakoli, and Agrawal, Surbhi (May 2021). "Quantifying the classification of exoplanets: in search for the right habitability metric". In: *European Physical Journal Special Topics* 230.10, pp. 2207–2220. DOI: 10.1140/epjs/s11734-021-00211-z. arXiv: 2104.02991 [astro-ph.EP].

Sainsbury-Martinez, F., Walsh, C., Cooke, G. J., and Marsh, D. R. (July 2024). "How Land-Mass Distribution Influences the Atmospheric Dynamics of Tidally Locked Terrestrial Exoplanets". In: *arXiv e-prints*, arXiv:2407.01480. DOI: 10.48550/arXiv.2407.01480. arXiv: 2407.01480 [astro-ph.EP].

Salazar, A. M., Olson, S., Komacek, T. D., Stephens, H., and Abbot, D. S. (Dec. 2020a). "The Effect of Substellar Continent Size on Ocean Dynamics of Proxima Centauri b". In: *AGU Fall Meeting Abstracts*. Vol. 2020, P013-0015, P013–0015.

Salazar, Andrea M., Olson, Stephanie L., Komacek, Thaddeus D., Stephens, Haynes, and Abbot, Dorian S. (June 2020b). "The Effect of Substellar Continent Size on Ocean Dynamics of Proxima Centauri b". In: *Astrophysical Journal Letters* 896.1, L16. DOI: 10.3847/2041-8213/ab94c1. arXiv: 2005.14185 [astro-ph.EP].

Schlawin, Everett, Leisenring, Jarron, Misselt, Karl, Greene, Thomas P., McElwain, Michael W., Beatty, Thomas, and Rieke, Marcia (Nov. 2020). "JWST Noise Floor. I. Random Error Sources in JWST NIRCam Time Series". In: *Astronomical Journal* 160.5, 231. DOI: 10.3847/1538-3881/abb811. arXiv: 2010.03564 [astro-ph.IM].

Schulze-Makuch, Dirk, Heller, René, and Guinan, Edward (Dec. 2020). "In Search for a Planet Better than Earth: Top Contenders for a Superhabitable World". In: *Astrobiology* 20.12, pp. 1394–1404. DOI: 10.1089/ast.2019.2161.

Schwieterman, Edward W. and Leung, Michaela (July 2024). "An Overview of Exoplanet Biosignatures". In: *Reviews in Mineralogy and Geochemistry* 90.1, pp. 465–514. DOI: 10.2138/rmg.2024.90.13. arXiv: 2404.15431 [astro-ph.EP].

Seager, S., Turner, E. L., Schafer, J., and Ford, E. B. (June 2005). "Vegetation's Red Edge: A Possible Spectroscopic Biosignature of Extraterrestrial Plants". In: *Astrobiology* 5.3, pp. 372–390. DOI: 10.1089/ast.2005.5.372. arXiv: astro-ph/0503302 [astro-ph].

Seeley, Jacob T. and Wordsworth, Robin D. (Nov. 2021). "Episodic deluges in simulated hothouse climates". In: *Nature* 599.7883, pp. 74–79. DOI: 10.1038/s41586-021-03919-z. arXiv: 2111.03109 [astro-ph.EP].

Serdyuchenko, A., Gorshelev, V., Weber, M., Chehade, W., and Burrows, J. P. (2014). "High spectral resolution ozone absorption cross-sections – Part 2: Temperature dependence". In: *Atmospheric Measurement Techniques* 7.2, pp. 625–636. DOI: 10.5194/amt-7-625-2014. URL: https://amt.copernicus.org/articles/7/625/2014/.

Sergeev, Denis E., Lambert, F. Hugo, Mayne, Nathan J., Boutle, Ian A., Manners, James, and Kohary, Krisztian (May 2020). "Atmospheric Convection Plays a Key Role in the Climate of Tidally Locked Terrestrial Exoplanets: Insights from High-resolution Simulations". In: *Astrophysical Journal* 894.2, 84. DOI: 10.3847/1538-4357/ab8882. arXiv: 2004.03007 [astro-ph.EP].

Shields, Aomawa L., Ballard, Sarah, and Johnson, John Asher (Dec. 2016a). "The habitability of planets orbiting M-dwarf stars". In: *Physics Reports* 663, p. 1. DOI: 10.1016/j.physrep.2016.10.003. arXiv: 1610.05765 [astro-ph.EP].

Shields, Aomawa L., Barnes, Rory, Agol, Eric, Charnay, Benjamin, Bitz, Cecilia, and Meadows, Victoria S. (June 2016b). "The Effect of Orbital Configuration on the Possible Climates and Habitability of Kepler-62f". In: *Astrobiology* 16.6, pp. 443–464. DOI: 10.1089/ast.2015.1353. arXiv: 1603.01272 [astro-ph.EP].

Shields, Aomawa L., Meadows, Victoria S., Bitz, Cecilia M., Pierrehumbert, Raymond T., Joshi, Manoj M., and Robinson, Tyler D. (Aug. 2013). "The Effect of Host Star Spectral Energy Distribution and Ice-Albedo Feedback on the Climate of Extrasolar Planets". In: *Astrobiology* 13.8, pp. 715–739. DOI: 10.1089/ast.2012.0961. arXiv: 1305.6926 [astro-ph.EP].

Smith, R, Jones, P, Briegleb, B, Bryan, F, Danabasoglu, G, Dennis, J, Dukowicz, J, Eden, C, Fox-Kemper, B, Gent, P, et al. (2010). "The parallel ocean program (POP) reference manual ocean component of the community climate system model (CCSM) and community earth system model (CESM)". In: *LAUR-01853* 141, pp. 1–140.

Snellen, I. A. G., de Kok, R. J., le Poole, R., Brogi, M., and Birkby, J. (Feb. 2013). "Finding Extraterrestrial Life Using Ground-based High-dispersion Spectroscopy". In: *Astrophysical Journal* 764.2, 182. DOI: 10.1088/0004-637X/764/2/182. arXiv: 1302.3251 [astro-ph.EP].

Snellen, I. A. G., Désert, J. -M., Waters, L. B. F. M., Robinson, T., Meadows, V., van Dishoeck, E. F., Brandl, B. R., Henning, T., Bouwman, J., Lahuis, F., Min, M., Lovis, C., Dominik, C., Van Eylen, V., Sing, D., Anglada-Escudé, G., Birkby, J. L., and Brogi, M. (Aug. 2017). "Detecting Proxima b's Atmosphere with JWST Targeting CO_2 at 15 μm Using a High-pass Spectral Filtering Technique". In: *Astronomical Journal* 154.2, 77. DOI: 10.3847/1538-3881/aa7fbc. arXiv: 1707.08596 [astro-ph.EP].

Song, Xinyi, Abbot, Dorian S., and Yang, Jun (July 2023). "Critical role of vertical radiative cooling contrast in triggering episodic deluges in small-domain hothouse climates". In: *arXiv e-prints*, arXiv:2307.01219. DOI: 10.48550/arXiv.2307.01219. arXiv: 2307.01219 [physics.ao-ph].

Spaulding-Astudillo, Francisco E. and Mitchell, Jonathan L. (June 2023). "The emergence of relaxation-oscillator convection on Earth and Titan". In: *arXiv e-prints*, arXiv:2306.03219. DOI: 10.48550/arXiv.2306.03219. arXiv: 2306.03219 [astro-ph.EP].

Sproß, L., Scherf, M., Shematovich, V. I., Bisikalo, D. V., and Lammer, H. (Apr. 2021). "Life as the Only Reason for the Existence of N_2-O_2-Dominated Atmospheres". In: *Astronomy Reports* 65.4, pp. 275–296. DOI: 10.1134/S1063772921040077. arXiv: 2103.09264 [astro-ph.EP].

Stolarski, R. S. (Jan. 1986). "Aeronomy of the Middle Atmosphere". In: *EOS Transactions* 67.9, pp. 114–115. DOI: 10.1029/EO067i009p00114-03.

Tesfa, T. K., Li, H. -Y., Leung, L. R., Huang, M., Ke, Y., Sun, Y., and Liu, Y. (May 2014). "A subbasin-based framework to represent land surface processes in an Earth system

model". In: *Geoscientific Model Development* 7.3, pp. 947–963. DOI: 10.5194/gmd-7-947-201410.5194/gmdd-6-2699-2013.

Thomas, Trent, Hu, Renyu, and Lo, Daniel (Dec. 2022). "Constraints on the Evolution and Ancient Composition of the Martian Atmosphere from Coupled CO_2-N_2-Ar Isotopic Evolution Models". In: *AAS/Division for Planetary Sciences Meeting Abstracts*. Vol. 54. AAS/Division for Planetary Sciences Meeting Abstracts, 209.04.

Tilley, Matt A., Segura, Antígona, Meadows, Victoria, Hawley, Suzanne, and Davenport, James (Jan. 2019). "Modeling Repeated M Dwarf Flaring at an Earth-like Planet in the Habitable Zone: Atmospheric Effects for an Unmagnetized Planet". In: *Astrobiology* 19.1, pp. 64–86. DOI: 10.1089/ast.2017.1794. arXiv: 1711.08484 [astro-ph.EP].

Tritscher, Ines, Pitts, Michael C., Poole, Lamont R., Alexander, Simon P., Cairo, Francesco, Chipperfield, Martyn P., Grooß, Jens-Uwe, Höpfner, Michael, Lambert, Alyn, Luo, Beiping, Molleker, Sergey, Orr, Andrew, Salawitch, Ross, Snels, Marcel, Spang, Reinhold, Woiwode, Wolfgang, and Peter, Thomas (June 2021). "Polar Stratospheric Clouds: Satellite Observations, Processes, and Role in Ozone Depletion". In: *Reviews of Geophysics* 59.2, e2020RG000702. DOI: 10.1029/2020RG000702.

Turbet, Martin, Bolmont, Emeline, Chaverot, Guillaume, Ehrenreich, David, Leconte, Jérémy, and Marcq, Emmanuel (Oct. 2021). "Day-night cloud asymmetry prevents early oceans on Venus but not on Earth". In: *Nature* 598.7880, pp. 276–280. DOI: 10.1038/s41586-021-03873-w. arXiv: 2110.08801 [astro-ph.EP].

Turbet, Martin, Bolmont, Emeline, Leconte, Jeremy, Forget, François, Selsis, Franck, Tobie, Gabriel, Caldas, Anthony, Naar, Joseph, and Gillon, Michaël (May 2018). "Modeling climate diversity, tidal dynamics and the fate of volatiles on TRAPPIST-1 planets". In: *Astronomy and Astrophysics* 612, A86. DOI: 10.1051/0004-6361/201731620. arXiv: 1707.06927 [astro-ph.EP].

Turbet, Martin, Leconte, Jérémy, Selsis, Franck, Bolmont, Emeline, Forget, François, Ribas, Ignasi, Raymond, Sean N., and Anglada-Escudé, Guillem (Dec. 2016). "The habitability of Proxima Centauri b. II. Possible climates and observability". In: *Astronomy and Astrophysics* 596, A112. DOI: 10.1051/0004-6361/201629577. arXiv: 1608.06827 [astro-ph.EP].

Valente, Ema F. S. and Correia, Alexandre C. M. (Sept. 2022). "Tidal excitation of the obliquity of Earth-like planets in the habitable zone of M-dwarf stars". In: *Astronomy and Astrophysics* 665, A130. DOI: 10.1051/0004-6361/202244010. arXiv: 2307.08770 [astro-ph.EP].

Van Eylen, Vincent and Albrecht, Simon (Aug. 2015). "Eccentricity from Transit Photometry: Small Planets in Kepler Multi-planet Systems Have Low Eccentricities". In: *Astrophysical Journal* 808.2, 126. DOI: 10.1088/0004-637X/808/2/126. arXiv: 1505.02814 [astro-ph.EP].

Van Looveren, Gwenaël, Güdel, Manuel, Boro Saikia, Sudeshna, and Kislyakova, Kristina (Mar. 2024). "Airy worlds or barren rocks? On the survivability of secondary atmospheres around the TRAPPIST-1 planets". In: *Astronomy and Astrophysics* 683, A153. DOI: 10.1051/0004-6361/202348079. arXiv: 2401.16490 [astro-ph.EP].

Vaughan, Sophia R., Birkby, Jayne L., Thatte, Niranjan, Carlotti, Alexis, Houllé, Mathis, Pereira-Santaella, Miguel, Clarke, Fraser, Vigan, Arthur, Lin, Zifan, and Kaltenegger, Lisa (Feb. 2024). "Behind the mask: can HARMONI@ELT detect biosignatures in the reflected light of Proxima b?" In: *Monthly Notices of the Royal Astronomical Society* 528.2, pp. 3509–3522. DOI: 10.1093/mnras/stae242. arXiv: 2401.09589 [astro-ph.EP].

Vaughan, Sophia R., Gebhard, Timothy D., Bott, Kimberly, Casewell, Sarah L., Cowan, Nicolas B., Doelman, David S., Kenworthy, Matthew, Mazoyer, Johan, Millar-Blanchaer, Maxwell A., Trees, Victor J. H., Stam, Daphne M., Absil, Olivier, Altinier, Lisa, Bau-

doz, Pierre, Belikov, Ruslan, Bidot, Alexis, Birkby, Jayne L., Bonse, Markus J., Brandl, Bernhard, Carlotti, Alexis, Choquet, Elodie, van Dam, Dirk, Desai, Niyati, Fogarty, Kevin, Fowler, J., van Gorkom, Kyle, Gutierrez, Yann, Guyon, Olivier, Haffert, Sebastiaan Y., Herscovici-Schiller, Olivier, Hours, Adrien, Juanola-Parramon, Roser, Kleisioti, Evangelia, König, Lorenzo, van Kooten, Maaike, Krasteva, Mariya, Laginja, Iva, Landman, Rico, Leboulleux, Lucie, Mouillet, David, N'Diaye, Mamadou, Por, Emiel H., Pueyo, Laurent, and Snik, Frans (Oct. 2023). "Chasing rainbows and ocean glints: Inner working angle constraints for the Habitable Worlds Observatory". In: *Monthly Notices of the Royal Astronomical Society* 524.4, pp. 5477–5485. DOI: 10.1093/mnras/stad2127. arXiv: 2307.15137 [astro-ph.EP].

Villanueva, G. L., Smith, M. D., Protopapa, S., Faggi, S., and Mandell, A. M. (Sept. 2018). "Planetary Spectrum Generator: An accurate online radiative transfer suite for atmospheres, comets, small bodies and exoplanets". In: *Journal of Quantitative Spectroscopy and Radiative Transfer* 217, pp. 86–104. DOI: 10.1016/j.jqsrt.2018.05.023. arXiv: 1803.02008 [astro-ph.EP].

Villanueva, Geronimo Luis, Liuzzi, Giuliano, Faggi, Sara, Protopapa, Silvia, Kofman, Vincent, Fauchez, Thomas, Stone, Shane Wesley, and Mandell, Avi Max (2022). *Fundamentals of the Planetary Spectrum Generator*.

von der Heydt, Anna S., Ashwin, Peter, Camp, Charles D., Crucifix, Michel, Dijkstra, Henk A., Ditlevsen, Peter, and Lenton, Timothy M. (Feb. 2021). "Quantification and interpretation of the climate variability record". In: *Global and Planetary Change* 197, 103399. DOI: 10.1016/j.gloplacha.2020.103399. arXiv: 2101.08050 [physics.ao-ph].

Walker, J. C. G., Hays, P. B., and Kasting, J. F. (Oct. 1981). "A negative feedback mechanism for the long-term stabilization of the earth's surface temperature". In: *Journal of Geophysical Research* 86, pp. 9776–9782. DOI: 10.1029/JC086iC10p09776.

Way, M. J., Aleinov, I., Amundsen, David S., Chandler, M. A., Clune, T. L., Del Genio, A. D., Fujii, Y., Kelley, M., Kiang, N. Y., Sohl, L., and Tsigaridis, K. (July 2017a). "Resolving Orbital and Climate Keys of Earth and Extraterrestrial Environments with Dynamics (ROCKE-3D) 1.0: A General Circulation Model for Simulating the Climates of Rocky Planets". In: *The Astrophysical Journal Supplement Series* 231.1, 12. DOI: 10.3847/1538-4365/aa7a06. arXiv: 1701.02360 [astro-ph.EP].

Way, M. J. and Del Genio, Anthony D. (May 2020). "Venusian Habitable Climate Scenarios: Modeling Venus Through Time and Applications to Slowly Rotating Venus-Like Exoplanets". In: *Journal of Geophysical Research (Planets)* 125.5, e06276. DOI: 10.1029/2019JE00627610.1002/essoar.10501118.3.

Way, M. J. and Georgakarakos, Nikolaos (Jan. 2017b). "Effects of Variable Eccentricity on the Climate of an Earth-like World". In: *Astrophysical Journal Letters* 835.1, L1. DOI: 10.3847/2041-8213/835/1/L1. arXiv: 1611.06133 [astro-ph.EP].

Way, M. J., Georgakarakos, Nikolaos, and Clune, Thomas L. (Dec. 2023). "Exploring Climate with Obliquity in a Variable-eccentricity Earth-like World". In: *Astronomical Journal* 166.6, 227. DOI: 10.3847/1538-3881/ad0373. arXiv: 2311.04167 [astro-ph.EP].

Webster, Peter J. (Jan. 1994). "The role of hydrological processes in ocean-atmosphere interactions". In: *Reviews of Geophysics* 32.4, pp. 427–476. DOI: 10.1029/94RG01873.

Westall, F., Höning, D., Avice, G., Gentry, D., Gerya, T., Gillmann, C., Izenberg, N., Way, M. J., and Wilson, C. (Mar. 2023). "The Habitability of Venus". In: *Space Science Reviews* 219.2, 17. DOI: 10.1007/s11214-023-00960-4.

Williams, Darren M. and Pollard, David (Jan. 2002). "Earth-like worlds on eccentric orbits: excursions beyond the habitable zone". In: *International Journal of Astrobiology* 1.1, pp. 61–69. DOI: 10.1017/S1473550402001064.

Winters, Jennifer G., Cloutier, Ryan, Medina, Amber A., Irwin, Jonathan M., Charbonneau, David, Astudillo-Defru, Nicola, Bonfils, Xavier, Howard, Andrew W., Isaacson, Howard, Bean, Jacob L., Seifahrt, Andreas, Teske, Johanna K., Eastman, Jason D., Twicken, Joseph D., Collins, Karen A., Jensen, Eric L. N., Quinn, Samuel N., Payne, Matthew J., Kristiansen, Martti H., Spencer, Alton, Vanderburg, Andrew, Zechmeister, Mathias, Weiss, Lauren M., Wang, Sharon Xuesong, Wang, Gavin, Udry, Stéphane, Terentev, Ivan A., Stürmer, Julian, Stefánsson, Gudmundur, Shporer, Avi, Shectman, Stephen, Sefako, Ramotholo, Schwengeler, Hans Martin, Schwarz, Richard P., Scarsdale, Nicholas, Rubenzahl, Ryan A., Roy, Arpita, Rosenthal, Lee J., Robertson, Paul, Petigura, Erik A., Pepe, Francesco, Omohundro, Mark, Murphy, Joseph M. Akana, Murgas, Felipe, Močnik, Teo, Montet, Benjamin T., Mennickent, Ronald, Mayo, Andrew W., Massey, Bob, Lubin, Jack, Lovis, Christophe, Lewin, Pablo, Kasper, David, Kane, Stephen R., Jenkins, Jon M., Huber, Daniel, Horne, Keith, Hill, Michelle L., Gorrini, Paula, Giacalone, Steven, Fulton, Benjamin, Forveille, Thierry, Figueira, Pedro, Fetherolf, Tara, Dressing, Courtney, D⃰**
Rodrigo F., Delfosse, Xavier, Dalba, Paul A., Dai, Fei, Cortés, C. C., Crossfield, Ian J. M., Crane, Jeffrey D., Conti, Dennis M., Collins, Kevin I., Chontos, Ashley, Butler, R. Paul, Brown, Peyton, Brady, Madison, Behmard, Aida, Beard, Corey, Batalha, Natalie M., and Almenara, Jose-Manuel (Apr. 2022). "A Second Planet Transiting LTT 1445A and a Determination of the Masses of Both Worlds". In: *Astronomical Journal* 163.4, 168. DOI: 10.3847/1538-3881/ac50a9. arXiv: 2107.14737 [astro-ph.EP].

Wolf, E. T. and Toon, O. B. (Jan. 2014). "Delayed onset of runaway and moist greenhouse climates for Earth". In: *Geophysical Research Letters* 41.1, pp. 167–172. DOI: 10.1002/2013GL058376.

– (June 2015). "The evolution of habitable climates under the brightening Sun". In: *Journal of Geophysical Research (Atmospheres)* 120.12, pp. 5775–5794. DOI: 10.1002/2015JD023302.

Wolf, Eric T. (Apr. 2017). "Assessing the Habitability of the TRAPPIST-1 System Using a 3D Climate Model". In: *Astrophysical Journal Letters* 839.1, L1. DOI: 10.3847/2041-8213/aa693a. arXiv: 1703.05815 [astro-ph.EP].

Wolf, Eric T., Shields, Aomawa L., Kopparapu, Ravi K., Haqq-Misra, Jacob, and Toon, Owen B. (Mar. 2017). "Constraints on Climate and Habitability for Earth-like Exoplanets Determined from a General Circulation Model". In: *Astrophysical Journal* 837.2, 107. DOI: 10.3847/1538-4357/aa5ffc. arXiv: 1702.03315 [astro-ph.EP].

Wolszczan, A. and Frail, D. A. (Jan. 1992). "A planetary system around the millisecond pulsar PSR1257 + 12". In: *Nature* 355.6356, pp. 145–147. DOI: 10.1038/355145a0.

Wordsworth, R. and Kreidberg, L. (Dec. 2021). "Atmospheres of Rocky Exoplanets". In: *arXiv e-prints*, arXiv:2112.04663. arXiv: 2112.04663 [astro-ph.EP].

Wunderlich, Fabian, Godolt, Mareike, Grenfell, John Lee, Städt, Steffen, Smith, Alexis M. S., Gebauer, Stefanie, Schreier, Franz, Hedelt, Pascal, and Rauer, Heike (Sept. 2019). "Detectability of Atmospheric Features of Earth-Like Planets in the Habitable Zone around Cool Host Stars". In: *EPSC-DPS Joint Meeting 2019*. Vol. 2019, EPSC-DPS2019-1567, EPSC-DPS2019–1567.

Yang, Jun and Abbot, Dorian S. (Apr. 2014). "A Low-order Model of Water Vapor, Clouds, and Thermal Emission for Tidally Locked Terrestrial Planets". In: *Astrophysical Journal* 784.2, 155. DOI: 10.1088/0004-637X/784/2/155. arXiv: 1403.0905 [astro-ph.EP].

Yang, Jun, Ji, Weiwen, and Zeng, Yaoxuan (Jan. 2020). "Transition from eyeball to snowball driven by sea-ice drift on tidally locked terrestrial planets". In: *Nature Astronomy* 4, pp. 58–66. DOI: 10.1038/s41550-019-0883-z. arXiv: 1912.11377 [astro-ph.EP].

Yang, Jun, Zhang, Yixiao, Fu, Zuntao, Yan, Mingyu, Song, Xinyi, Wei, Mengyu, Liu, Jiachen, Ding, Feng, and Tan, Zhihong (Sept. 2023). "Cloud behaviour on tidally

locked rocky planets from global high-resolution modelling". In: *Nature Astronomy* 7, pp. 1070–1080. DOI: 10.1038/s41550-023-02015-8. arXiv: 2306.12186 [astro-ph.EP].

Youngblood, Allison, France, Kevin, Loyd, R. O. Parke, Brown, Alexander, Mason, James P., Schneider, P. Christian, Tilley, Matt A., Berta-Thompson, Zachory K., Buccino, Andrea, Froning, Cynthia S., Hawley, Suzanne L., Linsky, Jeffrey, Mauas, Pablo J. D., Redfield, Seth, Kowalski, Adam, Miguel, Yamila, Newton, Elisabeth R., Rugheimer, Sarah, Segura, Antígona, Roberge, Aki, and Vieytes, Mariela (July 2017). "The MUSCLES Treasury Survey. IV. Scaling Relations for Ultraviolet, Ca II K, and Energetic Particle Fluxes from M Dwarfs". In: *Astrophysical Journal* 843.1, 31. DOI: 10.3847/1538-4357/aa76dd. arXiv: 1705.04361 [astro-ph.SR].

Zaliapin, I. and Ghil, M. (Mar. 2010). "Another look at climate sensitivity". In: *Nonlinear Processes in Geophysics* 17.2, pp. 113–122. DOI: 10.5194/npg-17-113-2010. arXiv: 1003.0253 [physics.ao-ph].

Zelinka, Mark D. and Hartmann, Dennis L. (Aug. 2010). "Why is longwave cloud feedback positive?" In: *Journal of Geophysical Research (Atmospheres)* 115.D16, D16117. DOI: 10.1029/2010JD013817.

Zeng, Guang, Morgenstern, Olaf, Williams, Jonny H. T., O'Connor, Fiona M., Griffiths, Paul T., Keeble, James, Deushi, Makoto, Horowitz, Larry W., Naik, Vaishali, Emmons, Louisa K., Abraham, N. Luke, Archibald, Alexander T., Bauer, Susanne E., Hassler, Birgit, Michou, Martine, Mills, Michael J., Murray, Lee T., Oshima, Naga, Sentman, Lori T., Tilmes, Simone, Tsigaridis, Kostas, and Young, Paul J. (Aug. 2022). "Attribution of Stratospheric and Tropospheric Ozone Changes Between 1850 and 2014 in CMIP6 Models". In: *Journal of Geophysical Research (Atmospheres)* 127.16, e2022JD036452. DOI: 10.1029/2022JD036452.

Zhang, Huihao, Wang, Ji, and Plummer, Michael K. (Jan. 2024). "Detecting Biosignatures in Nearby Rocky Exoplanets Using High-contrast Imaging and Medium-resolution

Spectroscopy with the Extremely Large Telescope". In: *Astronomical Journal* 167.1, 37. DOI: `10.3847/1538-3881/ad109e`. arXiv: `2311.18117 [astro-ph.EP]`.

Zieba, Sebastian, Kreidberg, Laura, Ducrot, Elsa, Gillon, Michaël, Morley, Caroline, Schaefer, Laura, Tamburo, Patrick, Koll, Daniel D. B., Lyu, Xintong, Acuña, Lorena, Agol, Eric, Iyer, Aishwarya R., Hu, Renyu, Lincowski, Andrew P., Meadows, Victoria S., Selsis, Franck, Bolmont, Emeline, Mandell, Avi M., and Suissa, Gabrielle (Aug. 2023). "No thick carbon dioxide atmosphere on the rocky exoplanet TRAPPIST-1 c". In: *Nature* 620.7975, pp. 746–749. DOI: `10.1038/s41586-023-06232-z`. arXiv: `2306.10150 [astro-ph.EP]`.